REPORT DOCUMENTATION PAGE

Form Approved OMB No. 0704-0188

1. AGENCY USE ONLY (Leave blank)	2. REPORT DATE 7 January 1998	3. REPORT TYPE AND DATES COVERED Conference Proceedings

4. TITLE AND SUBTITLE

Adaptive Optics for Industry and Medicine International Workshop

5. FUNDING NUMBERS

F6170897W0070

6. AUTHOR(S)

Conference Committee

7. PERFORMING ORGANIZATION NAME(S) AND ADDRESS(ES)

The Blackett Laboratory
Prince Consort Road
London SW7 2BZ
United Kingdom

8. PERFORMING ORGANIZATION REPORT NUMBER

N/A

9. SPONSORING/MONITORING AGENCY NAME(S) AND ADDRESS(ES)

EOARD
PSC 802 BOX 14
FPO 09499-0200

10. SPONSORING/MONITORING AGENCY REPORT NUMBER

CSP 97-1017

11. SUPPLEMENTARY NOTES

12a. DISTRIBUTION/AVAILABILITY STATEMENT

Approved for public release; distribution is unlimited.

12b. DISTRIBUTION CODE

A

13. ABSTRACT (Maximum 200 words)

The Final Proceedings for Adaptive Optics for Industry and Medicine, 9 June 1997 - 13 June 1997. Topics covered include: adaptive optics, nonlinear optical systems for improving laser beam quality, intracavity and extracavity beam correction, adaptive beam diagnostics.

19980203 028

14. SUBJECT TERMS

Imaging, Non-linear Optics, Optical Components, Adaptive Optics

15. NUMBER OF PAGES

16. PRICE CODE

N/A

17. SECURITY CLASSIFICATION OF REPORT	18. SECURITY CLASSIFICATION OF THIS PAGE	19. SECURITY CLASSIFICATION OF ABSTRACT	20. LIMITATION OF ABSTRACT
UNCLASSIFIED	UNCLASSIFIED	UNCLASSIFIED	UL

ADAPTIVE OPTICS FOR INDUSTRY AND MEDICINE

International Workshop

Shatura, Moscow Region, RUSSIA

June 9 to 13, 1997

CONFERENCE PAPERS

CSP 97-1017

Shatura Papers

1. E.M. Ellis & al. "Low-cost deformable mirrors"
2. M.J. Shaw & al. "Active Control of Phase Distortions in High Power Laser Systems"
3. A. Greenaway "UK Dual-Use Adaptive Optics Programme"
4. A.V. Kudryashov "Intracavity Adaptive Optics for Technology"
5. K. Nemoto & al. "Laser beam intensity profile control by adaptive optics"
6. P.-Y. Madec & al. "Development of an Adaptive Optics Sytem for SILVA"
7. Z. Zeng & al. "Laser beam shaping by deformable mirror"
8. D.Yu. Gorbenko & al. "Adaptive Systems with Modal Aperture Probing for Powerful Technological IR Lasers"
9. R.H. Dueck & al. "Low Cost Wavefront Sensor for Industrial Applications"
10. V. Samarkin "Computer Controlled Active Mirrors and Lens for Industrial Applications"
11. W. Jiang & al. "Applications of Shack-Hartmann wavefront sensor"
12. D. Voelz & al. "Optical Heterodyne Array Wavefront Sensing and Imaging"
13. B.M. Levine & al. "Shack-Hartmann wavefront sensing for optical metrology, and its application in real-time corrections of horizontal line of sight turbulence over near ground paths"
14. V.A. Tartarovski & al. "Adaptive Wavefront Sensor"
15. D.R. Williams & al. "Adaptive Optics for the Human Eye"
16. G. Vdovin & al. " Adaptive Optics for direct correction of a human vision"
17. V.V. Tuchin & al. "Controlling of the Optical Parameters in Biotissues"
18. S. Browne & al. "Liquid Crystal Phase Modulators for Time Varying Phase Distortion Production and Adaptive Optics"
19. G.D. Love & al. "The electrical and optical properties of liquid devices for adaptive optics"
20. A.F. Naumov "The Control Features of Liquid Crystal Modulators for Adaptive Optical Applications"
21. L. McMackin & al. "Prediction and Adaptive Correction of Optical Beam Jitter Caused by Organised Structure in Dynamic Air Flow Using Linear Stochastic Estimation"
22. H.J. Eichler & al. "Fiber Phase Conjugator as Wave Front Corrector for Industrial Laser Systems"
23. O.L. Antipov & al. "Phase Conjugate Mirror Based on Nd:YAG Crystal for High Power Laser Systems"
24. V.I. Shmalhausen & al. "Anisoplanatic Effect in Viewing at Short Distances"

The list of participants of the International Workshop
on Adaptive Optics for Industry and Medicine, 9-13 June 1997, Shatura, Russia.

1. **Gordon D. Love**, University of Durham, South Road, Durham DH1 3LE United Kingdom, E-mail:g.d.love@durham.ac.uk , fax: +44 0191 374 7465.

2. **Sergio R. Restaino**, Imaging branch, USAF Phillips Lab, PL/LIMI, Kirtland AFB, NM 87117, USA, fax: +1 (505) 846-2045

3. **David G. Voelz**, Imaging branch, USAF Phillips Lab, PL/LIMI, Kirtland AFB, NM 87117, USA, fax: (505) 846-2047; e-mail: voelz@plk.af.mil, mcmackin@plk.af.mil

4. **John Gonglewski**, Imaging branch, USAF Phillips Lab, PL/LIMI, Kirtland AFB, NM 87117, USA, fax: (505) 846-2047; e-mail:gonglewj@plk.af.mil

5. **David R. Williams**, director of Center for Visual Science, Univ. of Rochester, Rochester, NY 14627, USA.

6. **Lenore McMackin**, Imaging branch, USAF Phillips Lab, PL/LIMI, Kirtland AFB, NM 87117, USA, fax: (505) 846-2047; e-mail: mcmackin@plk.af.mil.

7. **Edric M. Ellis**, Blackett Laboratory, Imperial College, London SW7 2BZ, UK, fax:+44 171 594 7714 Internet:c.dainty@ic.ac.uk.

8. **Allan Greenaway**, Defense Research Agency, St. Andrews Road, Malvern, Worcs, WR14 3PS, UK, fax: +44 1684 894498

9. **David J.Robertson**, University of Durham, Department of Physics, South Road, Durham DH1 3LE, United Kingdom, fax: +44 0191 374 7465.

10. **Alexander Dehn**, Technische Universität Berlin, Optisches Institut, Sekr. P11, Str. d. 17. Juni 135, 10623, Berlin, Germany, fax: +49 30 314 26888, e-mail: alex@moebius.physik.tu-berlin.de.

11. **Gleb Vdovin**, Lab. of Electr. Instr. Delft Univ. of Technology, The Netherlands.

12. **Wenhan Jiang**, Hao Xian, Institute of Optics and Electronics, Chinese Academy of Sciences, P.O.Box 350, Shuangliu, Chengdu 610209, China, fax: +86-28-5180070, e-mail: whjiang@cdisn2.cdisn.cd.sc.cn.

13. **Zhige Zeng**, Institute of Optics and Electronics, Chinese Academy of Sciences, P.O.Box 350 Shuangliu, Chengdu 610209, China, fax: +86-28-5180070, email:hjiang@cdisn2.cdisn.cd.sc.cn.

14. **Koshichi Nemoto**, Komae Research Laboratory, Central Research Institute of Electric Power Industry, 11-1 Iwado-Kita 2-chome, Komae-shi, Tokyo 201 JAPAN, fax: +81 3 3488 6697, e-mail: nemoto@criepi.denken.or.jp.

15. **Geun-Young Yoon**, Institute of Laser Engineering, Osaka University, 2-6, Yamada-oka, Suita. Osaka 565, Japan, tel: 81-6-879-8762, fax: 81-6-877-0900, e-mail: yoon@ile.osaka-u.ac.jp.

16. **Takahisa Jitsuno**, Institute of Laser Engineering, Osaka University, 2-6, Yamada-oka, Suita. Osaka 565, Japan, tel.: 81-6-879-8762, fax. : 81-6-877-0900, e-mail: yoon@ile.osaka-u.ac.jp.

17. **Victor I. Shmalhausen**, International Laser Center, Moscow State University, Vorob'evy Gory, 119899 Moscow, Russia, fax: +7 095 939 3113.

18. **Andrei V.Larichev**, International Laser Center, Moscow State University, Vorob'evy Gory, 119899 Moscow, Russia, fax: +7 095 939 3113; e-mail: larichev@to.infn.it.

19. **Vladimir P. Lukin**, Institute of Atmospheric Optics, Russian Academy of Sciences, Av. Academicheskii, 1, Tomsk, 634055, Tomsk, Russia, fax: +7 3822 25 90 86.

20. **Peter A. Bakut**, NPO ASTROPHIZIKA, Volokolamskaya 112, Moscow, 123423 Russia, fax: 095 491 21 21, e-mail: bakut@litmal.msk.ru

21. **Alexander F.Naumov**, P.N.Lebedev Physical Institute, Samara Branch, Novo-Sadovaja Str. 221, Samara 443011, Russia. Fax:(+7) (846 2) 35-56-00, e-mail: naumov@info.ssu.samara.ru.

22. **Oleg L.Antipov**, Institute of Applied Physics of the Russian Academy of Science, 46 Uljanov Str., Nizhny Novgorod, 603600, Russia. Fax: +7(831)2363792, e-mail: antipov@appl.sci-nnov.ru.

23. **Anatoli N. Kravets**, Kovrov State Technology Academy, 19 Mayakovsky Str., Kovrov, 601910, Russia. FAX: (09232) 3-59-54, e-mail: romb@kiber.vladimir.su.

24. **Viktor V. Valuev**, "Sistema" SIC, Moscow, Russia, Leningradsky prospect, 80. Fax:+7 095 158-7889.

25. **Oleg I. Shanin**, 142100 Russia, Moscow Region, Podolsk, 24 Zheleznodorozhnaya str., SIA "Lutch", e-mail: lutch.pdlsk.@rex.iasnet.ru.

26. **Vadim V.Samarkin**, NICTL - Laser Research Center, Russian Academy of Sciences, Svyatoozerskaya 1, Shatura, Moscow Region, 140700 Russia. Fax: +7 (09645) 22532, e-mail:adopt@laser.nictl.msk.su.

27. **Valeri A. Tartakovski**, Institute of Atmospheric Optics of the Russian Academy of Sciences, P.O.Box 3984, Tomsk, 634055 Russia, Fax: (3822)-25-90-86, e-mail: zuev@iao.tomsk.su.

28. **Vladimir V. Shkunov**, Institute of problems in Mechanics, Russian Academy of Sciences, Vernadskogo pr. 101, Moscow, 117 526 Russia, fax: +7 095 434 35 08

29. **Voldemar P. Koronkevich**, Institute of Automatic and Electrometry Russian Academy of Sciences, Universitetski pr. 1, Novosibirsk, 630090 Russia, fax: +7 383 2 35 48 51, email: koronkevich.v.p@iae.nsk.su

30. **Valery.V.Tuchin**, Saratov State University, Astrakhanskaya 89, Saratov, 410071 Russia, e-mail: tuchin@scnit.saratov.su

31. **Vladislav Ya. Panchenko**, NICTL - Laser Research Center, Russian Academy of Sciences, Svyatoozerskaya 1, Shatura, Moscow Region, 140700 Russia.Fax: +7 (09645) 22532, e-mail: panch@laser.nictl.msk.su.

32. **Alexis V. Kudryashov**, NICTL Russian Academy of Sciences - Phillips Lab USAF, Svyatoozerskaya 1, Shatura, Moscow Region, 140700 Russia.Fax: +7 (09645) 22532, e-mail:kud@lado.phys.msu.su, koudriea@plk.af.mil.

33. **Mike J. Shaw**, I N Ross, Central Laser Facility, Rutherford Appleton Laboratory, Chilton, Didcot, Oxon, OX11, 0QX, United Kingdom. FAX: +44 123 544 5888, e-mail: mick.shaw@rl.ac.uk.

34. **Steve Browne**, the Optical Sciences Company, PO Box 25309, Anaheim, CA 92825, fax:+1 (714)772 -9870.

35. **Vladimir A. Semchishen**, NICTL -Laser Research Center, Russian Academy of Sciences, Svyatoozerskaya 1, Shatura, Moscow Region, 140700 Russia.Fax: +7 (09645) 22532, e-mail: panch@laser.nictl.msk.su.

36. **B.Martin Levine**, Adaptive Optics Associate, 54 Cambridge Park Drive, Cambridge, MA 02140, fax:+1 617 864 1348, e-mail:marty@aoainc.com.

37. **Janet Fender**, President of OSA, Imaging branch, USAF Phillips Lab, PL/LIMI, Kirtland AFB, NM 87117, USA, fax: (505) 846-2047.

38. **Chris J. Dainty**, Blackett Laboratory, Imperial College, London SW7 2BZ, UK. Fax:+44 171 594 7714, Internet: c.dainty@ic.ac.uk.

39. **Mathias Ridou**, Blackett Laboratory, Imperial College, London SW7 2BZ, UK. Fax:+44 171 594 7714, Internet: c.dainty@ic.ac.uk.

40. **Austin J. Roorda**, Center for Visual Science, Univ. of Rochester, Rochester, NY 14627, USA, fax: +1 716 271 3043.

41. **John Otten**, vice- president of Kestrel Corp., 6624 Gulton Court NE, Albuquerque, NM 87109 USA, fax: +1 505 345 2649.

42. **Ken-ichi Ueda**, Prof. of Univ. of Electro-Commun., 1-5-1 Chofugaoka, Chofu-shi, Tokyo, 182 Japan, fax: +81 424 85 8960

43. **David Hennage**, director of OSA

44. **Vladimir Seminogov**, NICTL - Laser Research Center, Russian Academy of Sciences, Svyatoozerskaya 1, Shatura, Moscow Region, 140700 Russia. Fax: +7 (09645) 22532, e-mail: panch@laser.nictl.msk.su.

45. **Francois Charbonnier**, Dr. of National d'Etudes et de Recherches Aerospatiaes, Physics Department, High Resolution Imaging Division, 29 Av. de la Division Leclerc, Chation, CEDEX,, BP 72, 92322 France, Fax: +33 01 46 73 41 48.

46. **Yanka I.Malashko**, "Sistema" SIC, Moscow, Leningradsky prospect, 80, Fax: +7 095 158-89-78.

47. **Diaz Santana Haro Luis**, Blackett Laboratory, Imperial College, London SW7 2BZ, UK, fax:+44 171 594 7714 ; Internet:c.dainty@ic.ac.uk.

48. **Van Neste Richard**, Fiso Technologies, inc., 2300-110 Leon-Harmel, Quebec City, Quebec, GIN 4I2, Canada, Fax: (418) 688 8067.

49. **Martin Fernando Vargas**, Lab. de Optica, Dept. Fisica, Universidad de Murcia, Campus de Espinardo (Edificio C), Murcia, 30071, Spain, Fax: 3468-363528.

50. **Hao Xian**, Institute of Optics and Electronics, Chinese Academy of Sciences, P.O.Box 350, Shuangliu, Chengdu 610209, China, fax: +86-28-5180070

51. **Edmund I.Akopov**, Executive director of SPIE Rus., Moscow, Mohovaya,12, SPIE/RUS

52. **Tatyana Cherezova**, International Laser Center, Moscow State University, Vorob'evy Gory, 119899 Moscow, Russia, fax: +7 095 939 3113.
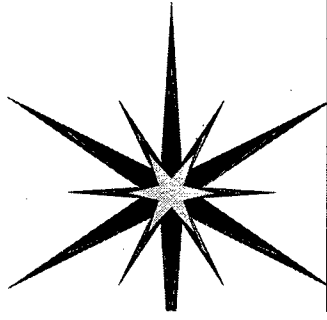
Low-cost deformable mirrors

E. M. Ellis, M. Ridou, M. L. Holohan
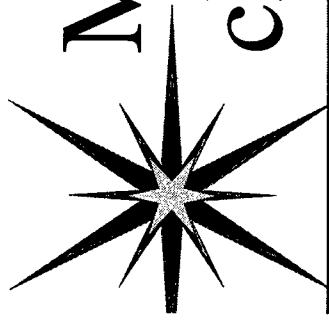and J. C. Dainty

Imperial College, London.
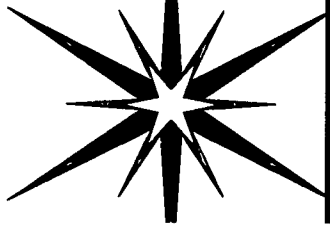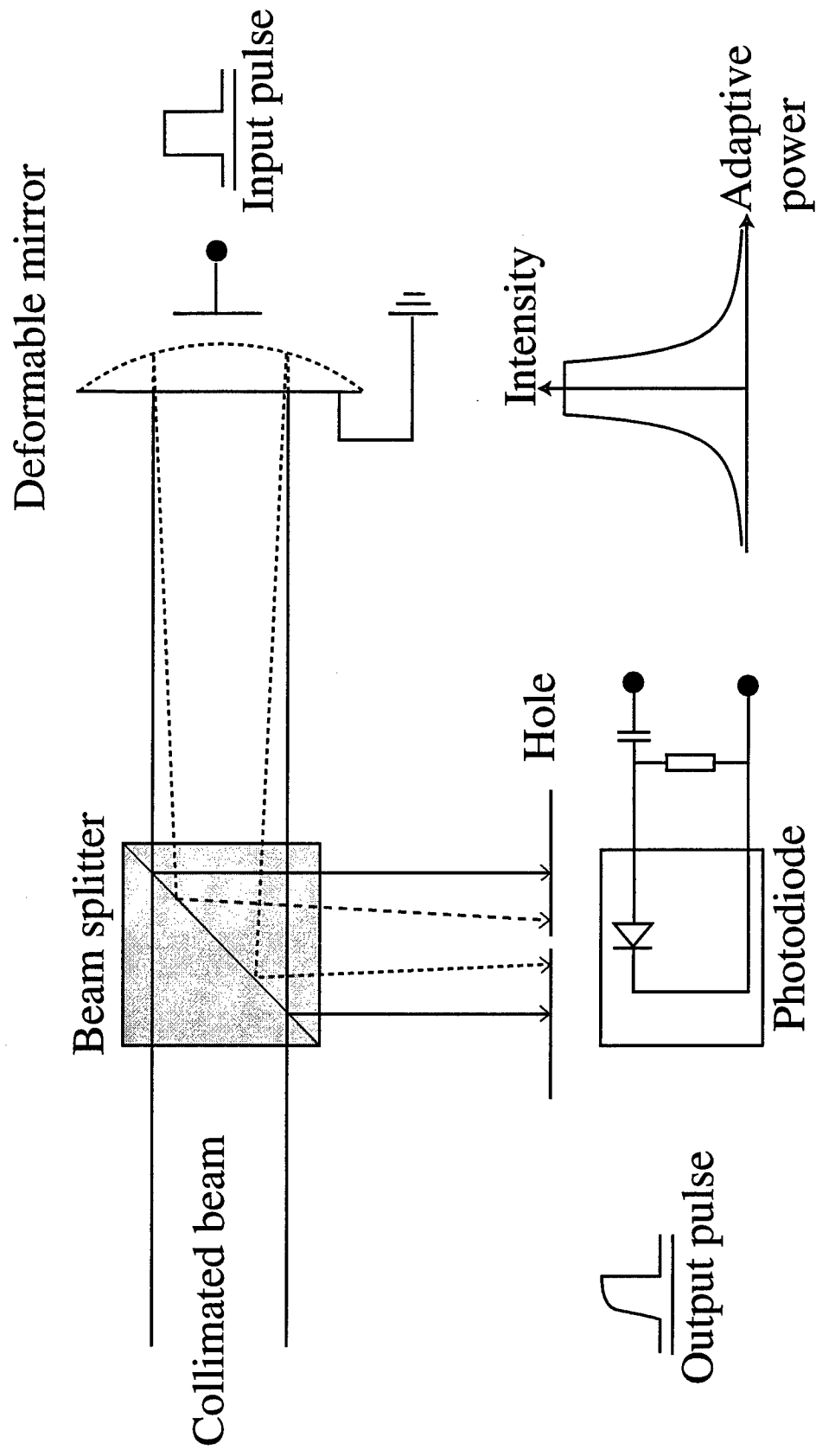
Low Cost Deformable Mirrors

- Context of Research: Low Cost AO Systems
  - ✦ IC Bimorph Mirrors: First Results
  - ✦ MSU/NICTL Bimorph 17-element Mirror
  - ✦ Delft 27-element Circular Membrane Mirror
  - ✦ Control Processors: C80 Experience
  - ✦ Future Research
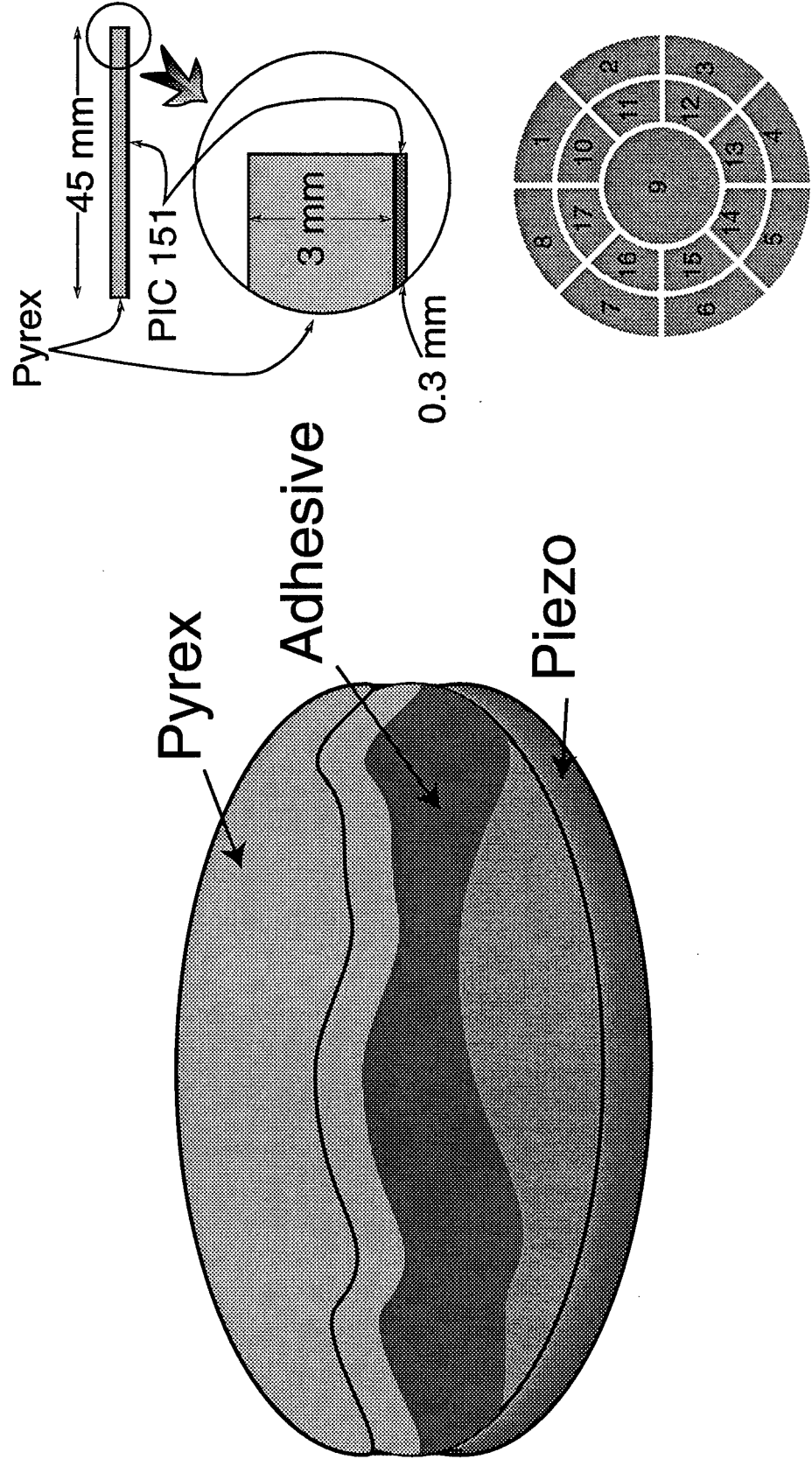
Measuring temporal characteristics

Deformable mirror

Input pulse

Beam splitter

Collimated beam

Hole

Photodiode

Output pulse

Intensity

Adaptive power

■ Interferometer Zernike Polynomials

j	$\{n, m\}$	polynomial
1	$\{1, 1\}$	$\rho \cos(\theta)$
2	$\{1, 1\}$	$\rho \sin(\theta)$
3	$\{2, 0\}$	$2\rho^2 - 1$
4	$\{2, 2\}$	$\rho^2 \cos(2\theta)$
5	$\{2, 2\}$	$\rho^2 \sin(2\theta)$
6	$\{3, 1\}$	$(3\rho^3 - 2\rho)\cos(\theta)$
7	$\{3, 1\}$	$(3\rho^3 - 2\rho)\sin(\theta)$
8	$\{4, 0\}$	$6\rho^4 - 6\rho^2 + 1$
9	$\{3, 3\}$	$\rho^3 \cos(3\theta)$
10	$\{3, 3\}$	$\rho^3 \sin(3\theta)$
11	$\{4, 2\}$	$(4\rho^4 - 3\rho^2)\cos(2\theta)$
12	$\{4, 2\}$	$(4\rho^4 - 3\rho^2)\sin(2\theta)$
13	$\{5, 1\}$	$(10\rho^5 + 3\rho - 12\rho^3)\cos(\theta)$
14	$\{5, 1\}$	$(10\rho^5 + 3\rho - 12\rho^3)\sin(\theta)$
15	$\{6, 0\}$	$20\rho^6 + 12\rho^2 - 30\rho^4 - 1$
16	$\{4, 4\}$	$\rho^4 \cos(4\theta)$
17	$\{4, 4\}$	$\rho^4 \sin(4\theta)$
18	$\{5, 3\}$	$(5\rho^5 - 4\rho^3)\cos(3\theta)$
19	$\{5, 3\}$	$(5\rho^5 - 4\rho^3)\sin(3\theta)$
20	$\{6, 2\}$	$(15\rho^6 + 6\rho^2 - 20\rho^4)\cos(2\theta)$
21	$\{6, 2\}$	$(15\rho^6 + 6\rho^2 - 20\rho^4)\sin(2\theta)$
22	$\{7, 1\}$	$(35\rho^7 + 30\rho^3 - 4\rho - 60\rho^5)\cos(\theta)$
23	$\{7, 1\}$	$(35\rho^7 + 30\rho^3 - 4\rho - 60\rho^5)\sin(\theta)$
24	$\{8, 0\}$	$70\rho^8 + 90\rho^4 - 20\rho^2 - 140\rho^6 + 1$
25	$\{5, 5\}$	$\rho^5 \cos(5\theta)$
26	$\{5, 5\}$	$\rho^5 \sin(5\theta)$
27	$\{6, 4\}$	$(6\rho^6 - 5\rho^4)\cos(4\theta)$
28	$\{6, 4\}$	$(6\rho^6 - 5\rho^4)\sin(4\theta)$
29	$\{7, 3\}$	$(21\rho^7 + 10\rho^3 - 30\rho^5)\cos(3\theta)$
30	$\{7, 3\}$	$(21\rho^7 + 10\rho^3 - 30\rho^5)\sin(3\theta)$
31	$\{8, 2\}$	$(56\rho^8 + 60\rho^4 - 10\rho^2 - 105\rho^6)\cos(2\theta)$
32	$\{8, 2\}$	$(56\rho^8 + 60\rho^4 - 10\rho^2 - 105\rho^6)\sin(2\theta)$
33	$\{9, 1\}$	$(126\rho^9 + 210\rho^5 + 5\rho - 60\rho^3 - 280\rho^7)\cos(\theta)$
34	$\{9, 1\}$	$(126\rho^9 + 210\rho^5 + 5\rho - 60\rho^3 - 280\rho^7)\sin(\theta)$
35	$\{10, 0\}$	$252\rho^{10} + 560\rho^6 + 30\rho^2 - 210\rho^4 - 630\rho^8 - 1$
36	$\{12, 0\}$	$924\rho^{12} + 3150\rho^8 + 420\rho^4 - 42\rho^2 - 1680\rho^6 - 2772\rho^{10} + 1$

■ Noll Zernike Polynomials

j	$\{n, m\}$	polynomial
1	$\{0, 0\}$	1
2	$\{1, 1\}$	$2\,\rho\cos(\theta)$
3	$\{1, 1\}$	$2\,\rho\sin(\theta)$
4	$\{2, 0\}$	$\sqrt{3}\,(2\,\rho^2 - 1)$
5	$\{2, 2\}$	$\sqrt{6}\,\rho^2\sin(2\,\theta)$ ⟵
6	$\{2, 2\}$	$\sqrt{6}\,\rho^2\cos(2\,\theta)$
7	$\{3, 1\}$	$2\sqrt{2}\,(3\,\rho^3 - 2\,\rho)\sin(\theta)$
8	$\{3, 1\}$	$2\sqrt{2}\,(3\,\rho^3 - 2\,\rho)\cos(\theta)$
9	$\{3, 3\}$	$2\sqrt{2}\,\rho^3\sin(3\,\theta)$
10	$\{3, 3\}$	$2\sqrt{2}\,\rho^3\cos(3\,\theta)$
11	$\{4, 0\}$	$\sqrt{5}\,(6\,\rho^4 - 6\,\rho^2 + 1)$
12	$\{4, 2\}$	$\sqrt{10}\,(4\,\rho^4 - 3\,\rho^2)\cos(2\,\theta)$
13	$\{4, 2\}$	$\sqrt{10}\,(4\,\rho^4 - 3\,\rho^2)\sin(2\,\theta)$
14	$\{4, 4\}$	$\sqrt{10}\,\rho^4\cos(4\,\theta)$
15	$\{4, 4\}$	$\sqrt{10}\,\rho^4\sin(4\,\theta)$
16	$\{5, 1\}$	$2\sqrt{3}\,(10\,\rho^5 + 3\,\rho - 12\,\rho^3)\cos(\theta)$
17	$\{5, 1\}$	$2\sqrt{3}\,(10\,\rho^5 + 3\,\rho - 12\,\rho^3)\sin(\theta)$
18	$\{5, 3\}$	$2\sqrt{3}\,(5\,\rho^5 - 4\,\rho^3)\cos(3\,\theta)$
19	$\{5, 3\}$	$2\sqrt{3}\,(5\,\rho^5 - 4\,\rho^3)\sin(3\,\theta)$
20	$\{5, 5\}$	$2\sqrt{3}\,\rho^5\cos(5\,\theta)$
21	$\{5, 5\}$	$2\sqrt{3}\,\rho^5\sin(5\,\theta)$
22	$\{6, 0\}$	$\sqrt{7}\,(20\,\rho^6 + 12\,\rho^2 - 30\,\rho^4 - 1)$
23	$\{6, 2\}$	$\sqrt{14}\,(15\,\rho^6 + 6\,\rho^2 - 20\,\rho^4)\sin(2\,\theta)$
24	$\{6, 2\}$	$\sqrt{14}\,(15\,\rho^6 + 6\,\rho^2 - 20\,\rho^4)\cos(2\,\theta)$
25	$\{6, 4\}$	$\sqrt{14}\,(6\,\rho^6 - 5\,\rho^4)\sin(4\,\theta)$
26	$\{6, 4\}$	$\sqrt{14}\,(6\,\rho^6 - 5\,\rho^4)\cos(4\,\theta)$
27	$\{6, 6\}$	$\sqrt{14}\,\rho^6\sin(6\,\theta)$
28	$\{6, 6\}$	$\sqrt{14}\,\rho^6\cos(6\,\theta)$
29	$\{7, 1\}$	$4\,(35\,\rho^7 + 30\,\rho^3 - 4\,\rho - 60\,\rho^5)\sin(\theta)$
30	$\{7, 1\}$	$4\,(35\,\rho^7 + 30\,\rho^3 - 4\,\rho - 60\,\rho^5)\cos(\theta)$
31	$\{7, 3\}$	$4\,(21\,\rho^7 + 10\,\rho^3 - 30\,\rho^5)\sin(3\,\theta)$
32	$\{7, 3\}$	$4\,(21\,\rho^7 + 10\,\rho^3 - 30\,\rho^5)\cos(3\,\theta)$
33	$\{7, 5\}$	$4\,(7\,\rho^7 - 6\,\rho^5)\sin(5\,\theta)$
34	$\{7, 5\}$	$4\,(7\,\rho^7 - 6\,\rho^5)\cos(5\,\theta)$
35	$\{7, 7\}$	$4\,\rho^7\sin(7\,\theta)$
36	$\{7, 7\}$	$4\,\rho^7\cos(7\,\theta)$
37	$\{8, 0\}$	$3\,(70\,\rho^8 + 90\,\rho^4 - 20\,\rho^2 - 140\,\rho^6 + 1)$
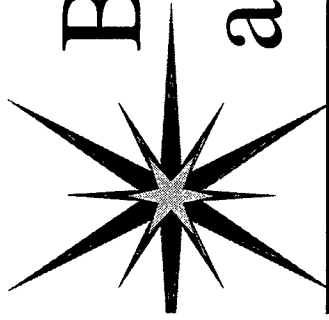
Bimorph mirrors in construction at IC
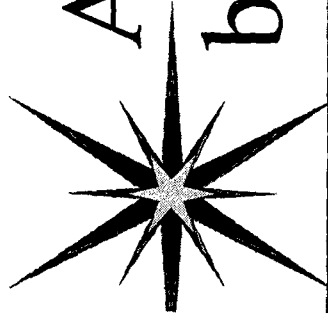

Pyrex

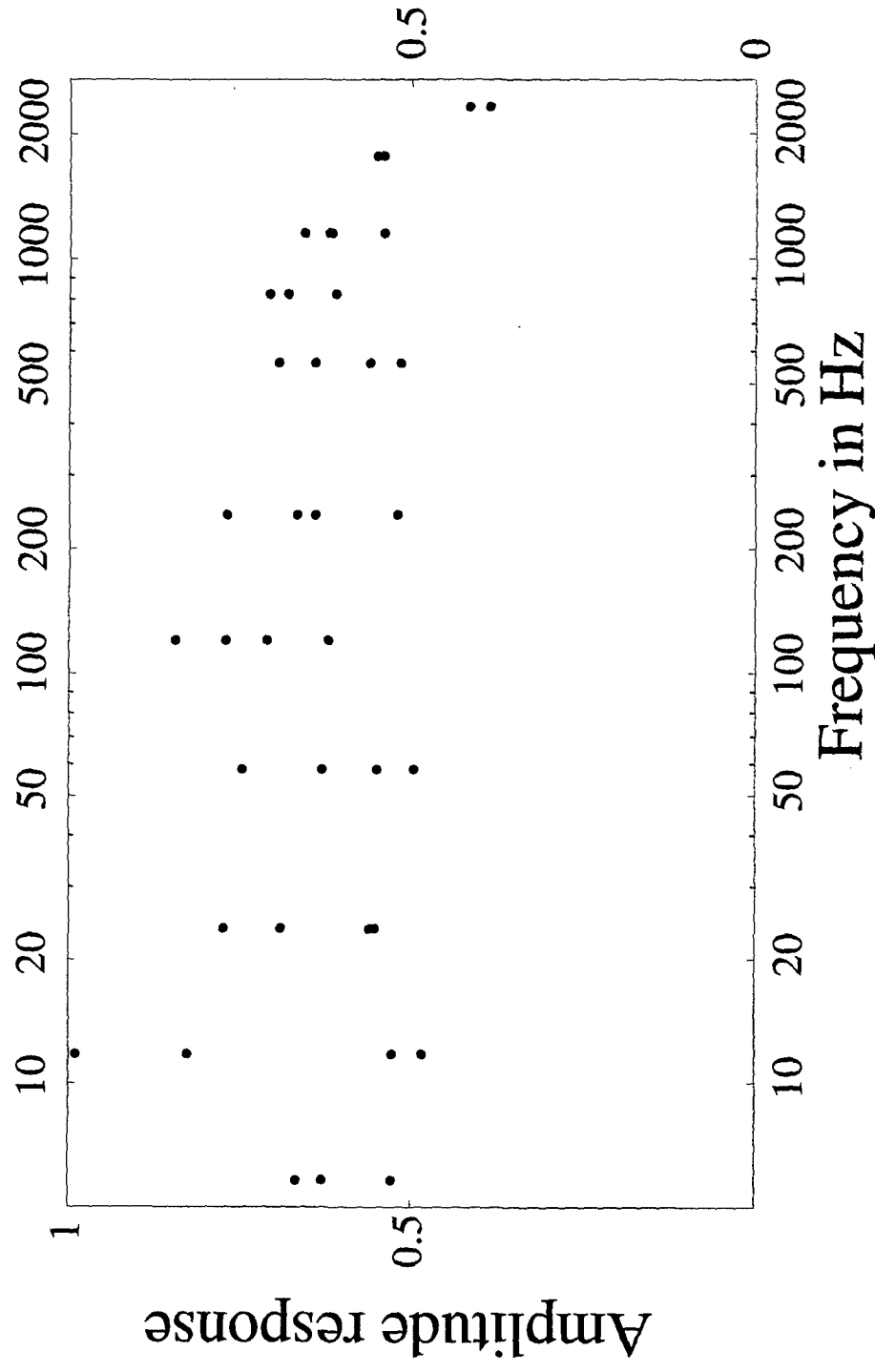45 mm

PIC 151

3 mm

0.3 mm

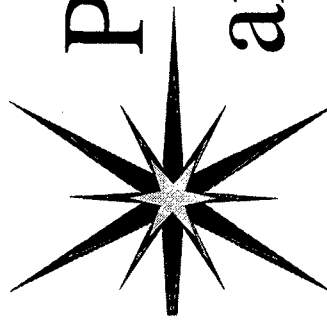Pyrex

Adhesive

Piezo

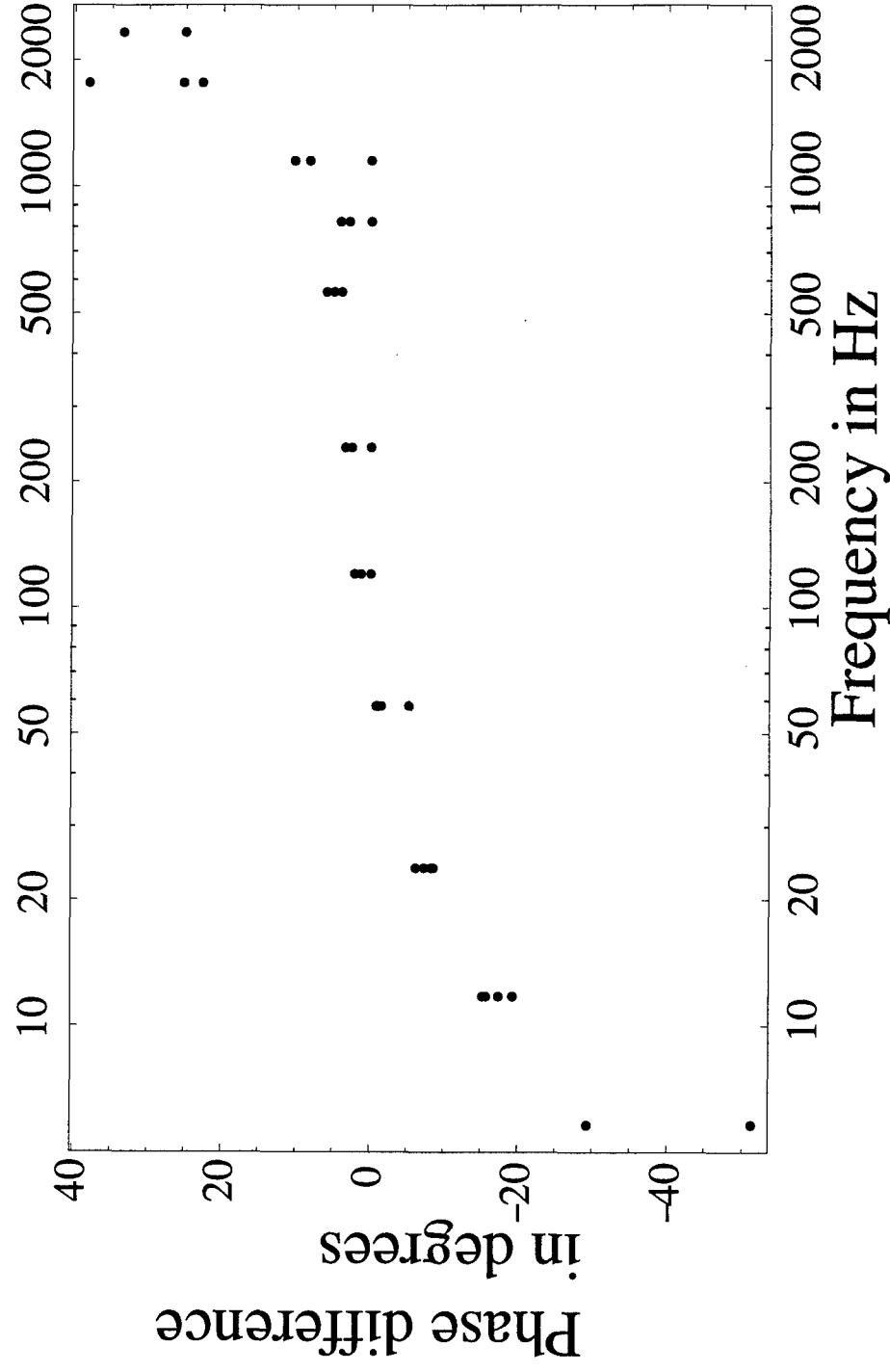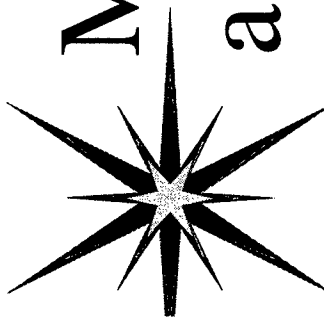# Zernike magnitudes at 160V for IC bimorph
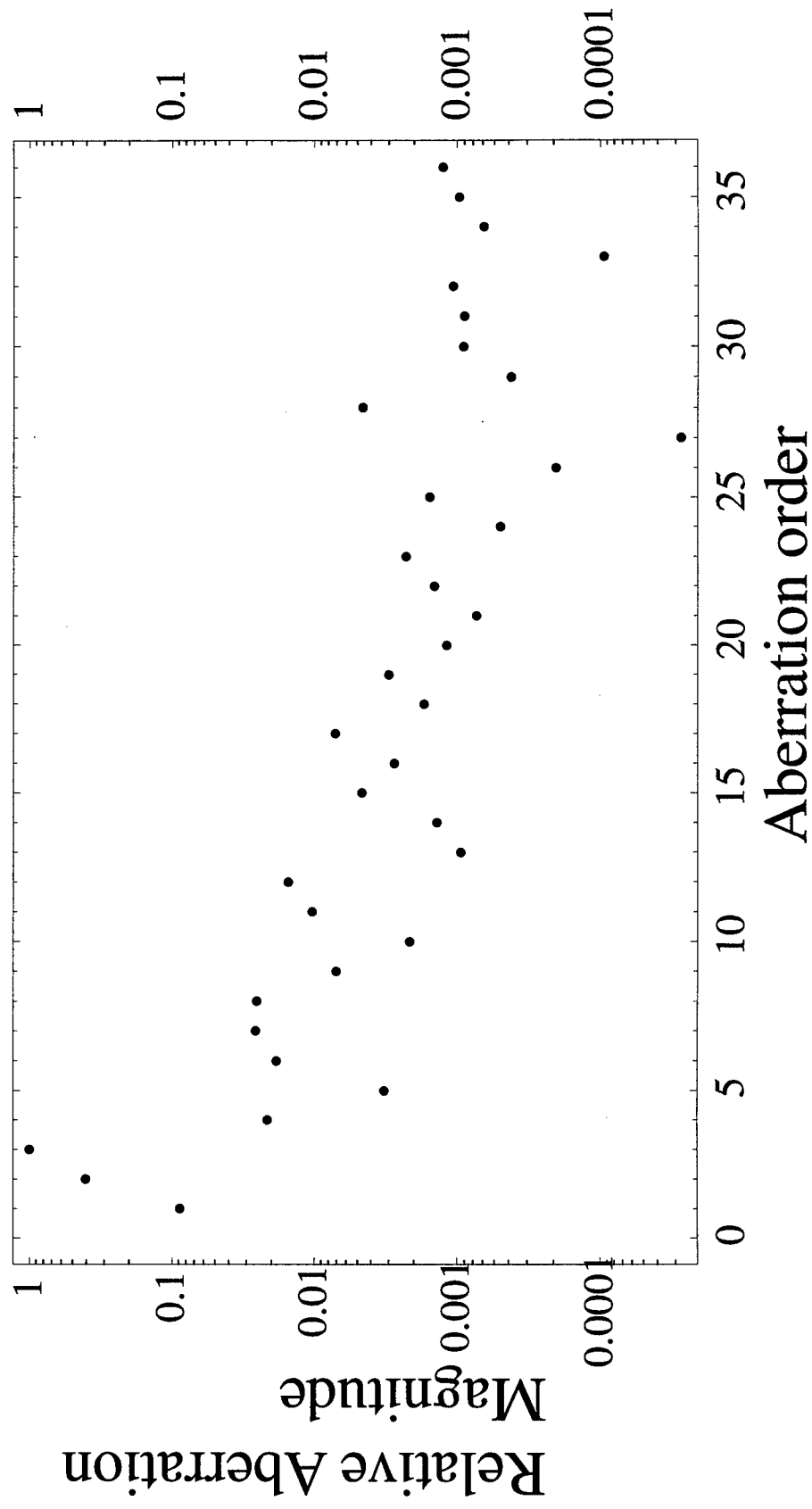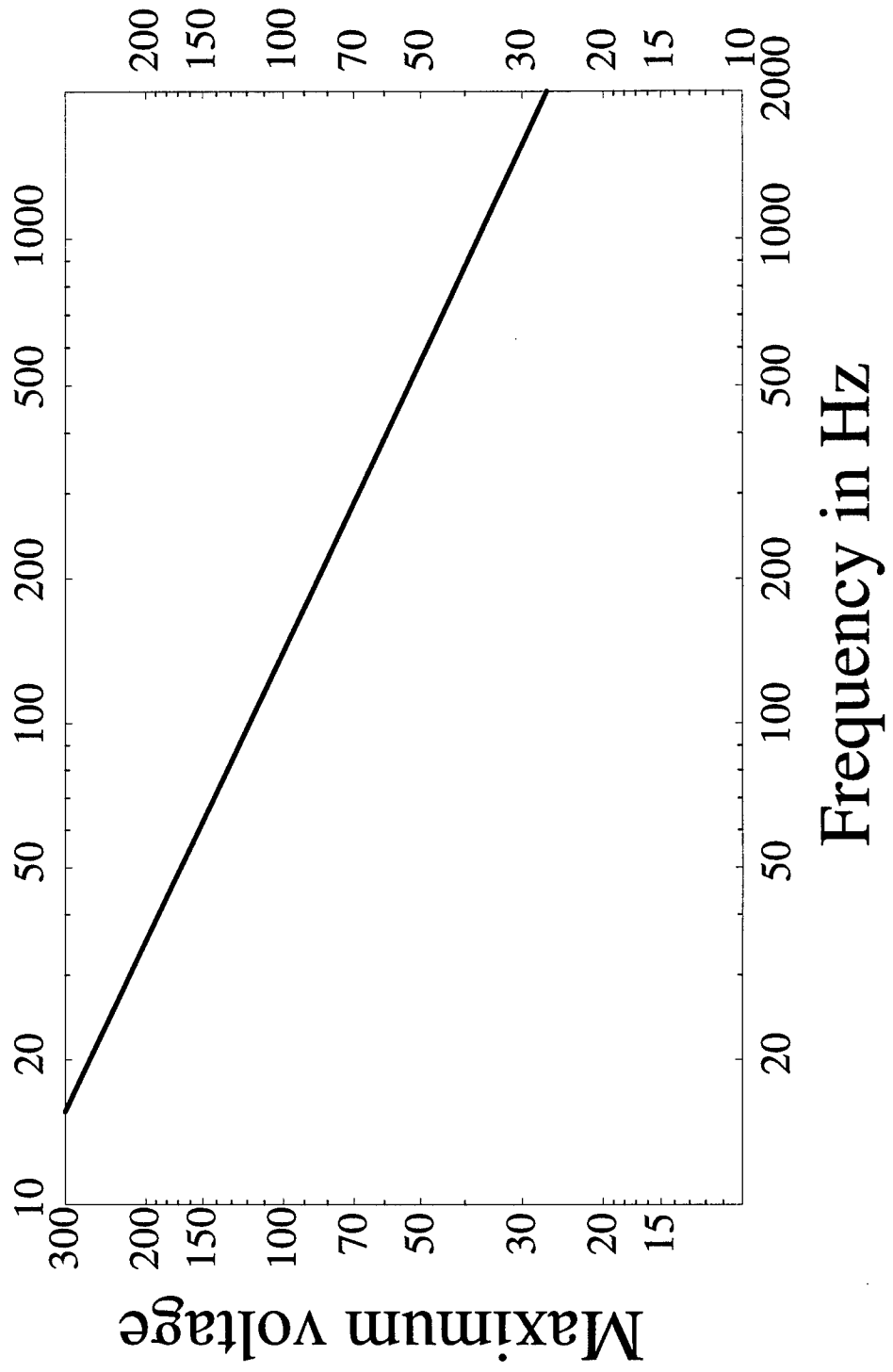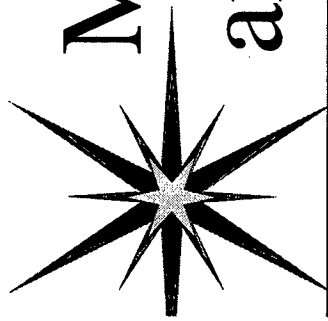
Amplitude response of IC bimorph with frequency

Phase difference between signal and response for IC bimorph
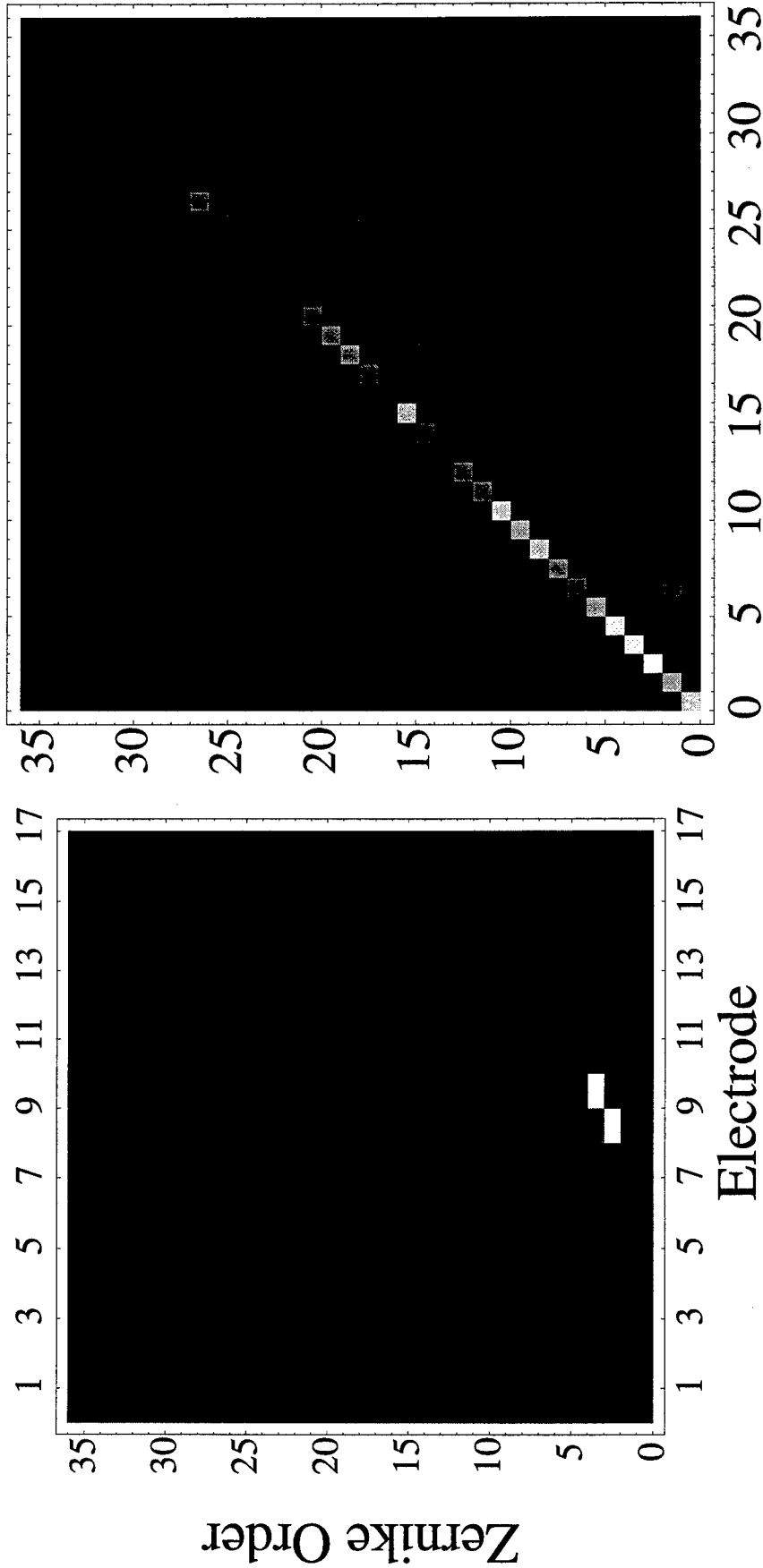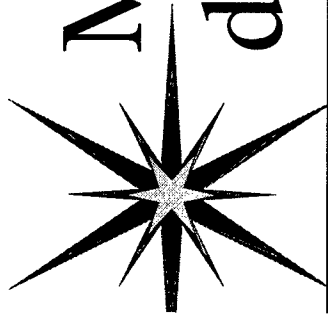
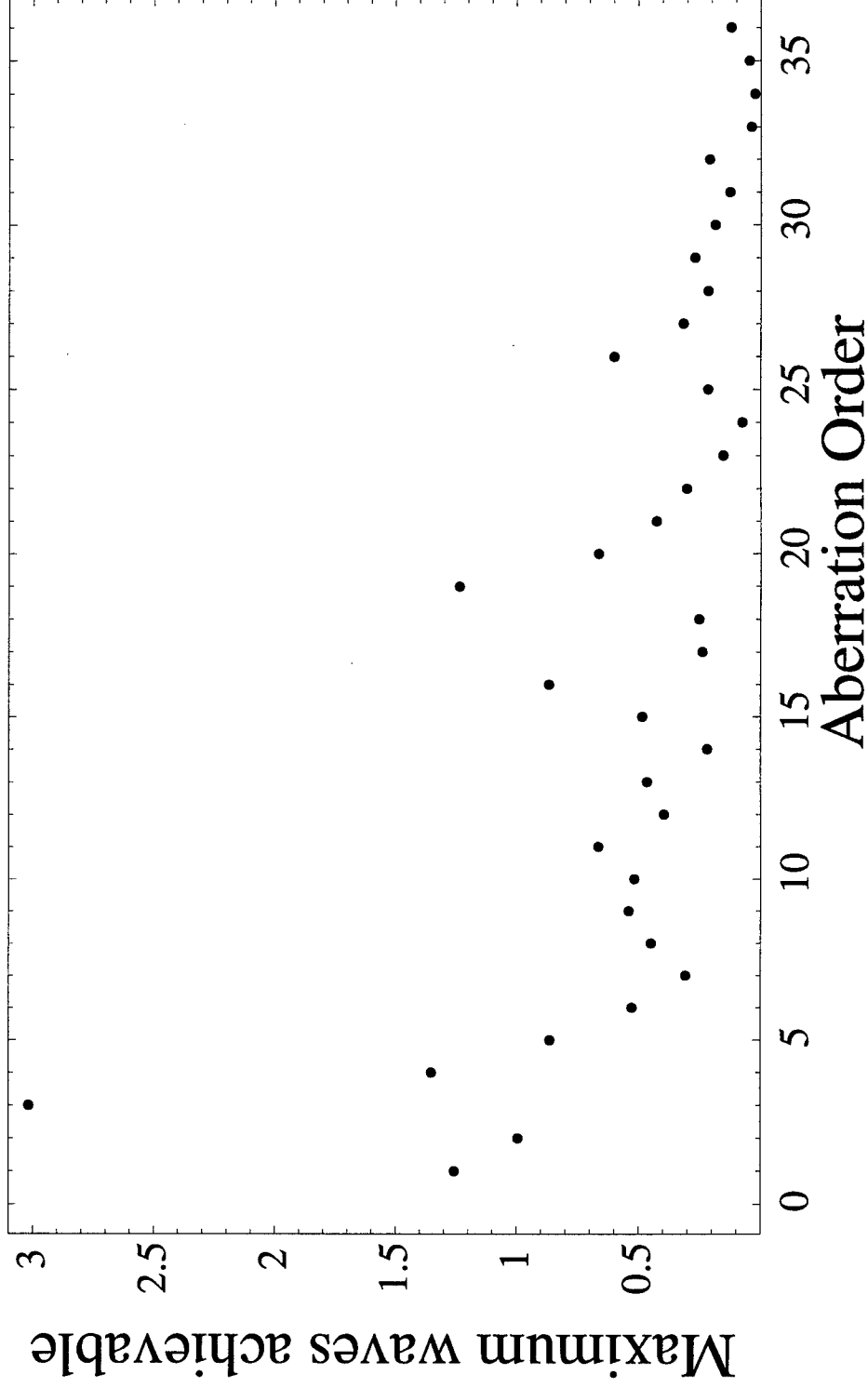# Maximum safe voltage change at a given frequency for a bimorph
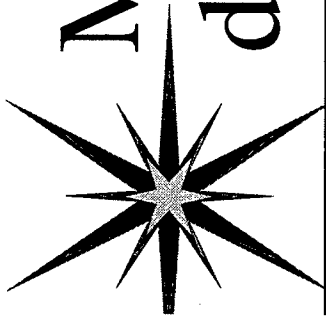
MSU bimorph transfer matrix
and transfer . inverse matrix

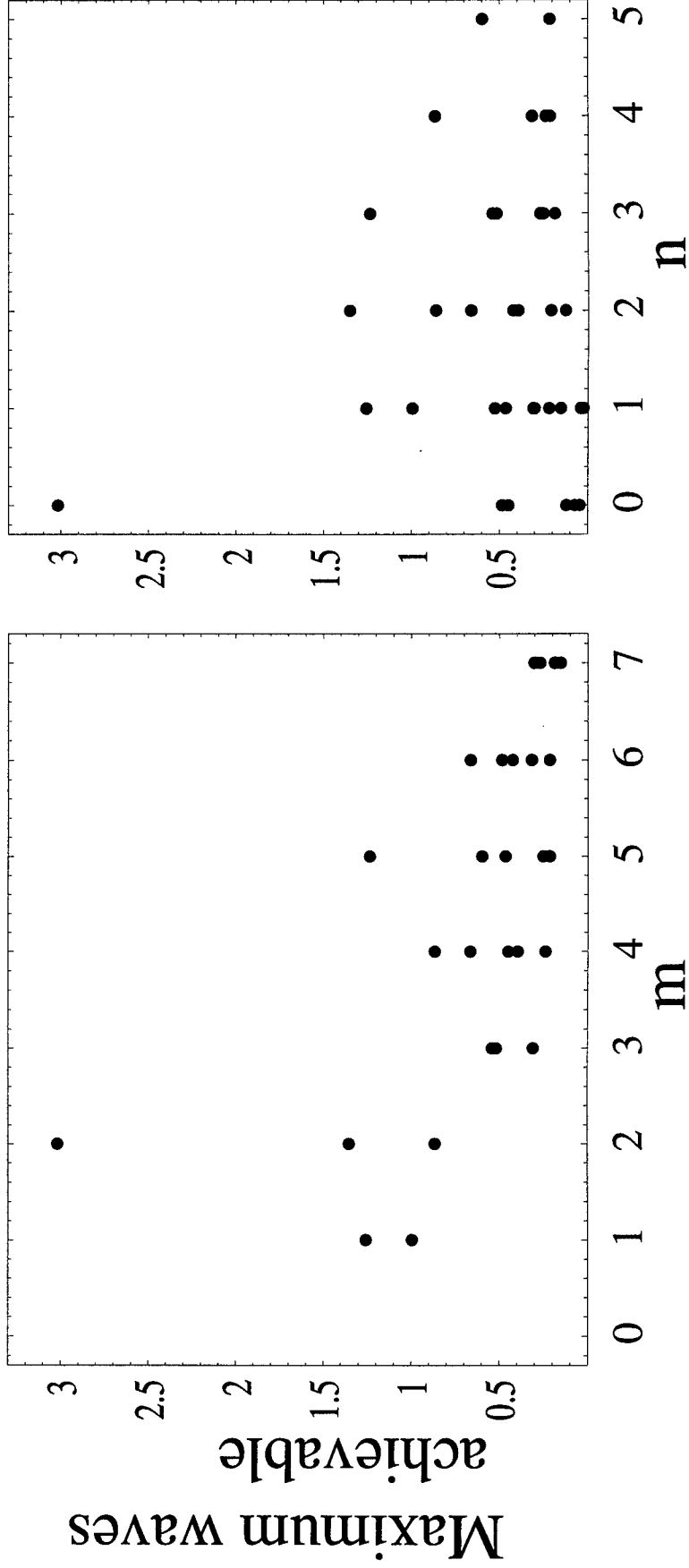# MSU bimorph maximum deflections for each order
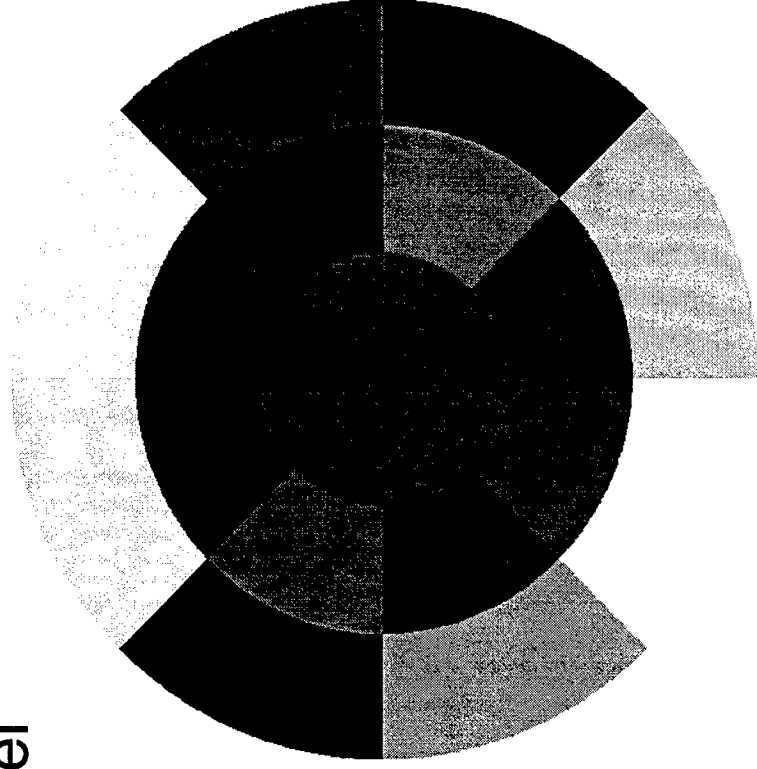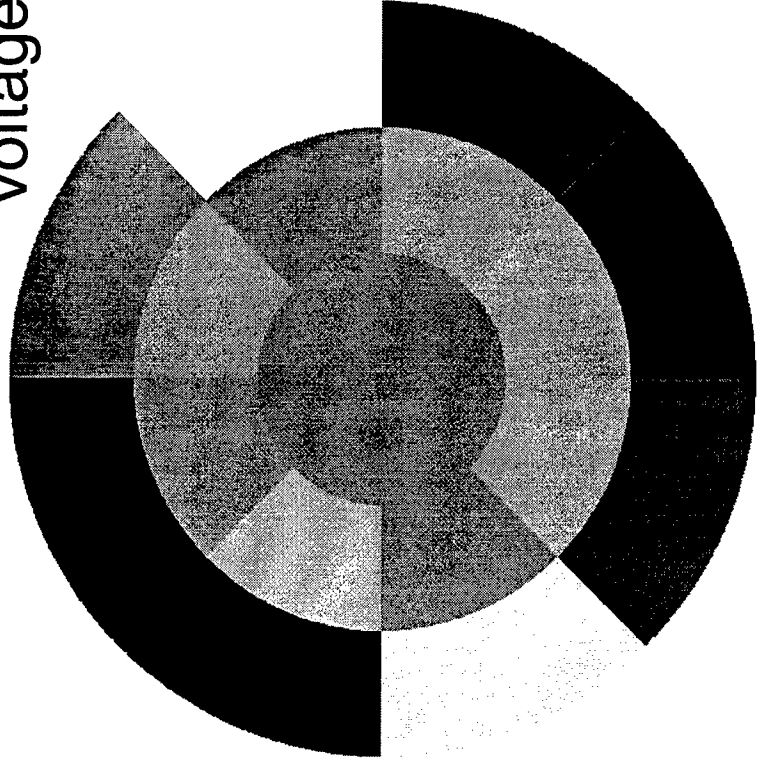

Maximum waves achievable vs. Aberration Order

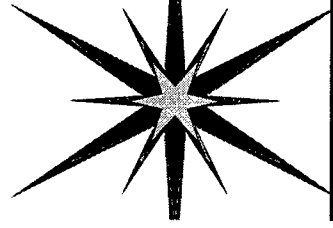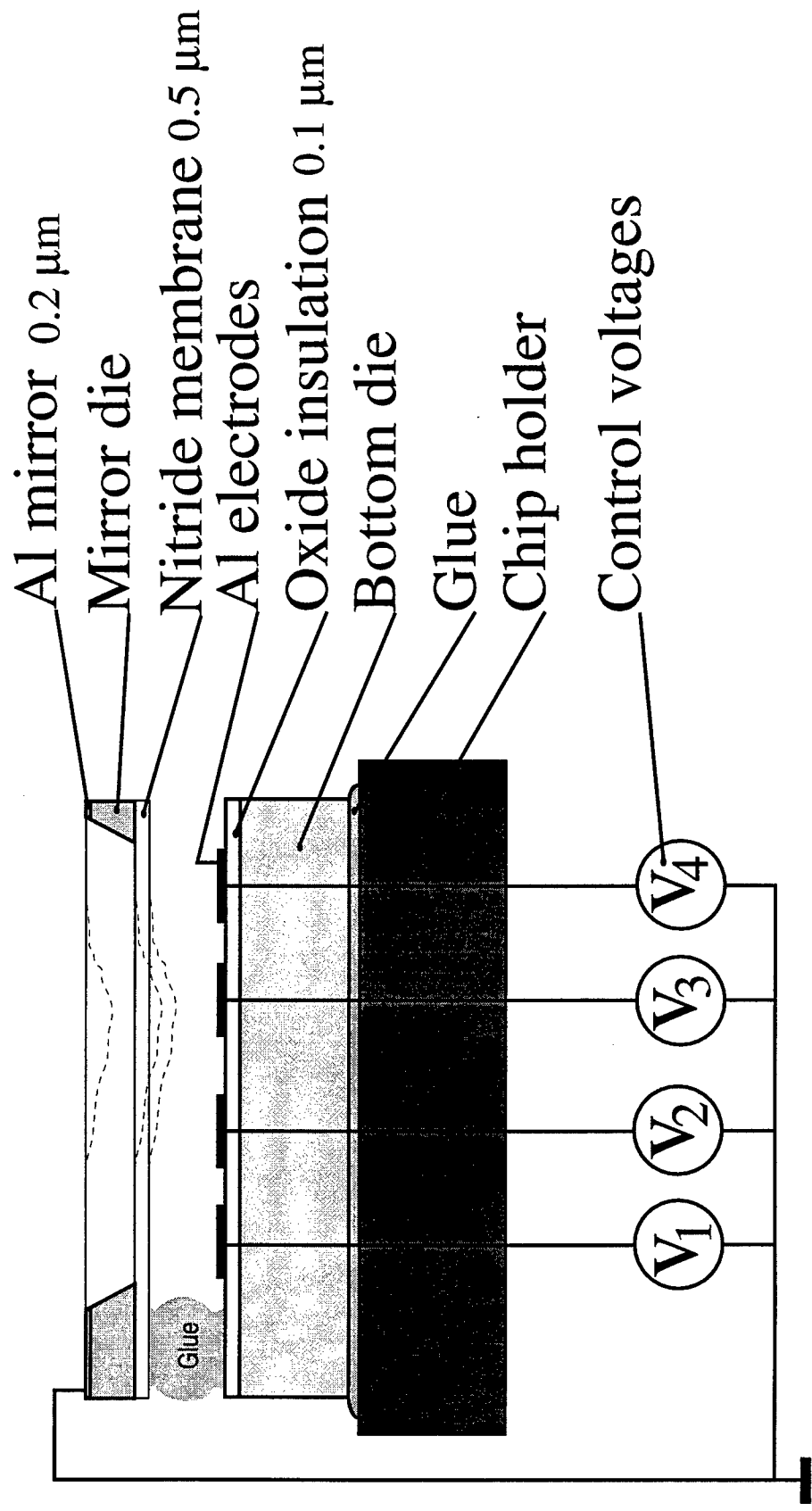# MSU bimorph maximum deflections in terms of n and m

Generating astigmatism on the MSU bimorph

grayscale indicates
voltage level

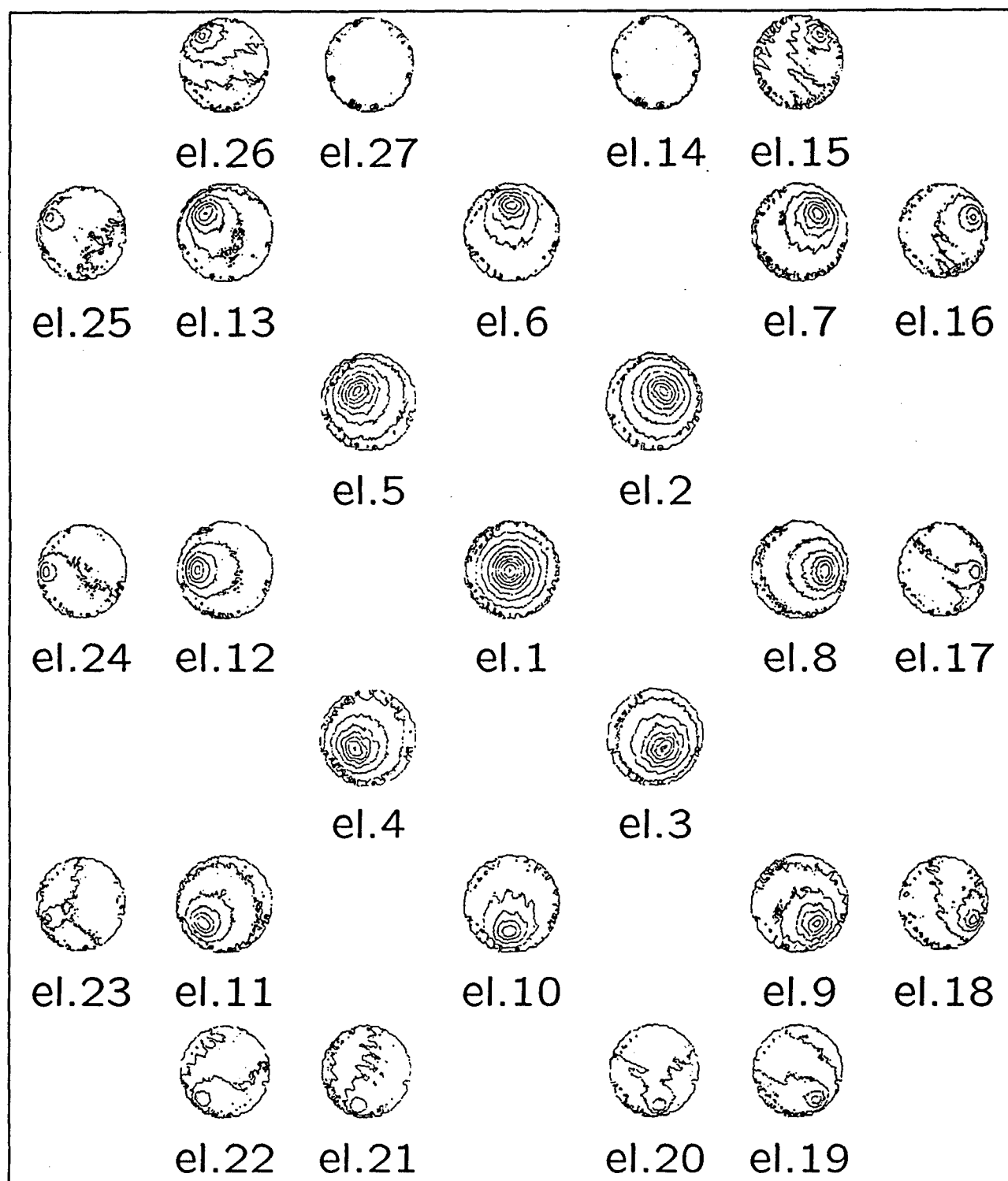# Membrane mirror schematic

Al mirror 0.2 μm
Mirror die
Nitride membrane 0.5 μm
Al electrodes
Oxide insulation 0.1 μm
Bottom die
Glue
Chip holder
Control voltages

Glue

V_1 V_2 V_3 V_4

el.26 el.27 el.14 el.15

el.25 el.13 el.6 el.7 el.16

el.5 el.2

el.24 el.12 el.1 el.8 el.17

el.4 el.3

el.23 el.11 el.10 el.9 el.18

el.22 el.21 el.20 el.19

Effect of 90V applied on each electrode:
Contour phasemap (step: 0.05λ).

Membrane mirror transfer matrix
and transfer . inverse matrix

Membrane mirror maximum deflections for each order
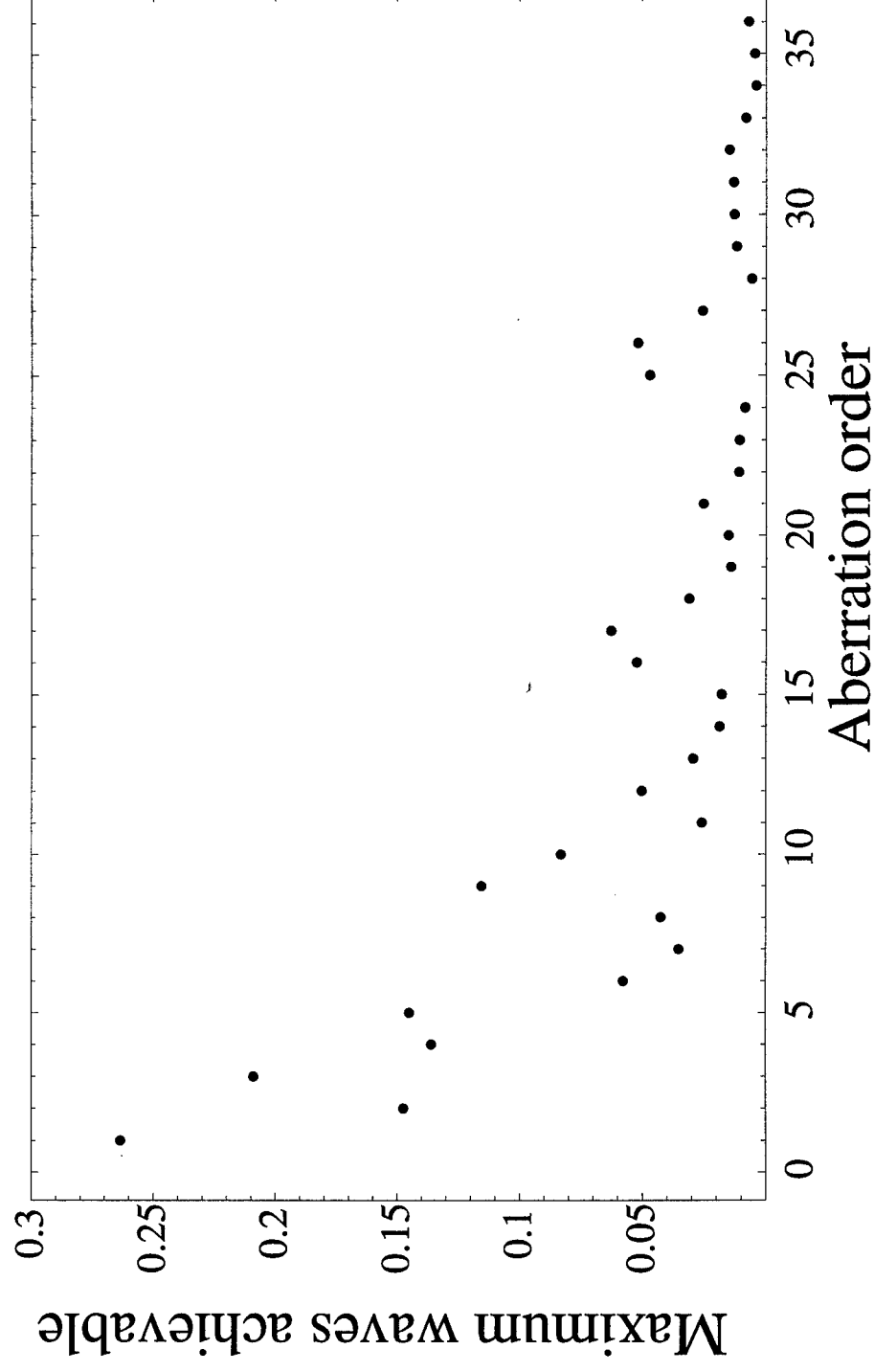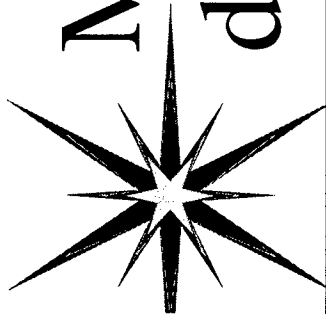
Membrane mirror maximum deflections in terms of n and m

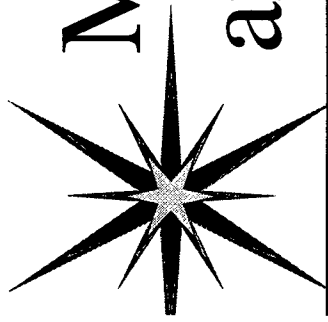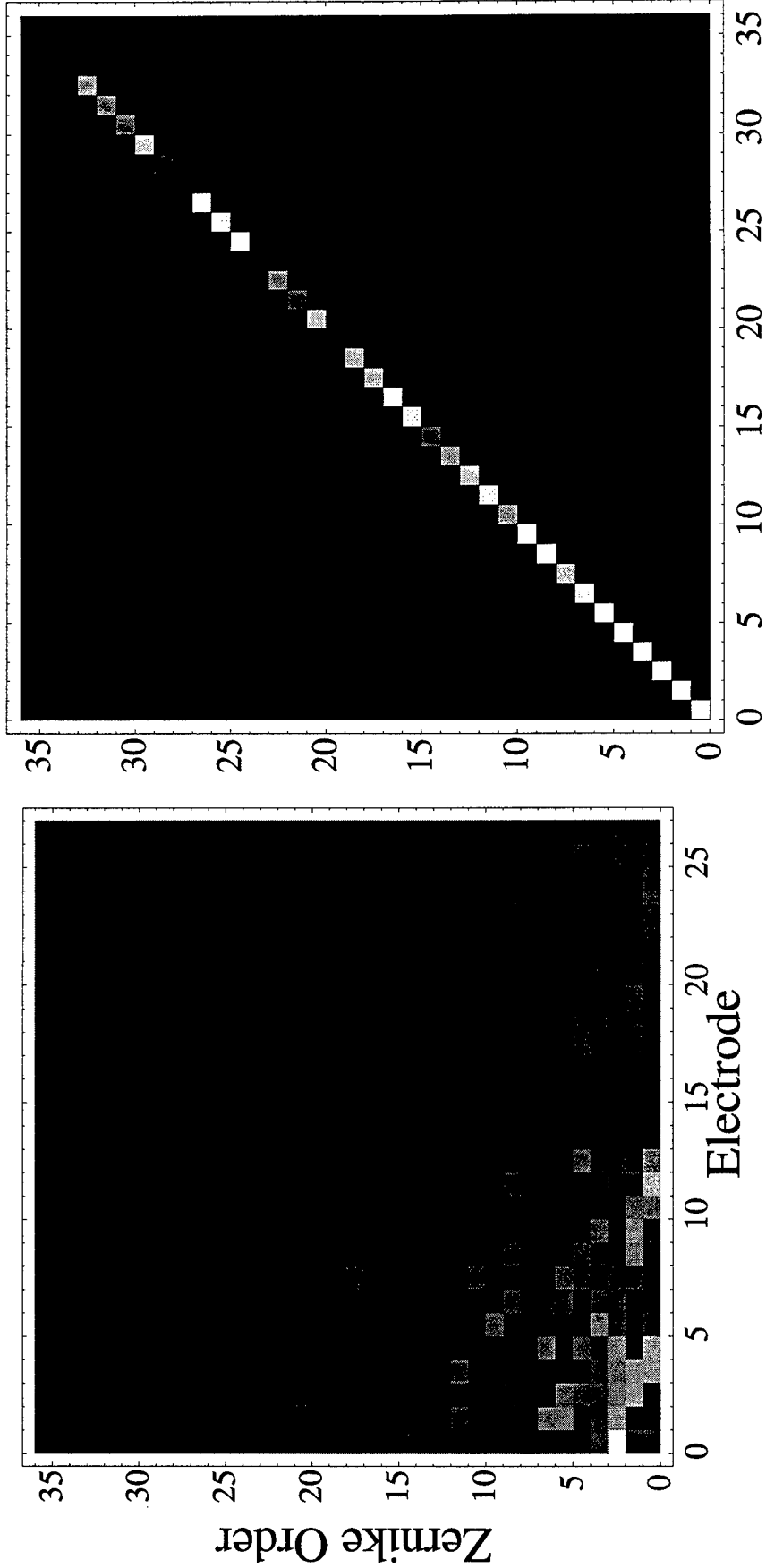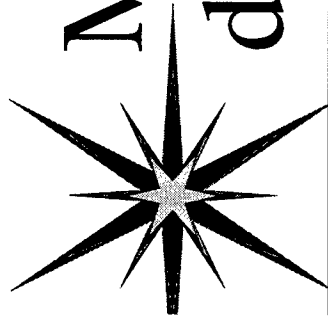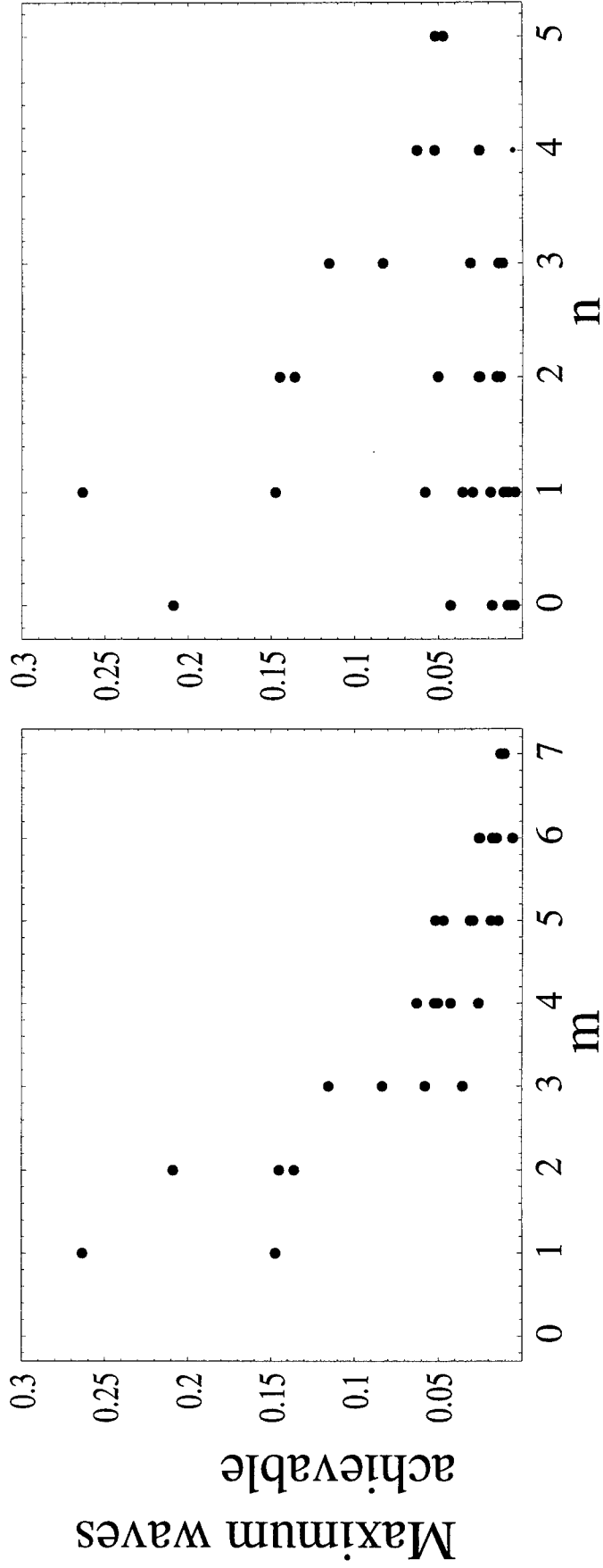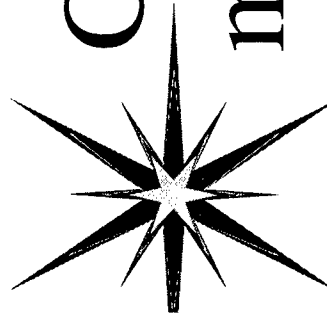# Generating astigmatism on the membrane mirror

grayscale indicates
voltage level
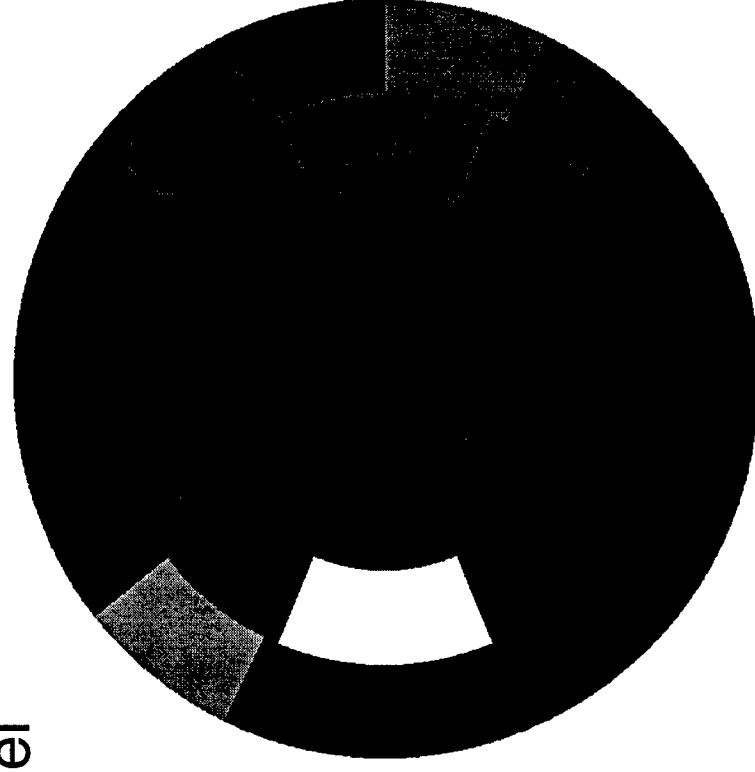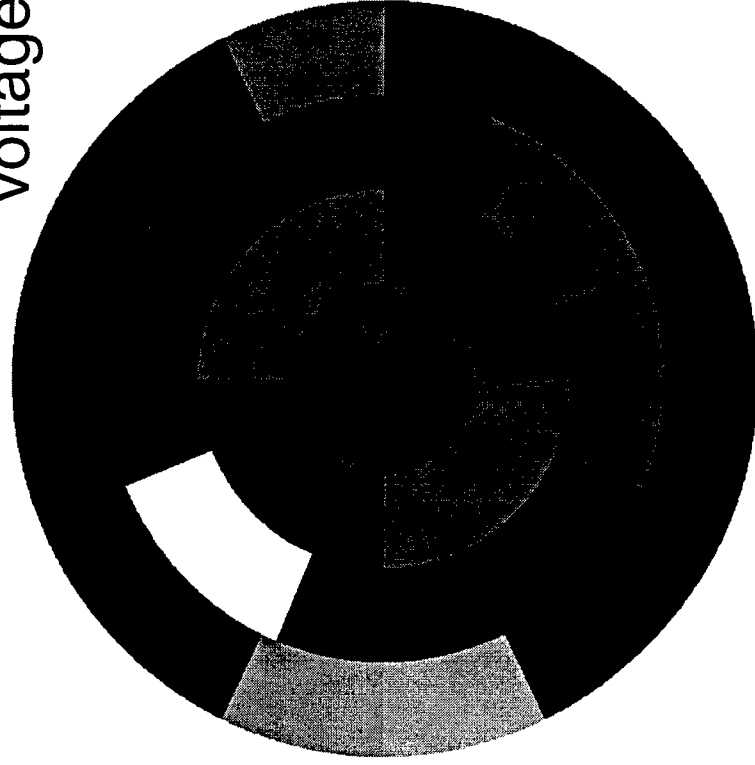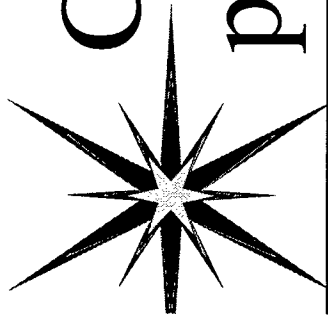
C80 processor raw centroiding performance

Legend:

Centroids
— 9
– – 16
-- 36

X-axis: Pixels per centroid (0, 10, 20, 30, 40, 50, 60)

Y-axis: Frame rate in MHz (0, 0.1, 0.2, 0.3, 0.4)

Active Control of Phase Distortions

in
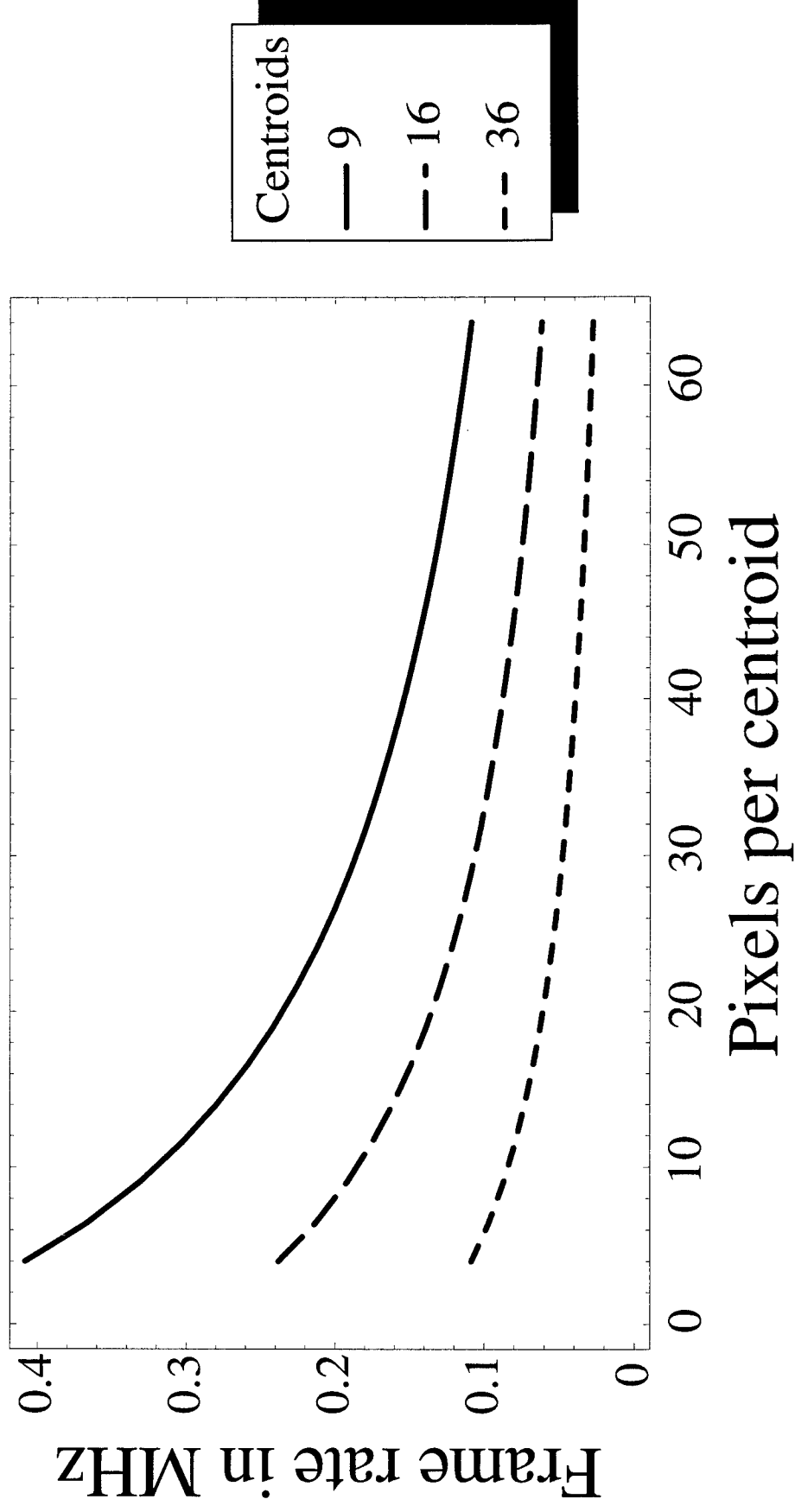
High Power Laser Systems

M J Shaw, I N Ross, C J Reason, D A Pepler

C N Danson, T Kaneko and C J Hooker

Central Laser Facility

Rutherford Appleton Laboratory

Chilton, Didcot, Oxfordshire

OX11 0QX,

United Kingdom

Comparison of Vulcan and Titania

Vulcan	Titania
Nd:glass, $\lambda = 1053$ nm	KrF excimer, $\lambda = 249$ nm
CPA beam diameter 190 mm	CPA beam diameter 150 mm
Energy 100J	Energy 2J
Pulse length 400 fs	Pulse length 300 fs
Focal spot (fwhm) 13 μm	Focal spot (fwhm) 1.5(8) μm
No. of times D.L. = 3	No. of times D.L. = 2 (12)
Passive aberrations ~ 3λ	Passive aberrations ~ 10λ
Thermal variations ~ 1 hr	Thermal variations ~ 10 m
Air motion: negligible	Air motion: few λ, t ~ 3 s

Outline of Talk

Vulcan and Titania lasers at the CLF
Nature and size of laser beam aberrations
Bimorph mirror construction and characterisation
Wavefront measurement
Mirror control algorithm
First results of aberration correction
Still to come . . . future work

Summary

Simple bimorph mirror:

- low voltage operation (± 64 V)
- multi-element, flexible layout
- cheap

Partially-automated control of curvature
Demonstrated correction of cylindrical error

Future Work

Close the control loop
Further develop algorithms and software:

- to control slopes at beam edges
- to compensate for hysteresis

Optimise the electrode geometry:

- hexagonal array?
- radius/sector?

Investigate optical addressing of electrodes

SSRC 354

Construction of Bimorph Mirror

Aluminium coating

Glass plate, t = 1.5 mm

Epoxy adhesive, t = 0.1 mm, with copper mesh ground plane

Type K PZT, t = 0.2 mm

Control electrodes (conductive ink)

Experimental Configuration

PC 1
Framestore & image analysis

PC 2
Control

File transfer

CCD camera

Gre-Ne laser (543.5 nm)

Screen

Laser beam expander

64-channel D-to-A converter

Hartmann plate with 11 x 11 holes

60-element bimorph mirror

Hartmann plate:
11 x 11 square grid of holes
Hole spacing 5 mm
Hole diameter 2 mm

Hysteresis of Adaptive Mirror

Single Actuator Response

Adaptive Mirror Control Algorithm

Capture Hartmann image

Table of spot positions for a plane reference wavefront

Analyse image and find centroids of the spots

Compare with reference and find Δx and Δy

Table of actuator positions in terms of Hartmann spot co-ordinates

Calculate x- and y- slopes at Hartmann spot coordinates

Calculate wavefront curvature at Hartmann spot coordinates

within the beam area

outside the beam area

Interpolate to find wavefront curvature at actuator positions

Interpolate to find wavefront slope at the edges of the beam

Calculate voltages to apply to actuators within the beam area to correct measured curvatures

Calculate voltages to apply to actuators outside the beam area to correct measured edge slopes

Adjust voltages to allow for effect of hysteresis

Apply calculated voltages to all actuators

Comparison of Mapping Methods

Actuator Mapping using Mirror Slopes

Correction of an Aberrated Beam

Correction of an Aberrated Beam

OPD after automated correction inside the beam

OPD after manual correction using edge actuators

OPD before correction
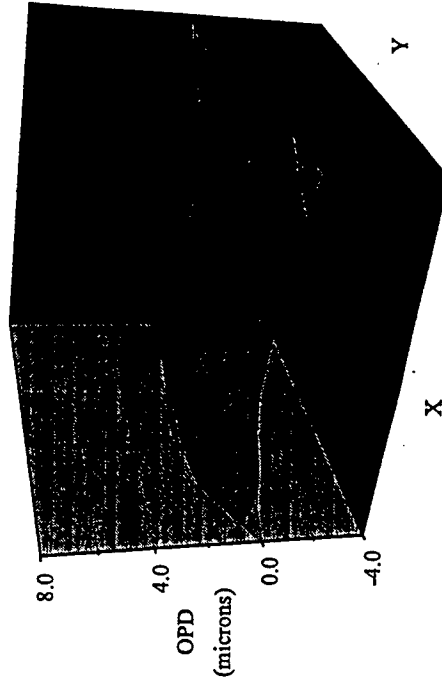
UK DUAL-USE ADAPTIVE OPTICS PROGRAMME

Alan Greenaway

DERA Malvern, St Andrews Road, Malvern WR14 3PS, UK

Abstract

A dual-use programme is being established in the UK in order to exploit current research on Adaptive Optics for large UK telescopes and to exploit a new programme on military uses of Adaptive optics. The dual-use programme will concentrate on the use of Adaptive Optics in laser materials processing. This will address only a restricted range of civilian uses of Adaptive Optics technology. The presentation will describe the scope of the dual-use programme, the range of applications that the programme is intended to address and the approaches that will be adopted in order to satisfy the requirements of the selected application areas.

Introduction

In terms of serious investment of manpower and finance, the UK is a late-entrant in Adaptive Optics. The UK astronomy community, through the Particle Physics and Astronomy Research Council (PPARC) led the way in 1994 with a significant programme intended to equip two large-aperture telescopes with Adaptive Optics correction and to use laser wavefront-sensing beacons to increase sky coverage beyond that which would be available if only natural guide-stars were used. A UK programme on Adaptive Optics for military applications has just started in April 1997.
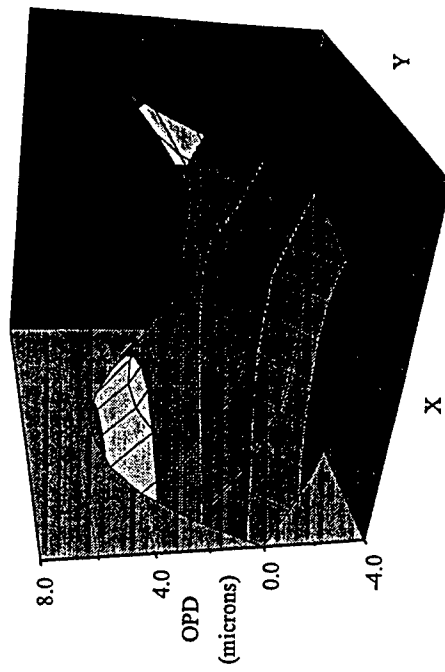
Athhough Adaptive Optics has been used in military applications for a considerable period and in restricted commercial applications (e.g. auto-focus) for a similar length of time, concerted attempts to apply Adaptive Optics with more than one degree of freedom to industrial processes are still relatively few. Entering a high-technology research area well behind other participants offers both advantages and a serious challenge. Because much of the fundamental technological developments (such as a range of wavefront modulator systems, a range of wavefront sensor systems and closure of feedback control-loops) have already been demonstrated, a programme on industrial applications can be kept within modest costs and does not require 'proof-of-principle' stages. However, the challenge is to ensure that the programme can deliver new and useful results in a short timescale and without the extensive heuristic experience that other groups have gained.

The proposed UK Dual-use programme is intended to bridge a gap between the funded UK programmes in astronomy and military applications and cost-critical industrial applications. The areas of application selected have been chosen to match, as closely as possible, areas of existing mutual interest to UK industry, military and academic bodies. The programme requires coordination of funding from various and the gestation period for establishment of the funding has been protracted and is still incomplete.

Strategy and Plans of UK Dual-use Programme

Neither the existing PPARC programme, nor the newly-started UK military programme on Adaptive Optics, will address directly the important issues concerned specifically with the control of lasers in materials processing. The industrial application of for cutting, welding, drilling, patterning and annealing are of significant interest to UK industry and provide benefit for the UK military and UK defence industry. The UK academic community also has a significant programme in this area, funded through the Engineering and Physical Science Research Council (EPSRC). For these reasons the application of Adaptive Optics to improvement of laser-based materials processing was selected as a suitable vehicle for a dual-use programme, funded by the Ministry of Defence (MoD), the Department of Trade and Industry (DTI), Industry and the EPSRC.

For materials processing applications the use of lasers as a tool offers advantages, over mechanical or chemical working of the material, which include speed of working, the ability to cut/pattern very fine detail over large workpieces, the absence of tool wear and vibration and the minimisation of induced thermal distortion in the workpiece.

The interaction of the laser beam with the material being worked upon is a complex process, involving not merely the removal of material from the area that is being actively worked but also the control of the ejected material. Adaptive optics offers an unprecedented opportunity for accurate and dynamic control of the manner in which the material is processed, through high-speed and flexible control of the laser-beam profile at the point of working.

Discussions with UK Industry have shown an encouraging level of interest in participation in a pre-competitive, dual-use Adaptive Optics programme to address issues specifically concerned with laser materials processing Requirements that have emerged as offering significant potential benefit from application of adaptive optics to industrial materials processing include:
- Accurate control of beam focus at the point of working. This is particularly important when precise patterning and drilling of surfaces with significant surface curvature or relief is required or when precise control of hole shape and depth is required.
- Accurate control of beam shape at the point of working. Such control can facilitate the use of beam-shapes tailored to the operation being undertaken, for example, focal spots elongated in the direction of working can be beneficial in cutting and welding operations, production of a halo around the working focus may help to control deposition of ejected material and thus improve the finish achieved, accurate control of the energy distribution between multiple foci can assist in accuracy and uniformity when parallel working is used to increase throughput.
- Intra-cavity control of the laser wavefront, to increase the quality of the beam exiting the laser cavity.

A prime concern that impinges on the range of industrial applications to which adaptive control of laser materials processing might be put, is the unit cost associated with adaptive

control systems. A consensus opinion appears to be that if the overall cost of an adaptive system for laser-beam control is £100k or more very few such units would be used and these only for very specialist or military applications. If unit costs could be reduced to £50k it appears that a modest number of units are likely to be employed, but to ensure widespread application one should aim for a unit cost that does not exceed £10-20k. At a £10k unit cost, opinion was that adaptive optics units would be fitted to almost every laser system for industrial materials processing applications.

Since the objective of the proposed dual-use programme is to address successfully a wide range of industrial applications, the reduction of unit costs to below £10k per unit, for production of 1000 or more units of low-order extra-cavity adaptive optics systems capable of handling industrially-useful power levels, has been selected as a prime objective of the programme. Use of bi-morph mirrors or use of large-scale spatial light modulators based on liquid crystals would appear to offer the potential for low-cost wavefront modulators. The achievement of cheap and effective wavefront sensing through a plasma and cloud of ejected material, and coupling such sensing through cost-effective electronics to achieve the requisite control, appears to offer a significant challenge.

Industrial interest in the programme spans the full range of laser types and, in order to keep the programme as generic as possible, it is intended that the main emphasis will be on extra-cavity adaptive optics for beam-shaping and control. For these extra-cavity applications it is intended that the scientific output of the programme will, once intellectual property rights (IPR) have been protected, be freely disseminated through the scientific press and a series of open seminars. It is expected that use of such IPR will be available under non-exclusive licence arrangements. However, provision will be made for participants in the programme to delay the granting of licences, or to delay dissemination of the results, if they consider that this is necessary to protect a significant commercial advantage.

The use of intra-cavity adaptive optics is not so easily managed in a collaborative and pre-competitive programme, because of the requirements of commercial confidentiality in laser manufacture. Thus it is intended that work applying technological developments within the programme to intra-cavity adaptive systems can be addressed by the programme participants, but that such studies would be on a bi-lateral or small-group basis, with further funding being required where significant effort was to be put into such studies.

The wavefront sensing required to ensure accurate control of the laser beam profile at point of working is a significant topic to be addressed within the programme. Assessment of focus may be made between laser pulses using various optical and mechanical techniques. Current approaches tend to rely on indirect methods, including mechanical sensing of the position of the surface to be worked or on maximisation of the scattering from the plasma and cloud of ejected material produced when the material is worked. Both of these approaches have the merit of simplicity, but are unlikely to lead to the accurate beam control that is required from this programme. More sophisticated methods using spectral diversity [1] have been shown to be capable of sensing the penetration of

the keyhole region during laser welding, even with cw laser radiation. However, none of these methods provide direct information concerning the condition of the laser beam at the point of impact with the workpiece.

If the scattering from the plasma generated by laser interaction with the material being worked is too strong, insufficient energy will reach the surface and the plasma generation will become self-limiting. It thus seems probable that efficient laser working of the surface will always be done under conditions where a large fraction of the incident energy is unscattered before it reaches the surface being worked. Under such conditions it should be possible to image directly the beam incident on the work-area and, thus, to provide accurate feedback on the beam condition.

Such direct imaging of the laser beam at the point of impact with the workpiece will be severely limited in contrast by emissions from the plasma and by scattering and emissions from the ejected material and the workpiece. The challenge, therefore, is to exploit mechanisms that will enhance the contrast in the image. Amongst the mechanisms that will be examined, individually and in combination, to facilitate such imaging are:
- Polarisation-sensitive imaging, using the polarisation to suppress emissions from the workpiece, plasma and ejected matter and, perhaps, scattering from the ejected material
- Narrow-band imaging, to suppress emissions from the workpiece, plasma and ejected material
- Multi-spectral imaging, to provide a mechanism for discrimination between emissions and different scattering mechanisms
- Coherent (e.g. heterodyne) detection, to discriminate between emissions and different scattering mechanisms.

Exploitation of mechanisms to enhance contrast is particularly important to permit the measurement of beam-shape in the wings of the beam profile. Although, these wings are unlikely to be used for cutting or patterning they may be used to control deposition of ejected material. In each case the 'imaging' or wavefront sensing must be achieved using a low-cost system, or a system that can, in the near future, be re-engineered to provide a low-cost solution.

Exploitation and benefits expected from UK Dual-use Programme

As far as possible consistent with protection of IPR results from the programme will be published at an early point. However, if the programme is successful in delivering results that a programme participant considers to offer a substantial commercial advantage, provision will be made to restrict the licence access of non-participants.

It is expected that each of the industrial participants (currently 5,) who between them have offered involvement in the programme at a level of £470k over the 3-year programme duration, will participate in the design and subsequent testing of a prototype, extra-cavity, adaptive-optics laser-beam control system. The system design will, as far as practical, be a

common module for the whole applications range to be tested. For this reason it is unlikely that the system will be fully optimised for any one of the applications to be tested, but an important aspect of the programme will be to make an assessment of the scope for cost-effective optimisation of the common module for each of the applications. Using this approach is expected to lead to the maximum commonality between applications and, thereby, the most cost-effective, if not fully optimum, solution to each requirement.

Important potential is considered to exist in the manufacture of large-scale hybrid circuits, where the application of adaptive control of laser heat treatment offers an unprecedented ability to initiate complex thermal cycles individually tailored to the requirements of individual components in the circuit.

The full programme has been costed at £1.4m over its 3-year duration. Applications that will be addressed include drilling, patterning, welding and annealing .

In terms of potential return on the investment, it is noted that patterning/perforation of aerofoils has been estimated to have the potential to effect a saving of 8-10% in aviation fuel costs[2]. If increased accuracy in drilling/patterning can contribute by 1% toward the level of fuel saving actually achieved, the total cost of the programme would be recovered by the MoD from savings in aviation fuel in under one year. Additionally, it has been suggested [3] that perforated aerofoils can be used to increase the stability of an aircraft when flying slowly in delicate operations such as landing.

Other applications that will be considered during the programme will include ophthalmic uses covering retinal imaging and therapy, where the increased resolution can provide increased diagnostic capability and reduced CO-lateral damage in retinal operations, and potentially, in corneal operations.

Collaboration

The programme participants would welcome the opportunity to discuss with other interested groups further collaborations on an equitable basis.

References
1   F M Haran, D P Hand and J D C Jones, "Process monitoring in laser welding, based on observations of optical signal oscillations", Appl. Opt. Div. Conf. Reading, 16-19 Sept 1996, IoP Publishing 1996.
2   S W Williams, BAe, private communication, see also OLE, March 1997, p43.
3   M Hindley, "Safe landings on a wing and some air", New Scientist, 14 Dec 1996, p18.

INTRACAVITY ADAPTIVE OPTICS FOR TECHNOLOGY

Alexis V. Kudryashov

Scientific Research Center for Technological Lasers
Russian Academy of Sciences

Shatura, Russia

June 9 - 13, 1997

The Results of Joint Work with:

Mr. V.V.Samarkin (NICTL)

Mr. S.A.Gnedoy (NICTL)

Mrs. T.Yu.Cherezova (MSU)

Dr. V.K.Popov (NICTL)

Dr. L.N.Kaptsov (MSU)

Prof. V.I.Shmalgauzen (MSU)

Prof. V.Ya.Panchenko (NICTL)

are presented in this report.

The Main Problems to Be Solved by Methods of Adaptive Optics in Laser Industry

1. Stabilisation and optimisation of different laser radiation parameters.

2. Formation and maintenance of given intensity distribution of laser beam on given surface.

## Applications:

Laser microtechnology.
Laser etching.
Laser heating technology.
Laser ophtalmosurgery.
Laser dermatology.

Different methods are used to obtain the desired result:

1. Complex optical systems.
2. Methods of kinoform flat optics.
3. Methods of nonlinear adaptive optics.
4. Extracavity adaptive optical systems.
5. Intracavity adaptive optical systems.

Design of adaptive optical system.
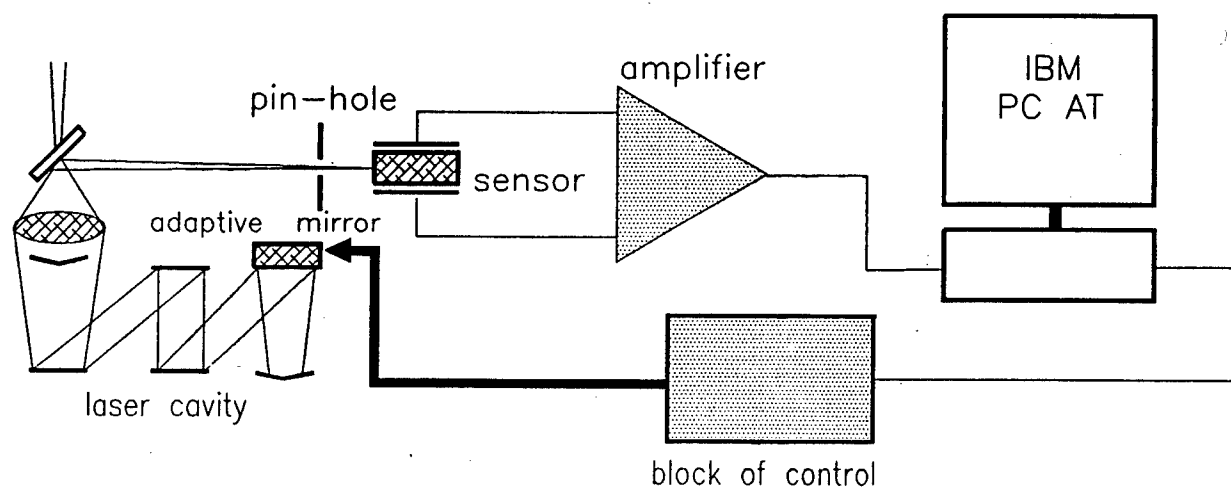
Aberrations to be reproduced or corrected.

| Type of laser	Type of aberrations	Amplitude	Frequency range
Solid state YAG laser (output power 500 W)	Range scale: astigmatizm coma spherical ab.	P–V – 8μ P–V – 2μ P–V – 3μ	up to 30Hz
CO_2 technological laser (output power 5 kW)	Range scale: defocus astigmatizm coma	P–V – 10μ P–V – 4μ P–V – 3μ	up to 1 Hz

Semi-passive bimorph mirror.

Main features: aperture — 40 mm, stroke — 7 μ,
number of actuaturs — 8, 13, 18,
mirror quality — 0.1 μ (P–V),
bandwidth — 2000 Hz,
material — glass, quartz, copper.

Design of bimorph mirror.

Glass reflecting plate
Common electrode
Piezodisk
Controlling electrodes
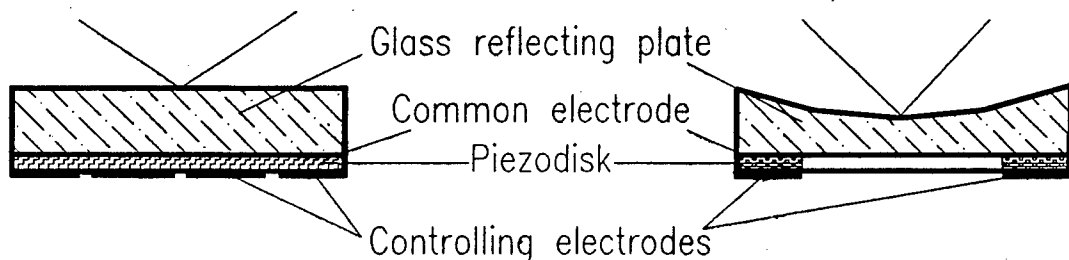
Scheme of electrodes position.
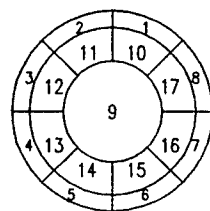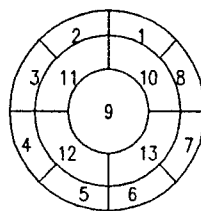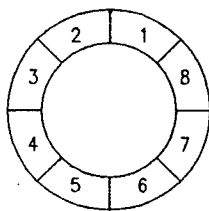
Photo of the bimorph mirrors.
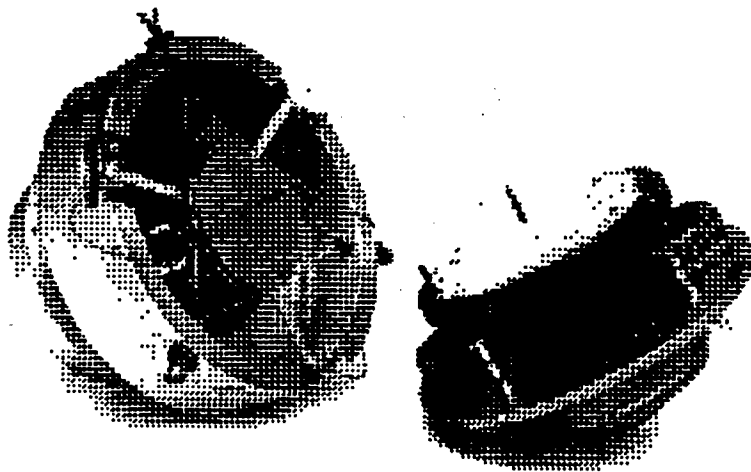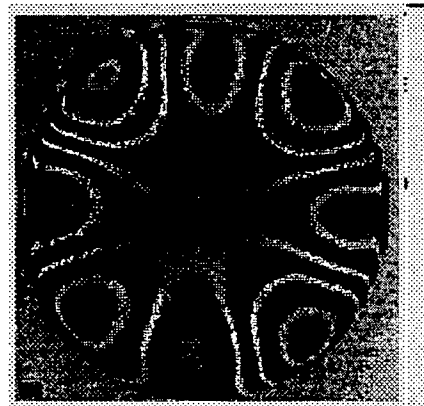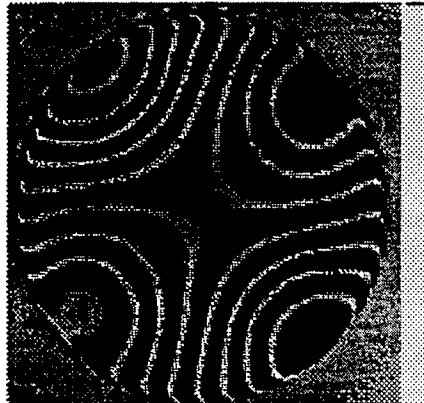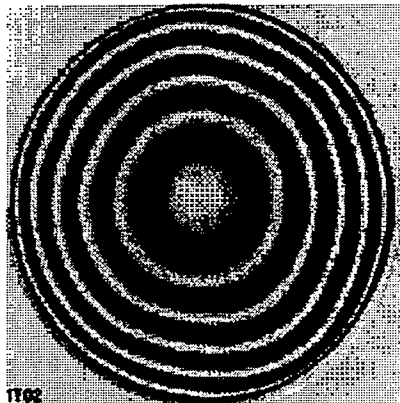
The interferometric patterns of the mirror:
defocus, astigmatism, one electrode response profile,
profile for +120V at odd electrodes and -120V at even ones.

RMS of a Several Aberrations Approximation with 17-electrode Bimorph Mirror.

Defocus – 0,3%
Astigmatism – 0,7%
Coma – 8%
Spherical aberration – 3%

Influence function of different electrodes.

Flat bimorph mirror.

El. N 10.
Appl. vol.-150V
P-V - 1.41μ.
Step - 0.2μ.

El. N 9.
Appl. vol.-150V
P-V - 1.58μ.
Step - 0.2μ.

El. N 11.
Appl. vol.-150V
P-V - 1.57μ.
Step - 0.2μ.
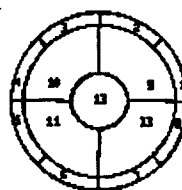
El. N 6.
Appl. vol.-150V
P-V - 0.57μ.
Step - 0.05μ.
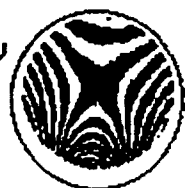
El. N 6.
Appl. vol.+150V
P-V - 0.49μ.
Step - 0.05μ.

Spherical bimorph mirror.

El. N 1.
Appl. vol.-150V
P-V - 1.89μ.
Step - 0.25μ.

El. N 2.
Appl. vol.-150V
P-V - 1.98μ.
Step - 0.25μ.
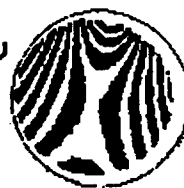
El. N 3.
Appl. vol.-150V
P-V - 1.76μ.
Step - 0.25μ.
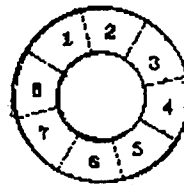
# Water-cooled Bimorph Mirror.

Main features: aperture – 100 mm, stroke – 10μ,
number of actuators – 18,
mirror quality – 0.2μ (P–V),
bandwidth – 1500 Hz,
material – copper, molybdenum.

Design of water-cooled mirror.

Reflecting plate   Canals for cooling water

Bimorph plate

Controlling electrodes
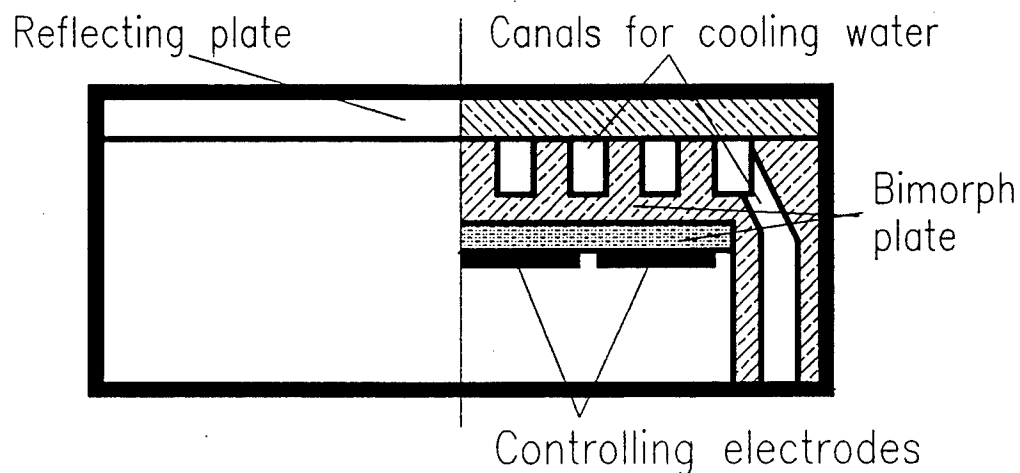
Photo of the experimental prototype.
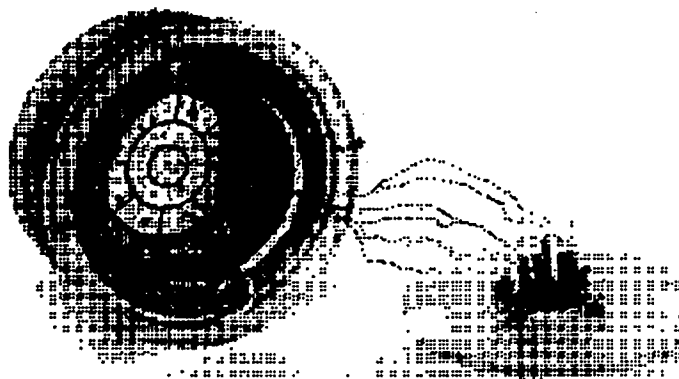
Formation of Spatial Characteristics of the Excimer Laser Beam.

Experimental setup.
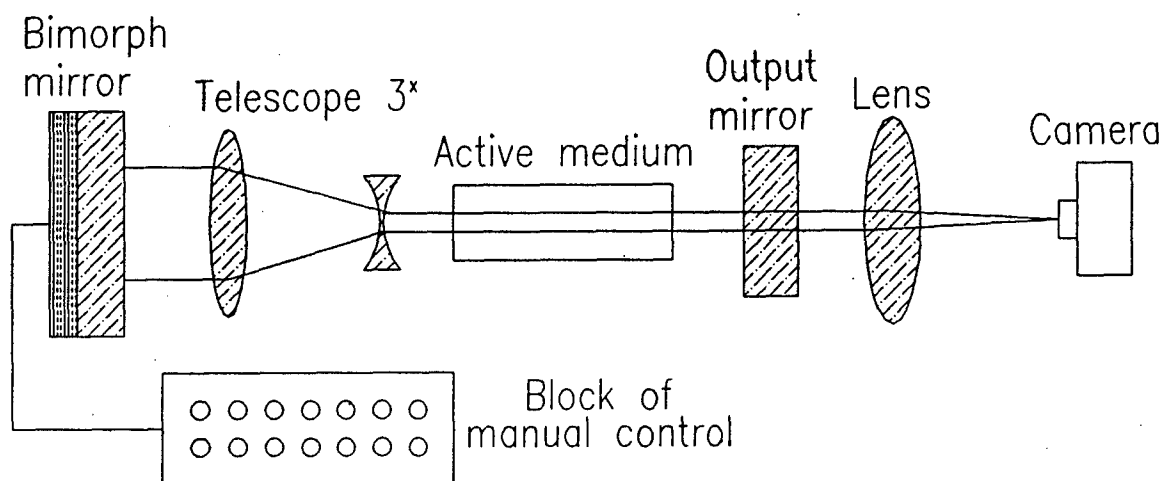
Main output parameters:
duration of a pulse — 30 ns;
wavelength — 308 nm;
energy of pulse — 30 mj.

Photo of spatial intensity distribution.
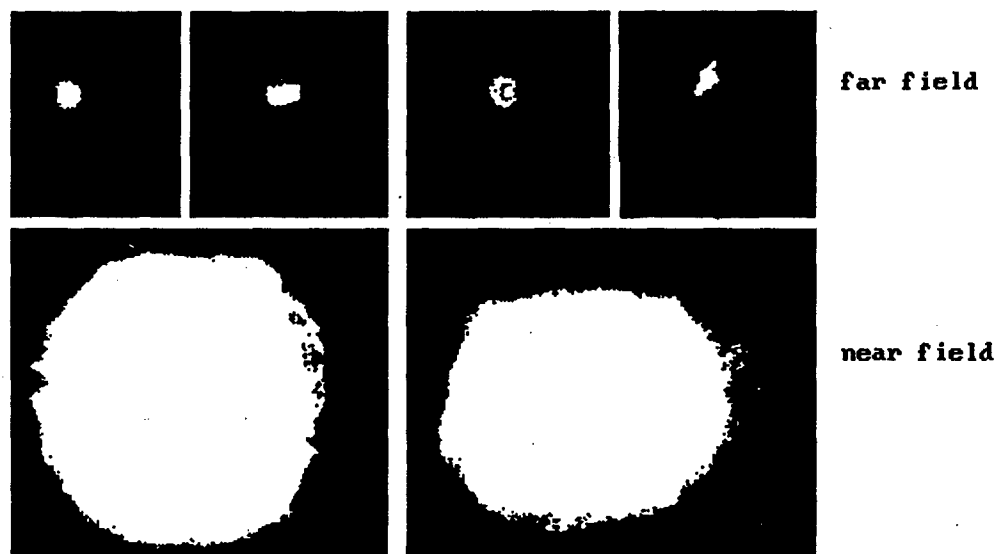
Control of Copper-Vapor Laser Radiation by Adaptive Mirror.

Experimental setup.
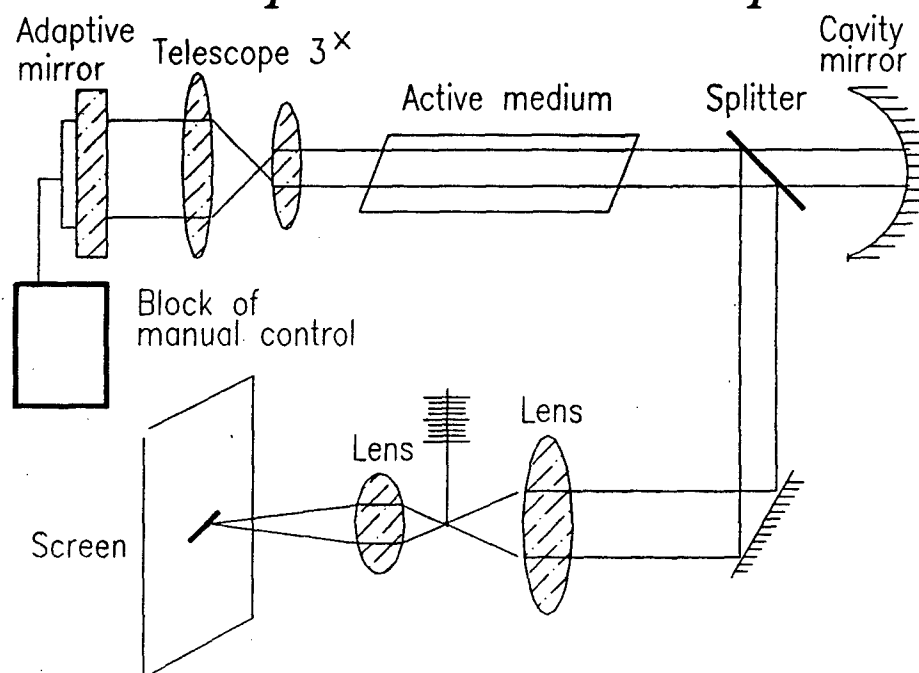
Divergency decreased from 0.25 mrad (without mirror control) to 0.08 mrad. Calculated divergency − 0.04 mrad.

Photo of spatial intensity distribution in the far field.

0.1mm
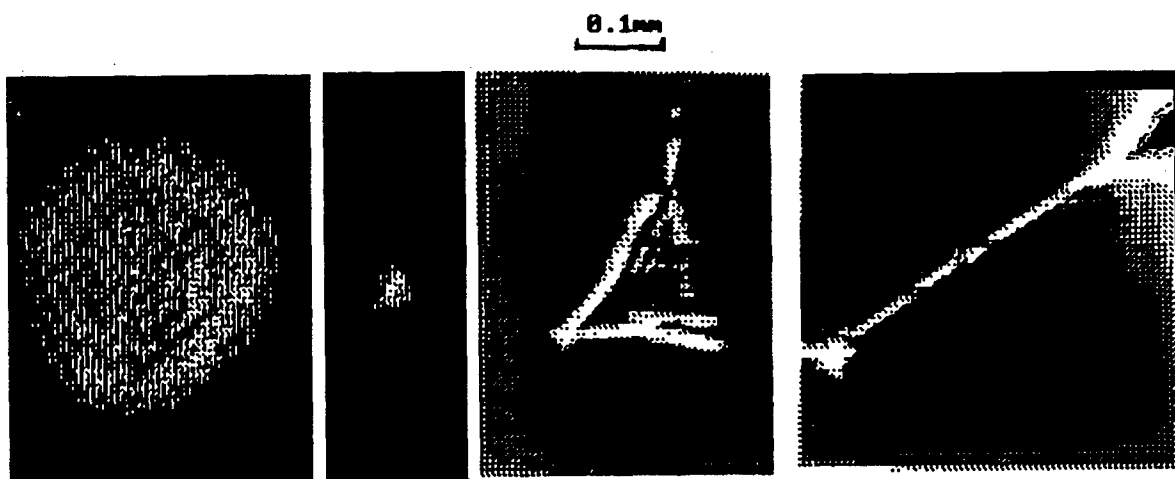
Control of CO2 Laser Radiation by Water-cooled Bimorph Mirror.

Exprimental setup with commercial laser TL-5.

amplifier   double oscillograph

pin-hole

sensor

adaptive mirror

laser cavity

oscillator

Main results:

U, V   W, kW

100   4

50   2
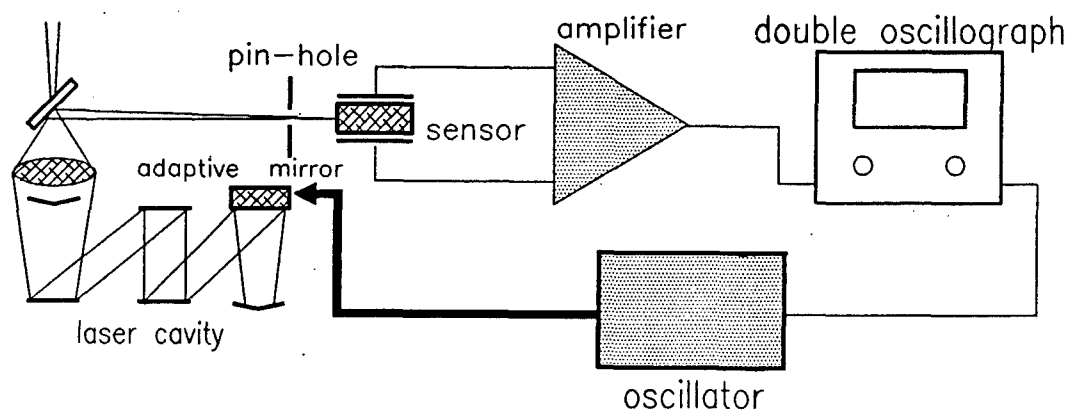
0   0.26   0.52   0.78 t,ms
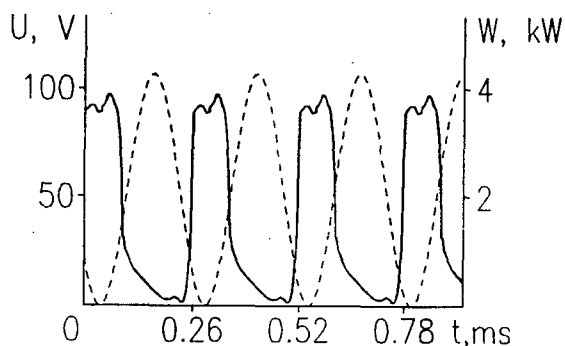
frequency of modulation – 3.8 kHz;
average
output power – 1 kW.

Influence of the surface shape of adaptive mirror on the output mode structure.

I,arb.un.

5

4   U=-300V

3   0V

2

1   +300V

0   5   10   15   X, мм
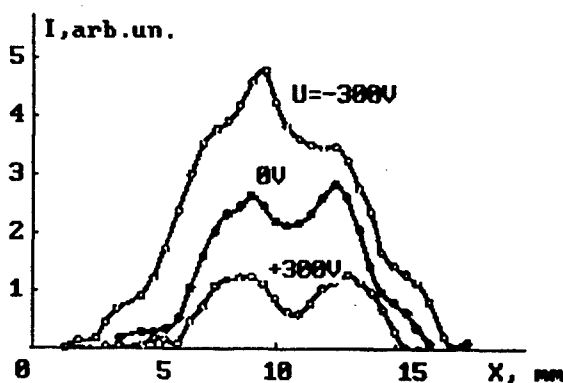
Schematic setup of the CW CO_2 laser ($\lambda = 10.6$ μm)
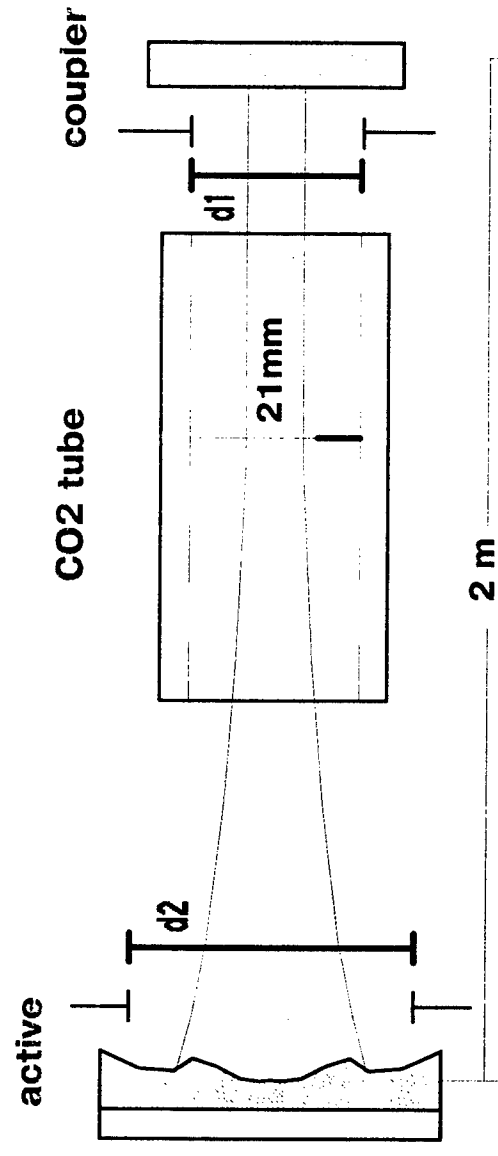
d1, d2 - diaphragms

Construction of bimorph deformable mirror.
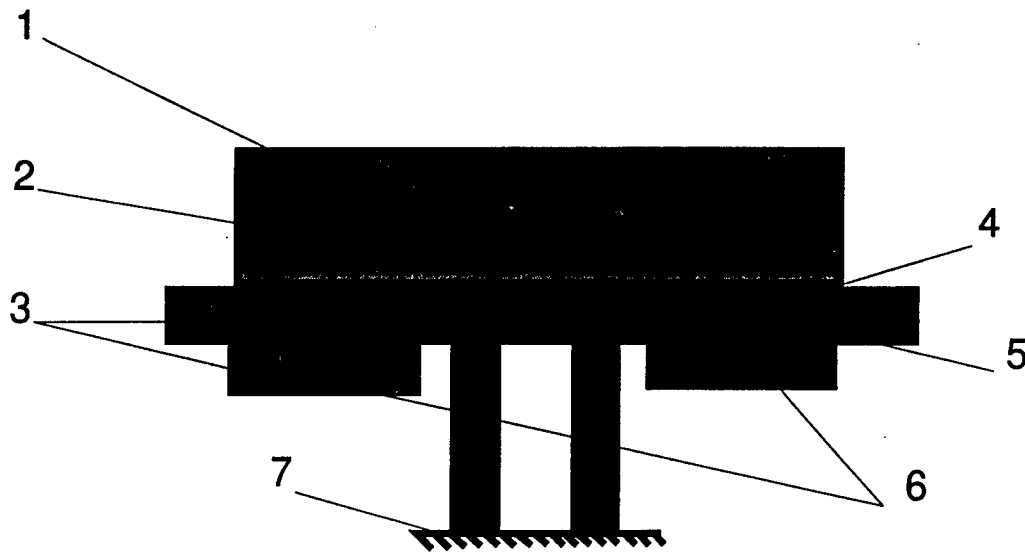
1- reflecting coating
2- glass plate
3- piezoceramic actuator disks
4- grounded electrode
5- common electrode e1
6- segmented ring electrodes e2, e3
7- baseplate

Scheme of segmented electrodes
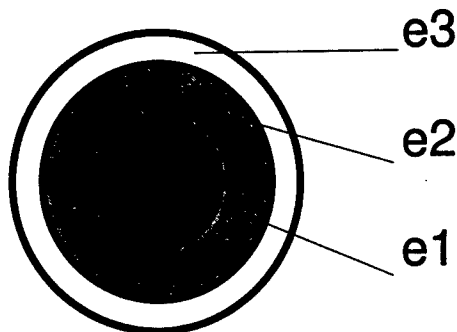
Experimental setup for mirror deformation measurements
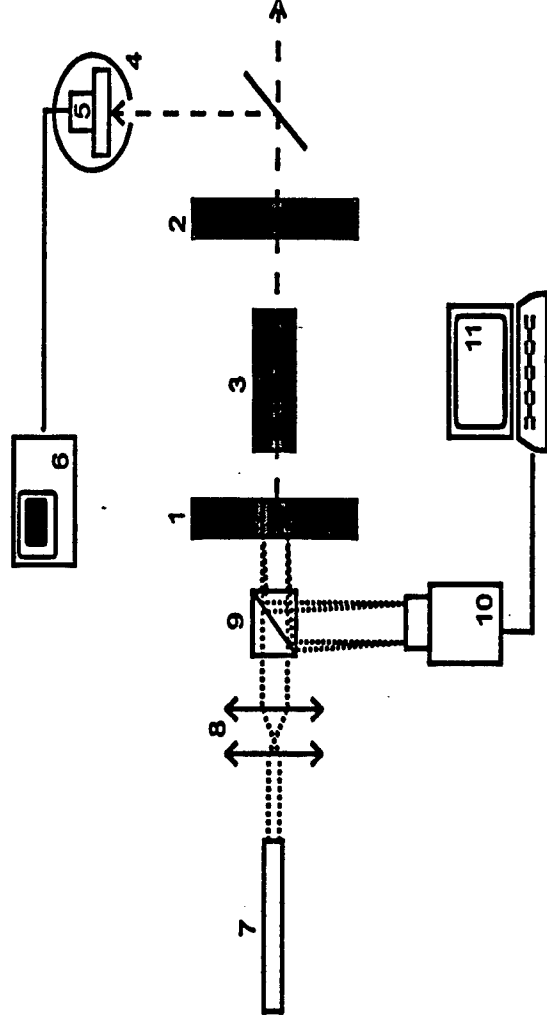
1 - mirror under test, 2 - cavity mirror, 3 - flash-lamp pumped laser rod, 4 - integrating sphere, 5 - photodiode, 6 - oscilloscope, 7 - He-Ne laser, 8 - telescope, 9 - beam splitting cube, 10 - CCD camera, 11 - IBM computer.

The reflection from both sides of mirror (1) created a Fizeau interferometric fringe pattern registered by CCD camera (10) and then developed with a special program in IBM computer (11). The output laser beam profile was registrated by photodiode (5). Intracavity light power is about 160 W.

Laser beam profile vs. cavity mirror deformation

a) b)
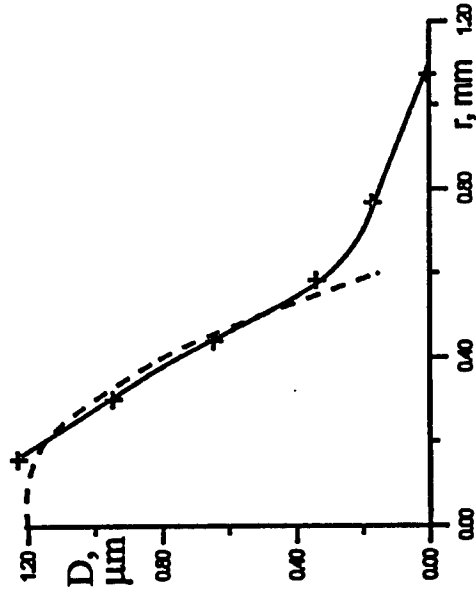
Intracavity laser mirror deformation (result of interferogramm reconstruction). Mind, that the scales on axes strongly differs.
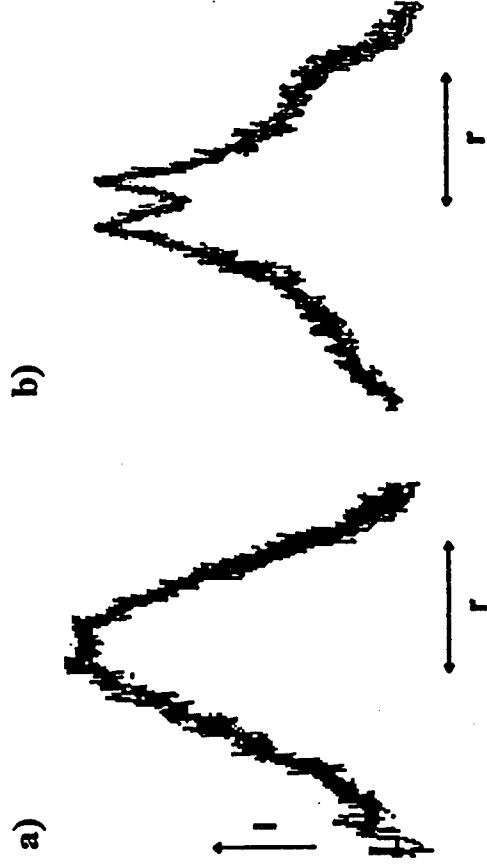
Output beam profile in multy mode regime of laser generation for resonator stability parameter $g1g2=0.2$ (a) and $g1g2=0.1$ (b). Some gap could be seen in the center of the laser beam due to high mirrors deformation in the center. The closer to the edge of stability zone, the greater is the influence of laser mirrors deformation on output beam profile.

Temporal behavior of the intracavity laser mirror under light heating
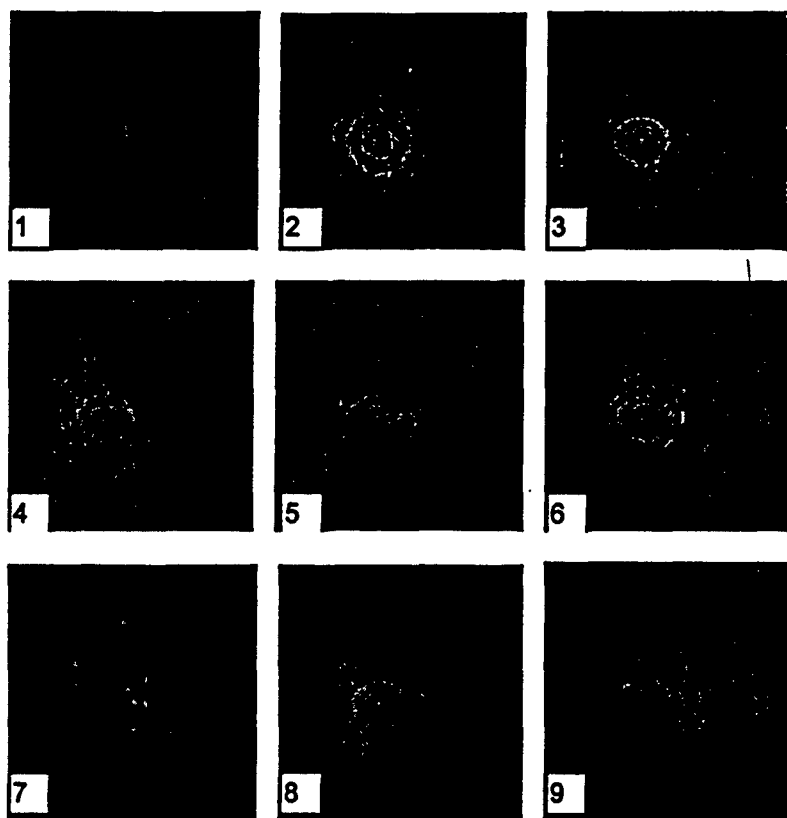
2.5 mm

These interferogramms presents the time change of intracavity mirror surface under light heating. Time step between pictures $\Delta t = 0.5$ sec. First picture corresponds to the moment of the starting laser generation. Transmission coefficient of mirror under test was $P = 0.2\%$.

Pictures 1 - 5 showes the change of the curveture radius, while on pictures 6 - 9 one can see only a slight fluctuation of the fringe pattern on the edge of the interferogramm.
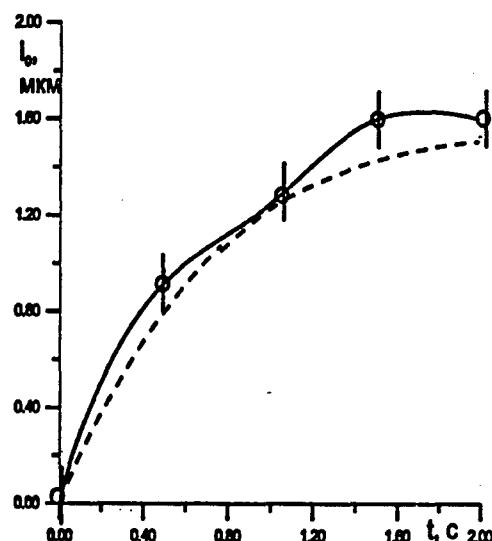
This curve presents the time dependance of laser cavity mirror deformation I_0. The whole process of reaching stationary regime takes about 2 seconds. This curve is well approximated by following expression:

$$I_0 = I_{os}(1 - \exp(-t/\tau))$$

where $\tau = 0.7$ sec.

Conclusion

- The thermal deformation of laser cavity mirrors causes the change of stability region and also modifies the output laser beam structure.

- Detailed study of the resonator mirrors interferogramms shows that the main thermal instability of the mirrors surface is observed at the edge of the fringe pattern. This could be one of the reasons for the higher instability of the output laser beam at the edge rather than in the center.

- Maximum time of mirrors profile stabilization after switching on the flash lamp is about 2 seconds for the intracavity beam power 160 W. This time depends strongly on the quality of the dielectric mirror cover.

Compensation of thermal lens aberrations.

Experimental setup.
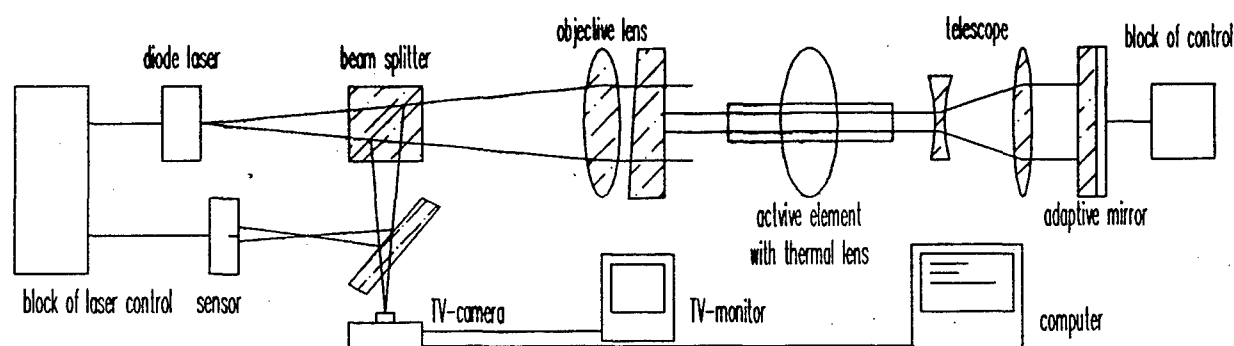
Amplitude of thermal lens aberrations.

A1, A2, — astigmatizm, K1, K2 — coma, SP — spherical aberration

Pump current — 26 A. Results are given in microns.

	A1	A2	K1	K2	SP
Before correction	−0.22	1.90	−0.27	−0.24	−0.06
After correction	−0.02	0.41	−0.17	−0.05	0.03

Interferogram of active element

| without thermal lens | aberrations of thermal lens | correction of this aberrations by adaptive mirror |

Control and Formation of the Solid State Laser Radiation.

Experimental setup.

Photodiode Camera Lens Lens Bimorph mirror Active element

Pin-hole

Computer Block of control
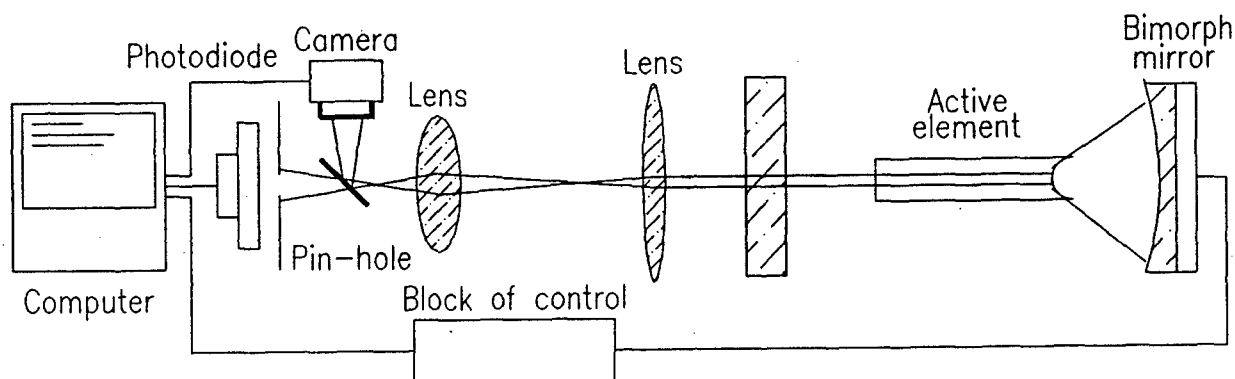
Main output parameters of laser radiation:
output power in multymode regime — 60 W;
in single mode regime — 7 W,
pump current — 32 A, 5 kW lamp.

Decreasing the divergency of a laser beam.

Far field distribution.
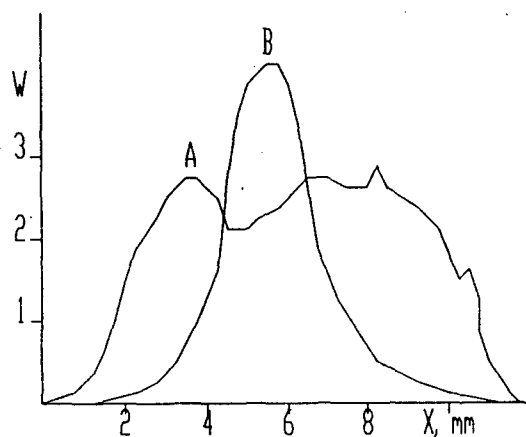
A — loop opened

B — loop closed
(divergency reduced
three times)

Different far field intensity distribution of a solid state laser radiation.

Single mode regime.
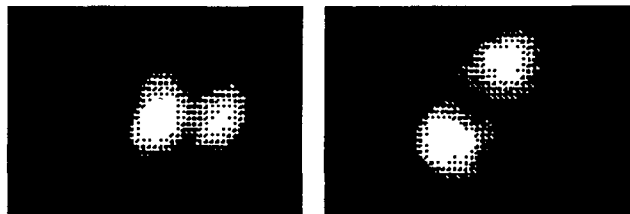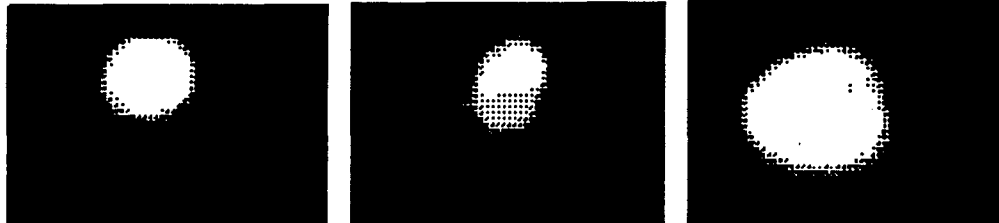
Multymode regime.
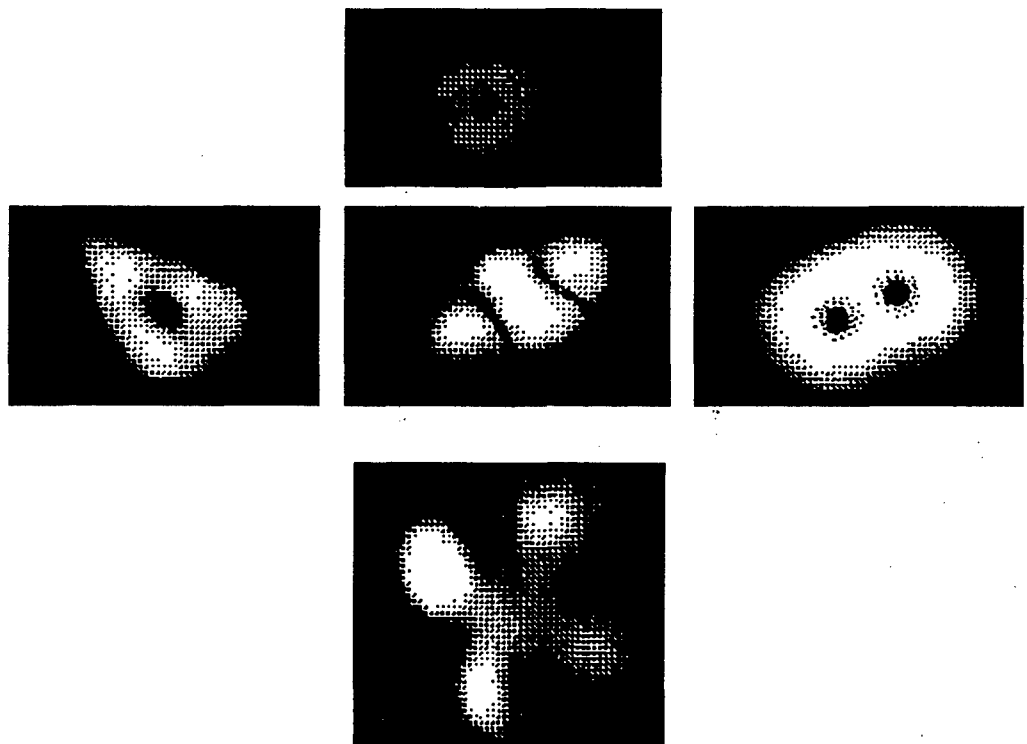
MAIN RESULTS

For example, for output super-Gaussian beam profile of the 8th order

RMS of the mirror profile approximation is 0.025%

Mirror Profile Vs. Radius
A - theoretical profile, B - bimorph mirror profile
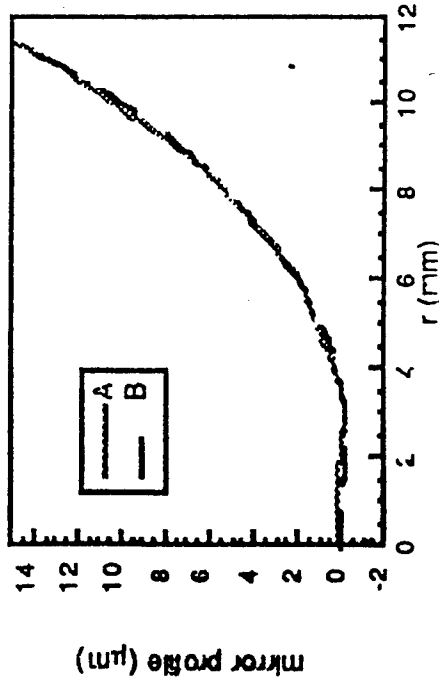
Near-field intensity distributions for super-Gaussian mode of the 8th order
A - theoretical mode, B - mode, produced with bimorph mirror
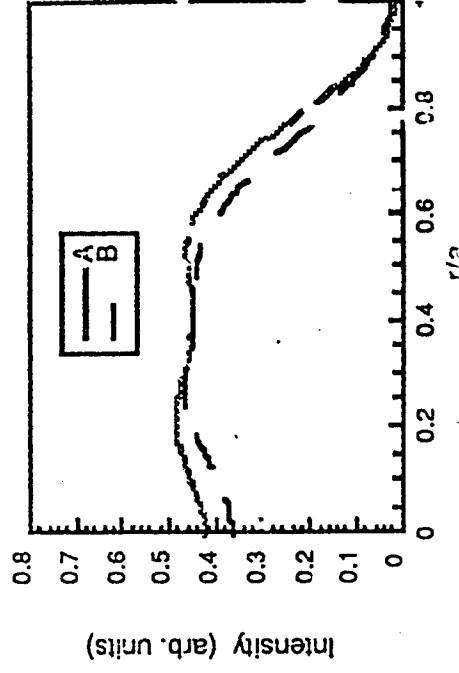
Laser beam intensity profile control by adaptive optics

Koshichi Nemoto, Takashi Fujii, Naohiko Goto, Takuya Nayuki
Komae Research Laboratory, Central Research Institute of Electric Power Industry, 11-1 Iwado-Kita 2-chome, Komae-shi,
Tokyo   201 JAPAN,Fax:intl.+81 3 3488 6697,   e-mail: nemoto@criepi.denken.or.jp
and Yoshi-kazu Kanai
Leonix corporation, 4-15-3 Higashi-Koigakubo, Kokubunji, Tokyo 185 JAPAN

Laser irradiation efficiency has a strong affect on the cost of laser isotope separation. We are developing a laser beam intensity profile control device based on coordinate transformation in order to improve the laser irradiation efficiency. In this paper, we attempt to obtain the optimum surface profile of the deformable mirror automatically.

The Fresnel equation, which describes the beam propagation characteristics, shows that the complex amplitude at the location of the image can be controlled by modifying the phase distribution. Therefore, if we can generate the phase distribution necessary for intensity profile transformation using a deformable mirror, we can transform an arbitrary intensity profile to other profiles. This method will transform beams to various profiles as long as the deformable mirror can produce the necessary surface profiles and the compatibility condition is satisfied.

The feedback control loop is shown in Fig. 1. The beam reflected by a deformable mirror is monitored on the screen by a CCD camera. The image data is transferred from the image processor to a computer through a GPIB bus, and evaluated by the computer. The computer calculates the supplied voltage of nine actuators based on the evaluation values of the profiles. The deformable mirror is designed to transform a Gaussian profile to a rectangular one, and has nine moving points and four fixed points[1]. When we control the laser beam intensity profile, the relation between the surface profile of the deformable mirror and the intensity profile of the reshaped laser beam is more complicated than that of phase compensation because the complex amplitude of the reshaped beam is the Fourier or Fresnel transformation of the beam reflected on the deformable mirror. Moreover, the characteristics of actuators are not linear and depends on the stress. Thus, the transfer function of this system is complicated. We adopted Genetic Algorithm (GA) for controlling a deformable mirror because we can treat this system as a black box using GA. GA is one of the optimum value calculation algorithms for obtaining the maximum or minimum value of a function f(x) in restricted region. The only feedback value is the fitness value, which describes the degree of similarity of the beam profile to a rectangular contour.

Figure 2 (a) and (b) show the initial Gaussian beam profile and the optimum beam profile reshaped to a rectangular contour, respectively. The optimum intensity profile was obtained within the limits of the deformable mirror system. In every trial, each maximum fitness value converges to the same value after more than 30 iterations. Moreover, each average fitness value also converges to the same level. However, since the mutation rate was set to large value, the average value did not converged to the same value as the maximum value. The spatial coherency of the beam is shown to be conserved after intensity profile transformation, since we can observe the interference fringes between the reshaped beam and the reference beam.

Reference   1) K. Nemoto et.al, Optics Lett., 21(3),p.168(1995)

Fig.1 Schematic diagram of the control system

(a)   (b)

Fig.2 Initial (a) and obtained beam profile (b)

Development of an Adaptive Optics System for SILVA

P.-Y. Madec, V. Michaud, D. Rabaud, F. Charbonnier, R. Deron, L. Rousset-Rouvière
Office National d'Etudes et de Recherches Aérospatiales
B.P. 72, 92322 Châtillon - France

C. Gallou, E. Delavaut, P. Dupuy, G. Delarue
Commissariat à l'Energie Atomique
Centre d'Etudes de Saclay - 91191 Gif sur Yvette - France

1. Introduction

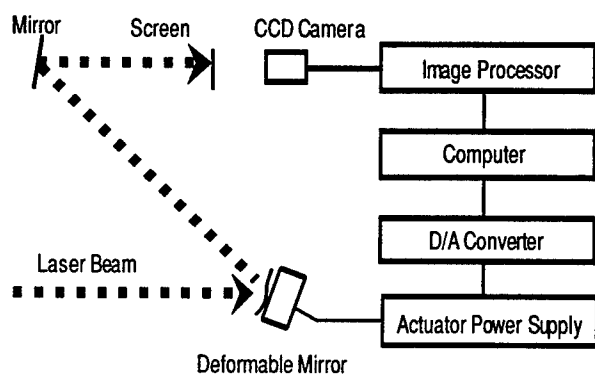To propose an alternative to currently used uranium enrichment processes, the Combustible Cycle Department of the CEA (the French Atomic Energy Commission) is developing a process called SILVA, a French acronym for Atomic Vapour Isotope Separation by Laser. To optimise the performance of the SILVA prototype, ONERA and CEA are developing and implementing an Adaptive Optics system designed to reshape the wavefront of the dye laser beams used to ionize the uranium vapour.

The Adaptive Optics system consists of a deformable mirror with 48 actuators and a wavefront sensor (WFS) including 21x21 analysis points. From the measurements supplied by the analyzer, a real-time computer determines the action to be applied to the deformable mirror. The control computer system architecture is based on a modular and upgradable design. The Adaptive Optics system developed can thus easily be reconfigured and especially adapted to the SILVA improvements expected during the optimization phases.

This paper first recalls the principle of the SILVA process, then describes the Adaptive Optics system developed and the characteristics of its main components. The system performance simulated by dedicated software developed by ONERA and CEA is indicated. Finally, first experimental characterization results are presented.

2. SILVA Principle

The SILVA process is now under study at CEA. It could ultimately replace gas diffusion for uranium enrichment with isotope 235 [2.1, 2.2, 2.3].

The SILVA process includes two subsystems :

• The separator which generates the atomic vapour

• The laser system which supplies the photons used to selectively ionize the uranium 235.

Selective ionization of uranium 235, carried out in three steps, requires using a high-power laser beam obtained by multiplexing several visible wavelengths. The laser system outputs this beam which is reflected in the separator by a set of mirrors to illuminate the vapour.

For optimal ionisation of all the uranium 235 atoms, the beam illumination profile must remain sufficiently uniform throughout its propagation. The beam wavefront, which plays a major role in the variation of the illumination profile, must therefore be controlled. This is done using an Adaptive Optics system with a deformable mirror, a wavefront sensor and real-time computer.

Adaptive optics systems were designed and have been in use for several years at ONERA for military and civilian applications. A dedicated system has been adapted to correction of a dye laser beam wavefront. This laser, consisting of an oscillator and dye amplifiers, shows particular spatial characteristics. The rectangular geometry cross-section laser beam exhibits high spatial frequency intensity non-uniformities, in particular a large over-shoot in intensity near the edges, which may introduce wavefront measurement errors. This problem is mentioned in Section 4.2.

In the future, several from those systems could be required to shape the SILVA process beam, at least one per color.

3. General Description of an Adaptive Optics System

An Adaptive Optics system is a servo closed-loop opto-mechanical set-up which compensates for the phase errors of an optical wave in real time [3.1].

This is made possible by the use of a deformable mirror located in the optical path. The mirror consists of a thin glass plate and actuators located behind it. The driving of these actuators can control the profile of the mirror's reflective surface to compensate for the phase errors in the reflected optical wave.

The second major component of an Adaptive Optics system is the wavefront sensor. This component measures the phase errors to be compensated for by the deformable mirror. There are several types of wavefront sensors. The one chosen for the SILVA system is based on the Hartmann-Shack principle [3.2].

Finally, to control the deformable mirror by a feedback loop, it is necessary to have a computer architecture to process the wavefront sensor signals in real time to determine the control voltages to be applied to the deformable mirror.

The specifications of these components are determined by the spatial and temporal characteristics of the errors to be corrected and the correction accuracy to be achieved [3.2, 3.3]. In particular, the number of degrees of freedom of the Adaptive Optics system, generally determined by the number of actuators of the deformable mirror, is given by the spatial spectrum of the phase errors to be compensated for. Similarly, the desired correction bandwidth is given by the temporal spectrum of the errors to be corrected.

Preliminary measurements made on the dye laser beam of the prototype SILVA system showed that the main phase errors to be compensated for were defocusing and astigmatism, as well as aberrations at a higher spatial frequency whose amplitude was sufficient to significantly degrade the quality of the dye laser beams. An optical

quality better than $\lambda/20$ rms is required for the corrected wavefront. This specification, to which is added the requirement for adapting to the rectangular geometry of the optical pupil of SILVA, led to use a deformable mirror with 8 x 6 actuators in a square mesh.

Since so far we do not have a sufficiently fast wavefront sensor, the characteristic variation times of the errors to be corrected are not known. At the request of CEA, the Adaptive Optics system developed should privilege accurate spatial analysis of the errors. The correction bandwidth obtained is not a crucial requirement. However, the real-time computer system designed must be sufficiently powerful and reconfigurable to be able to evolve toward large bandwidth Adaptive Optics.

4. Description of the Components

4.1. Deformable Mirror

The deformable mirror obtained for SILVA was manufactured by CILAS [4.1] (Figure 4.1). It includes 8 x 6 actuators located in a square mesh with a spacing of 9.5 mm. Each motor has a mechanical excursion of ±5 μm obtained with a control voltage of ±400 V. The first mechanical resonance frequency is higher than 14 kHz.

The mirror surface roughness is very weak. The errors at rest are mainly due to defocusing and astigmatism. In closed-loop operation, the mirror flatness is better than $\lambda/10$ peak-to-peak ($\lambda/45$ rms).
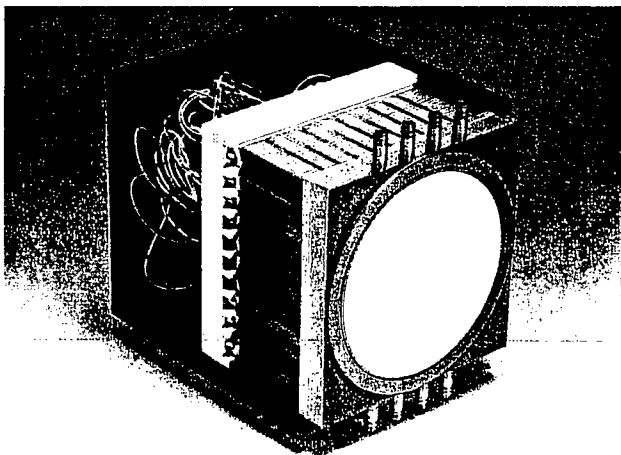

Figure 4.1 : Deformable mirror with 48 actuators made by CILAS; the mechanical cover was removed to show the piezoelectric actuators.

This type of mirror with a backside water-cooling system of its reflective surface, can operate in presence of laser beam power up to 5 kW. The water flow is generated by nozzles visible in the photograph of Figure 4.1.

4.2. Wavefront sensor

The Hartmann-Shack analyser principle is based on geometrical optics [4.2]. The wavefront is sampled by a matrix of microlenses, each defining an analysis subpupil. The phase errors then occur as a simple tilt of the wavefront. The tilt causes shifting of the image formed in the focus of the subpupil with respect to a reference position given by the position of each image for a perfectly flat wavefront. All these shiftings are measured

to determine the local wavefront tilt in each subpupil. These measurements can be used either to reconstruct the wavefront by the help of specific algorithms or, to control a deformable mirror, which is also a form of reconstruction.

The local shifting of the images is measured by a CCD camera located in the focus plane of the microlenses whose video output signal is digitized and processed. Processing consists simply of calculating the position of the center-of-gravity of the image formed in the focus plane of each subpupil.

The wavefront sensor developed for SILVA must satisfy two requirements : first to be able to control a deformable mirror to provide an Adaptive Optics system and secondly, in the absence of correction, characterise precisely the wavefront errors of the dye laser system. This second requirement makes it necessary to define an analyser whose spatial resolution is as high as possible and which therefore has a large number of subpupils. To optimise the control of the deformable mirror, the geometry of the latter must be adapted to that of the analyser. It is preferable to have a whole number of subpupils between each actuator. To meet these two requirements, one sensor with 21 x 15 subpupils was chosen.

The choice of the analyser CCD sensor was guided by the number of pixels required in each subpupil. This number dimensions the field of analysis of each subpupil, i.e. the sensor measurement dynamic range. A large number of pixels allows analysis of large phase errors. However, too many pixels is penalising for the response time of the Adaptive Optics system. Indeed, the more pixels in the sensor, the higher the feedback loop control frequency and therefore the smaller the correction bandwidth. A 256 x 256 pixels CCD sensor made by DALSA company capable of a rate of 150 images per second was chosen. There are therefore 12 x 12 pixels for each subpupil.

Finally, after settling the physical specifications of the analyser, we needed to evaluate its measurement accuracy [4.3]. Where $\sigma^2\phi$ is the analyser measurement noise variance expressed in rad^2 we have:

$$\sigma^2_\phi = \frac{\pi^2}{2} \frac{1}{<N>} \left(\frac{N_T}{N_D}\right)^2 + \frac{\pi^2}{3} \frac{\sigma^2_e}{<N>^2} \frac{N_S^4}{N_D^2}$$

where:

* $<N>$ is the average number of photons detected per subpupil and per frame, expressed in electrons per pixel per frame

* σ_e is the standard deviation of the CCD electronic read noise expressed in electrons per pixel per frame

* N_T is the full width at half maximum of the image profile in the focus plane of the microlenses expressed as a number of pixels

* N_D is the full width at half maximum of the diffraction limited profile in the focus plane of the microlenses expressed as a number of pixels

* N_S^2 is the number of pixels used to compute the center-of-gravity.

Since the dynamic range is defined as the ratio between the maximum number of electrons that can be cumulated in each pixel and the standard deviation of the read noise, the DALSA sensor used has a dynamic range of 500. Furthermore, at half the CCD saturation, $<N>$ is equal to approximately 35,000 electrons per pixel per frame. For SILVA, the errors to be measured are mainly defocusing and astigmatism. For instance, the full width at half maximum of the image in the focus of each microlens is limited by diffraction. We therefore have $N_T/N_D = 1$. For Shannon sampling of each image, we determine the focal length of the microlenses such that $N_D = 2$. Finally, the number of pixels used to calculate the center-of-gravity is set to around 10.

Based on these characteristics, the measurement accuracy is $\lambda/160$ rms, where λ is the mean wavelength of the wavefront sensor, i.e. approximately 0.6 µm. It should be noted that it is very difficult to achieve such an accuracy experimentally, mainly due to local turbulences in the test room and vibrations.

Finally, although it can be formally demonstrated that the calculated position of the center-of-gravity of the image in each subpupil is equal to the spatial mean of the first derivative of the corresponding wavefront, it should be noted that this result is true only if the intensity is uniform in the subpupil. However, one of the features of the SILVA dye laser beams is to exhibit non-uniform intensity at spatial scales smaller than a subpupil.

The wavefront sensor measurement accuracy was simulated at ONERA. Typical phase errors of the SILVA system were considered. The intensity distribution used was based on experimental measurements made on the CEA bench facilities. The conclusion of the simulations is that the intensity variations encountered are not a limiting factor for characterisation of the phase errors expected on the SILVA dye laser beams. Criteria were defined to evaluate the phase measurement accuracy that can be achieved for a given intensity profile. These criteria are based on the spatial spectrum of the intensity distribution in the pupil.

4.3. Real-Time Computer

The computer was derived from developments conducted at ONERA in collaboration with the French company SHAKTI [4.4] for space observation applications. Its architecture is capable of controlling an Adaptive Optics system with a large bandwidth. Using two CPU cards with a total of 12 Texas Instrument TMS320C40 Digital Signal Processors, it is capable of controlling 100 actuators at frequencies up to 2500 Hz.

However, for applications requiring less computer power, it is possible to use a powerless dedicated version of these cards which can be inserted in an ordinary PC.

The computer includes all the electronics used to compute the deformable mirror control voltages from the analogue video signal output by the camera. Its main components include:

- A remote digitization unit
- A digital video signal equalizer unit
- A real-time CPU unit

- A video display unit.

Developed entirely by SHAKTI, it is capable of controlling the 48 actuators of the deformable mirror using the video signal from the DALSA CCD camera.

The maximum control frequency achievable with this architecture is 30 Hz which allows a correction bandwidth of a few Hz. This computer could achieve a control frequency of 500 Hz without any modification, simply by using a 64 x 64 pixel CCD sensor.

The architecture developed includes two racks. The first contains the digitization unit and the second, to the VME standard, contains the equalizer, CPU and graphic display cards. Both racks are controlled via a workstation providing the user interface. The workstation is used for initialising the cards and having them perform the functions required for management of the system.

Remote Digitization Unit

This unit consists of a rack in single Eurocard format. It is capable of digitizing the video signal from any camera on 12 bits at rates up to 10 Mpixels/s. The digitization noise is less than one bit. The unit performs many operations, including dynamic sensor windowing, offset adjustment and digitizing by double correlated sampling. The digitization clocks are set from the workstation by software.

After being digitized, the signal is sent to the VME computer containing the equalization card and CPU card. The digital video signal can therefore be transmitted over long distances without any loss of quality, even in severe electromagnetic environments.

Video Signal Equalizer Card

So as not to introduce any bias on calculation of the intensity center-of-gravity in each subpupil, it is necessary for all the pixels to have the same flux response. If $I(i,j)$ is the raw signal supplied by the pixel on the ith line and j^{th} column, $I(i,j)$ depends on the received flux $F(i,j)$ as follows:

$$I(i,j) = G(i,j)\,F(i,j) + O(i,j)$$

where $G(i,j)$ is the pixel sensitivity and $O(i,j)$ its offset.

The equalizer card is used to obtain a uniform response on all the pixels by subtracting an offset plane representing all the $O(i,j)$ from the image consisting of all the $I(i,j)$ then multiplying the result by a gain plane consisting of all the $1/G(i,j)$. All these operations are done in real time The offset and gain planes can be recorded experimentally. They are loaded into a memory space on the card which performs equalization in real time at rates up to 10 Mpixels/s.

After being equalized, the video signal is thresholded to eliminate any unilluminated pixels whose only contribution to calculation of the center-of-gravity is the read noise. Therefore, only around 10 pixels are preserved for calculation.

The equalized and thresholded video signal is then sent to the CPU card via a private video bus located on the card front edge. The data rate on the bus can be up to 10 Mwords/s. This private bus frees the VME bus to which

the card is connected and which is used only to set the parameters, such as the gain and offset planes and acquire the experimental data in real time (analyser measurements, deformable mirror commands).

Display Card

This card is used for video display of the digitized and equalized video signal supplied by the equalizer card. So as not to slow down the private video bus, this card is located in wiretap mode: it merely extracts data from the bus as needed without disturbing transmission. It is one of the basic components for adjusting the Adaptive Optics system.

CPU Card

This card is at the heart of the computer architecture. It provides the computation power required for real-time control of the loop.
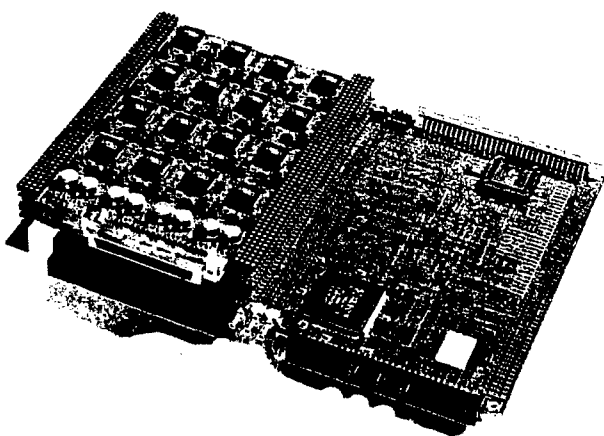

Figure 4.2. : SHAKTI motherboard equipped with a CPU module with 3 DSPs and a 64-output DAC module

It consists of a motherboard on which various modules can be mounted (Fig. 4.2). The motherboard dialogues with the VME bus and retrieves the digitized data transferred via the private bus. It includes programmable logic components so that it can accept any type of data format from the video bus on its input and send the computed data in any format on its output. The power of this card resides in the possibility of completely reconfiguring it by dynamically downloading new programmes into its programmable logic. This means that the same computer architecture can be easily used for different applications. This capability has been widely used in recent years at ONERA.

Different modules can be mounted on the motherboard. For SILVA, two CPU modules are used, each including three Texas Instrument TMS320C40 DSPs. The first module computes the centres of gravity. The first DSP is used for this computation as such, the second stores the computed data in a buffer and the third stores the equalized images from the wavefront sensor. These buffers are accessible by both the C40 DSPs and the VME bus which allows the user to retrieve the data in real time for analysis. This operation is possible even when the system is operating in closed-loop mode. The second module computes the deformable mirror control voltages from the results supplied by the first module. The computation consists of multiplying the precalibrated control matrix discussed below by a vector containing the

analyser measurements. The multiplication is performed by the first DSP, and the second DSP stores the computed control voltages in a buffer accessible to user.

The card performance is limited by the center-of-gravity computation. This operation, the most costly in CPU time and data transfer time, can only be performed by a single DSP. Each of the processors is potentially capable of processing 5 Mpixels/s. However, for SILVA, the maximum rate achieved is limited to 2 Mpixels/s, which corresponds in our case to a frame frequency of 30 Hz. This limitation is due to the real-time software used to compute the centres of gravity. If, during testing on the Adaptive Optics system, it appears that the specified bandwidth is too small, the software will be first optimised to achieve the maximum performance capabilities of the component. If the bandwidth is still too small, the use of a sensor with fewer pixels will have to be considered. For instance, a CCD camera with 64 x 64 pixels would allow a control frequency of 500 Hz to be achieved without optimization.

The third module mounted on the motherboard is a DAC with 64 converters. Each operates on 12 bits with a conversion speed of 2 V/μs and one-half bit of noise. The output conversion dynamic range is continuously adjustable up to +10 V.

4.4. Control Software

The software architecture used to control the SILVA Adaptive Optics system was entirely developed by ONERA. This architecture includes function libraries available in servers accessible on the TCP/IP network and a graphic user interface. The software can be executed on a workstation or a PC type computer.

Programming of the function libraries is structured on three different levels:

• The lowest level includes the functions close to the machine. The programmes depend on the computer hardware used. Programmes are either in C or C40 assembler and can only be written by real-time computing specialists.

• The medium level includes the basic functionalities required for an Adaptive Optics system, such as measurement acquisition and mirror control. The programmes are sequences of low level functions. They are in C or C++ and can be written by software developers.

• The highest level includes tools for using the Adaptive Optics system, such as control matrix computation or offset plane acquisition. The programmes in this case are sequences on medium level functions. Written in TCL, an interpreted language in the public domain, they use function servers created from medium level libraries. They can be developed by engineers specialised in Adaptive Optics.

The graphic user interface is used to control the complete system from a graphic menu using the mouse. Written in TCL-TK, which is the graphic extension of TCL, it is a sequence of high level functions which allow the user to select the physical parameters to be set for the system.

This programming philosophy has many advantages. Programming on several levels means that only part of the software needs to be rewritten in case of upgrade of the

equipment or modification of the Adaptive Optics system specifications or even a change of application.

It is obvious that this saves considerable development time and thereby reduces the cost. It also allows the different levels to be developed in parallel and requires only limited number of specialists in real-time computing. Finally, the use of an interpreted language and function servers makes it easy for the user to modify the interface or test new capabilities by constructing his own management application, leaving an enormous amount of space for imagination and creativity.

5. Control Algorithms

5.1. Control Matrix Computation

All the physical phenomena relating the wavefront sensor to the deformable mirror are assumed to be linear. We ca take the example of an aberrant wave for which the analyser outputs a measurement vector. The aim is to find a control matrix which, multiplied by the measurement vector, yields a mirror control voltage vector that minimises the residual variance of the wave phase after correction.

This is done by defining a matrix characterising the influence of the mirror on the wavefront sensor. This matrix, called interaction matrix and denoted D, is obtained by applying a unit command to each motor in turn and recording each measurement vector associated with each motor. All the measurement vectors are arranged in columns to form matrix D.

Then for any control vector $|V>$, it is possible to calculate the measurement vector $|\epsilon>$ by:

$$|\epsilon> = D |V>$$

Calculating $|V>$ from $|\epsilon>$ amounts to invert the above equation.

As a general rule, interaction matrix D is rectangular (there are more measurements than there are actuators to be controlled). A criterion must therefore be chosen to calculate the control matrix. Since the resulting matrix must minimise the residual errors after correction, the least squares minimisation criterion is used, yielding the following result:

$$({}^tD\, D) |V> = {}^tD\, |\epsilon>$$

where ${}^tD$ is the transposed matrix of D.

The control matrix is therefore computed by inverting the matrix product $({}^tD\, D)$, a symmetric square matrix. The singularity of this matrix is analysed by determining its eigenvectors and eigenvalues. This yields:

$$({}^tD\, D) = P\, \Delta\, {}^tP$$

where:

• P : column matrix of eigenvectors

• Δ : diagonal matrix of eigenvalues.

An eigenvector represents a spatial deformation profile of the deformable mirror. The corresponding eigenvalue represents its sensitivity to the wavefront analysis. If one of the eigenvalues is zero, matrix $({}^tD\, D)$ is not invertible. This mode with a zero eigenvalue can then be filtered out to calculate the control matrix. The result becomes:

$$D^* = P\, \Delta^{-1}\, {}^tP\, {}^tD$$

where
• D^* : optimal control matrix
• Δ^{-1} : inverse of the eigenvalue matrix in which the inverse of the eigenvalues corresponding to the modes to be filtered out is replaced by 0.

This makes it possible to compute the control matrix after filtering out the modes that are relatively insensitive to the wavefront analysis to prevent them from causing too much noise on the command.

The tools used to record the interaction matrix, determine the eigenvalues and eigenvectors, display them, select the modes to be filtered and finally compute the control matrix are available in the computer function libraries.

This last matrix is used by the CPU card to generate the deformable mirror control voltages in real time.

5.2. Temporal Correction

An Adaptive Optics system is a servo closed-loop system. It is governed by control system equations. It is a multivariable servo system which can be separated into as many single-variable feedback systems operating in parallel as there are actuators on the deformable mirror. In this case, if the control variables are the eigenvectors described above, then they become eigenmodes of the system and they are independent because of the orthogonality property of these modes.

To ensure feedback loop stability and accuracy, a recursive algorithm is executed by the real-time computer CPU card to apply various temporal correctors. For instance, the user can easily defined a PID type controller or a Smith controller or any other type.

In the case of SILVA, since the temporal constraints are not very severe, a simple integral controller is used to cancel the static errors of the dye laser optical beam and ensure a bandwidth of a few Hz.

6. Performance

6.1. Simulations

6.1.1. Bandwidth

ONERA has been conducting theoretical research on the control of Adaptive Optics for several years [6.1]. The temporal behaviour of each in the system components is well known. The open-loop transfer function of the SILVA Adaptive Optics can therefore be completely simulated. In the case of use of simple integral action, it can be written:

$$G(s) = K_i\, \frac{1 - e^{-Ts}}{T^2\, s^2}\, e^{-\tau s}$$

where:
s is Laplace variable ($s = j\omega$; $\omega = 2\pi f$; $j^2 = -1$)
K_i is integral controller gain
T is control period
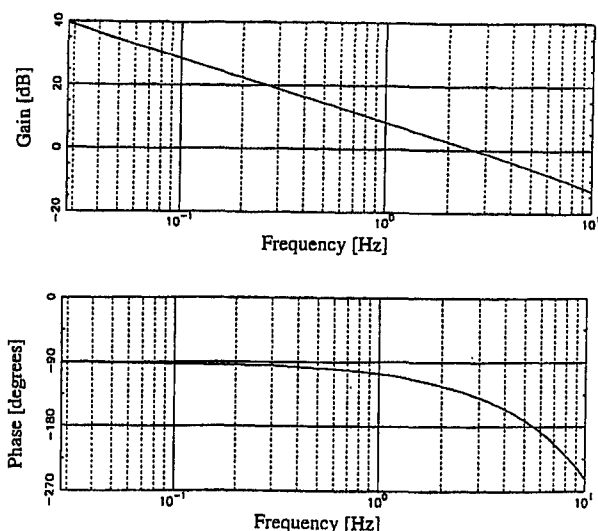τ is pure control delay.

Figure 6.1. : Bode diagram of the simulated open-loop transfer function

For a 30 Hz sampling frequency and a measured pure delay of 28 ms due only to reading of the CCD, the gain K_i is set to a value of 0.65 to obtain a phase margin of 45 degrees. Therefore, the closed-loop gain does not exceed 2.3 dB. Figure 6.1 shows the gain and phase of the simulated open-loop transfer function. The 0 dB cut-off frequency is 2.7 Hz.

Experimental measurements were made on the SILVA Adaptive Optics. The results are given in Figure 6.2, showing the gain and phase of the open-loop transfer function for an integral action gain of 0.65. This confirms the simulation results, with a 0 dB cut-off frequency of 2.7 Hz and a phase margin of 45 degrees.
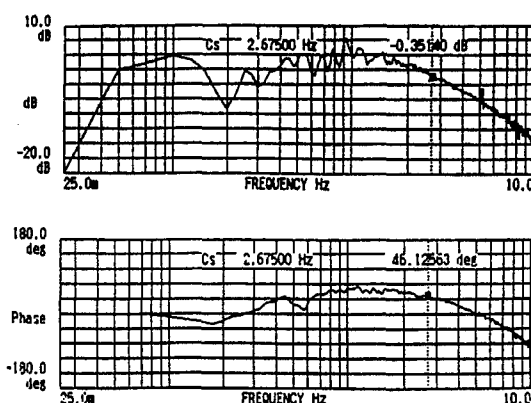

Figure 6.2. : Bode diagram of the experimental open-loop transfer function

6.1.2. Correction Accuracy

ONERA has a range of numerical simulation software to model the behaviour of each of the components of an Adaptive Optics system and the phase errors to be corrected. The deformation profile of each of the actuators is taken into account as well as operation of the Hartmann-Shack analyser and its measurement accuracy according to the number of subpupils, the flux and the read noise. The control matrix is computed from simulation of the optical interaction matrix. The modal

filtering methods described above are taken into account. Finally, the loop transfer function is represented.
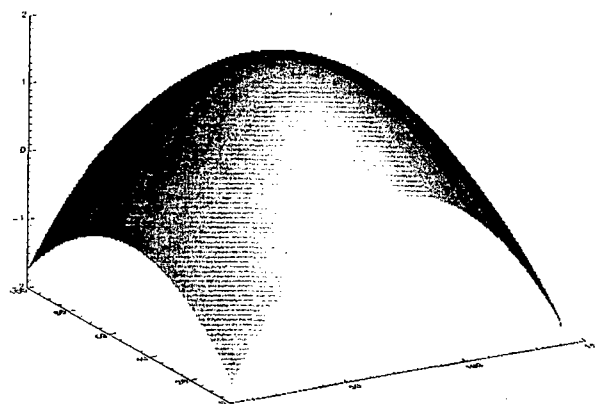
Figure 6.3-a : Defocusing before correction
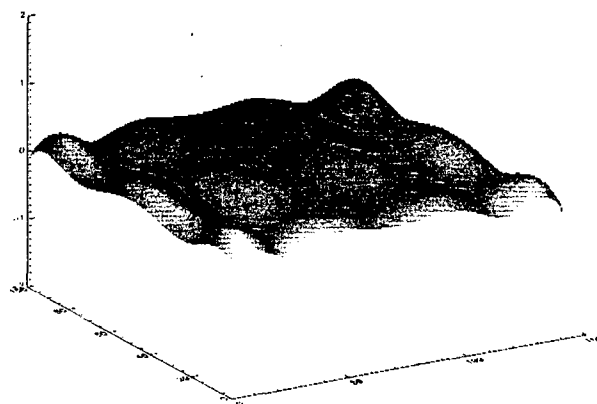
Figure 6.3-b : Defocusing after correction

From this set of software, the SILVA Adaptive Optics system correction accuracy was modelled for the main errors present on the dye laser beam. Two parameters were calculated:

- The ratio between the peak-to-peak error before correction and the peak-to-peak error after correction, denoted G_{cc}

- The ratio between the peak-to-peak error before correction and the standard deviation after correction, denoted G_{cc}/rms

For defocusing, we found $G_{cc} = 9.3$ and $G_{cc}/rms = 66$. For astigmatism, we obtained $G_{cc} = 8$ and $G_{cc}/rms = 60$. The correction accuracy achieved is mainly limited by the number of actuators of the deformable mirror and the deformation profile of each actuator. Figures 6.3-a and 6.3-b show the 3D defocusing before and after correction. The two graphs are to the same scale. For instance, for defocusing exhibiting a peak-to-peak error of λ, a residual error of $\lambda/66$ is obtained after correction.

6.1.3. Propagation Simulation

Figures 6.4-a and 6.4-b show the illumination and typical wavefront profile of a laser beam from the SILVA system. The measurements were made using a CCD camera for illumination and a Hartmann-Shack wavefront sensor for the optical phase. Figure 6.4-a shows the edge effects visible in one dimension of the illumination profile, characteristic of beam guidance by amplifier ducts.
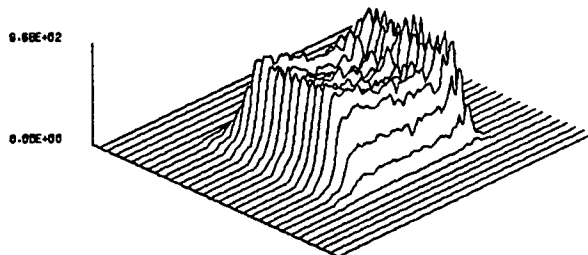

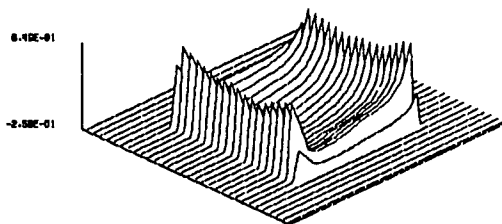Figure 6.4-a : Measured dye laser beam illumination profiles

Figure 6.4-b : Measured dye laser beam wavefront profiles

Figures 6.5-a, 6.5-b and 6.5-c illustrate the improvement expected in the beam shape during propagation. These profiles result from numerical simulation of propagation by a double Fourier transform computation code. The initial intensity profile is the same, and only the wavefront considered has changed:

• Figure 6.5-a : The two main curvatures (mean curvature and astigmatism) of the initial wavefront are corrected. This case is representative of the results that can be achieved in the absence of Adaptive Optics. Correction is obtained using spherical and cylindrical lenses.

• Figure 6.5-b : The first 15 Legendre modes of the initial wavefront are corrected using Adaptive Optics. It is recalled that since the pupil geometry is rectangular, the optical phase can be decomposed on the orthonormal base of the Legendre polynomials.

• Figure 6.5-c : The wavefront is perfectly flat.

The light intensity distribution of the beam on either side of the pupil image is computed to analyse its uniformity during propagation in the uranium vapour separator. The propagation distance considered in the simulation is equal to $(a^2/4\lambda)$, where a is the beam radius and λ is the wavelength. It is checked that better uniformity of the beam illumination distribution during propagation is preserved after total or partial correction of the wavefront.
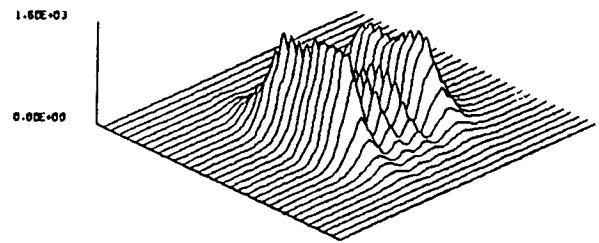
Figure 6.5-a : Simulated illumination profile without Adaptive Optics: defocusing and astigmatism corrected.
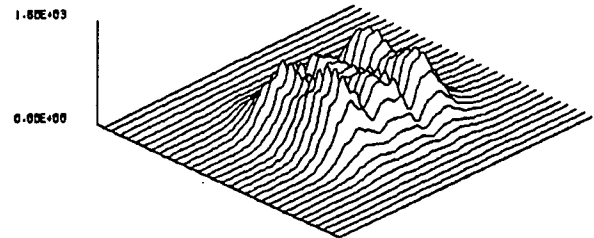
Figure 6.5-b : Simulated illumination profile with Adaptive Optics: first 15 Legendre polynomials corrected.
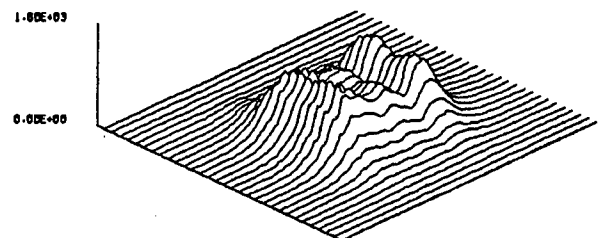
Figure 6.5-c : Simulated illumination profile for a flat wavefront.

6.2. Experimental Characterisations

6.2.1. Correction Accuracy

The purpose is to measure the maximum correction accuracy of the Adaptive Optics system developed. For this purpose, the experiment consists of correcting the intrinsic flatness errors of the deformable mirror and evaluating the resulting surface quality. The experimental setup used is described in Figure 6.6.

We first used a reference flat mirror whose flatness evaluated by the Zygo was equal to $\lambda/16$ peak-to-peak. The measurement supplied by the wavefront sensor were recorded to be used as reference during the tests. The reference flat mirror was then replaced by the CILAS deformable mirror of which only an area of 24 x 36 mm was used (5 x 4 actuators). The feedback loop was then closed and the surface condition of the deformable mirror after correction was evaluated by the Zygo.
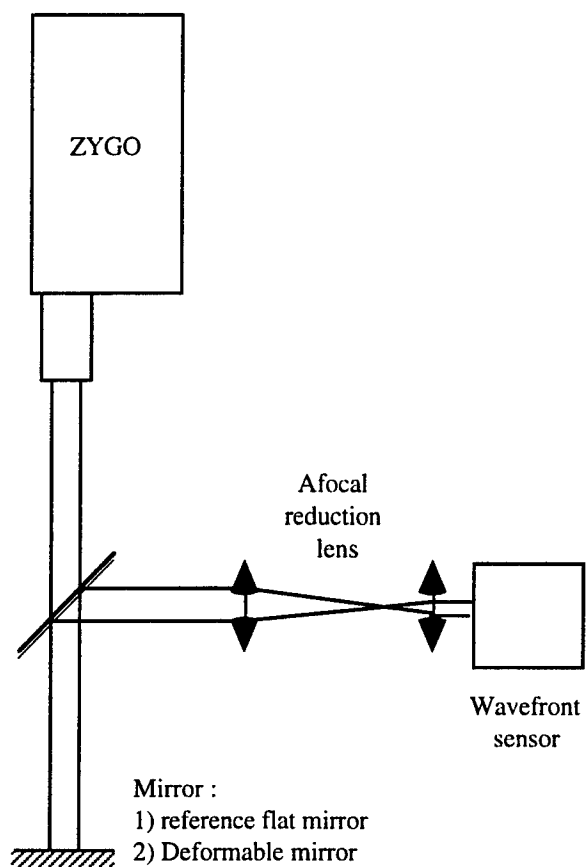
Figure 6.6 : Experimental setup for evaluating the correction accuracy of the Adaptive Optics system

Figure 6.7-a shows the surface condition of the deformable mirror at rest. It exhibits a peak-to-peak error of $\lambda/2$ (for an rms error of $\lambda/10$). Figure 6.7-b shows the surface condition of the deformable mirror after correction. It exhibits a peak-to-peak error of $\lambda/11$ (rms error of $\lambda/46$). The correction accuracy achieved is excellent and consistent with the stated objectives.
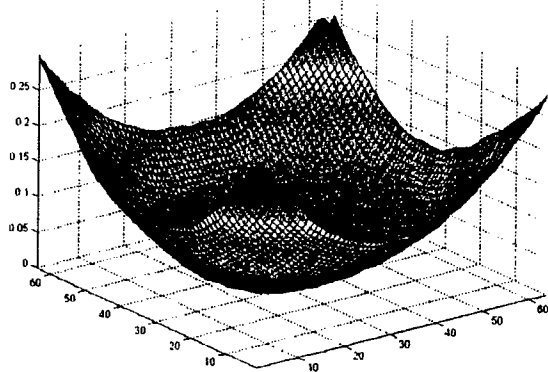
Figure 6.7-a : Surface condition of the deformable mirror at rest
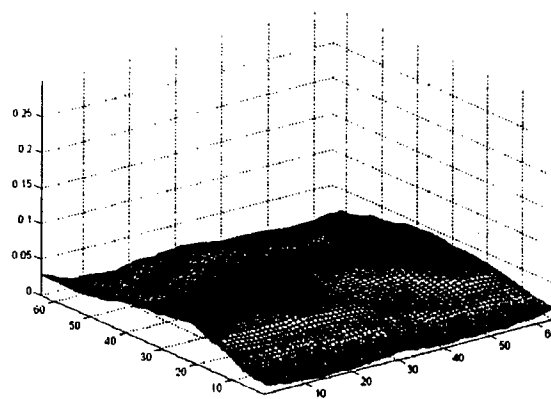
Figure 6.7-b : Surface condition of the deformable mirror after correction

6.2.2. Reshaping of the Laser Beam

The purpose of this experiment, described in Figure 6.8, is to correct the phase of an He-Ne laser beam (beam 1) to make it identical to another, so-called reference beam (beam 2).

CHANNEL A   CHANNEL B
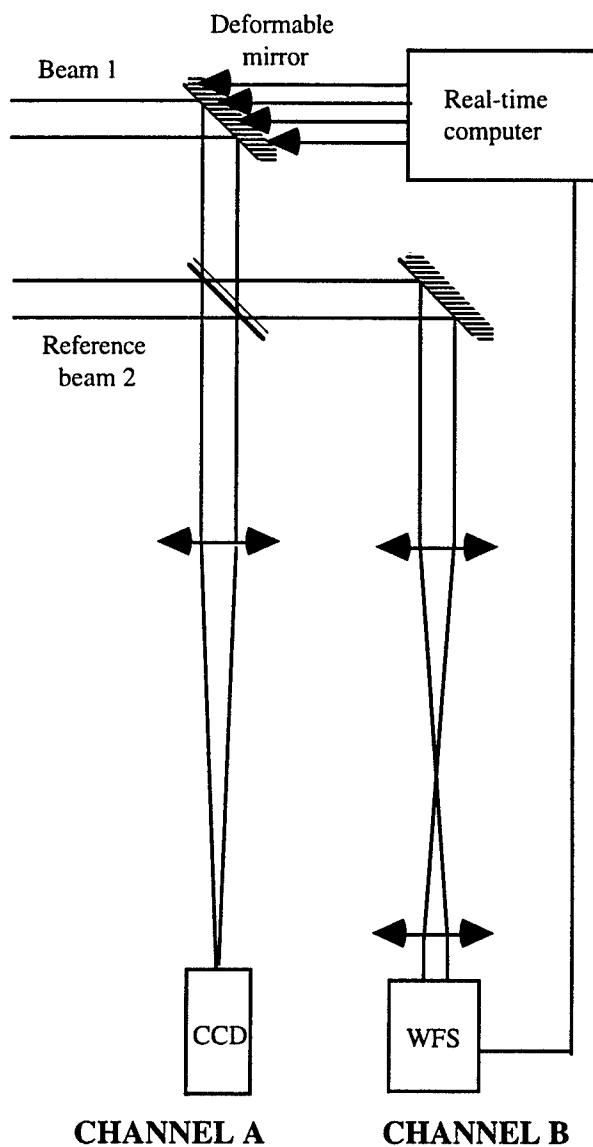
Figure 6.8 : Experimental laser beam shaping setup

The phases of the two beams are compared using the corresponding far-field images recorded by the CCD camera of the setup described. With beam 1 masked, the wavefront sensor measures the phase errors of beam 2 which are then used as reference in the rest of the experiment. The image supplied by the CCD camera is recorded. The reference beam is then masked to use only beam 1. The feedback loop is closed. The wavefront sensor (WFS) measures the phase error between the two beams and the real-time computer evaluates the voltages to be applied to the deformable mirror to give beam 1 the same phase profile as beam 2. The image supplied by the CCD camera is recorded again.

Figure 6.9 shows the far-field images obtained with each of the two beams. The recorded image of the reference beam is on the left and the recorded image of beam 1 reshaped by the Adaptive Optics system is on the right. Comparison of these two images shows the operational quality of the system developed.
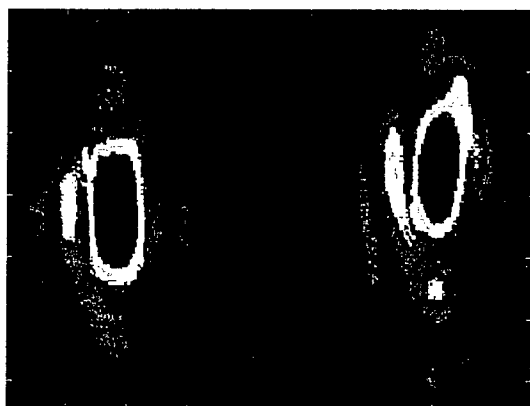

Figure 6.9 : Far-field image: beam 2 on the left, beam 1 on the right

7. Conclusion

An adaptive optics system was developed for the SILVA prototype. Its development benefited from research conducted by ONERA for several years on large bandwidth Adaptive Optics dedicated to space observation.

The system consists of a deformable mirror with 48 actuators and a wavefront sensor with 21 x 21 subpupils. It corrects the wavefront errors present on the dye laser systems. The control frequency of the system is limited to 30 Hz. The hardware and software computer architecture designed is flexible and reconfigurable, which is very desirable for a prototype during the testing and optimisation phase. In particular, it will allow a control frequency of 500 Hz to be achieved simply by using a 64x64-pixel CCD camera.

This system was integrated and tested in the laboratory at ONERA. Its performance is consistent with the simulations made. It is now installed at CEA where it is operating on one of the dye laser beams of the SILVA prototype.

8. References

[2.1] I. Bass et al, "High-average-power dye laser at Lawrence Livermore Laboratory", Applied Optics November. 1992, Vol 31, n° 3

[2.2] R. Hackel, "High performance of copper pumped dye lasers"

[2.3] D. Doizi, "Séparation isotopique par laser", "Les lasers et leurs applications scientifiques et médicales", Institut d'Etudes Scientifiques de Cargèse, France, 20 June to 2 July 1994 (F).

[3.1] P-Y. Madec , "Imagerie à haute résolution en optique active et en optique adaptative", summer school in Cargèse, France, "Systèmes optiques", 1 to 13 July 1991, les Editions de Physique (F).

[3.2] G. Rousset, "Implementation of Adaptive Optics", First International Meeting on Wave Propagation in Random Media, Seattle (USA), August 4-5 1992

[3.3] F. Roddier, "The problematic of Adaptive Optics design", summer school in Cargèse, France, "Adaptive optics for astronomy", 1993, ICO

[4.1] CILAS : Compagnie Industrielle des Lasers, Route de Nozay, 91460 Marcoussis, France

[4.2] G. Rousset et al, "Visible wavefront sensor development", workshop sur "Adaptive optics in solar observations", Freibourg, 8-9 September 1987

[4.3] G. Rousset, "Wavefront sensing", summer school in Cargèse, France, "Adaptive optics for astronomy", 1993, ICO

[4.4] SHAKTI company, 1 place Gabriel Péri, 13001 Marseille, France

E-mail : shakti@papayus.topnet.fr

[6.1] M. Demerlé et al, "Servo-loop analysis for Adaptive Optics", summer school in Cargèse, France, "Adaptive optics for astronomy", 1993, ICO

Experimental simulation of a Laser beam reshaping

Far field images :
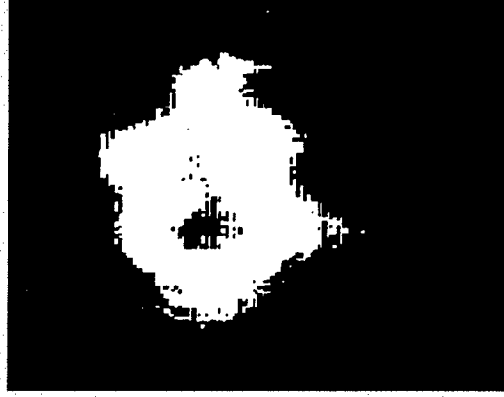
- Undisturbed beam
- Disturbed beam
- Corrected beam

ONERA

Simulated Intensity of the reshaped Laser beam after propagation in the Separation Module

1) No A.O. Correction.

2) A.O. Correction on 15 Legendre polynomials

3) Full A.O. Correction

ONERA

Laser beam shaping by deformable mirror

Zhige Zeng,   Ning Ling,   Wenhan Jiang

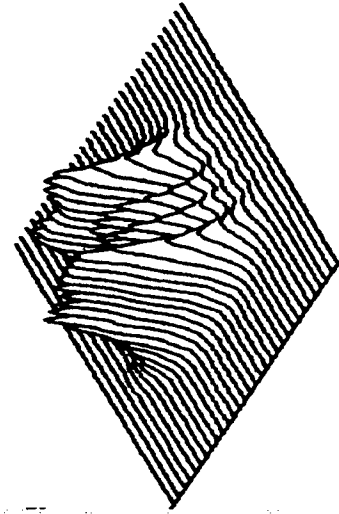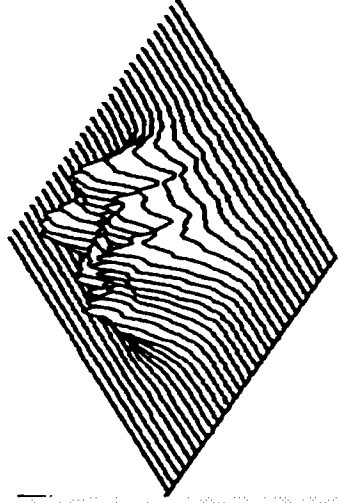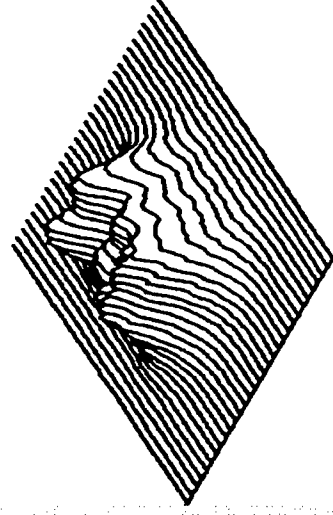(Institute of Optics & Electronics, Chinese Academy of Sciences,

P.O.Box 350, Shuangliu, Chengdu, China, 610209)

ABSTRACT

In inertial confinement fusion, different shapes and intensity distributions of focal spots are desired for different physical experiments. In this paper, the two methods of phase retrieval (Geometric Transformation and Iterative Fourier Transformation) in controlling laser's focal intensity profile are been introduced. Deformable mirrors with different actuator numbers and arrangements (triangle and rectangle) are simulated to compare fitting capabilities for the given wave-front profile. The possibilities of using Adaptive Optical technology with these two methods to control laser's focal intensity profile are been compared and analyzed by computer simulations.

Keywords: beam shaping, Adaptive Optics, deformable mirror, computer simulation

1. INTRODUCTION

There are some applications in laser technology to form some kinds of focal intensity profiles or intensity distributions. Especially in inertial confinement fusion (ICF) system, a high power laser pulse is focused on a target to induce nuclear fusion. Different shapes and intensity distributions of focus spots are desired for different physical experiments. Some demands are critical such as uniformity of light intensity distribution and sharp edge of the focus spot, very low background intensity level outside the spot. In recent years, there are some methods for laser beam shaping. Reflective[1] and refractive[2][3] surfaces have been used to redistribute the energy of a laser beam to a uniform beam with circular shape. These methods generally require complicated aspherical surfaces that are difficult to fabricate and are useful only in a limited set of situations. Some binary and diffractive optical components[4][5][6] are also used to form the beam shaping system. These components have the adequate freedoms and precision to form various types of phase distribution. The drawback of them is that they can not tolerate for daily changing of original phase of laser beam. The original phase is often changing that may influence the desired intensity distributions at the focus spot. By now, another effective method for getting desired focal intensity profiles is to obtain the phase modulation by inserting deformable mirror (DM) [7][8][9] in incident beam.

DM is a reflective component that it has the better performances of transmissive efficiency, destroying threshold and the adaptability for different environments than the other components. Because the DM can adjust its surface shape at any time to adapt the wave-front changed, it tolerates to different demands of experiments. In this paper, two methods of phase retrieval (*Geometric transformation* and *Iterative Fourier Transformation*) of using DM to retrieve beam phase at pupil plane for controlling focal intensity profile will be described. The fitting capabilities of DM with different actuator arrangements are also analyzed by computer simulations. The possibilities of using Adaptive Optical technology to control laser's focal intensity profile are discussed.

2. THEORY

The relation between complex amplitude a(x, y) at mirror and complex amplitude A(u,v) at focal spot can be represented by far-field diffractive equation[10]:

$$A(u,v) = \frac{1}{i\lambda f} \cdot e^{ikz} \cdot e^{i\frac{k}{2f}(u^2+v^2)} \cdot \iint_{\Sigma} a(x,y) \cdot e^{-i\frac{k}{f}(ux+vy)} dxdy \tag{1}$$

Here, (x,y) and (u,v) are the coordinates at the mirror and the focal plane, λ is wave length, f is the focus length of lens, Σ is pupil area and k=2π/λ.

The main ideal to reshape the intensity distribution of focal spot is to insert a phase function $\phi(x,y)$ into a(x, y), and the expected intensity distribution at focus spot is gotten. The principle is expressed as fig.1.

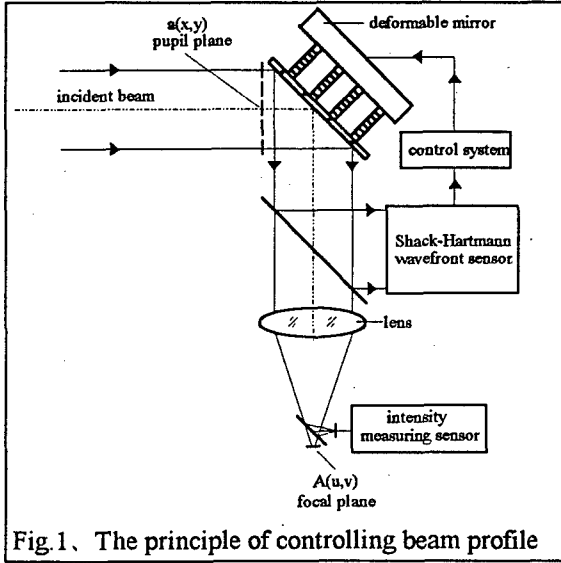Fig.1. The principle of controlling beam profile

Incident beam enters the optical system and the phase distribution of wave-front is detected by S-H sensor. At the same time, the focal intensity profile is detected by an intensity detecting sensor (CCD camera). Comparing the data by CCD with that by S-H sensor, we can control the DM to insert the desired phase distribution into the beam. After inserting the additional phase, the wave-front at focus spot becomes:

$$A(u,v) = \frac{1}{i\lambda z} \cdot e^{ikz} \cdot e^{i\frac{k}{2f}(u^2+v^2)} \cdot \iint_{\Sigma} |a(x,y)| \cdot e^{i\phi_1(x,y)} \cdot e^{i\phi(x,y)} \cdot e^{-i\frac{k}{f}(ux+vy)} dxdy$$

$$= \frac{1}{i\lambda z} \cdot e^{ikz} \cdot e^{i\frac{k}{2f}(u^2+v^2)} \cdot \iint_{\Sigma} |a(x,y)| \cdot e^{i\left[\phi_{all}(x,y) - \frac{k}{f}(ux+vy)\right]} dxdy \qquad (2)$$

$\phi(x,y)$ is the phase produced by DM, $\phi_1(x,y)$ is the original phase of incident beam, and $\phi_{all}(x,y) = \phi_1(x,y) + \phi(x,y)$.

The intensity distribution on focal plane is:

$$\tilde{I}(u,v) = |A(u,v)|^2 \qquad (3)$$

From descriptions above, the focal intensity profile is determined by phase distribution $\phi(x,y)$ resulted from the surface shape of DM. $\phi(x,y)$ can be solved by following two methods through the relation between intensity distribution at pupil plane and that at focal plane.

2.1. Geometric transformation method (GTM)

Approximating the far-field integral in eq.(2) by *stationary phase method* originated by Olof Bryngdahl[11], it can be shown that a point (x,y) in the pupil plane is mapped to a point (u,v) in the focal plane given by the relation

$$\begin{pmatrix} x \\ y \end{pmatrix} \rightarrow \begin{pmatrix} u \\ v \end{pmatrix} = \begin{bmatrix} f/k \cdot \partial\phi_{all}(x,y)/\partial x \\ f/k \cdot \partial\phi_{all}(x,y)/\partial y \end{bmatrix} \qquad (4)$$

If the desired mapping is defined by

$$\begin{pmatrix} x \\ y \end{pmatrix} \rightarrow \begin{pmatrix} u \\ v \end{pmatrix} = \begin{bmatrix} u(x,y) \\ v(x,y) \end{bmatrix}$$

The necessary phase $\phi_{all}(x,y)$ to produce this mapping is the solution of the partial differential equations as eq.(5):

$$\frac{\partial\phi_{all}(x,y)}{\partial x} = \frac{k}{f} \cdot u(x,y) \qquad \frac{\partial\phi_{all}(x,y)}{\partial y} = \frac{k}{f} \cdot v(x,y) \qquad (5)$$

$\phi(x,y)$ can be obtained by $\phi_{all}(x,y) - \phi_1(x,y)$ if $\phi_1(x,y)$ is measured by S-H sensor and the relationship between point (u,v) and (x,y) is known. The DM surface shape S(x,y) is given as

$$S(x,y) = \phi(x,y)/(k/2) = \left[\phi_{all}(x,y) - \phi'(x,y)\right]/(k/2) \qquad (6)$$

In our application, incident beam truncated by rectangular window is expected to be reshaped to the uniform focus spot. Assume the size of truncate window at pupil plane is $(\pm x_0, \pm y_0)$ and the size of focus spot is $(\pm u_0, \pm v_0)$. The relationship between point (u,v) and (x,y) can be solved based on energy conservation principle given by *Parseval's theorem*, the energy of pupil plane is equal to that of focal spot:

$$E_{obj}(x_0,y_0) = \int_{-x_0}^{x_0} \int_{-y_0}^{y_0} I(x,y)dxdy = \tilde{E}_{foc}(u_0,v_0) = 2u_0 \cdot 2v_0 \cdot \sigma$$

Here σ is uniform intensity distribution at focal plane. The relation between (x,y) and (u,v) can be obtained similarly as point (x_0,y_0) and (u_0,v_0). We can get the following equation:

$$\sigma = \frac{1}{4u_0v_0} \int_{-x_0}^{x_0} \int_{-y_0}^{y_0} I(x,y)dxdy$$

$$uv = u_0v_0 \frac{\int_{-x}^{x} \int_{-y}^{y} I(x_1,y_1)dx_1dy_1}{\int_{-x_0}^{x_0} \int_{-y_0}^{y_0} I(x,y)dxdy} \tag{7}$$

u, v are the function of x and y. In this transformation system by using this method, the compatibility condition[2] must be satisfied by the input and output beams.

$$\frac{\partial u(x,y)}{\partial y} = \frac{\partial v(x,y)}{\partial x} \tag{8}$$

The eq.(8) expresses is that $\phi_{all}(x,y)$ must simultaneously satisfy both equations in eq.(5). From above list, the desired focal intensity profiles are obtained if the DM can produce the necessary surface profiles determined by eq. (6), (7) and (8).

2.2. Iterative Fourier Transformation method (IFTM)

The relation between pupil plane and focal plane can be expressed by Fourier Transformation (FT) because of the existence of focusing lens. The complex amplitude at pupil plane is transformed to that at focal plane by FT. The desired intensity distribution will be obtained by inserting a phase function that can be gotten by *IFTM* into original phase. *IFTM* is also called *Gerchberg-Saxton algorithm*[12] which was originally invented in connection with the problem of phase retrieval from two intensity measurements (pupil and focal plane), and had been modified by J.R.Fienup[6][13] and Guozhen Yang etc.[14] in some applications successfully. The main principle of *IFTM* is as following and shown as fig.2.

①Constructing original complex amplitude $a_0(x,y)$ by intensity I(x,y) and phase function $\phi_0(x,y)$ which can be formed by random number:

$$a_0(x,y) = \sqrt{I(x,y)} \cdot \exp[i\phi_0(x,y)]$$

This algorithm in k-th iterative consists of the following four steps ② ~ ⑤:
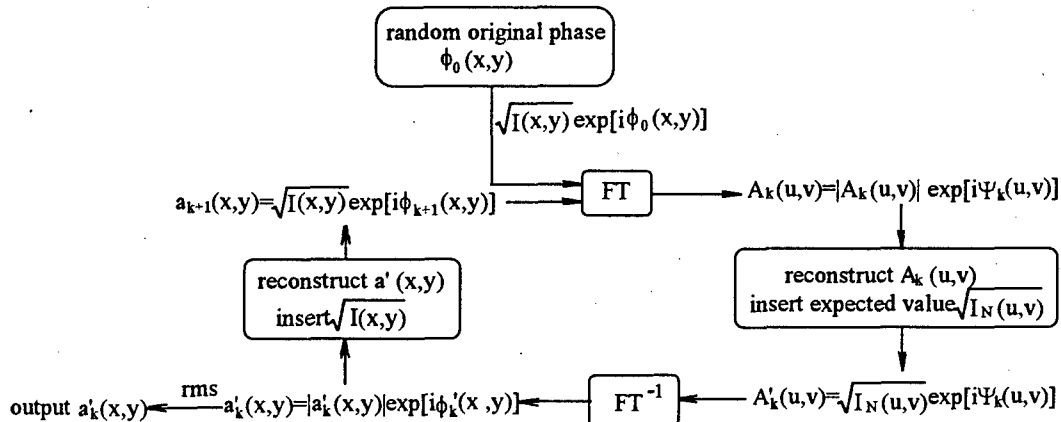

Fig.2. Principle of *Iterative Fourier Transformation method*

②Fourier transform the complex amplitude of pupil plane to that of focal plane:

$$A_k(u,v) = |A_k(u,v)| \exp[i\Psi_k(u,v)] = FT\{|a_k(x,y)| \exp[i\phi_k(x,y)]\}$$

③ Replace the modules of the computed results $|A_k(u,v)|$ with the expected Fourier modules $\sqrt{I_N(u,v)}$ to form a new amplitude at focal plane:

$$A'_k(u,v) = \sqrt{I_N(u,v)}\,\exp[i\Psi_k(u,v)]$$

④ Inverse Fourier transform the complex amplitude at focal plane to that at pupil plane:

$$a'_k(x,y) = |a'_k(x,y)|\exp[i\phi'_k(x,y)] = FT^{-1}[A'_k(u,v)] = FT^{-1}\left[\sqrt{I_N(u,v)}\,\exp[i\Psi_k(u,v)]\right]$$

⑤ Replace the modules of the computed results $|a'_k(x,y)|$ with the measured ones $\sqrt{I(x,y)}$ to form a new amplitude of the pupil plane:

$$a_{k+1}(x,y) = \sqrt{I(x,y)}\cdot\exp[i\phi'_k(x,y)] = \sqrt{I(x,y)}\cdot\exp[i\phi_{k+1}(x,y)]$$

⑥ Return to step ② until mean-square error of $|a'_k(x,y)|$ to $|a_{k+1}(x,y)|$

$$MSExy = \sum_{m=0}^{M-1}\sum_{n=0}^{N-1}\left[|a'_k(x_m,y_n)|-|a_{k+1}(x_m,y_n)|\right]^2 \Big/ \sum_{m=0}^{M-1}\sum_{n=0}^{N-1}\left[|a_{k+1}(x_m,y_n)|\right]^2 \tag{9}$$

satisfies the setting constraint. The expected phase at pupil plane and intensity at focus spot will be output.

This algorithm is used for any problems in which particular constraints are known in both pupil and focal plane. The iterations continue until the computed Fourier transform satisfies the Fourier-domain constraints or its inverse transform satisfies the pupil plane constraints, then one has found a solution that a Fourier transform pair satisfies all the constraints in both domains. We use three parameters to represent the intensity quality of focal spot quantitatively:

① The mean square error of simulated amplitude (MSEuv) to desired amplitude at focal spot.

$$MSEuv = \frac{\sum_{m=0}^{M-1}\sum_{n=0}^{N-1}\left[|A(u_m,v_n)|-\sqrt{I_N(u_m,v_n)}\right]^2}{\sum_{m=0}^{M-1}\sum_{n=0}^{N-1}I_N(u_m,v_n)}$$

② Light energy efficiency (LEE) defined as the ratio of energy concentrated in effective dimension at focal spot to all energy of incident beam.

$$LEE = \left[\int_{-u_0}^{u_0}\int_{-v_0}^{v_0}\tilde{I}(u,v)\cdot du\cdot dv\right]\Big/\left[\int_{-x_0}^{x_0}\int_{-y_0}^{y_0}I(x,y)\cdot dx\cdot dy\right]\times 100\%$$

③ The sharpness at the edge of intensity distribution (Grad) at focal plane defined as length that intensity rises from minimum to peak value.

3. COMPUTER SIMULATION

There is a requirement in a physics experiment that the intensity of incidence beam with six-order super-Gauss rectangular profile which is truncated by rectangular window be formed rectangular uniform intensity at the focus spot by the optical system with parameters as table 1.

Table 1, System parameters

| 1 | wave length | 1.054μm |
2	laser aperture	220mm × 220mm (rectangle)
3	size of focus spot	300μm × 300μm (rectangle)
4	original energy distribution	$I(x,y) = \exp[-2(x/x_0)^6]\cdot\exp[-2(y/y_0)^6]$
5	focus lens	f/D=7

The intensity distribution at pupil plane can be expressed:

$$I(x,y) = e^{-2(x/x_0)^6}\cdot e^{-2(y/y_0)^6} \tag{10}$$

Here, x_0 and y_0 are the Gaussian half widths and also the half widths of truncate window. Assume $x_0=y_0=150$mm, the beam intensity distribution is as fig.3:
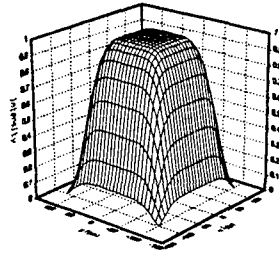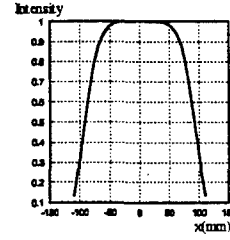
(a)2-D graph   (b)1-D graph

Fig.3、Beam's origin intensity distribution at mirror
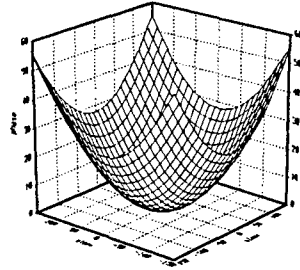
3.1. Geometric transformation method (GTM)

Assume incident beam is planar wave-front. Joining eq.(5)、(7)、(8) and (10), the desired phase function will be solved as:

$$\phi(x,y) = \frac{k}{f}\left\{\frac{u_0}{p(x_0)}\int_0^x p(x_1)dx_1 + \frac{v_0}{p(y_0)}\int_0^y p(y_1)dy_1\right\}$$

and

$$p(t) = \int_{-t}^t e^{-2(t_1/t_0)^6} dt_1$$

The computed desired phase distribution is as fig.4.
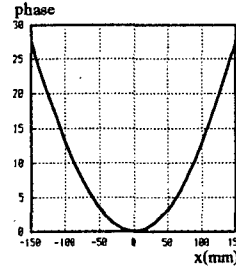
(a)2-D graph   (b)1-D graph

Fig.4、Computed value of phase distribution

After removing defocus, the actual needed phase distribution is as fig.5.
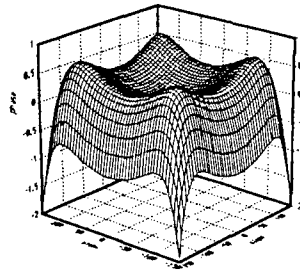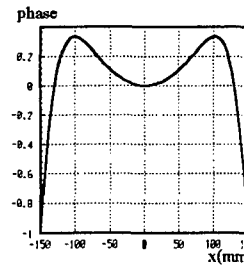
(a)2-D graph   (b)1-D graph

Fig.5、Phase distribution after removing defocus

The diffractive intensity distribution is: $\bar{I}(u,v) = \frac{1}{(\lambda z)^2}\left[R_r^2(u,v) + R_i^2(u,v)\right]$

and

$$R_r = \iint_\Sigma |a(x,y)| \cdot \cos\left[\phi(x,y) - \frac{k}{f}(ux+vy)\right]dxdy$$

$$R_i = \iint_\Sigma a(x,y) \cdot \sin\left[\phi(x,y) - \frac{k}{f}(ux+vy)\right]dxdy$$

The computed intensity distribution at focus spot is as fig.6.

(a)2-D graph   (b)1-D graph

Fig.6、 Computed value of beam intensity distribution at focal plane

From fig.6, there are oscillations on the top of intensity profile. These are caused by finite truncate window at pupil plane. By our simulations, the smaller the truncation window is, the more oscillations the intensity distribution is. When the truncate window is enlarged twice (600mm × 600mm), the oscillations are fewer and the center is flatter as fig.7.
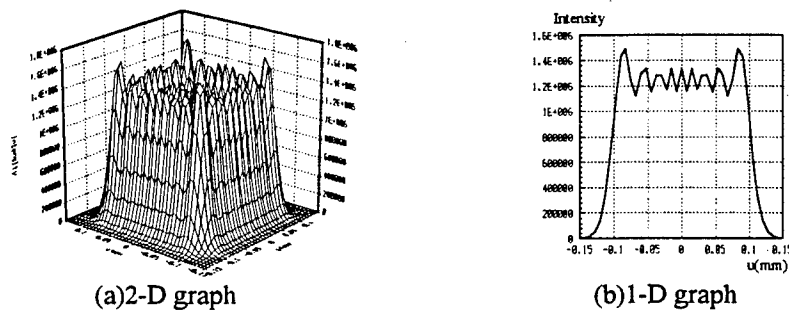

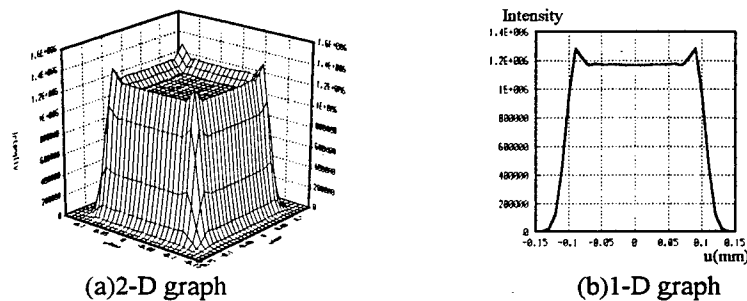(a)2-D graph   (b)1-D graph

Fig.7、 Intensity distribution at focal spot with truncate window 600mm × 600mm

We can get the value of MSEuv、 LEE、 Grad as table 2 expressed from fig.6. The shortage of this method is the large amount of computation if the higher computing precision to be satisfied.

3.2. Iterative Fourier Transformation method (IFTM)

The convergence of this method had been proved by J.R.Fienup that the algorithm decreases the mean-square error MSExy (or stays the same) in eq. (9) at each iteration. In practice, this algorithm usually decreases the MSExy rapidly for the first few iterations but much more slowly for later iterations. The speed of convergence also depends on the type of constraints imposed[10]. It has been found that the computed convergent phase is strongly depending on the different original phase distributions. Fig.8 shows the one-dimensional intensity distribution after 1200 iterations with two original phase distributions which are random in ranges of $(-\pi,\pi)$ and $(-\pi/10,\pi/10)$ respectively.

(a)Initial phase area $(-\pi,\pi)$ (b)Initial phase area $(-\pi/10,\pi/10)$
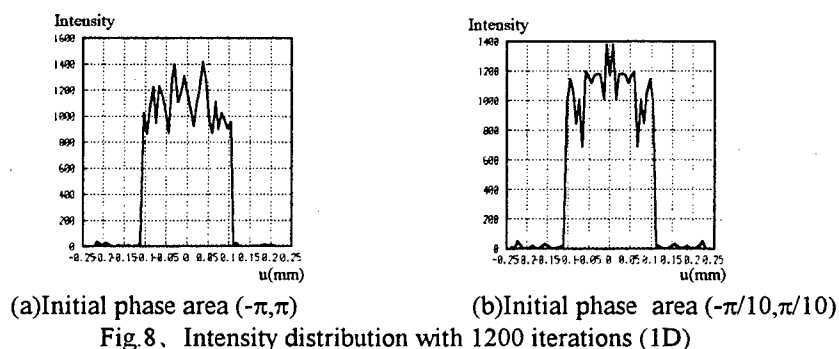
Fig.8、 Intensity distribution with 1200 iterations (1D)

After analyzing for the computing results, we find that the more approximate the original phase is to the theory value, the more exact the resulting intensity distribution is to the desired ones and the iterative times are relatively fewer. For this reason, the computed phase distribution by *GTM* may be used as the original phase in this algorithm. Fig.9 shows the computed results by this method with 120 iterations.

(a)3-D graph   (b)2-D graph

Fig.9、 Intensity distribution with 120 iterative

From fig.9, MSEuv、 LEE and Grad by *IFTM* are gotten and compared with those by *GTM* from fig.6 as table 2.

Table 2、 The performance parameters of two methods

method	MSEuv	LEE	Grad (μm)
GTM	0.030162	93.82%	52.8
IFTM	0.018838	99.19%	7.42

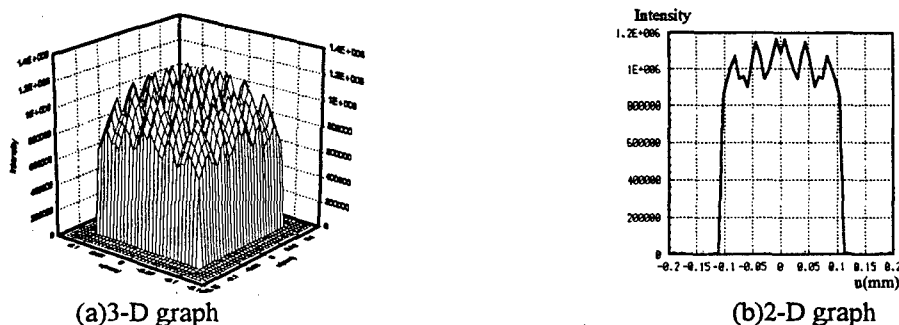By using *IFTM*, the edge of the intensity distribution is much sharper, the center of the intensity is flatter, and the lateral lobes result from diffraction is smaller than those by using *GTM*. This method has performances of fast computing speed by using *fast Fourier transformation*, favorable stability and convergence.

4. FITTING CAPABILITY OF DEFORMABLE MIRROR

DM is the key component of this beam shaping system. It changes the beam phase when the actuators of DM move to change the mirror surface. Its surface can be adjusted arbitrarily and maintained for a long time. The fitting capabilities of DM to expected surface shape with different actuator arrangements and actuator numbers have been investigated. The four probable arrangements as Fig.10 are simulated when the incident angle is 45°.

(a)35-actuator   (b)40-actuator   (c)48-actuator   (d)60-actuator
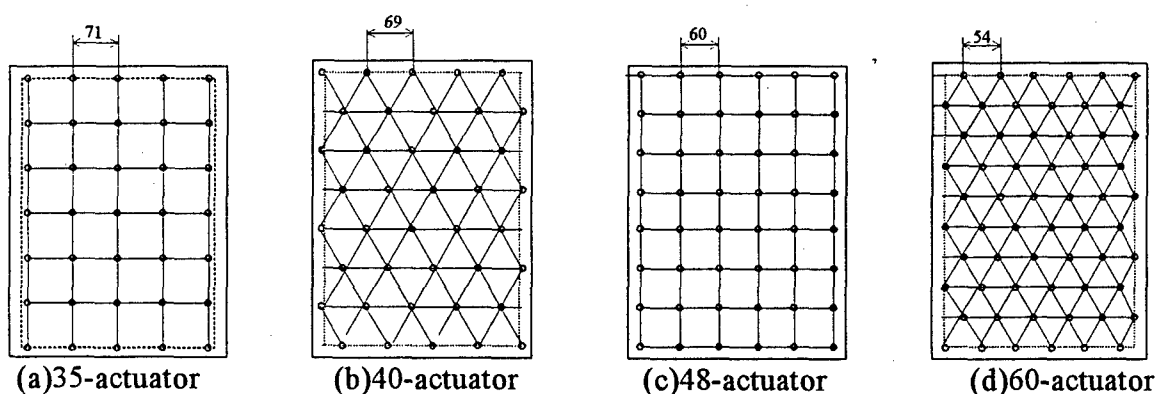
Fig.10、 Several actuator arrangements with different number

Deformations of DM caused by all actuators form the complicated surface profile. It is very important that the obtained profile approximates to the desired mirror surface as well as possible. The fitting capability of DM with above four actuator arrangements is investigated as following.

Assume the influence function $f(r)$ can be represented as Gaussian shape: $f(r) = \exp\left[-(|\vec{r}|/\omega_0)^\alpha\right]$

Here, α is Gaussian index, ω_0 is half width, r is the distance apart from driving actuator. The values of ω_0 and α depend on the actuator space、 mirror stiffness、 connecting structure between actuators and mirror etc. The following parameters are used in the simulations: α=2.2 and ω_0=9.165mm. The resulted wave-front can be represented as:

$$g(|\vec{r}|) = \sum_{i=1}^{N}\left[f(\vec{r},\vec{r_j})\cdot C_j\right] = \sum_{i=1}^{N}\left\{\exp\left[-\left(\frac{|\vec{r}-\vec{r_j}|}{\omega_0}\right)^{\alpha}\right]\cdot C_j\right\}$$

Here, $\vec{r}$ is an arbitrary point on the mirror, N is actuator number, $\vec{r_j}$ is the coordinate of the i-th actuator, and C_j is the driving signal of the i-th actuator. represented in matrix:

$$\vec{g_i} = \vec{A}_{ij} \times \vec{C_j} \qquad (1 \le i, j \le N)$$

This matrix can be solved by SVD, and the least square estimate $\vec{C_j'}$ of $\vec{C_j}$ can be obtained:

$$\vec{C_j'} = (C_1, C_2, \cdots, C_N)^T$$

For a point (x_i, y_j) on the mirror, there is a corresponding $\vec{A}_{ij}'$ that the wave-front is resulted:

$$\vec{g_i'} = \vec{A}_{ij}' \times \vec{C_j'}$$

So, the fitting error may be represented as:

$$rms = \sqrt{\frac{1}{N}\sum_{i=1}^{N}\left[\vec{g_i'}(\vec{r}) - \vec{g_i}(\vec{r})\right]}$$

The intensity distribution at focal spot and the actual wave-fronts by adding the fitting errors of the different DM are showed as fig.11, the computed results are showed as table 3.
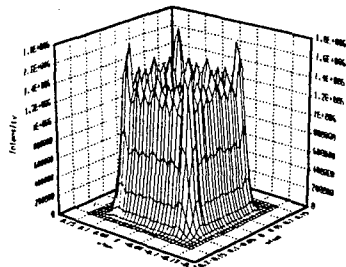
| (i)3-D intensity | (ii)2-D intensity | (iii)actual wave-front |
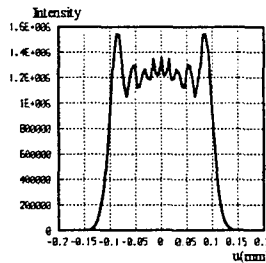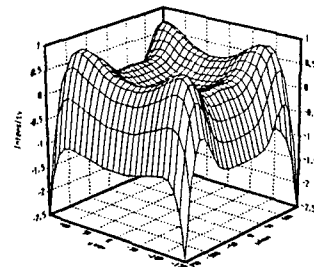
(a), 35-actuator

| (i)3-D intensity | (ii)2-D intensity | (iii)actual wave-front |

(b), 40-actuator

| (i)3-D intensity | (ii)2-D intensity | (iii)actual wave-front |

(c), 48-actuator
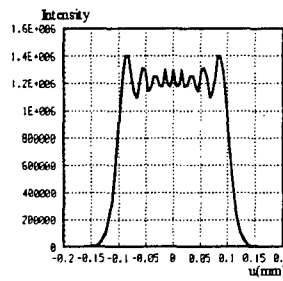
|(i)3-D intensity | (ii)2-D intensity | (iii)actual wave-front |
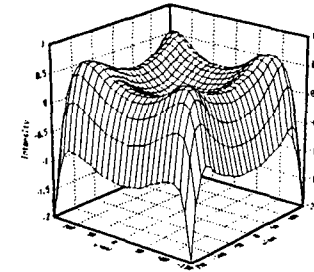
(d)、60-actuator

Fig.11、Intensity distribution of four arrangements for fitting wave-front

Table 3、The capability of four arrangements for active mirror to fit wave-front

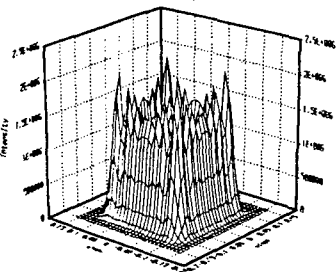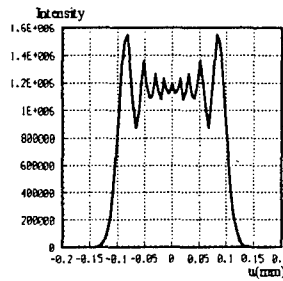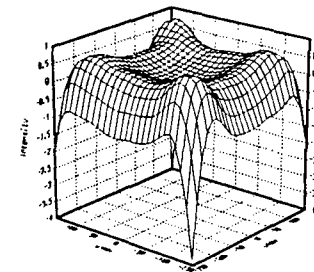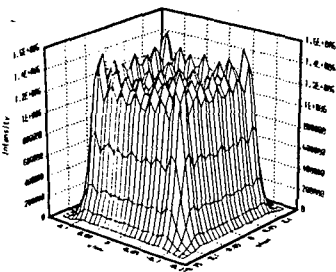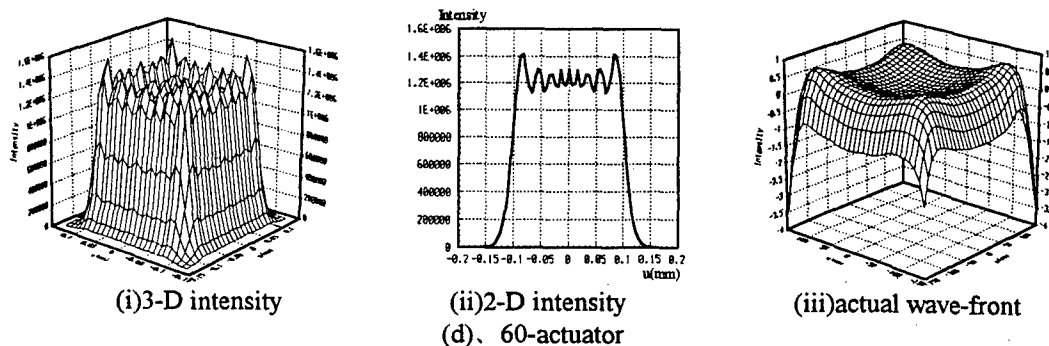| N0.	actuator number	arrangement	fitting error: rms (λ)
1	35	rectangle	0.021293
2	48	rectangle	0.012763
3	40	triangle	0.018575
4	60	triangle	0.015813

From the simulated results as fig.11, MSEuv、LEE and Grad are as table 4.

Table 4、The performance parameters of four arrangements by simulations

actuator number	arrangement	MSEuv	LEE	Grad (μm)
35	rectangle	0.071456	91.09%	61.63
40	triangle	0.095204	91.18%	61.63
48	rectangle	0.062939	91.21%	61.63
60	triangle	0.065385	91.23%	61.63

Some conclusions can be obtained from the simulative results:

①The DM with 48-actuator and rectangular arrangement has the smallest fitting error for desired wave-front in four arrangements.

②The wave-front fitted by DM with triangular actuator arrangement is asymmetry because of the asymmetry of actuators.

③Although the fitting error from 60-actuator with triangular arrangement is as small as 48-actuator, the many more actuators could increase the complexity of system.

5. CONCLUSION

Computer simulations have been done to demonstrate the possibility of using DM with adaptive technology for beam shaping in ICF system. To obtain a high energy efficiency, intensity distribution with uniform profile and sharp edge at the focus spot, the beam energy must be redistributed by inserting the necessary phase function.

Two methods of phase retrieval have been investigated to compute the necessary phase distribution for this application. It has been found that *GTM* based on using a stationary phase approximation to the far-field integral is inadequate to get the desired intensity distribution because of the top modulation and the inadequately sharp edge of the focal intensity profile. A better result has been obtained by using *IFTM*.

Calculating equations based on *GTM* have the direct expresses and help us understand the relations of focal intensity profiles with beam and pupil parameters. *IFTM* has faster computing speed by using *Fast Fourier Transformation*. It will be performed when intensity information and some restraints (pupil and focal domains) are known. From the simulation, it is obvious that *IFTM* is more applicable than *GTM*.

DM with different actuator numbers and arrangements (triangle and rectangle) are investigated to demonstrate its fitting capabilities for the given wave-front profiles. Adding the fitting error produced by DM, the focal intensity profiles become worse than the computed result of phase retrieval. DM with 48 actuators and rectangular arrangement has the best fitting capability for known wave-front in four actuator arrangements.

ACKNOWLEDGMENTS

REFERENCES

1. J.W.Ogland, "Mirror System for Uniform Beam Transformation in High-Power Annular Lasers" , Appl. Opt. Vlo.17, pp.2917-2923, 1978.
2. P.W.Rhodes and D.L.Shealy, "Refractive Optical Systems for Irradiance Redistribution of Collimated Radiation: Their Design and Analysis" , Appl. Opt. Vlo.19, pp.3545-3553, 1980.
3. D.shafer, "Gaussian to Flat-Top Intensity Distributing Lens" , Opt. Laser Technol. Vol.3, pp.159-160, 1982
4. Wai-Hon LEE, "Method for Converting a Gaussian Laser Beam into a Uniform Beam" , Optics Communications, Vol.36, No.6, pp.469-471, 1981.
5. Nicholas C.Roberts, "Multilevel computer-generated holograms with separable phase functions for beam shaping" , Applied Optics, Vol 31, No.17, pp.3198-3120, 1992.
6. J.R.Fienup, "Iterative method applied to image reconstruction and computer-generated holograms" , Applied Engineering, Vol.19, No. 3, pp.297-305, 1980.
7. G.Y.Yoon, T.Jitsuno, M.Nakatsuka, and Y.Kato, "Laser beam shaping by the wave-front control using deformable mirror" , Proceedings of 3rd Symposium on Laser Spectroscopy, Vol.3 No.4, pp.221-229, 1995.
8. Koshichi Nemoto, Takashi Fujii, Naohiko Goto and Takuya Nayuki, "Transformation of a laser beam intensity profile by a deformable mirror" , Optics Letters, Vol.21, No.3, Feb.1, pp.168-170, 1996.
9. Phillip H.Malyak, "Two-mirror unobscured optical system for reshaping the irradiance distribution of a laser beam" , Applied Optics, Vol.31, No.22, pp.4377-4383, 1992.
10. M.Born and E.Wolf, *Principles of Optics*, pp.749 (Pergamon, New York, 1959).
11. Olof Bryngdahl, "Geometrical transformations to optics" , J. Opt. Soc Amer. Vol.64, No.8, Aug.1974, pp.1092-1099.
12. R.W.Gerchberg and W.O.Saxton, "A Practical Algorithm for the Determination of Phase from Image and Diffraction Plane Pictures" , Optik, Vol.35, No.2, pp.237 ~ 246, 1972.
13. J.R.Fienup, "Phase retrieval algorithms: a comparison" , Applied Optics, Vol.21, No. 15, 1 August, pp1982
14. Guozhen Yang, Benyuan Gu, The retrieval problems of amplitude and phase in optical system , Acta Physica Sinica, Vol.30, No.3, pp410-413, 1981

Adaptive Systems with Modal Aperture Probing
for Powerful Technological IR Lasers.

D.Yu. Gorbenko, Ya.I. Malashko, A.S. Rumyantsev, V.V. Valuev

"Sistema" SIC, Moscow, Russia, Leningradsky prospekt, 80.   Fax: (095) 158-5671

The characteristics of the adaptive systems with sequential and parallel multifrequencies modal probing were studies.

Locking of an adaptive optical system sequential modal probing with the CO_2 gas-dynamic laser emission of 80 kW output power was fulfilled. The AOS task was to maximize angular on-axis brightness which was realized by analyzing of diffractionally coupled beam in the equivalent far field. Optical scheme contained a cooled flexible correcting mirror with 19 hexagonally located piezoactuators with the steps of 33 mm and local correcting amplitudes up to 10 μm [1,2]. Correcting mirror was used also as a modulating mirror.

To increase AOS time-band perfection up to $1 \div 2$ Hz although infringing the spatial band the correcting mirror operated in so-called modal mode forming the simplest specified surfaces during probing and correction: two tilts, two cylinders $z \sim x^2$, $z \sim y^2$ and a "saddle" $z \sim xy$. The given functions reflected low-frequency spatial aberrations in a beam.

Resonance frequencies of correcting mirror structure and laser power fluctuation spectrum were investigated and their influence on the stability of AOS operation.

The resulting success of the experiment was conditioned by the choice of such probing frequency (1,1 kHz) which coincides neither with the own resonances of mirror nor with the spectral bands of laser power fluctuations. The increase of average angular beam brightness was two times.

To increase AOS time-band pass a multifrequency parallel probing was applied [3].

Although the described linear system doesn't have wide time-and-spatial bands, it has a wide range of correction which is very important for powerful laser system with low-frequency phase perturbations distortion of large amplitudes.

Referencies.

1. M.A. Kurin, A.S. Rumyantsev. Adaptive Mirrors for Powerful Lasers. Proc. of the Int. Conf. on Lasers'96 N1505 (STS Press, McLean, VA, 1997).
2. Ya. I. Malashko, A.B. Ignatiev, V.V. Valuev, V.N. Kas'kov. Angular Brightness Increase of a Gas-Dynamic CO_2-Laser Beam by Means of a Linear Adaptive System. Proc. of the Int. Conf. on Lasers'96 N 0505 (STS Press, McLean, VA, 1997).
3. V.V. Valuev, V.N. Kas'kov, Ya. I. Malashko, V.A. Andrus'chenko. Adaptive Optical System with Multifrequency Aperture Probing. Proceedings of the Int. Conf. on Lasers'95 p. 543 (STS Press, McLean, VA, 1996).

Foto
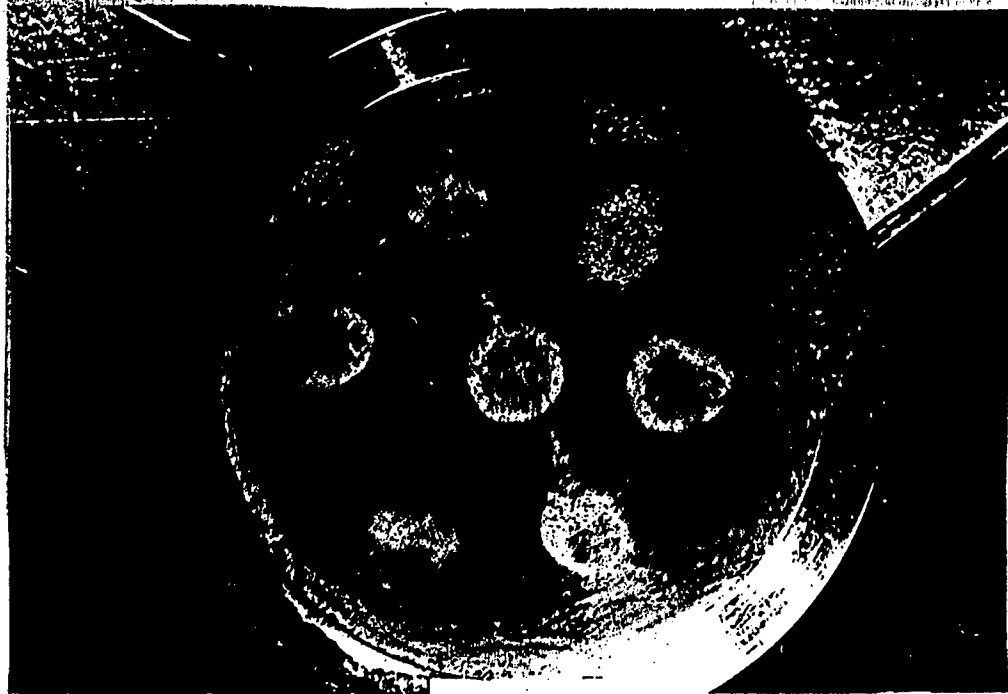
Seven subapertures are
excited on the different
frequencies (29-45 kHz)
Black colour is the
dust on the modulating
mirror

Fig. 1 The 19-element zonal AM
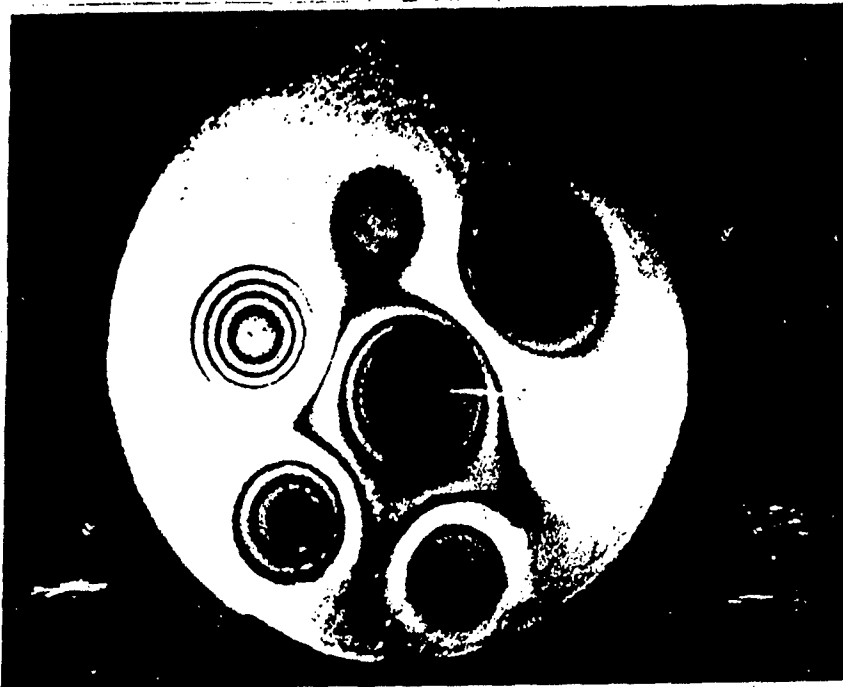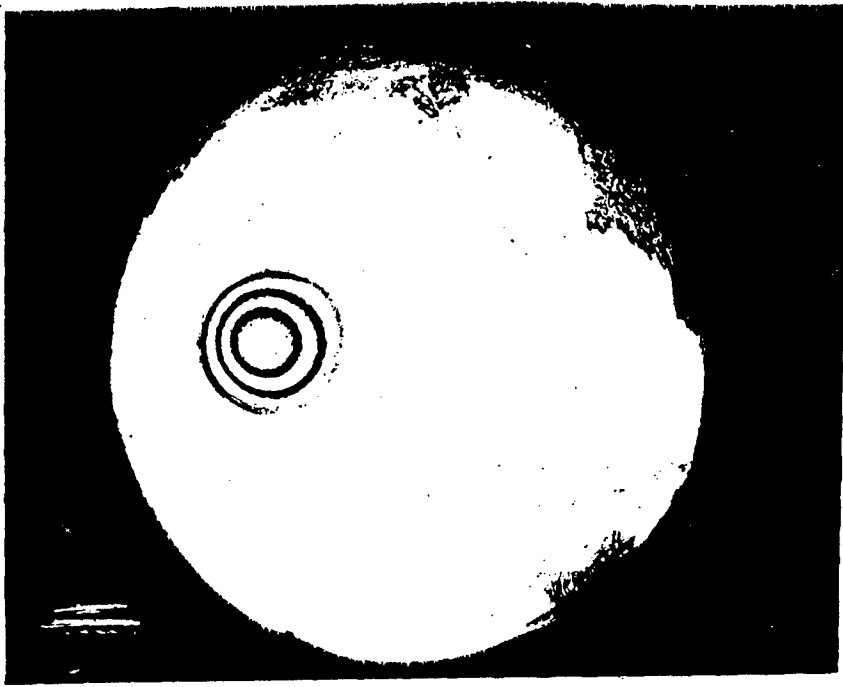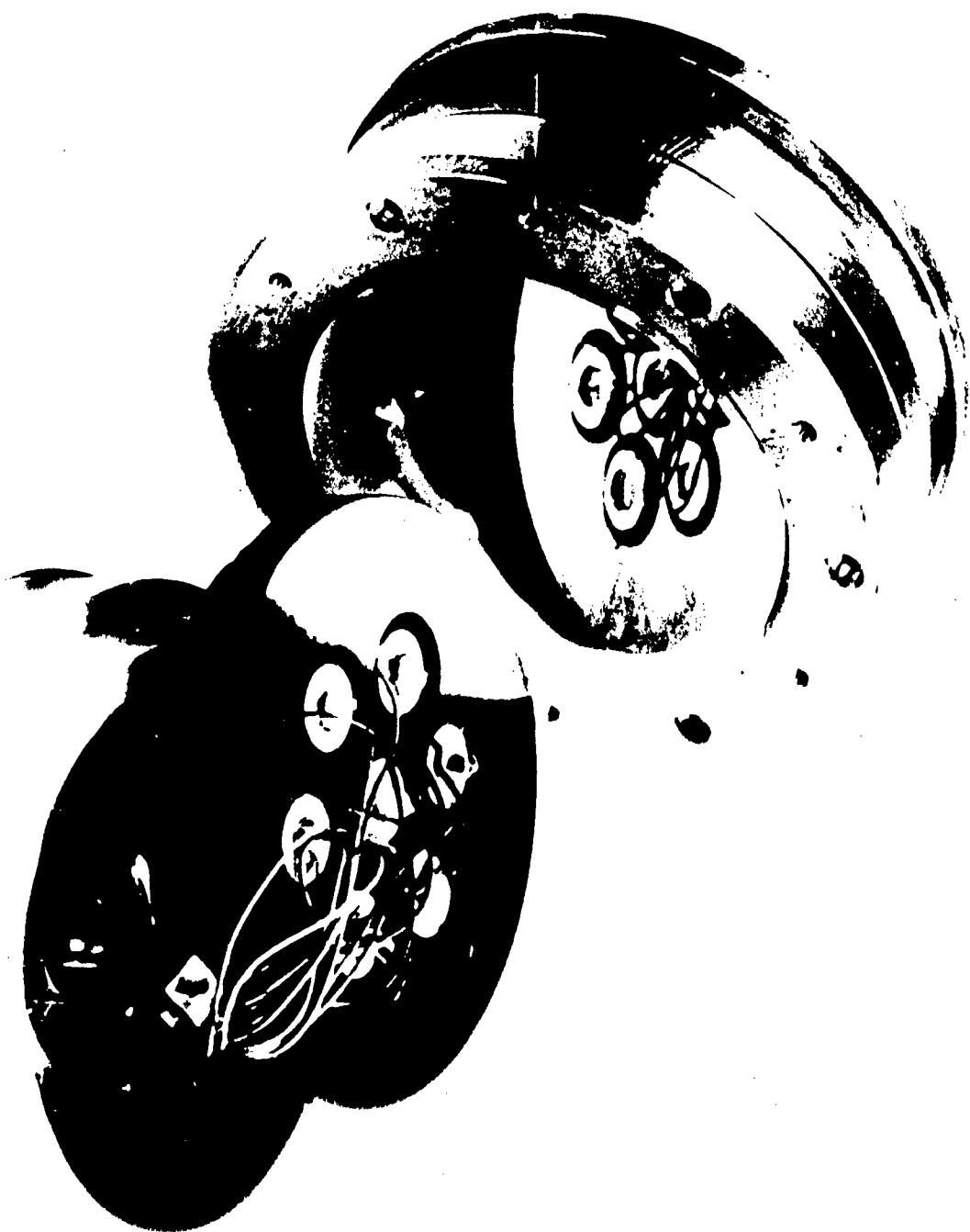
1. Work diameter — Ø 132 mm

2. Weight — 35 kg

3. Reflection factor — $\rho_{\lambda=10,6\mu m}=99\%$

4. Spacing between actuators — R=33mm

5. Local shifts — $\Delta=\pm10$ μm

6. Work voltage — $U_w=\pm300V$

7. Resonance frequency — $f_R>1kHz$

Values of resonance frequencies
28877, 30438, 32974,
35455, 38661, 42061,
46240   Hz

CONTROLLED DEFORMABLE
WATER-COOLED MIRRORS

MOLYBDENUM, 19 ACTUATORS-RIGHT.
BRONZE, 19 AND 61 ACTUATORS BOTTOM
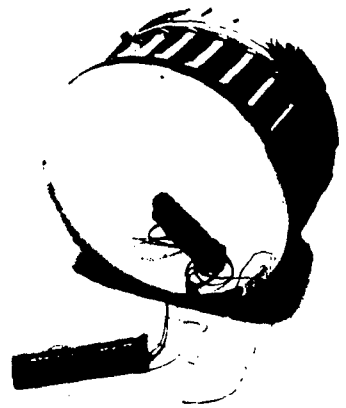
MODAL CONTROLLED
DEFORMABLE MIRRORS

BRONZE, CONVECTIONAL COOLING

sic "Sistema"

Low Cost Wavefront Sensor for Industrial Applications

Robert H. Dueck
Joseph E. Cass
Jeffrey L. Vaughn
Stephen L. Browne
Glenn A. Tyler

the Optical Sciences Company
P.O. Box 25309
Anaheim, CA 92825-5309
(714) 772-7668

10 June 1997

Introduction

- The Optical Sciences Company has developed a low-cost wavefront sensor (WFS) and beam profiler
- The sensor has proved to be an important tool in aiding optical system alignment of high power lasers
- The sensor is capable of estimating both intensity and phase profiles in near real time (currently 5 Hz) → *phase/io*
- The sensor is capable of measuring pulsed mode wavefronts
- In this presentation we describe
  - the workings of the sensor hardware,
  - features of the graphical user interface, and
  - how the WFS can be applied to the measurement of high power lasers

The Wavefront Sensor

- The wavefront sensor uses the concept of the Hartmann test
- A two dimensional array of lenses is used to divide the beam into subapertures
- Each individual lens forms an independent focus on a CCD array
- Each spot location is an estimate of the average phase gradient (or tilt) over the corresponding subaperture
- The sensor works equally well for white-light sources

The Optical Sciences Company

WFS Description

- A frame grabber board records the CCD focal plane data to a PC Pentium computer
- The computer calculates spot locations to the millipixel level, using either matched filter or centroid techniques
- A "perfect" plane wave is used to calibrate the sensor
- The spot locations for the plane wave are stored and used as reference locations
- Tilts are introduced to calibrate the lenslet focal lengths
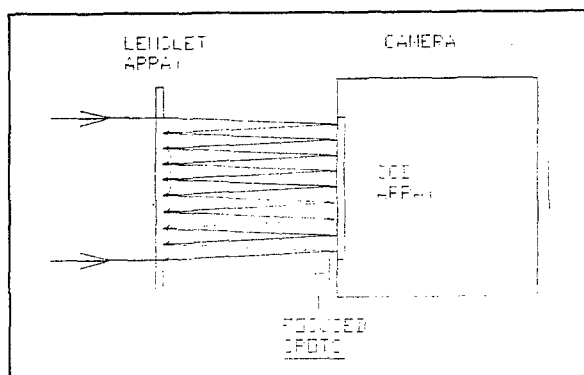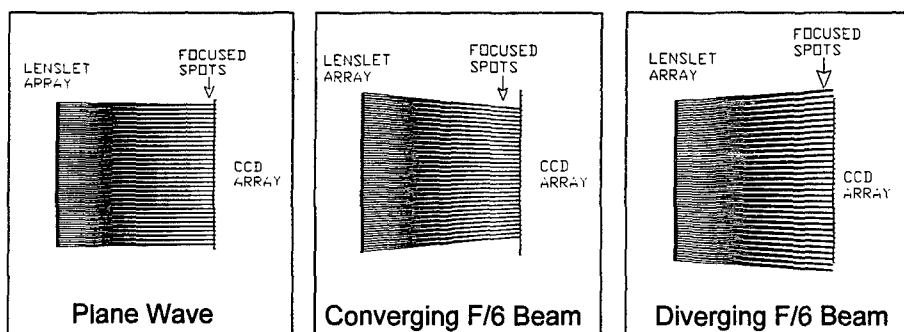
The Optical Sciences Company

WFS Optical Block Diagram

- Shown here is the simplest configuration of the wavefront sensor

Example Aberrations

Focus aberrations

| Plane Wave | Converging F/6 Beam | Diverging F/6 Beam |

WFS Optical Block Diagram

● Shown here is the simplest configuration of the wavefront sensor

Example Aberrations

Focus aberrations

LENSLET ARRAY

FOCUSED SPOTS

CCD ARRAY

Plane Wave

LENSLET ARRAY

FOCUSED SPOTS

CCD ARRAY

Converging F/6 Beam

LENSLET ARRAY

FOCUSED SPOTS

CCD ARRAY

Diverging F/6 Beam

The Optical Sciences Company
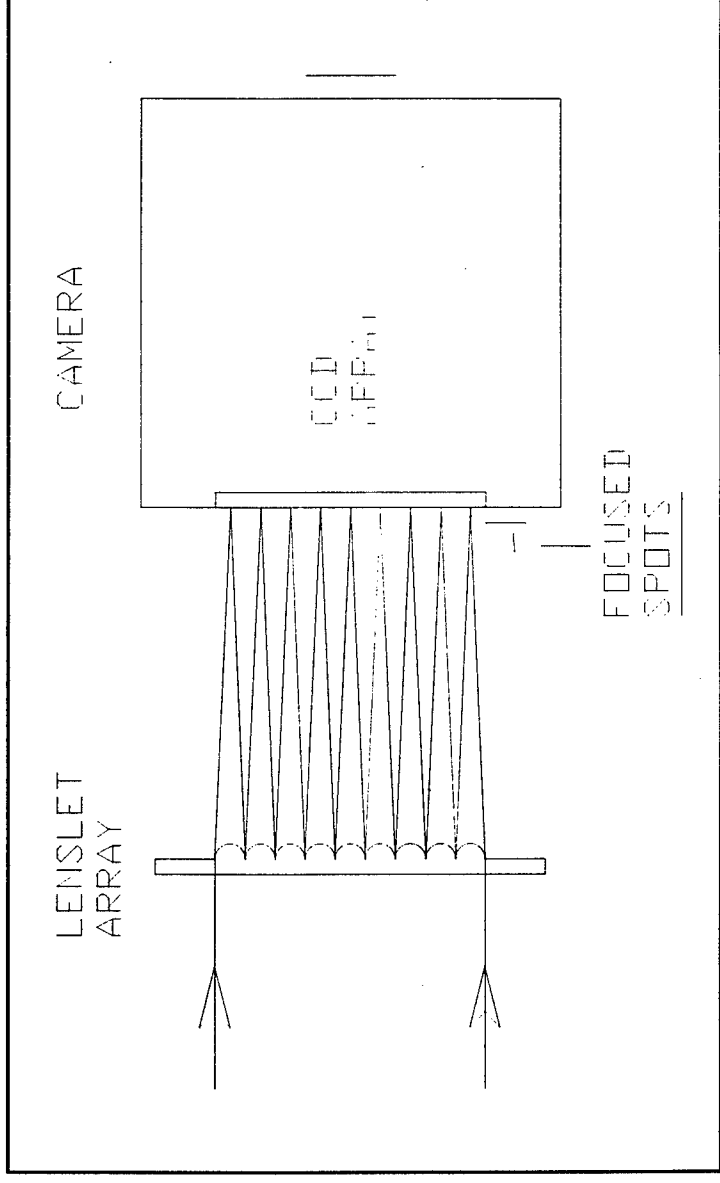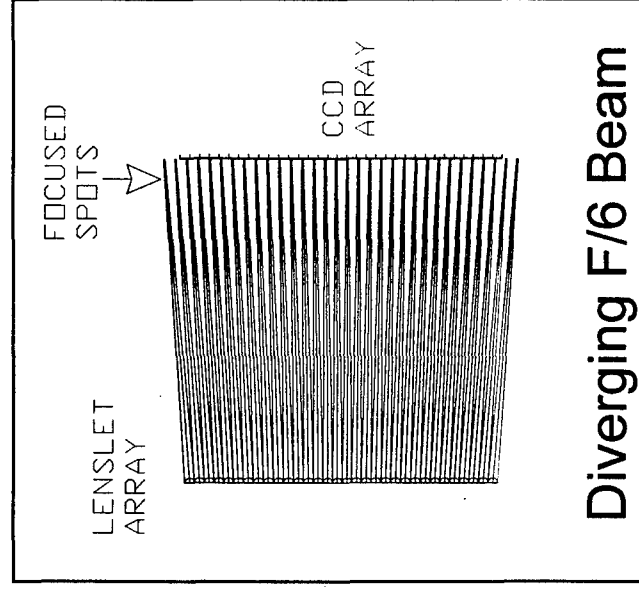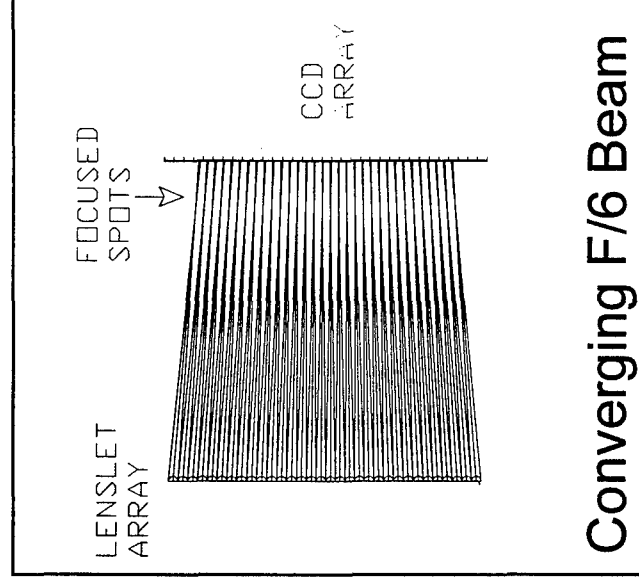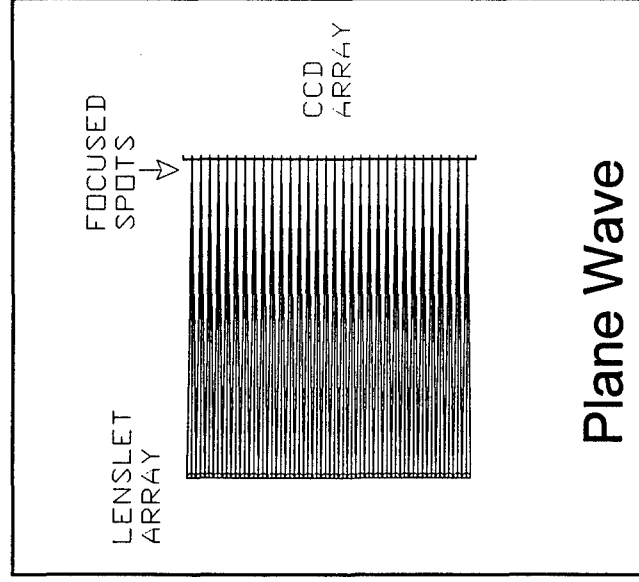
Measuring a Test Wavefront

- New spot locations are found for the distorted wavefront under test

- The new spot locations are differenced from the previously calibrated and saved "nominal" spot positions

- These differences are proportional to the test wavefront's phase differences across the subapertures

- Custom software is used to reconstruct the wavefront phase from this two dimensional set of phase differences

Thresholded Centroid Subaperture Spot Finding

- Within each region, K, the spot is located using a thresholded centroid algorithm

$$\hat{x}_K = \sum_{\substack{j,i \in K \\ V_{ji} > T_{ji}}} i V_{ji} \Bigg/ \sum_{\substack{j,i \in K \\ V_{ji} > T_{ji}}} V_{ji}$$

$$\hat{y}_K = \sum_{\substack{j,i \in K \\ V_{ji} > T_{ji}}} j V_{ji} \Bigg/ \sum_{\substack{j,i \in K \\ V_{ji} > T_{ji}}} V_{ji}$$

- The sum is calculated using only those pixels in region, K, for which the gain-and-offset corrected pixel output, V_{ji}, exceeds the threshold value, T_{ji}.

Wavefront Reconstruction

- The subaperture slopes (phase gradients), **s**, are related to the wavefront phase points, ϕ, by the so-called gradient matrix, Γ

$$\boldsymbol{s} = \Gamma\phi$$

- An estimate of the wavefront phase can therefor be "reconstructed" from a measurement of the slopes

$$\hat{\phi} = \left(\Gamma\Gamma^T\right)^{-1}\Gamma^T s$$

$$\equiv \mathrm{H}\, s$$

- H is the wavefront reconstructor
- Γ (and therefor **H**) are be determined *a priori* from a knowledge of the subaperture/actuator geometry, which is defined by the user during initialization
- It is possible to reconstruct Zernike coefficients directly from the subaperture slopes, without first reconstructing phase. This saves time.

The Optical Sciences Company

Slope Discrepancy

- Geometry lets us calculate the set of slopes consistent with the calculated phases:

$$\hat{S} = \Gamma\hat{\Phi}$$

- The slope discrepancy, $\left|s - \hat{s}\right|^2$, is related to the amount of noise in the original slope measurements.
- The true noise is greater than the slope discrepancy:
  - There are more slope measurements than phase points, and
  - The reconstructor manifests its own noise gain in converting slope measurements to phase.
- After correcting for these two effects, we get a good estimate of the wavefront phase reconstruction error.

The Optical Sciences Company

Matched Filter Subaperture Spot Finding

- We start with a pre-defined hypothetical function, G(x,y), which looks much like the subaperture spot
- We minimize the function

$$F_{nm} = \sum_{j,i \in K} V_{ji}\, G(x_i - x_m, y_j - y_n)$$

  - we start with a good guess for the spot location (perhaps from the centroid): $(x_{m'}, y_{n'})$, and evaluate $F_{m'n'}$
  - we choose four values for $(x_{m''}, y_{n''})$: left, right, above, and below $(x_{m'}, y_{n'})$, and evaluate $F_{m''n''}$ for each
  - we perform parabolic interpolation in each dimension to find the true minimum of F_{mn} to sub-pixel accuracy.

BC-906
- 9 -

The
Optical
Sciences
Company

Matched Filter Versus Centroid

- The advantage of the centroid is that it is *fast.*
- The advantage of the matched filter is that it is *optimal*
  - it emphasizes the bright pixels, which have the greatest signal-to-noise ratio,
  - so it is as immune to noise as is theoretically possible,
  - especially if time permits, wherein continued iterations can find the true minimum of F_{mn}.
- Depending on the signal levels and accuracy requirements of the system, and the need for speed, one of these algorithms is better suited than the other.
- We have provided a choice

BC-906
- 10 -

The
Optical
Sciences
Company

Features of the Wavefront Sensor

- The intensity and phase information can be used to estimate quantities such as:
  - rms phase error
  - peak to valley phase error
  - WFS accuracy (using slope discrepancy)
  - beam quality
  - Zernike polynomials
  - diffraction point spread functions
  - MTF
  - X and Y overall tilt
- Wavefront sensor results can be presented as:
  - contour plots
  - isometric plots
  - vector plots (showing gradients) and
  - simulated interferometric fringes (as with an interferometer)

The Optical Sciences Company

Wavefront Sensor Hardware

- *Either* Sony XC-77 RS-170 camera (~$1K)
  - CCD focal plane with 640x480 13 μm square (effective) pixels
  - 6x8 mm array size – limits measurable beam size to 6 mm
- *or* Pulnix TM-1001 digital camera (~7K)
  - CCD focal plane with 1024x1024 9 μm square pixels
  - 9x9 mm array size – permits beam size to 9 mm
- Lenslet array (~$1K)
  - F/25 elements
  - 0.5 mm or 0.2 mm diameter subapertures
- MuTech frame grabber (~$2K) + (~$1K for digital input)
- Pentium-class computer (~$2k)

The Optical Sciences Company

Sensor Noise Sources

- The main sources of noise:
  - signal shot noise (when signals are low)
  - dark current
  - camera read-out noise
    * preamp & digitizer
    * pixel jitter (caused by inaccuracies in horizontal line synchronization)
  - fixed pattern noise (when not compensated)
  - camera pixel structure noise (variations in pixel spacing)
  - quantization noise (8 bits)
- In the case of strong signals, pixel structure noise dominates when the spots are not near the calibrated spot locations

BC-906
- 15 -
The Optical Sciences Company

Sample Wavefront Measurements

- Wavefront measurements were made with 12 subapertures across a 6 mm diameter circle
- The lenslet array was 15.2 mm from the CCD
- At 1.064 μm wavelength, the relationship between spot displacement and subaperture tilt was 2.48 pixels/wave
- The spot size (full-width at half-maximum) was about 5 pixels
- The nominal separation between spots (and therefor subapertures) was 38.46 pixels.
- This allows the measurement of up to 15 waves of phase difference across each subaperture

BC-906
- 16 -
The Optical Sciences Company

Raw Camera Image

- The many pixels across each spot provide high accuracy (λ/40 rms)
- The wide spot separations yield large dynamic range (15 waves across each subaperture)
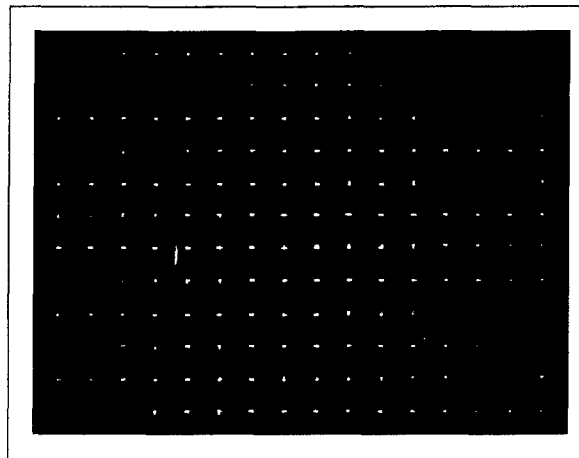
Graphical User Interface
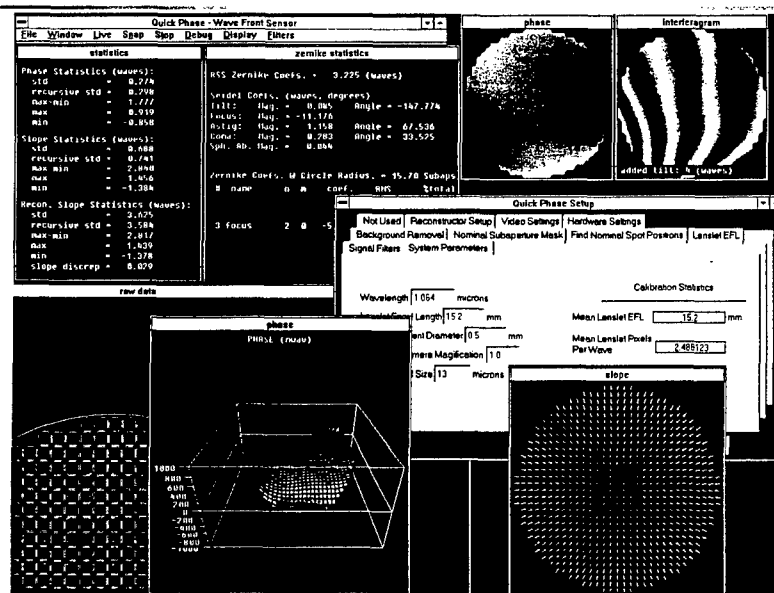
Interfero-gram

Cardfile Style Setup

Slope Quiverplot

Laser Cavity Wavefront

interferagram	phase
added tilt: 4 (waves)	PHASE (nwau)
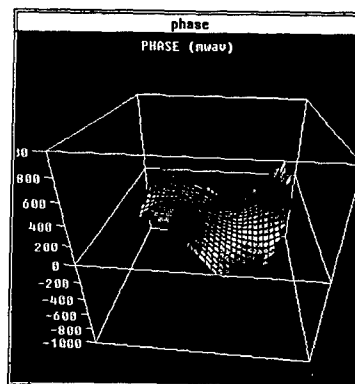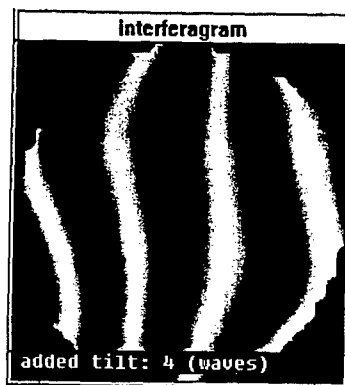
- Thermal loading of high energy rod causes aberration
- Significant trefoil ($\cos 3\theta$) is present

BC-906
- 21 -

Adjusting for Collimation
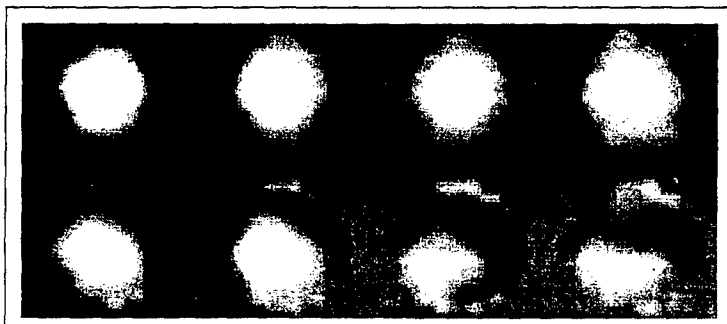
- As part of the laser system alignment, various stages of the optics were brought into collimation
- Shown above is a series of reconstructed wavefronts, during which a lens is adjusted to bring the beam into best collimation
- A full wave of focus aberration was removed (lower right)

BC-906
- 22 -

Aligning Multiple Amplifier Rings

- The wavefront sensor is very sensitive to overall beam tilt
- When tilts where not removed from the wavefronts during reconstruction, the results were used to detect alignment errors between the different amplifier rings
- Each amplifier ring was brought into alignment with the master oscillator

BC-906
- 23 -
The Optical Sciences Company

Conclusions

- The wavefront sensor is able to provide intensity and phase information on a laser system in quasi-real time
- Significant characteristics, such as Zernike modes, Seidel coefficients, WFS accuracy, and wavefront statistics, can be displayed
- The rapid update of optical measurements makes alignment and adjustment quite easy
- A choice of spotfinding and reconstruction algorithms lets the user tradeoff accuracy, dynamic range, and speed
- Many other options (such as tilt and/or focus removal) aid in wavefront analysis
- This wavefront sensor proved to be an excellent tool in the development and understanding of laser systems

BC-906
- 24 -
The Optical Sciences Company

Vadim Samarkin

NICTL - Laser Research Center
Russian Academy of Sciences

COMPUTER CONTROLLED ACTIVE MIRRORS AND LENS FOR INDUSTRIAL APPLICATIONS

Bimorph adaptive mirror

1. Kokorowsky S.A. "Analysis of adaptive optical elements made from piezoelectric bimorph", JOSA, **69**, 1979

2. Lipson S.G., Steinhaus E. "Bimorph piezoelectric flexible mirror", JOSA, **69**, 1979

Main Requirements to adaptive mirrors:

- deformable range of mirror surface
- small number of controlling channels
- simplicity of production and application
- low cast of mirrors
- high temperature stability

Glass bimorph mirrors

reflective
coating

glass
plate

defocus control
electrode

common
electrode

piezodisk

controlling
electrodes
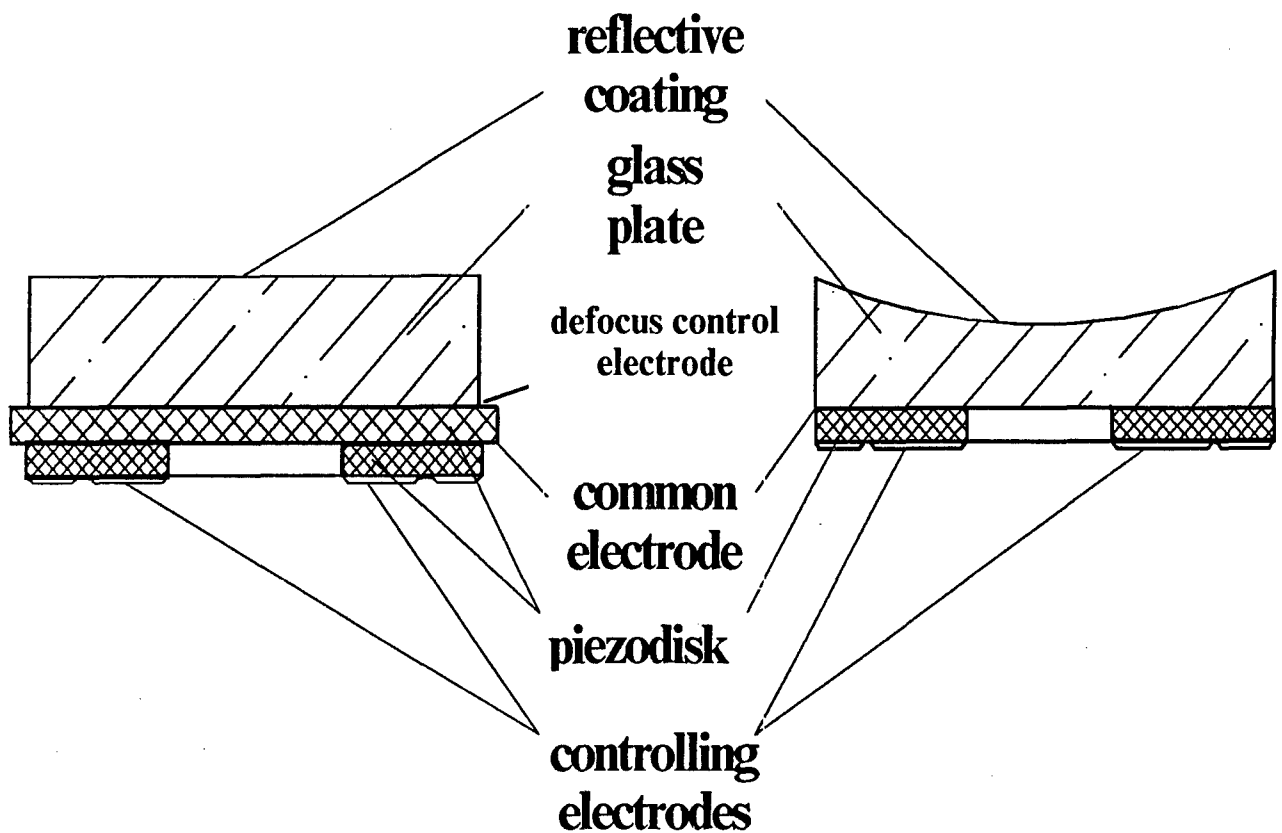
Main features :

aperture	-40mm
surface deformation	-7 μ
number of actuators	-8,13,17
mirror quality	-0.1 μ (PV)
frequency bandwidth	-2 kHz
reflecting coefficient	$\geq$98% at λ=0.63 μ
reflective/ protective coatings	Al / Al$_2$O$_3$
control voltage	$\pm$300 V
hysteresis	$\leq$10%

Water cooled bimorph mirrors

Reflective plates

Water delivering channels

piezodisks

Waffle type cooling structure
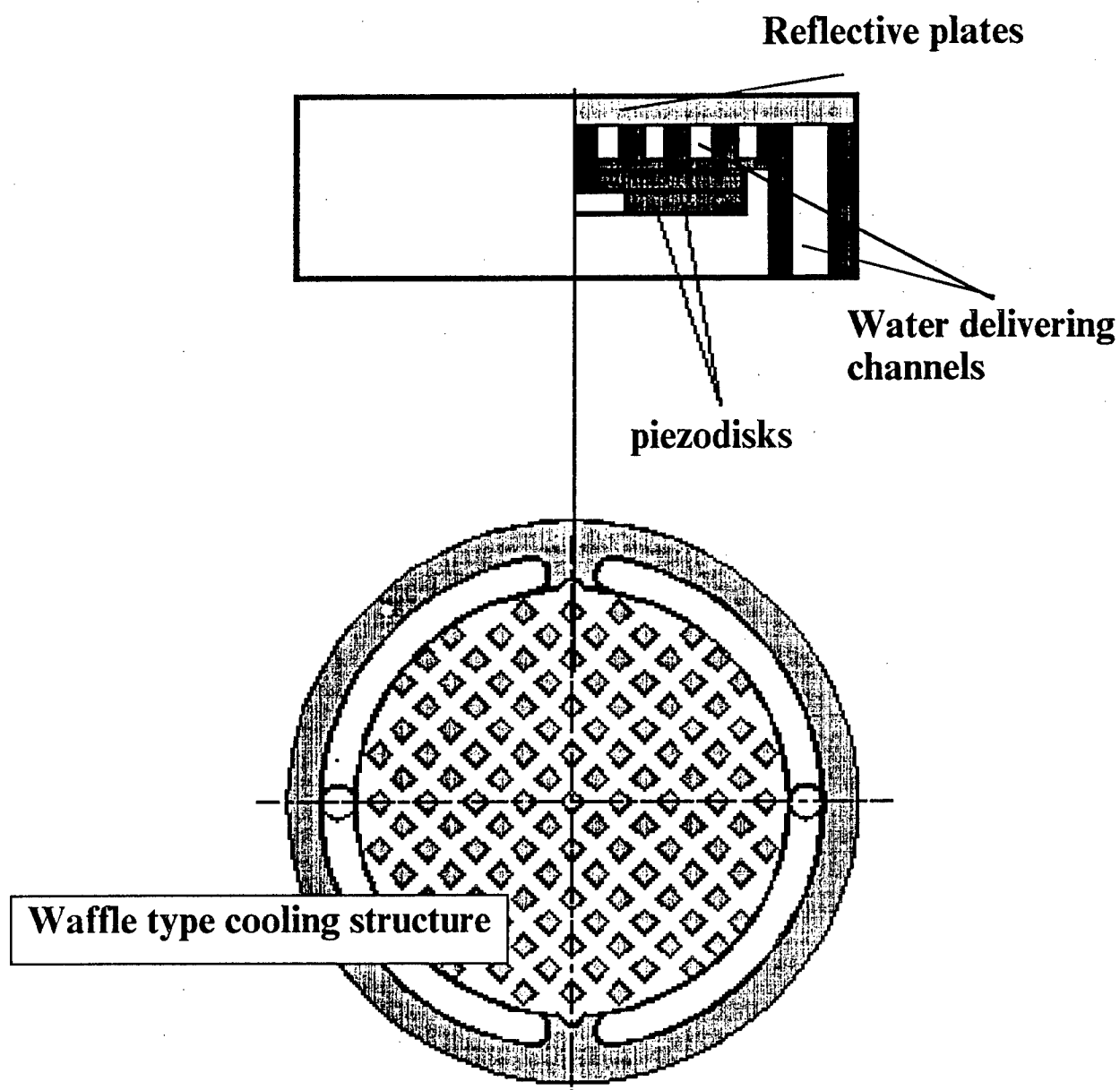
Main features:
aperture - 100 mm
deformation of surface - 6 μ
number of actuators - 1, 9, 18
mirror quality - 0.3μ
frequency bandwidth - >3 kHz
material - copper, molibdenum
reflecting coefficient - >99% at λ=10.6 μ
reflective/protective coatings - copper/Al_2O_3
control voltage - 300V

BIMORPH ADAPTIVE MIRROR
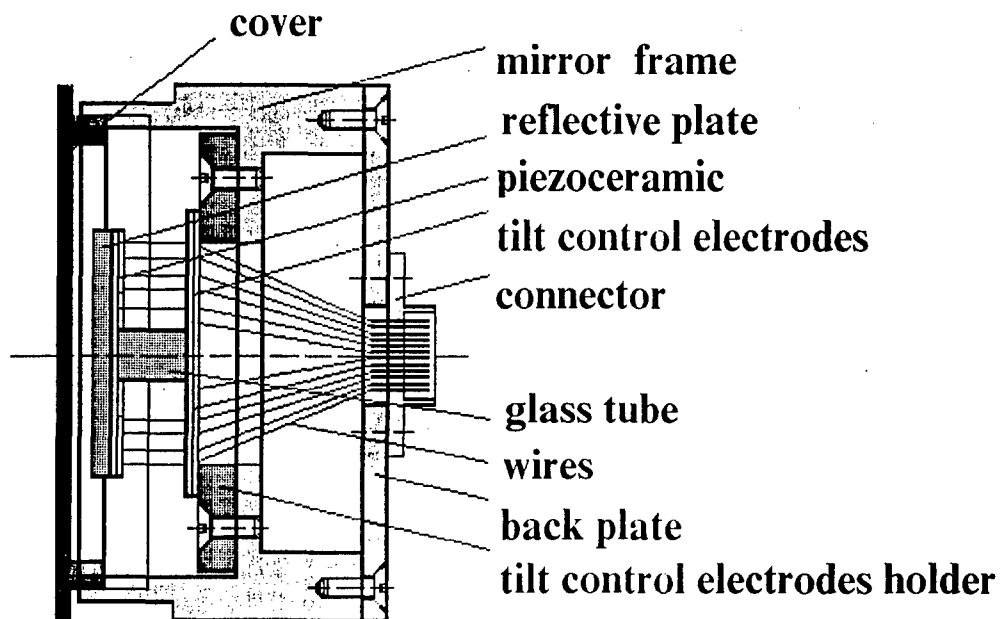
General design of the adaptive mirrors with tilt and piston control
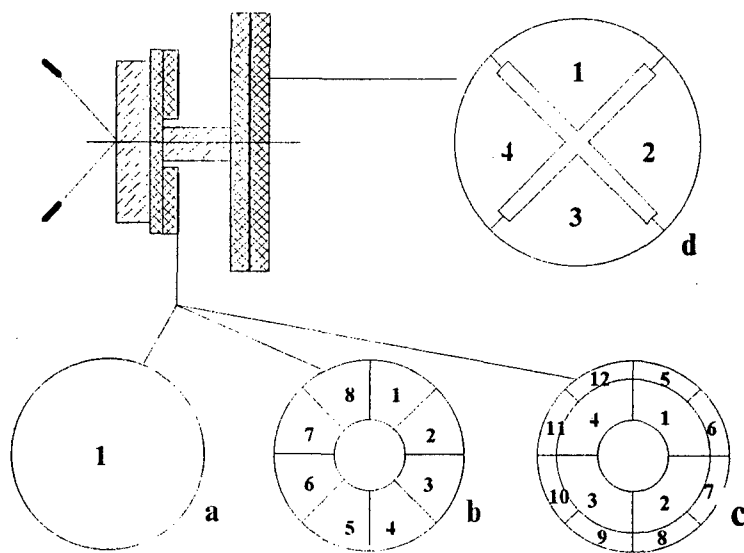
Schemes of control electrodes of the adaptive mirrors for:
   a) defocusing control;
   b) astigmatism and defocusing control;
   c) second-order aberrations control;
   d) tilt and piston control

Main features of adaptive mirrors

Aperture - 40 mm
Stroke (peak-to-valley) - 4 mkm
Generation/compensaton of aberrations:
    piston - 10 mkm
    tilt - 0.8 mrad
    defocus - 4 mkm
    astigmatism - 6 mkm
    coma - 0.8 mkm
    spherical aberration- 0.75 mkm
Number of controlling electrodes - 1, 9,14,18
Histeresis -   <10%
Drive voltage -   ±300 V
Capasitance -   50 nF
Full amplitude bandwidth -   1 kHz
Surface figure - λ/4 (λ=0.633mkm)
Residual aberration - λ/10 (λ=0.633mkm)
Thermostability of surface shape -   0.04 mkm/^{o}C
Material-   glass LK5, Si
Reflecting coating -   Cr/Al/SiO$_2$
Reflection coefficient -   ≥ 90% in the wavelength
                                        range 0.4 ÷ 0.7 mkm

mirror substrate material	α, x 10^6/K	m, μm/1°C	mirror thickness, mm	mirror aperture, mm
quartz	0.55	- 0.21	2.5	40
Si	2.54	-0.035	2.6	40
piezoceramic	≈ 3	0	0.35	40
glass LK5	3.5	0.04	3.0	40

Temperature dependences of defocus changing for different kinds of mirror substrate materials (m - defocus changing value per 1°C)

Influence function of different electrodes

El.12
Appl.vol. 150V
P-V -1.49μ
Step -0.3μ

El.11
Appl.vol. 150V
P-V -1.58μ
Step -0.3μ

El.13
Appl.vol. 150V
P-V -1.57μ
Step -0.3μ
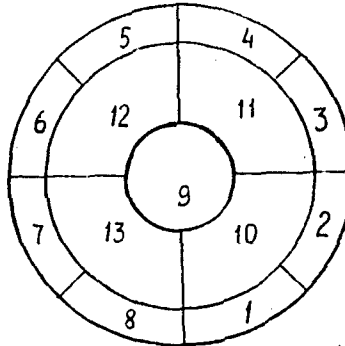
El.8
Appl.vol. 150V
P-V -0.69μ
Step -0.1μ

El.1
Appl.vol. 150V
P-V -0.65μ
Step -0.1μ
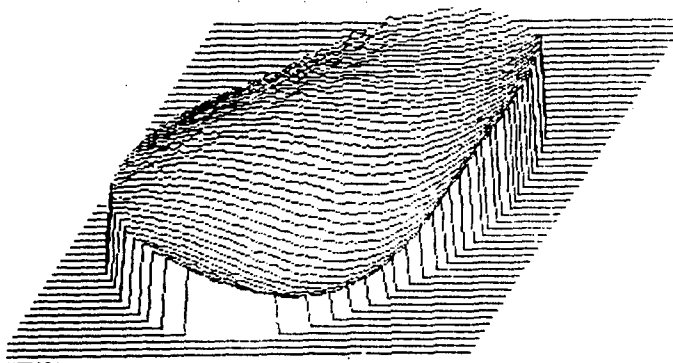
Surface profile of influence function of 13 electrodes bimorph mirror.
+150v and -150V voltage was applied to periferical electrode 1.

Type of mirror	Residual aberrations, μm	P-V of mirror surface, μm	Sensitivity of electrode 1, μm/V	Sensitivity of electrodes 2-9, μm/V	Sensitivity of electrodes 10-13, μm/V
Defocus	0.074	0.27	$11.2*10^{-3}$	-	-
Defocus+ astigmatism	0.063	0.38	$13.86*10^{-3}$	$4.41*10^{-3}$	-
2nd order aberrations	0.049	0.24	$11.5*10^{-3}$	$2.5*10^{-3}$	$1.0*10^{-3}$

Residual aberrations and sensitivity of the adaptive mirrors
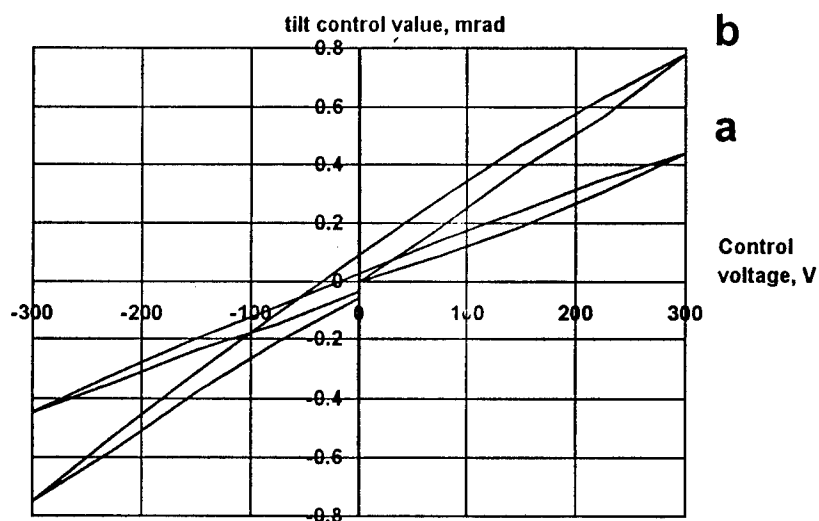
Experimental curves showing tilt control ranges by using of
a - one electrode
b - two electrodes

CONTROL SYSTEM
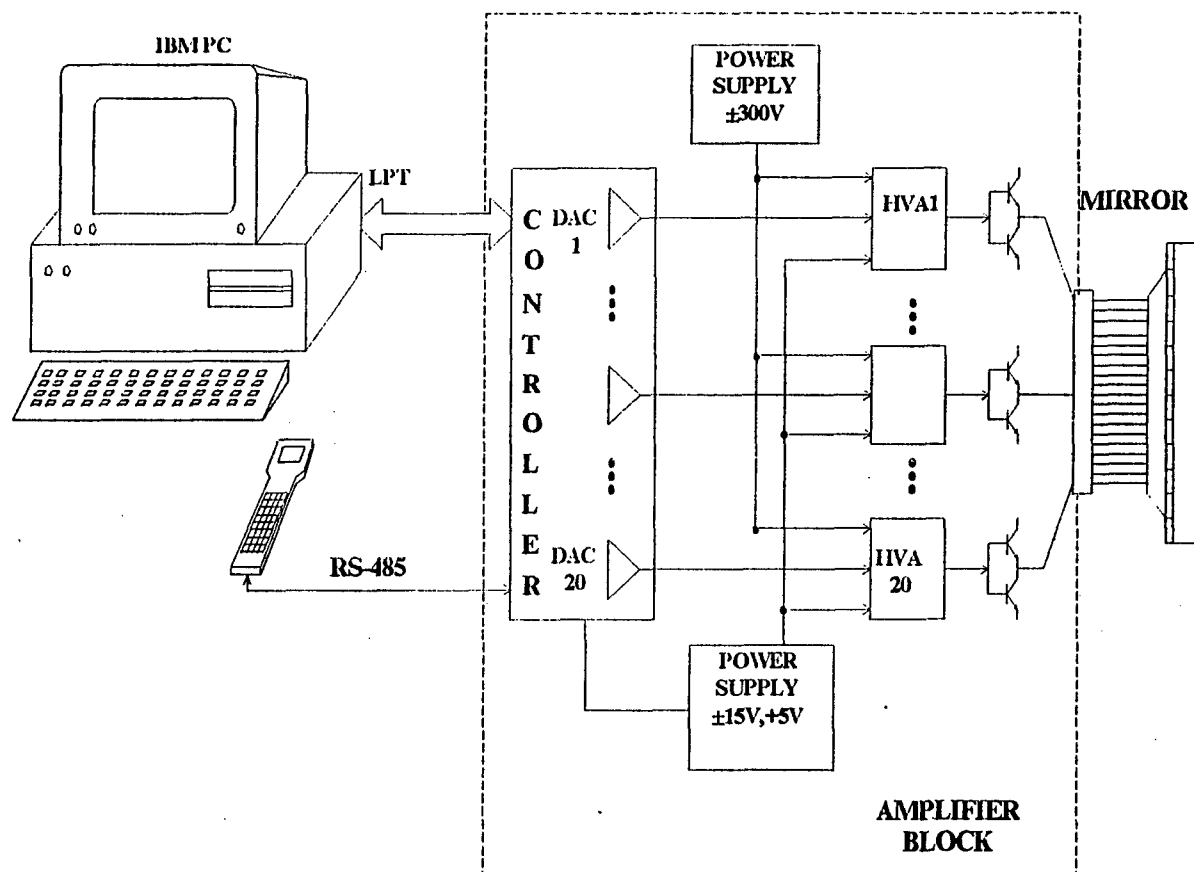
Configuration of RTV-300 system

Channels	20
Max. frequency in all channels	500 Hz
Output voltage	±300 V
Max. output current of a single channel	80 mA
Max. capacitive load per channel	0.2 μF
Velocity of voltage build-up	0.2 V/1 μs at 0,2 μF load
	0.7 V/1μs at 0,02 μF load
Nonuniformity of amplification factors in channels	5%
Sequential channel	RS-485, 9600 bit/s
Consumed power	200 W

SOFTWARE

Software includes the special subprogram-functions:

Zero -   to set 0 volts at all the electrodes.

Read -   to read the given set of voltage values at the elecrodes from the file.

Write -   to record the current voltage values at the electrodes into the file.

Gain -   to enter a factor of amplification for the set of voltages.

Rotation - to enter a rotation angle of voltage arrangements.

Real time - to go to a submenu of real time operations .
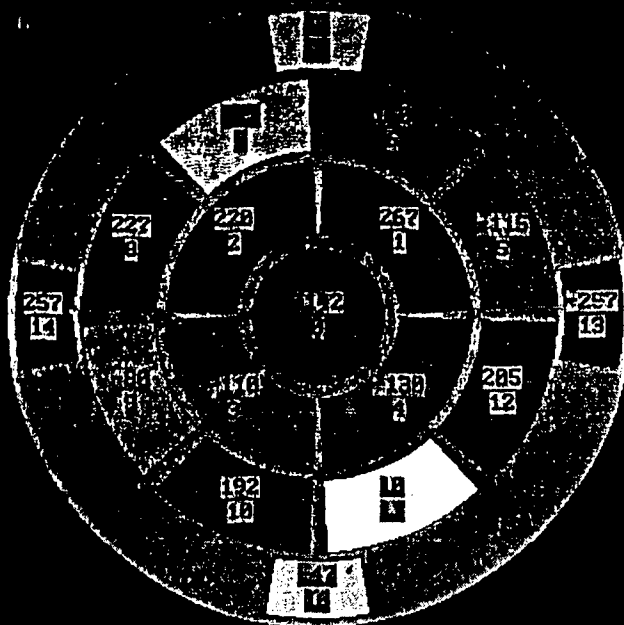
lens frame
piezoelectric plate
glass plate
glass lens
immersion liquid
back plate
front plate
wires
connector
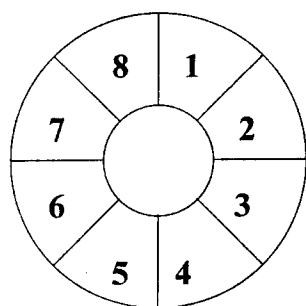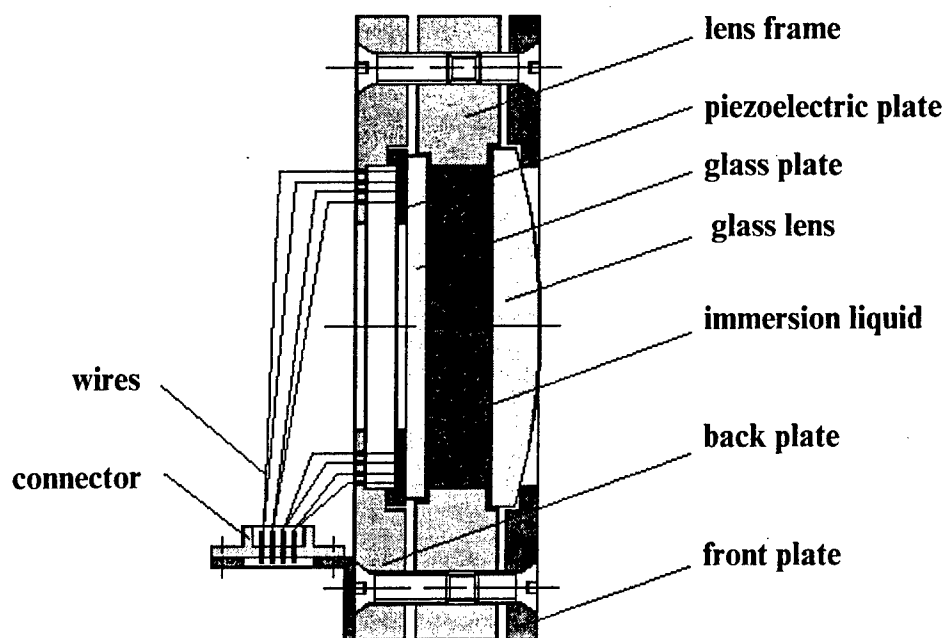
General design of controlled lens and scheme of control electrodes

Residual aberrations	μm	0.12
Sensitivity of electrode 1	μm/V	$0.9*10^{-3}$
Defocus The same electrical voltage is applied to all the electrodes simultaneously.	μm/V	$1.97*10^{-3}$
	μm at 300V	0.6
Astigmatism The positive electrical voltage is applied to electrodes 1, 5 and the negative one to electrodes 3, 7 simultaneously.	μm/V	$3.35*10^{-3}$
	μm at 300V	1.0

Characteristics of the controlled lens

Applications of Shack-Hartmann wavefront sensor

Wenhan Jiang, Zeping Yang, Hao Xian, Lingtao Jiang, Xuejun Rao, Bin Xu

Institute of Optics and Electronics, Chinese Academy of Sciences
P. O. Box 350 Shuangliu, Chengdu 610209, China
Fax: +86-28-5180070, e-mail: whjiang@cdisn2.cdisn.cd.sc.cn

Abstract

Shack-Hartmann wavefront sensor can measure both intensity distribution and phase gradients of optical filed with high frame rate. It is not only widely used for wavefront sensing in adaptive optics system but also for inspection of optical components and systems, diagnosis of laser beam quality and atmospheric turbulence measurement. We have developed several S-H sensors. The results of measurements by using these sensors in different areas are reported in this paper.

1. Introduction

Shack-Hartmann (S-H) wavefront sensors are widely used in adaptive optical systems.[1] By using a proper data acquisition and processing equipment, the S-H sensor can measure spatial and temporal characteristics of intensity and wavefront phase profile of optical beam simultaneously, providing detailed dynamic information of laser beams and optical systems. From these data the detailed near-field and far-field specifications can be obtained. It can be calibrated by a reference beam in advance. In field measurement, it is not necessary to have a on-line reference and is not as sensitive to the environment as interferometer. It is a powerful tool for laser beam diagnosis and optical quality control. We have developed several types of S-H sensors for different applications, such as inspection of optical components and systems, diagnosis of laser beam quality, and atmospheric turbulence measurement. In this paper some results of these applications are presented.

2. Construction of S-H sensors

The S-H sensor for laser beam diagnosis and atmospheric turbulence measurement is shown in Fig.1a. Lenses 1 and 2 are the aperture matching optics for converting the beam aperture to the aperture of lenslet array 3. Lenslet array divides the aperture into subapertures and forms a spot array at the focus plane. Lens 4 matches the size of spot array to the detecting area of CCD 5. By A/D converter 6 the output of CCD is acquired by the computer 7. The whole system is calibrated by a collimator as a reference and the centroids of reference spot array are stored in the computer.

The S-H sensor for inspection of optical components and systems is shown in Fig. 1b. A laser 10 is used as the light source and is expanded and collimated by lenses 9 and 1. A flat mirror is used as the reference during the calibration procedure. When the S-H sensor is used for inspecting spherical elements, the beam is focused by a lens and calibrated by a spherical mirror.
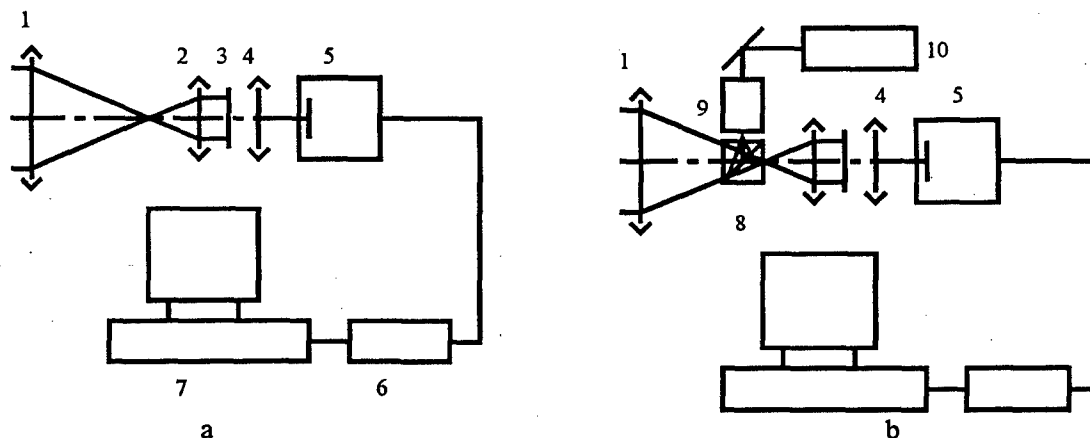
Figure 1. Structure of Shack-Hartmann sensor

3. Laser beam diagnosis

We have developed S-H sensors for UV, visible and IR wavelengths and used for laser beam diagnosis and optical system inspection. The software for wavefront reconstruction from the measured wavefront slopes in subapertures using different algorithms has been developed.[2] From the reconstructed wavefront and intensity distribution, various parameters such as p-v and rms phase error, Zernike coefficients, PSF and MTF, encircled energy and M^2 can be calculated.

3.1. Beam quality of a non-stable cavity laser[3]

In order to obtain the dynamic change of beam quality of a non-stable cavity laser, wavefront profiles of the laser beam were measured by a S-H sensor. The sampling rate is about 12 frames/sec. One sample (the 5th frame) of the wavefront phase error is shown in Figure 2. The coefficients of Zernike polynomials of the first 16 frames are shown in Figure 3 as a function of time, among which the astigmatism in X and Y (terms 4 and 5) directions are the largest two aberrations. Figure 4 shows the rms of the wavefront phase of each samples, the temporal changes of the wavefront phase error are obvious. The upper curve is the total wavefront error σ_{tot} and the lower curve is the dynamic changes of wavefront $\sigma_{dym} = \sqrt{\sigma_{tot}^2 - \sigma_0^2}$, σ_0 is the static error.

Figure 5 is the PSF pattern for far field of 16 frames computed from measured wavefront phase errors and intensity distribution data at near field. The change of R/R_0, the ratio of beam radius to the diffraction limit, is shown in Figure 6.
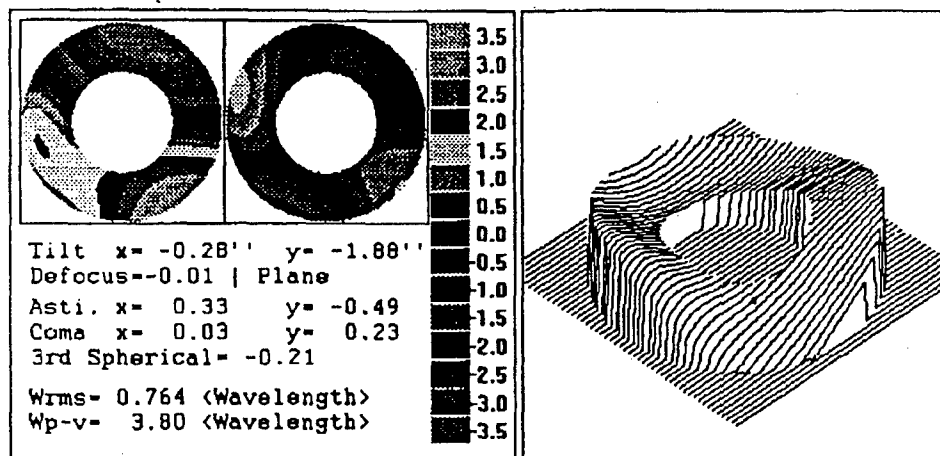
Figure 2. Wavefront phase error of laser beam.
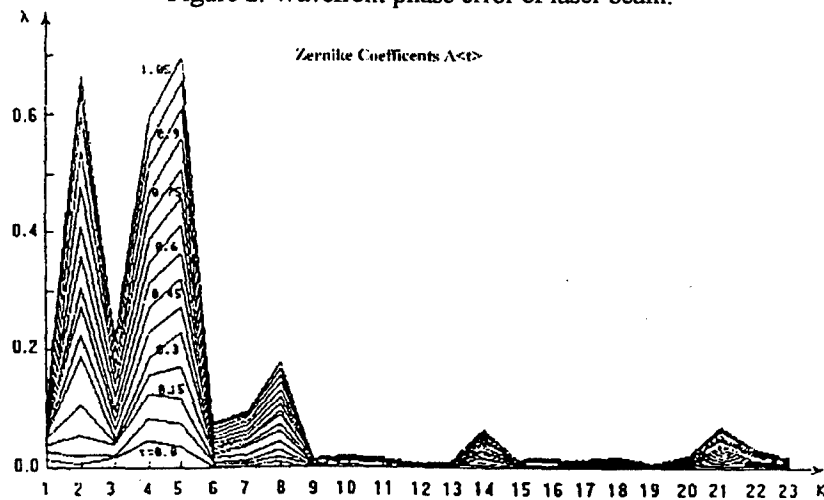
Figure 3. Temporal change of Zernike coefficients.
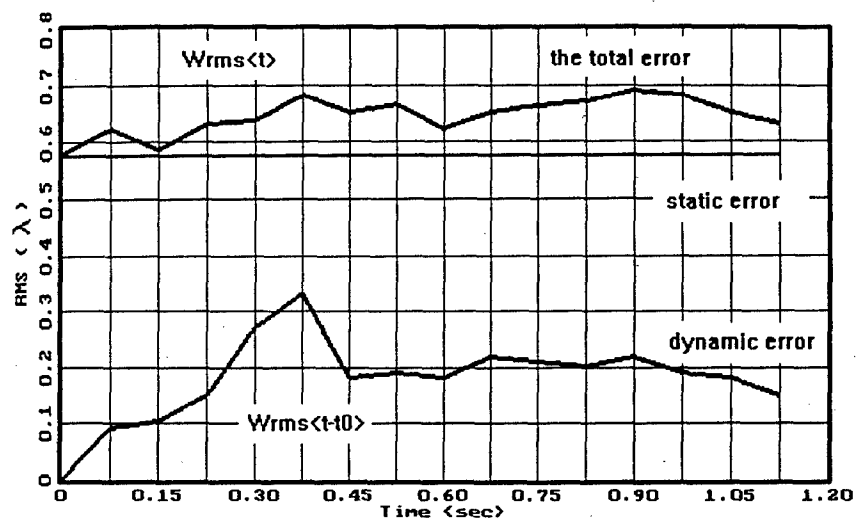
Figure 4. Temporal change of rms wavefront errors.
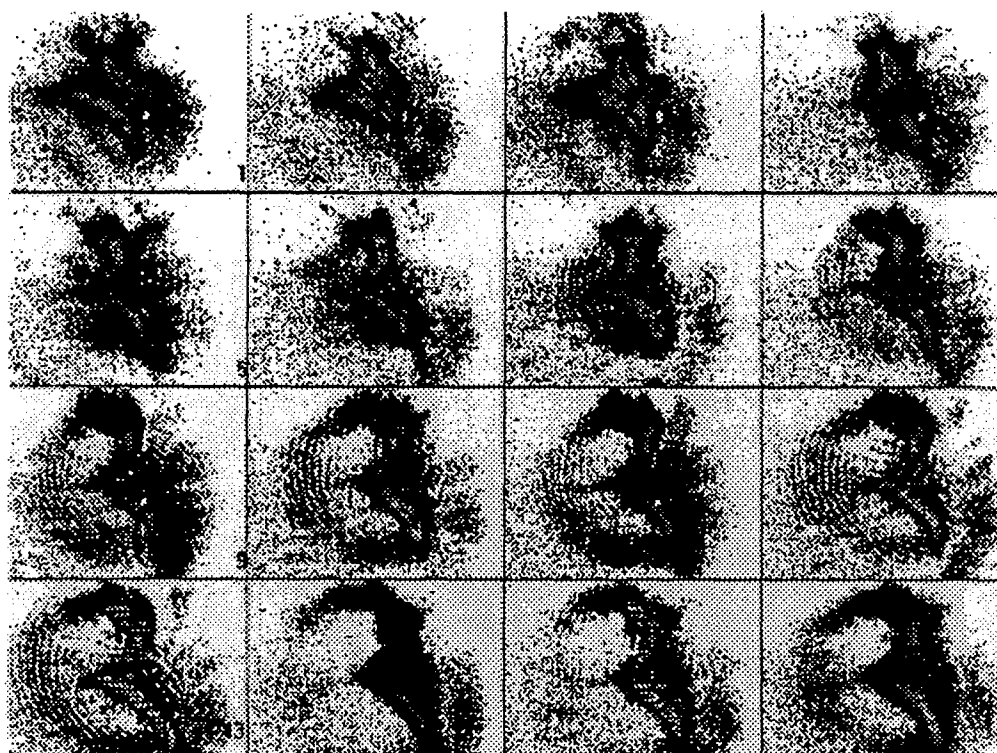
Figure 5. PSF pattern at far field computed from near-field measurements.
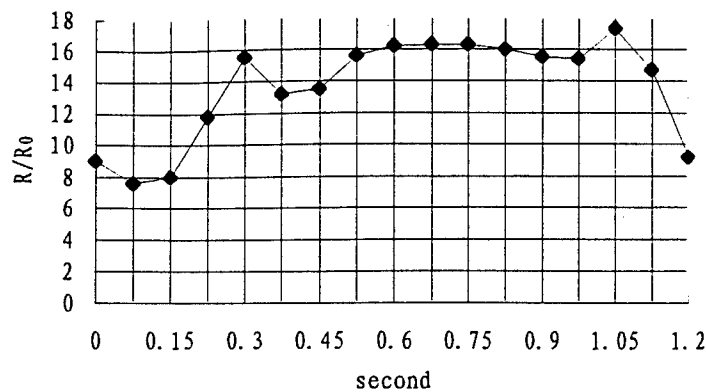
Figure 6. Change of the ratio of beam radius to the diffraction limit.

3.2. Beam diagnosis of a high energy laser for inertial confinement fusion (ICF)

In the laser driver for ICF, high intensity concentration at the focus and high efficiency for harmonic transform are desired. High power laser beam with minimum wavefront error is highly demanded. To improve the beam quality and analyze its influence factors, a careful investigation of the wavefront aberration is necessary. The main sources of wavefront aberration in ICF driver are: (1) static error of the optical system, including figure errors of optical components, inhomogeneity of optical materials and alignment errors, (2) thermal effect of pump light on amplifiers and its recovering process, (3) thermal turbulence in the optical path and (4) non-linear effect of the high energy laser.

Figure 7 shows the optical path of an ICF facility in the Shanghai Institute of Optics and Fine Mechanics, Chinese Academy of Sciences. The pulse Nb glass laser is amplified by a series of amplifiers. In order to investigate the wavefront errors of this facility, a H-S sensor has been developed (Fig.1a). The main specifications are:

Size of lenslet array:	26x26,
Dynamic range:	1.5λ/subaperture (λ=1.06μm),
Uncertainty of measurement:	λ/20 rms,
Pixel number of the CCD:	512x512.
Apertures of matching lenses:	Φ50mm.

The wavefront errors measured at the point 1 are shown in Figure 8. Figure 8a is the static wavefront error of the amplifiers a1, a2, a3, and a4 measured by passing a continuous laser through the amplifiers. The main components are defocus, astigmatism and coma. Figure 8b, 8c, and 8d are the errors of a pulse amplified by a1, a1 and b1, and a3 respectively. The static error is the main source in these stages, the thermal effect is also detected but not significant. In these stages the power of laser pulse is not as high as in the end part of the amplifier chain.

We measured the recovering process of the thermal effect at point 2. The aperture of the amplifier is Φ100mm. After a high power pulse passing through the system, the aberrations of in Φ50mm area at the edge of the amplifier aperture are measured continuously. Figure 9 shows the temporal change of defocus in 16 minutes after the pulse. An attenuate periodic change of defocus is obviously. It is due to the thermal conduction and balance process from the edge to the center.
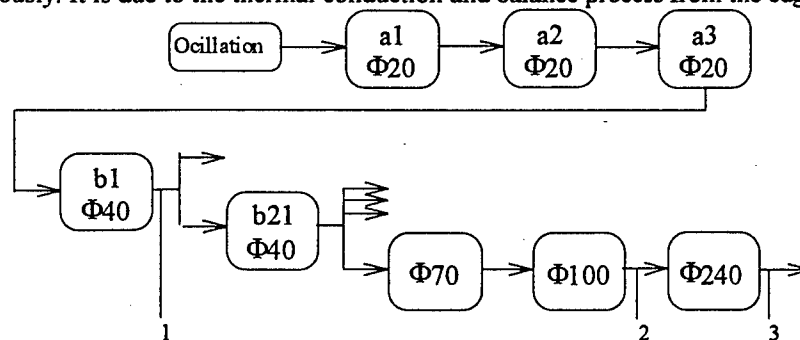
Figure7. Optical path of the ICF facility in the Shanghai Institute of Optics and Fine Mechanics.
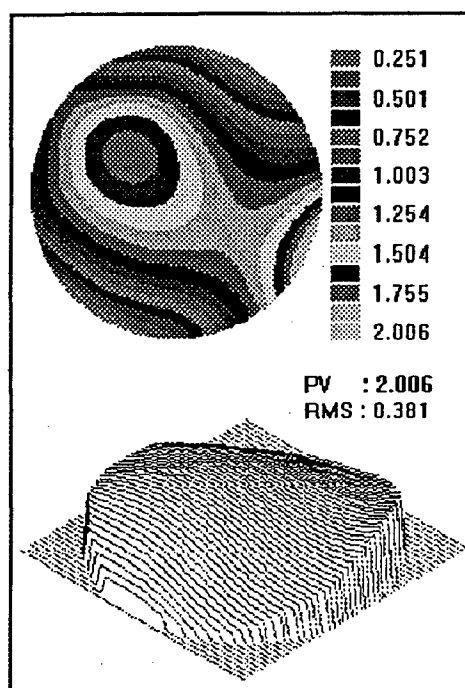
a. Static error of amplifiers a1, a2, a3, and a4.
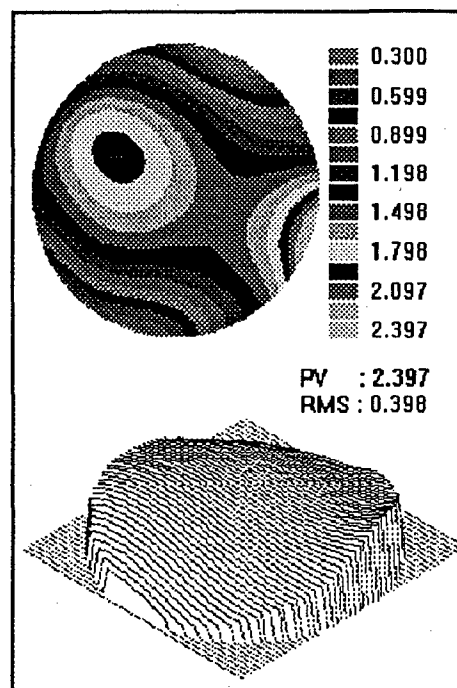
b. Pulse amplified by a1.
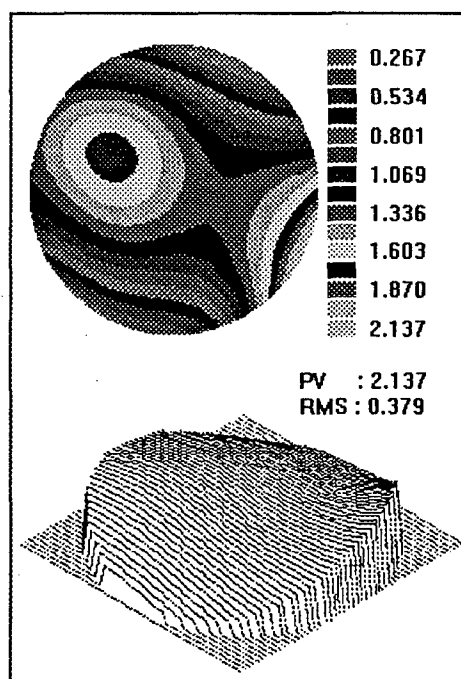
c. Pulse amplified by a1 and b1.
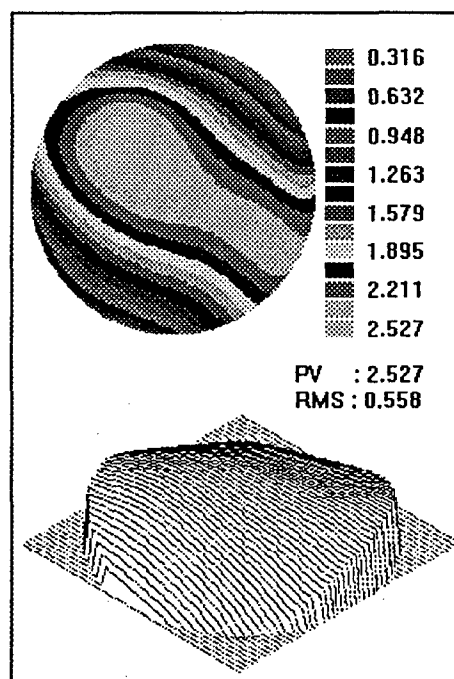
d.Pulse amplified by a3.

Figure 8. Wavefront errors of the Shanghai ICF laser.
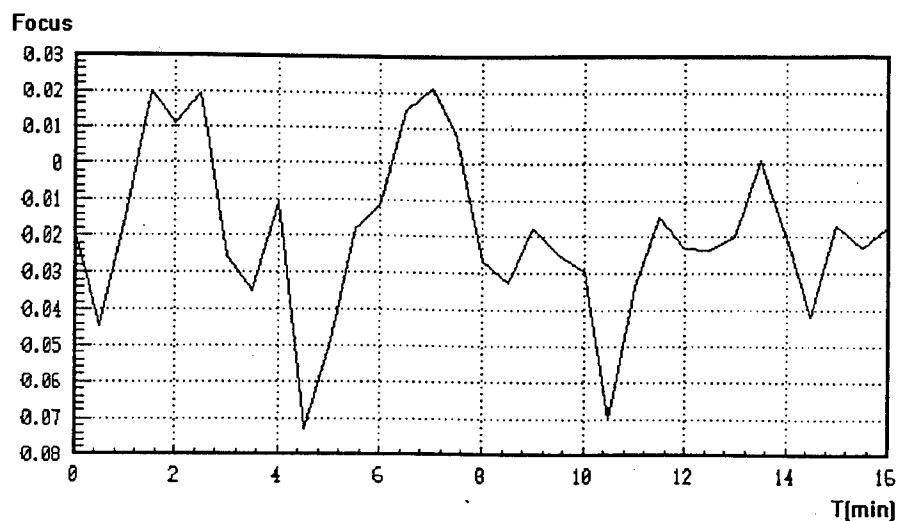
Figure 9. Change of defocus after laser pulse.

4. Inspection of optical elements and systems

The traditional methods for inspection of large optical elements and systems are interferometer and Focaut knife edge. The influence of environment to the interferometric inspection for large elements is serious and the Focaut test is difficult to give quantitative results. The S-H sensor is less sensitive to the environment as the interferometer because the reference is off-line and the dynamic effects can be eliminate by averaging of multi-frames. A H-S wavefront sensor for optical inspection is developed (Figure 1b). In this sensor a He-Ne laser is projected as the light source.

Figure 10 is two layouts for inspecting large spherical and flat mirrors. Figure 11 is a measurement of a spherical mirror of diameter Φ600mm. Figure 12 shows an inspection for an optical system consisting of two aspherical mirrors (Φ630mm and Φ120mm).
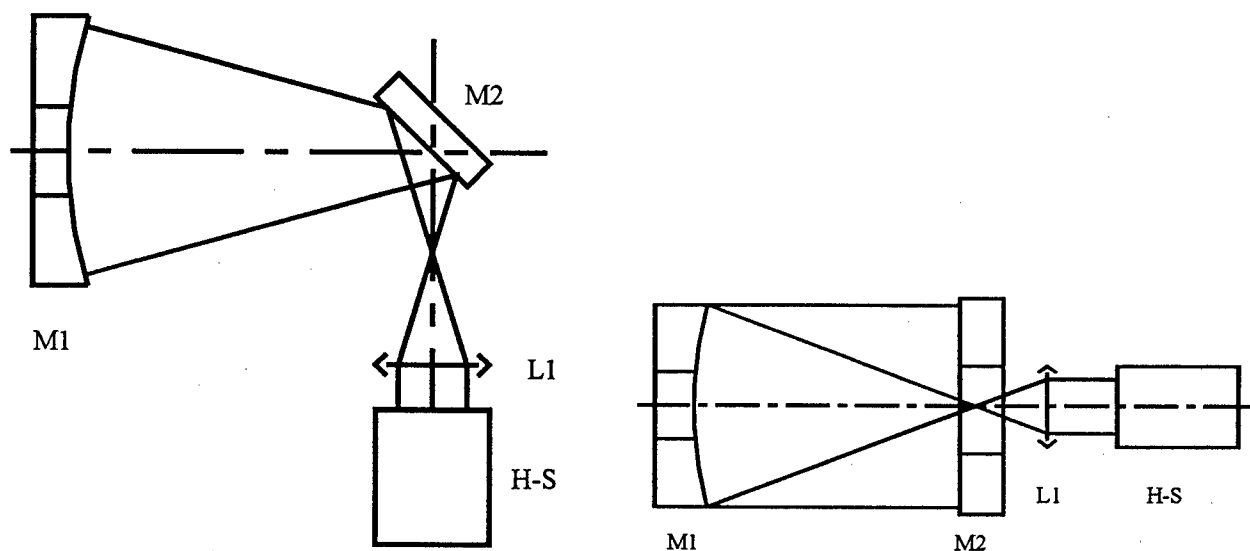
Figure 10. Two layouts for inspecting large spherical and flat mirrors.
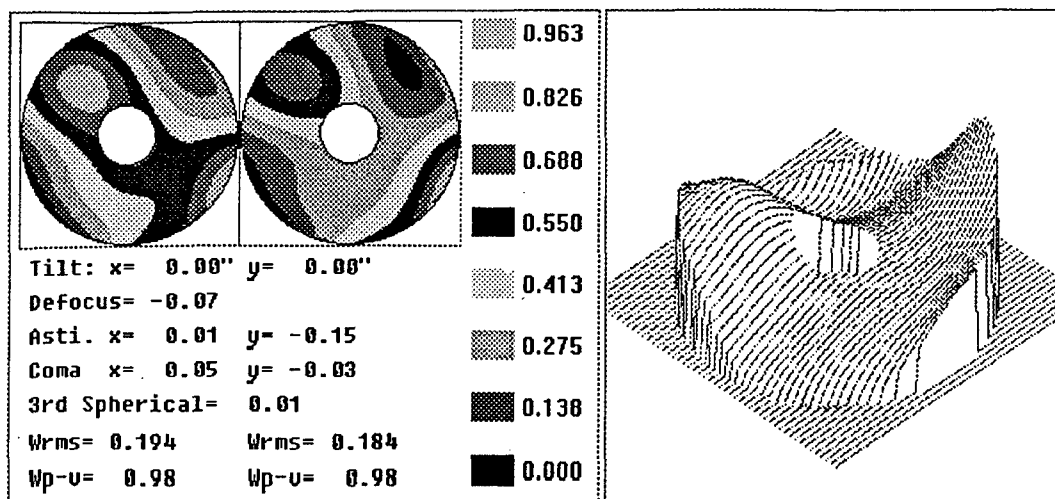
Figure 11. A measurement of a spherical mirror of diameter Φ600mm.
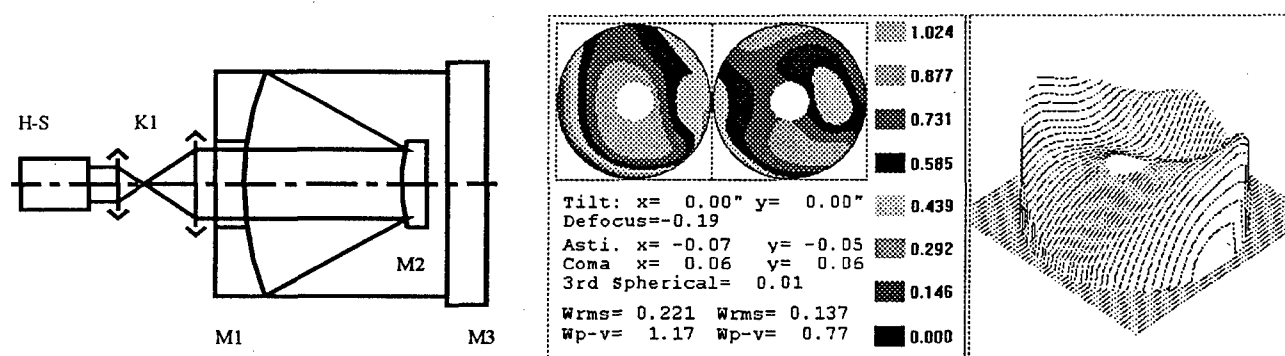
Figure 12. A measurement of an optical system.

5. High resolution measurement of atmospheric turbulence[4]

Atmospheric turbulence results in fluctuations of arrival angle. By a S-H sensor with high frame rate CCD, the atmospheric turbulence can be sampled with high spatial and temporal resolutions. A large volume of data can be measured and the detailed parameters of turbulence can be obtained. The key is to compress the data in real-time for storage. We developed a S-H sensor with high frame rate CCD and a multi-DSP processor and successfully used this sensor for atmospheric turbulence measurement.

In this system, a 37 subaperture lenslet array is arranged in triangle pattern, forming focus spot in 7 rows (Figure 13). Each row has 4 to 7 spots. A CCD camera with 830 Hz frame rate and 128x128 pixels are used to detect the Hartmann spots. If the spot images were stored, the data rate would be around 14 Mbytes/sec. The interested data are the centroid positions of spots which are the measures of wavefront slopes. If we only store the slope data of subapertures, the data rate is only 0.061 Mbytes/sec and the ratio of data compression is 221:1.

A multi-DSP processor developed by us is used to computing the wavefront slopes in subapertures in real-time and the slope data are stored in the extension memory of a personal computer. Figure 14 is the diagram of the system. A personal computer is used as the host computer. There are 4 processing modules in the system. In each module a TMS 320C50 DSP is used as processor and a dual-port memory (2Kx16bits) as the communication buffer between host computer and the DSP. Data acquisition circuit receives image data from the CCD camera, and load them to the image buffers in processing modules according the address from the Lock-up-table (LUT). LUT is a memory whose input address is the coordinates of the pixel and output data is the code indicating to which buffer the image data should be send to.

Four processing modules work in parallel. Each module processes 1 to 2 spots of each row. In Figure 13 the dispatching scheme of the processing task is given. The first code in each square indicating the active filed of subaperture is the number of DSP module for processing this aperture and the second code is the number of subaperture which is processed by this DSP. As much as 9 to 10 subapertures are processed by each module in one frame period. By using a 16 Mbytes expanded RAM, as much as 200,000 frames can be stored in one measurement period. The atmospheric turbulence can be sampled by 37 subapertures with frame rate 830 Hz for about 260 seconds continuously.

From these data the detailed specifications of optical turbulence can be deduced. From each frame the wavefront phase profile can be reconstructed, the structure function D and coherence length r_0 can be obtained. By large number of frames the statistic parameters, such as power spectrum of arrival angle fluctuation both in subapertures and in the whole aperture and the probability density function of r_0, can be obtained. Figure 15 is the power spectrum of arrival angle fluctuation measured in a 500m horizontal path. Figure 16 shows the probability density function of r_0. The circles are experimental results and curve is fitted by a theoretical model.
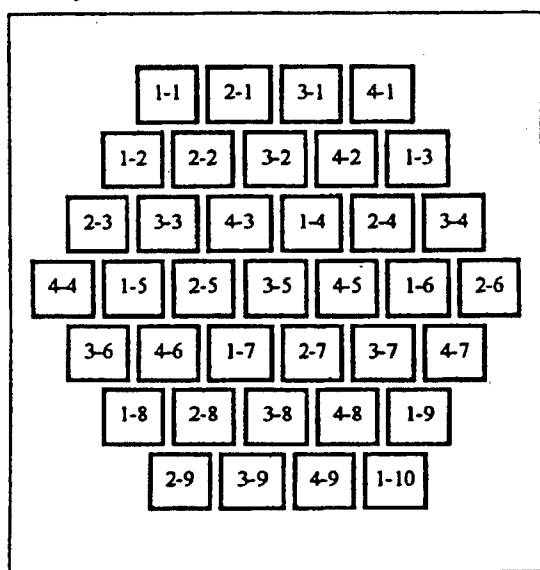
Figure 13. Active field of subaperture and processing task dispatching.
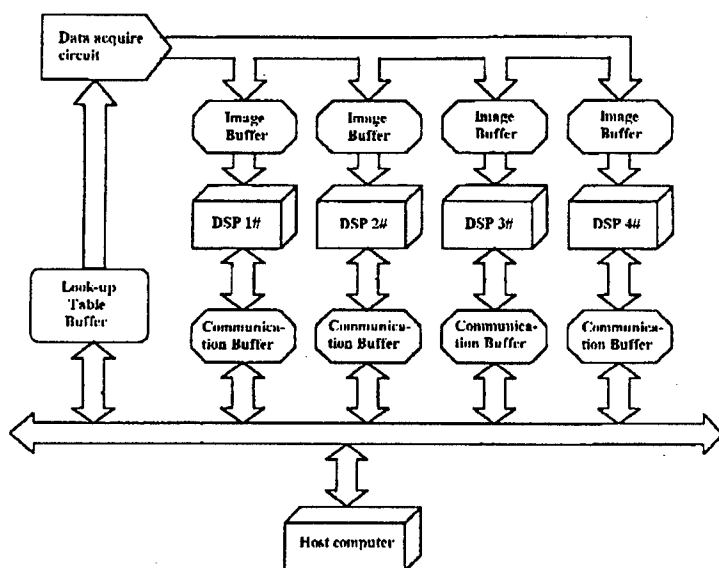
Figure 14. Diagram of the real-time processing system.
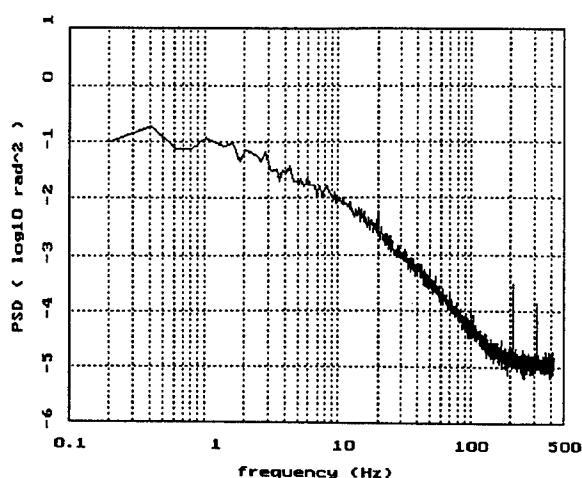
Figure 15. Power spectrum of arrival angle fluctuation.
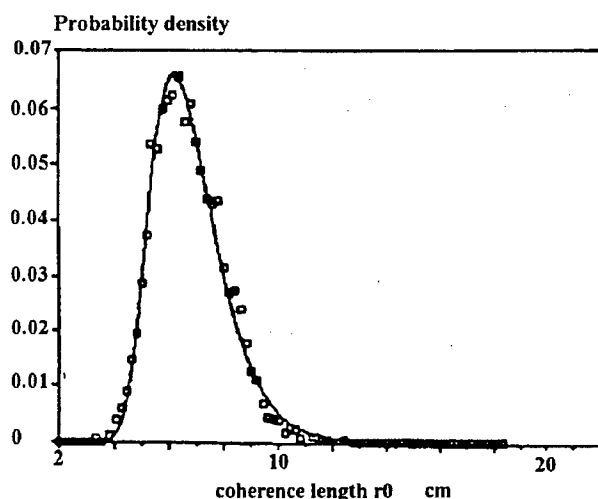
Figure 16. Probability density function of r_0.

6. Conclusion

S-H sensors are widely used in Adaptive Optical systems as wavefront sensors. The capability of measuring both intensity distribution and phase gradients of optical field with high frame rate makes it a powerful tool in many other applications. In this paper, only a part of applications is reported. We believe that S-H wavefront sensor will have more application fields in the future.

7. References

1. R.K.Tyson, "PRINCIPLES OF ADAPTIVE OPTICS", Academic Press, Inc. 1991.
2. Wenhan Jiang, Huagui Li,"Hartmann-Shack wavefront sensing and wavefront control algorithm", *Adaptive Optics and Optical Structures,SPIE* Volum 1271.
3. Huagui Li, Wenhan Jiang, "Application of H-S Wavefront Sensor for Quality Diagnosis of Optical System and Light Beam", *ICO-16 Satellite Conference on Active and Adaptive Optics*, August 2-5, 1993, Garching/Munich, Germany.
4. Lingtao Jiang, et. "High resolution measurement for optical effect of atmosphere turbulence", *SPIE* Vol. 2828.
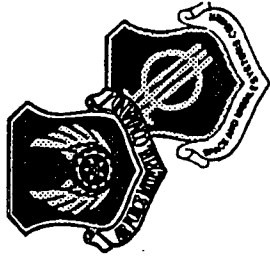
Optical Heterodyne Array Wavefront Sensing and Imaging

BY

DAVID VOELZ AND LENORE MCMACKIN

USAF Phillips Laboratory
Kirtland AFB, NM

MATT FETROW

Applied Technology Associates
Albuquerque, NM

International Workshop - Adaptive Optics for Industry and Medicine
June 9-13, 1997, Shatura, Russia

PURPOSE OF PRESENTATION

Propose a coherent, heterodyne array imaging approach for use as:

- Diagnostic tool for observing / measuring adaptive elements
  - where both speed and precision is required

- Tool for measuring line-of-sight changes in objects that are deforming

OUTLINE

- Approach
- Multi-frame processing concept
- Comparison with Shack-Hartmann
- Laboratory system description
- Laboratory image results
- Recent practical innovations

HETERODYNE ARRAY IMAGING
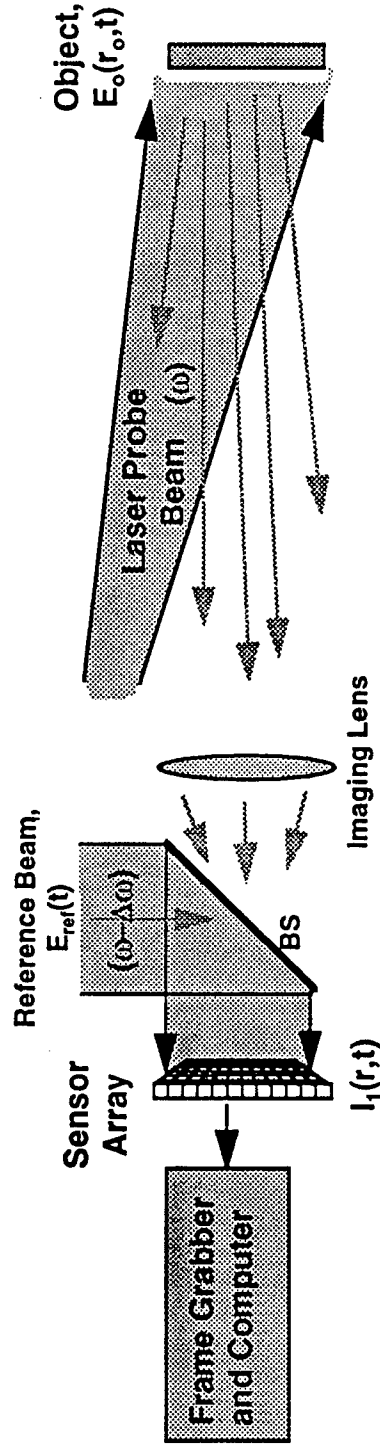
The lens forms an image of the optical field at the object

$E_1(r,t) = A_1(r)\exp\{j\phi_1(r)\}\exp\{j\omega t\}$ $\propto E_o(r_o,t)$;   Intensity image $= A_1(r)^2$

This field is mixed with a reference beam given by $E_{ref}(t) = A_{ref}\exp\{j(\omega-\Delta\omega)t\}$

$I_1(r,t) = |E_1(r,t) + E_{ref}(t)|^2 = A_1(r)^2 + A_{ref}^2 + 2 A_1(r)A_{ref}\cos\{\Delta\omega t+\phi_1(r)\}$

This signal is sampled in time at each pixel - the signal is examined at the beat frequency $\Delta\omega$, to extract the amplitude and phase components. A complex exposure is formed in the computer

$\hat{E}_1(r) = 2 A_1(r)A_{ref}\exp\{j\phi_1(r)\}$

DOUBLE-EXPOSURE HETERODYNE IMAGING:
LINE-OF-SIGHT DEPTH CHANGE
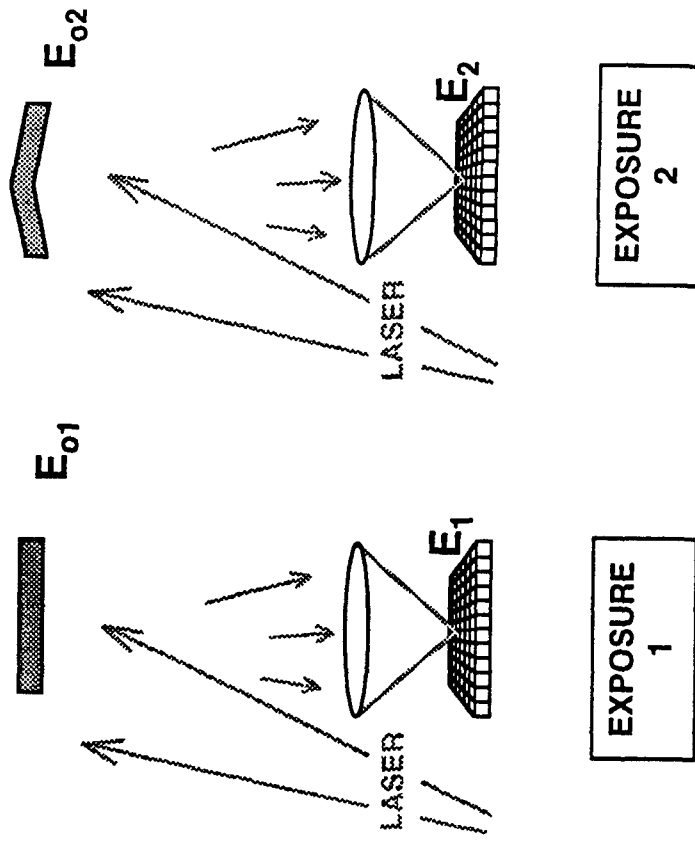
$E_1(x_1,y_1) \propto E_{o1}(x_o,y_o)$

$E_2(x_1,y_1) \propto E_{o1}(x_o,y_o)\exp\{j\Delta\phi_{o1}(x_o,y_o)\}$

Digital addition of object complex fields:

$|E_1 + E_2|^2 = C[1+\cos\{\Delta\phi_{o1}(x_o,y_o)\}]$

Digital phase-difference calculation:

$\arg\{E_2\bullet E_1{}^*\} = \Delta\phi_{o1}(x_o,y_o)$

WHY HETERODYNE ?
(vs. SHACK-HARTMANN)

- High resolution - lots of pixels (standard video resolution is easily attained)

- Wavefront recovery is quick: simple demodulation step, no reconstructor required

- No cross-spatial calculations required - good candidate for integrated parallel architecture (put it on a chip)

Disadvantages:

- Modulo 2π ambiguities - limits effective range of depth measurement

- Coherent light issues - fringing, speckle noise

HETERODYNE IMAGING LABORATORY SCHEMATIC

OBJECT

IMAGING LENS

PROBE BEAM

BS

RS-170 video

CAMERA

COMPUTER + FRAME GRABBER

Pentium and Matrox board

LASER

Argon 514 nm

BS

AOM

AOM

40 MHz

40 MHz - 8 Hz

REFERENCE BEAM LEG
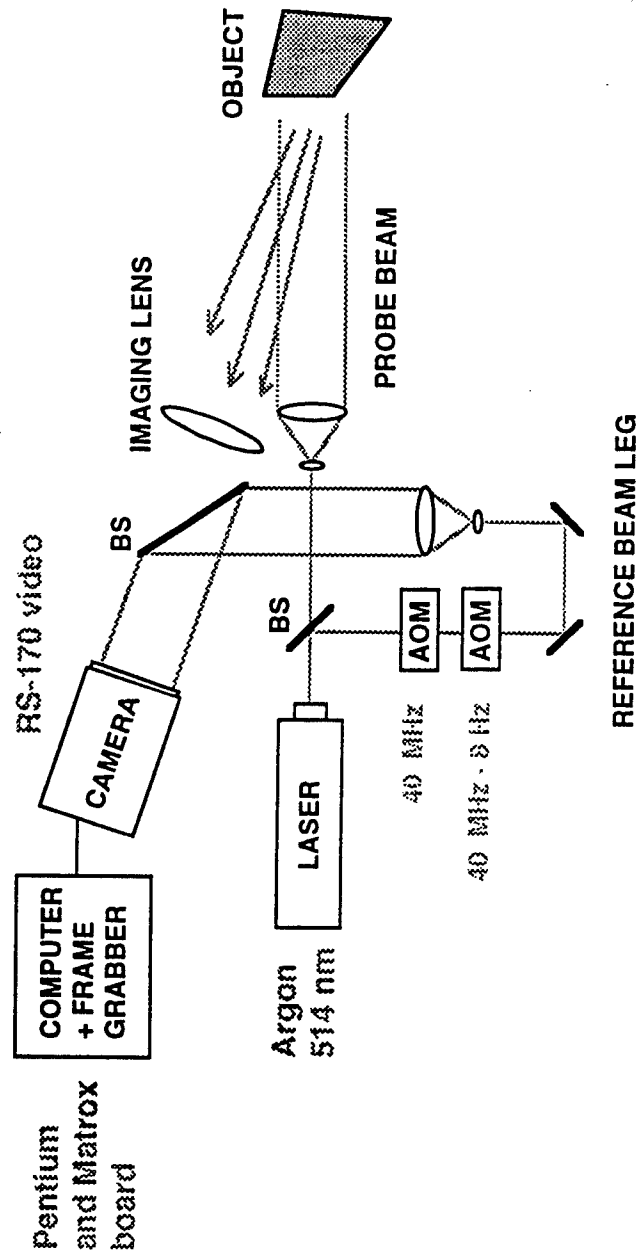
CAMERA RESOLUTION: 640 x 480 pixels
CAMERA FRAME RATE: 30 Hz
BEAT FREQUENCY: 8 Hz
FRAMES DEMODULATED: 16

OPTICAL LAYOUT
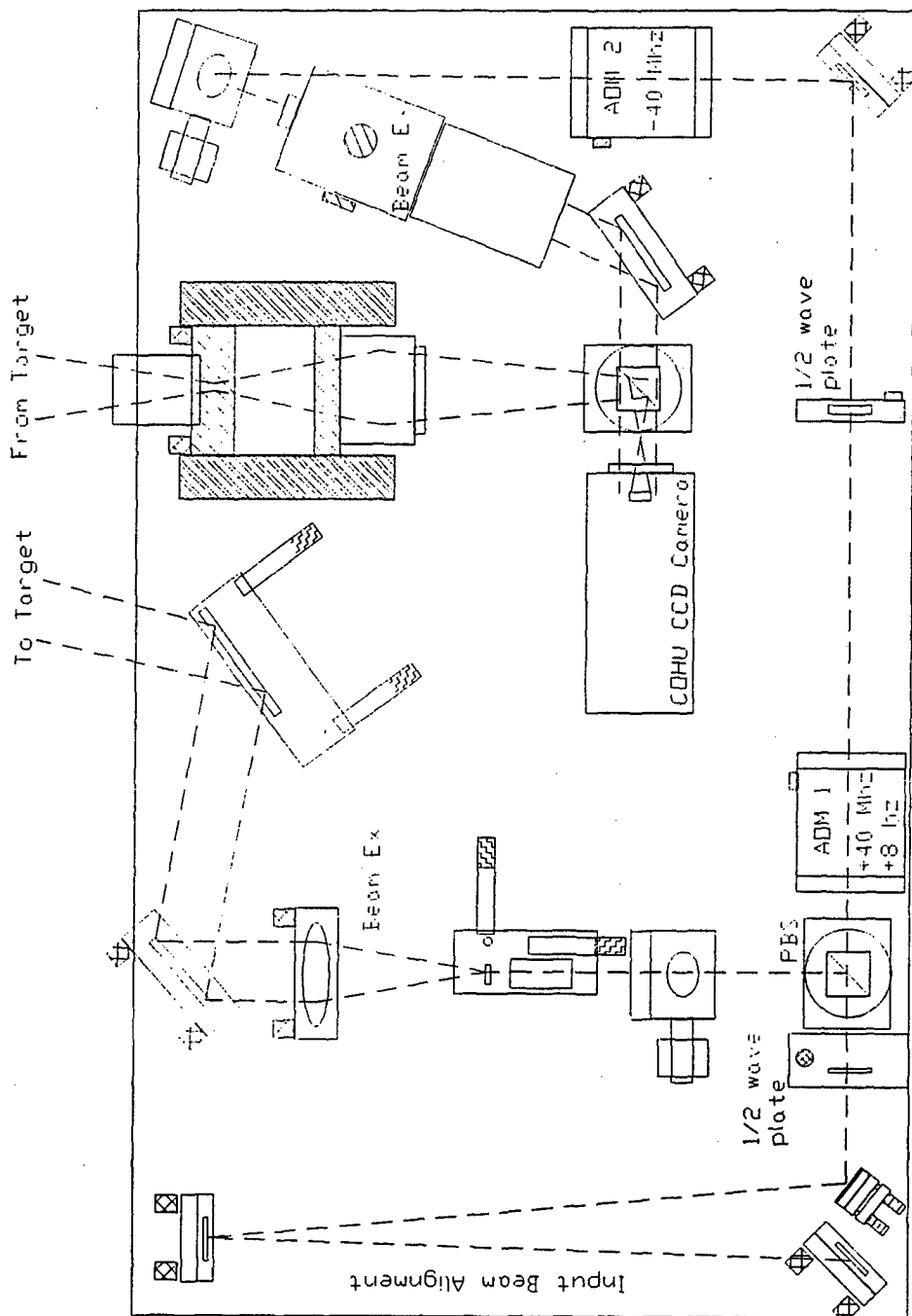
DOUBLE PULSE HETERODYNE

AIR CAN COOLS WHEN USED
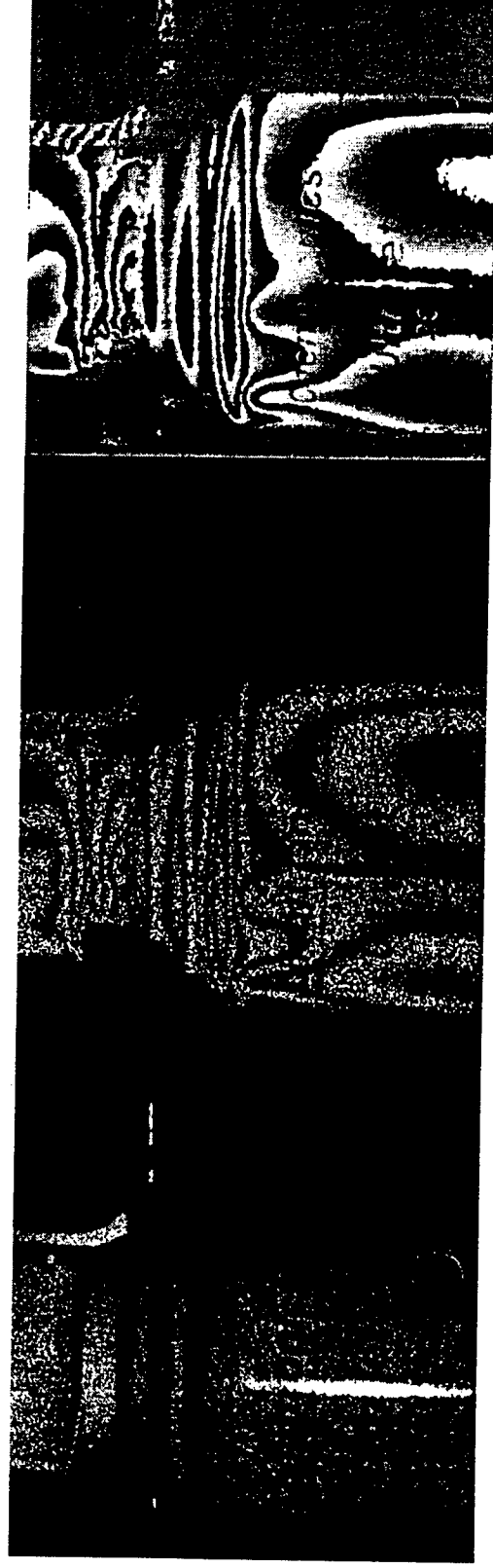
DC Image

Sum of Two Heterodyne
shots, ΔT=45 s

Phase Difference of
Two Heterodyne, ΔT=45 s

DOUBLE PULSE HETERODYNE

LEFT BAR IS BEING HEATED AT MIDDLE HOLE

BOTH ALUMINUM BARS TIED TO SAME METAL PLATE
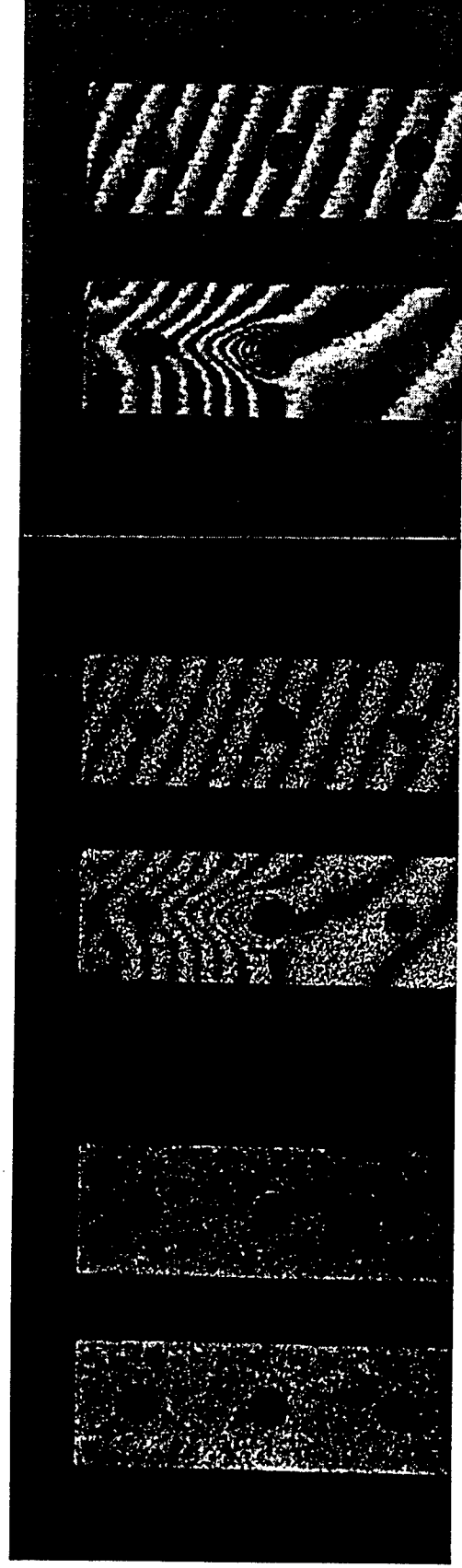
DC Image

Sum of Two Heterodyne shots, ΔT=45 s

Computer Display Updates at 2 Hz.

Phase Difference of Two Heterodyne, ΔT=45 s

MEM MIRROR MEASUREMENT

MEM W/ SIN WAVE VOLTAGE AT 1 HZ
FRAMES RECONSTRUCTED AT 7.5 (30/4) HZ

MICROELECTROMECHANICAL
MIRROR HAS A CONTINUOUS
MEMBRANE AND 10 CONCENTRIC
ACTUATORS

CENTER 3 ACTUATORS NOT
OPERATIONAL
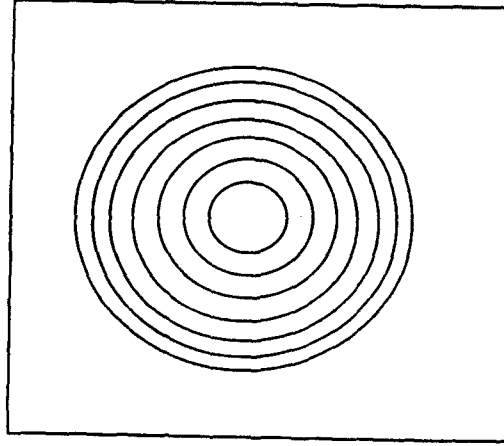
MEM MIRROR MEASUREMENT
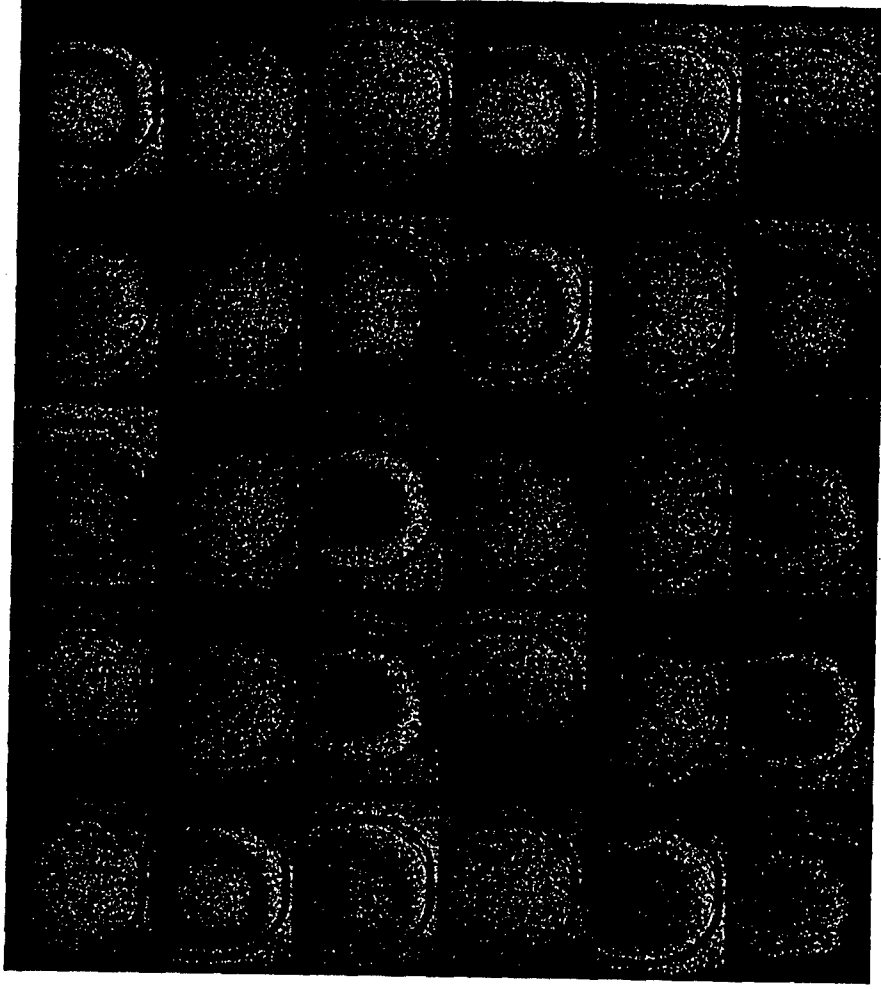
MEM W/ SIN WAVE VOLTAGE AT 1 HZ

FRAMES RECONSTRUCTED AT 7.5 (30/4) HZ

Frame 1

Frame 6

max-min y axis is 1 micron

white to black is 1.63 microns of change

RECENT INNOVATIONS

- Affordable laser sources with useful power and adequate coherence length

- Very stable RF sources and AOMs for producing small frequency shifts

- Affordable high frame rate CCD cameras

- Increased data capture rates and available memory for off-the-shelf computers and frame grabbers

- Concept introduced: digital comparison of complex frames

- Concept introduced: wavelength diversity with digital complex frames to extend dynamic range of depth measurement (digital super heterodyne)

AOA

Adaptive Optics
Associates

Shack-Hartmann wavefront sensing for optical metrology, and its application in real-time corrections of horizontal line of sight turbulence over near ground paths

B. Martin Levine, Robert Zielinski, Theresa Bruno, Franklin Landers, Elizabeth Martinsen, Allan Wirth, Andrew Jankevics, and Manuel Toledo-Quinones

Adaptive Optics Associates
54 CambridgePark Drive
Cambridge, MA 02140
(617)864-0201 (voice)
(617)864-1348 (fax)
marty@aoainc.com

Presented at the International Workshop on Adaptive Optics for Industry and Medicine, Shatura, Russia, 10 June 1997

06-05-1997

Shack-Hartmann wavefront sensing for optical metrology

Automated Hartmann Sensor

AΦA — ☀
Adaptive Optics Associates

COLLIMATING LENS

HARTMANN LENS ARRAY

FOCAL SPOT

SPOT CENTROID MEASURES TILT IN SUBAP.

INCOMING WAVEFRONT

PUPIL IMAGE PLANE

• Hartmann Sensing with Lens Array

06-05-1997

Hartmann Sensor with Relay

AΦA — ☀
Adaptive Optics Associates

RELAY LENS

CCD

COLLIMATING LENS

HARTMANN LENS ARRAY

FOCAL SPOT

PUPIL IMAGE PLANE

HARTMANN SPOT IMAGES

Addition of Relay Lens between MLM and CCD
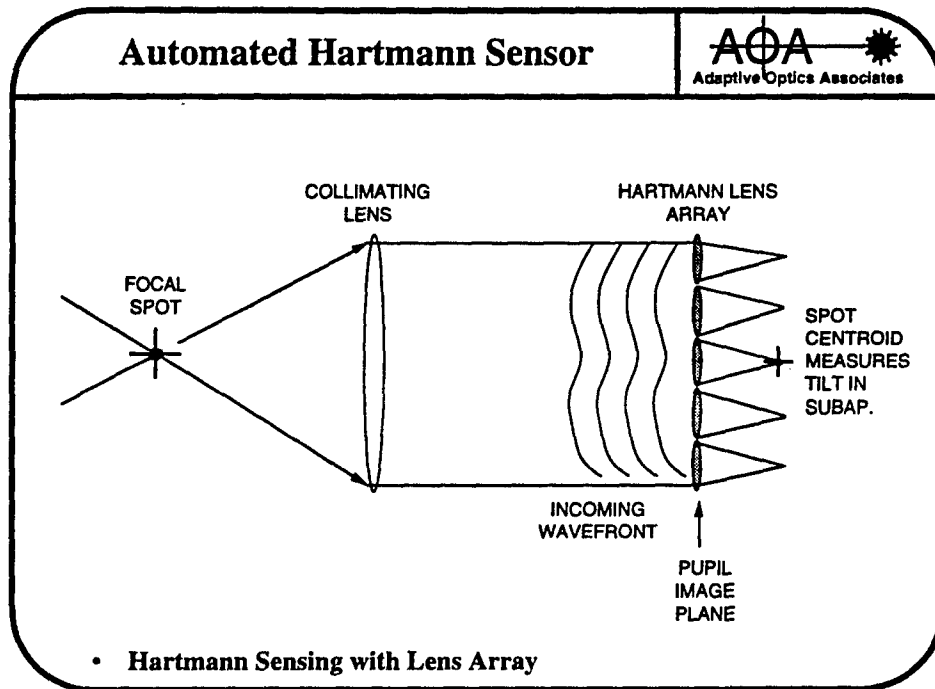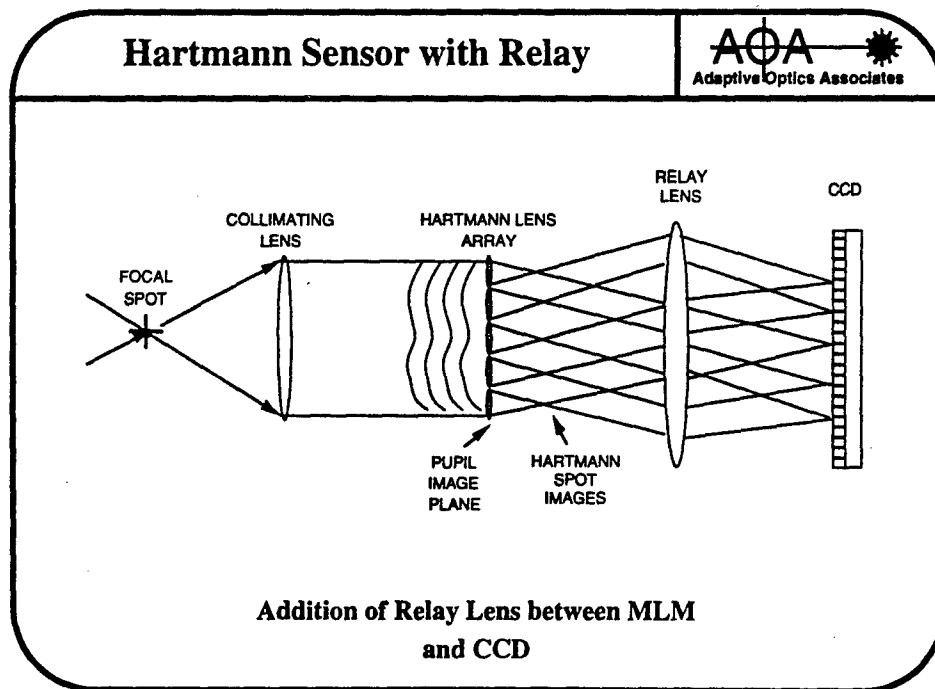
06-05-1997

Shack-Hartmann wavefront sensing for optical metrology

Pupil Imaging with Relay

AΦA — Adaptive Optics Associates
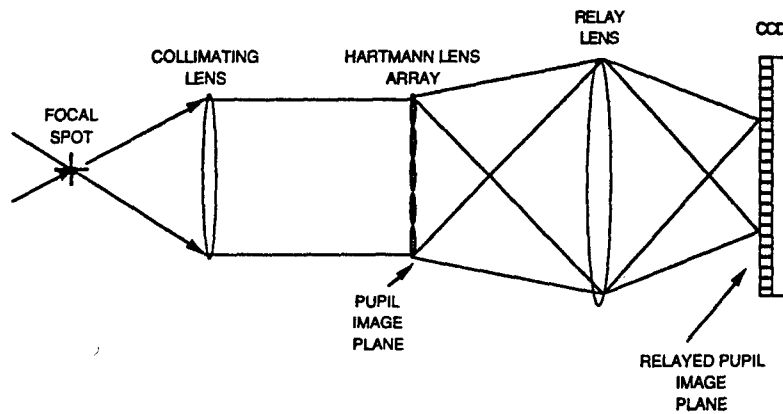
Relay Lens / CCD moved to Pupil Image Plane

06-05-1997

MLM grid in pupil

AΦA — Adaptive Optics Associates
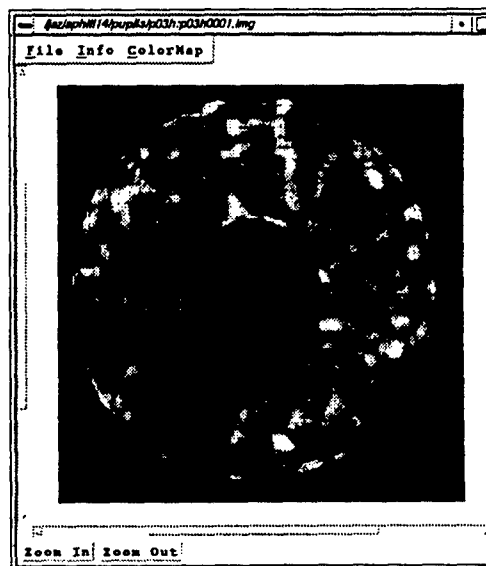
06-05-1997

Shack-Hartmann wavefront sensing for optical metrology

Spot Following

Lens array

"Close" Spots are Matched, then tracked back to Pupil

Best Focus -1mm

Best Spot Focus
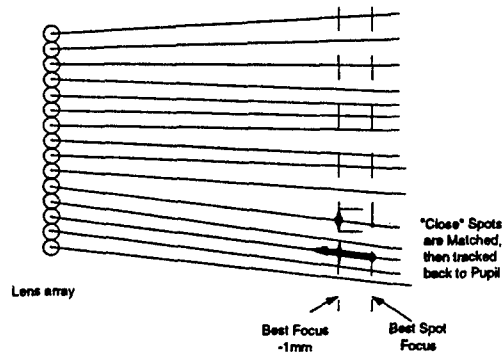
- Use of two spot image locations to match
- spots to pupil subapertures

06-05-1997

Applications of S-H wavefront sensing

- white light illumination
  - MEMS mirrors
  - rear view mirrors
  - (atmospheric turbulence)
- laser illumination
  - aspheric optics
  - laser gain media
  - atmospheric turbulence (laser comm)

06-05-1997

Page 3

Shack-Hartmann wavefront sensing for optical metrology

Laser comm field trials

AΦA ☀
Adaptive Optics Associates

- To determine requirements for an adaptive optics system to be used in laser communication over a horizontal path.
  - determine requirements through field measurements
- Demonstrate laser beam compensation in a communications experiment
  - tip/tilt
  - tip/tilt + higher order

06-05-1997

Wavefront sensor layout

AΦA ☀
Adaptive Optics Associates

06-05-1997

Page 4
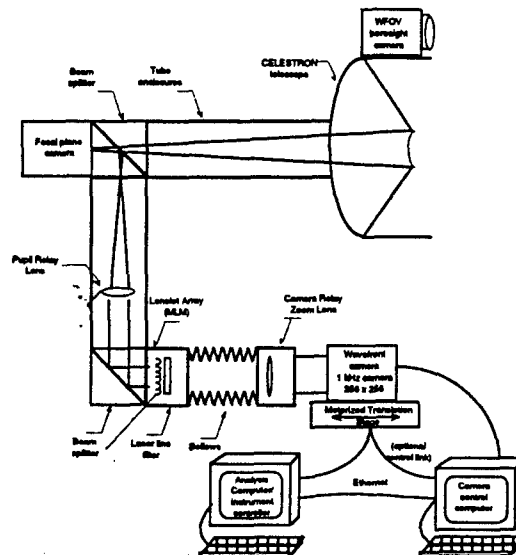
Shack-Hartmann wavefront sensing for optical metrology

Laser test range

A⊕A
Adaptive Optics Associates

06-05-1997

Test data-- Hartmann spot images

A⊕A
Adaptive Optics Associates

- **Data rates:**
  - 1KHz frame rate
  - 1024/2048 contiguous images
- **Intensity statistics**
- **Wavefront reconstructions**
  - Adaptive optics requirements

06-05-1997

Shack-Hartmann wavefront sensing for optical metrology

Data reduction

AOA
Adaptive Optics Associates

Hartmann spot image reduction

Spot images

| Wavefront reconstructions to optical path differences (opd) | Zernike polynomial decomposition to opd's | | Subaperture intensity |

Opd histogram mean, variance (Data screening)

Power spectral density (psd) of opd fluctuations by temporal frequency and Zernike mode

Intensity histogram mean, variance (Data screening)

Aperture averaging histogram, variance Reduction of receiver intensity fluctuations

Opd variance by temporal frequency and Zernike mode

Strehl ratio Prediction of transmitter quality by bandwith and mode of correction

06-05-1997

Intensity fading data reduction

AOA
Adaptive Optics Associates

- **Spot image with boxes**
  - Sum of intensities within subaperture
  - (WAVELAB kernel extension)
- **Average of spot images used as reference for reconstruction**

File Info ColorMap

Zoom In Zoom Out

06-05-1997

Shack-Hartmann wavefront sensing for optical metrology

Intensity histograms
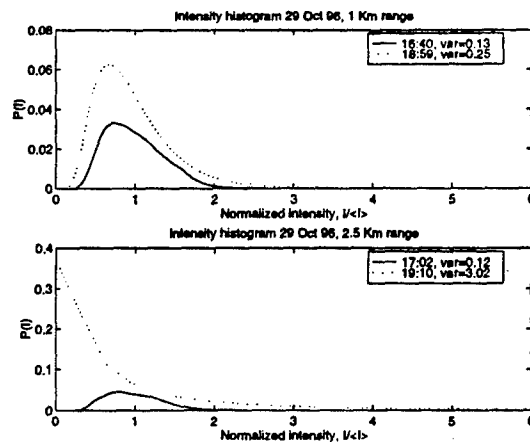
06-05-1997

OPD data reduction

- Spot images thresholded for deeply faded subapertures
  - threshold based on dark frame value
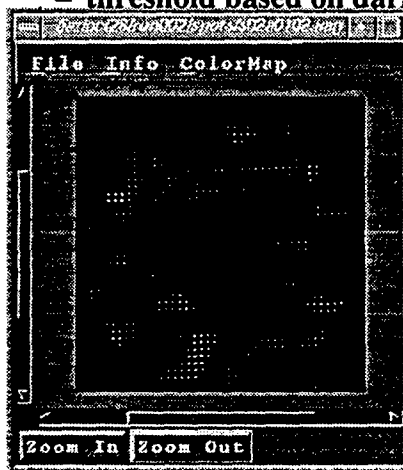
06-05-1997

Shack-Hartmann wavefront sensing for optical metrology

OPD histograms

A⊕A
Adaptive Optics Associates

OPD histogram 29 Oct 96, 1 Km range

16:40, rms = 0.19 um
18:59, rms = 0.28 um

OPD histogram 29 Oct 96, 2.5 Km range

17:02, rms = 0.16
19:10, rms = 0.73 um

06-05-1997

OPD rms summary

A⊕A
Adaptive Optics Associates

* **Over day and temporal hour of day (example)**
  - 0 hrs = sunrise; 6 hrs = noon; 12 hrs = sunset

OPD vs time for 1km range

13-Aug-96
14-Aug-96
29-Oct-96
29-Oct-96
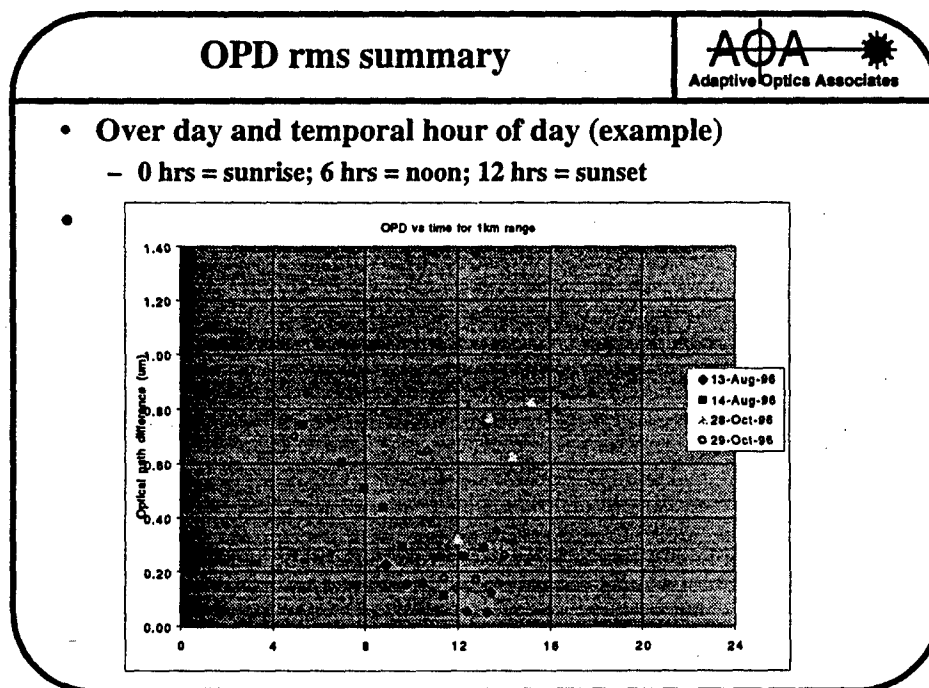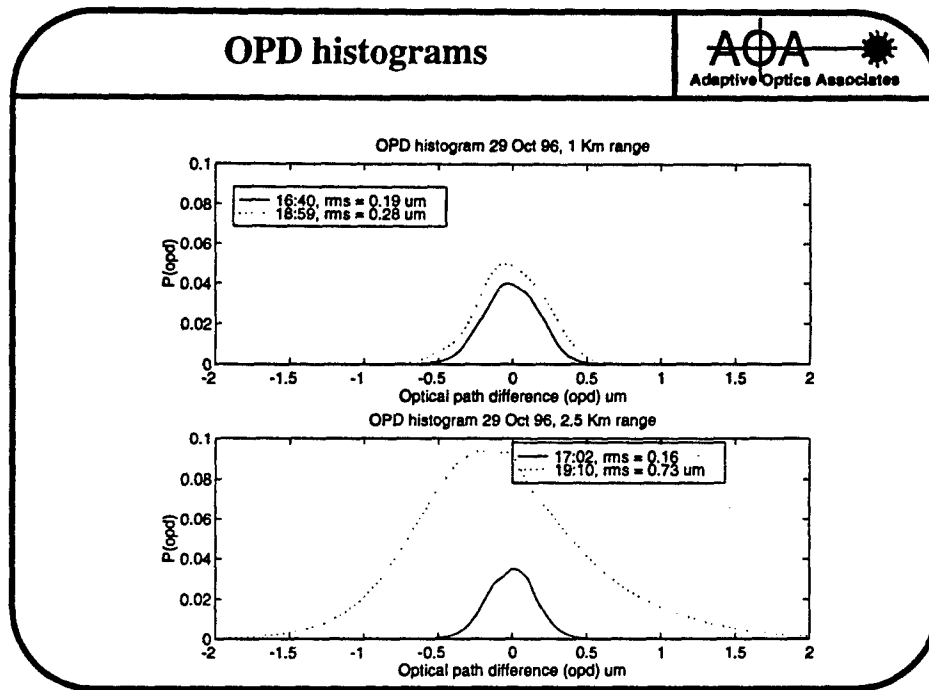
06-05-1997

Shack-Hartmann wavefront sensing for optical metrology

PSD comparison

- Ref. Bester et. al., Astrophysical J. v392:357-374, 1992
- Non Kolmogorov spectrum for near ground turbulence
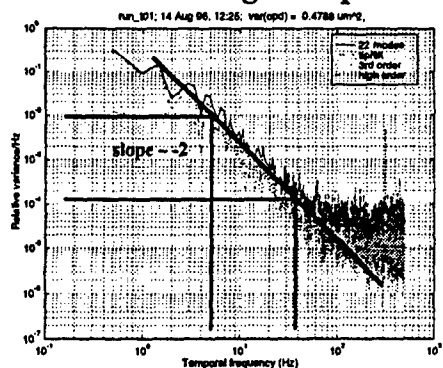
Kolmogorov slope ~ -5/3

06-05-1997

PSD comparison
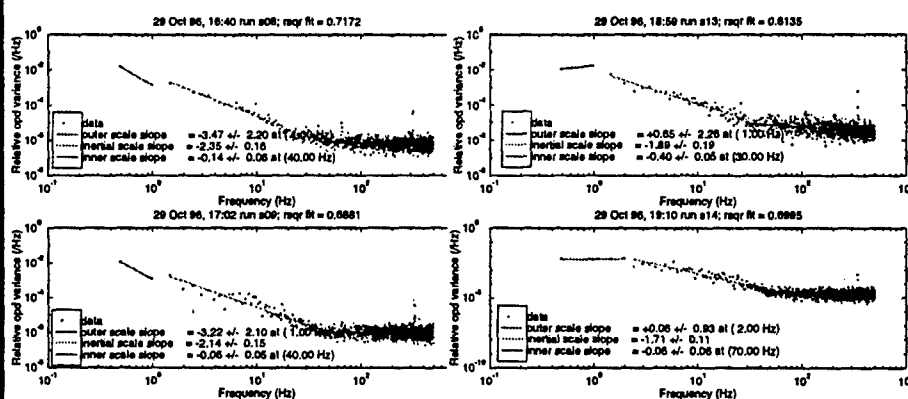
06-05-1997

Page 9

Shack-Hartmann wavefront sensing for optical metrology

PSD analysis

Power spectral density   **Integrated psd**

$$\sigma^2_{opd}(f) = \int^f PSD(u)du$$

06-05-1997

Temporal variance and Strehl ratio

$$\text{Strehl}(f) = \exp\{-[\sigma_\phi^2 - \sigma_\phi^2(f)]\}$$

$$\sigma_\phi^2 = (2\pi/\lambda)^2\,\sigma^2_{opd}$$
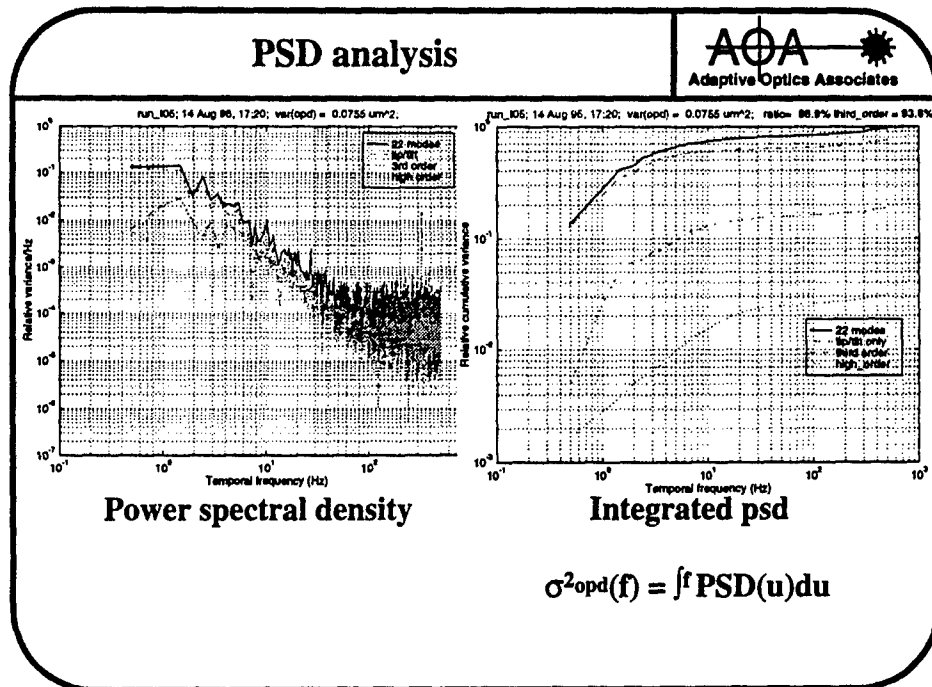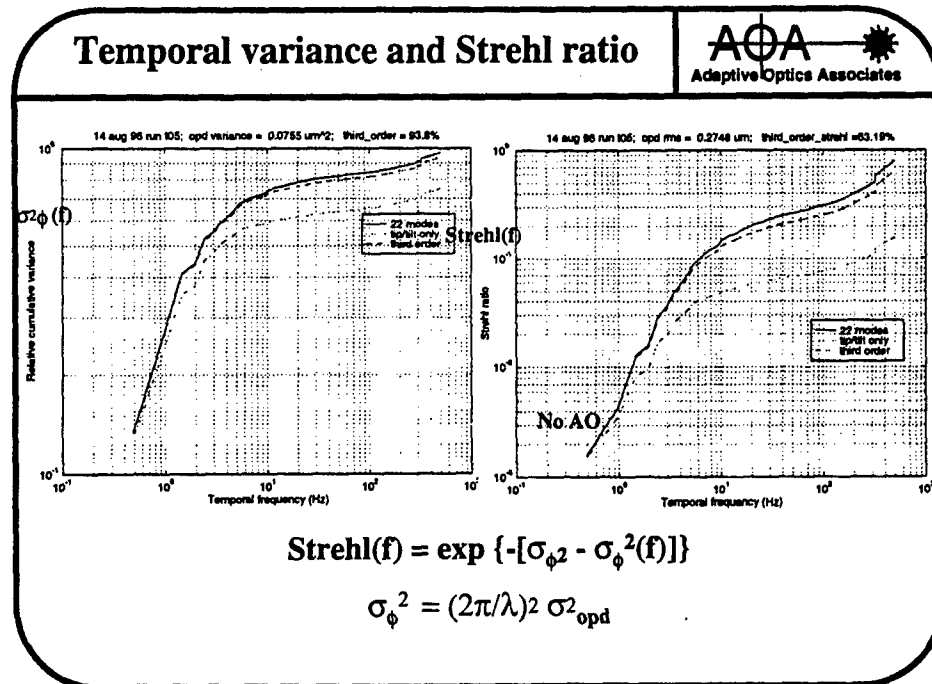
06-05-1997

Shack-Hartmann wavefront sensing for optical metrology

Strehl ratio comparisons

AΦA
Adaptive Optics Associates
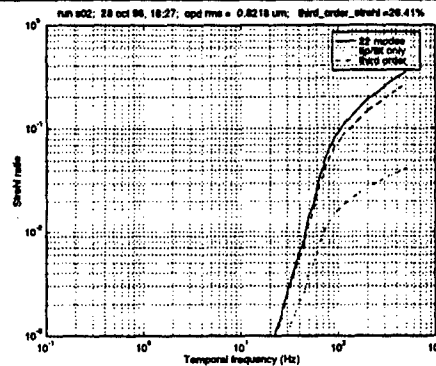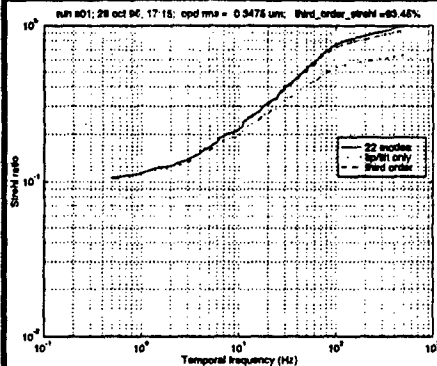
- $\lambda = 1.3 \ \mu m$
- Range = 1 Km
- no AO needed (s01), full AO needed (s02)

06-05-1997

Temporal bandwidths for 1 Km range

AΦA
Adaptive Optics Associates

- % of time Strehl ratio achieved at bw < 100Hz
- 22 Zernike polynomials

Wavelength/Strehl ratio	0.1	0.2	0.3	0.4	0.5
0.6328μm	75%	70%	65%	50%	20%
1.3μm	90%	90%	85%	85%	80%

06-05-1997

Shack-Hartmann wavefront sensing for optical metrology

AO system recommendations

- Adaptive optics will enhance transmission in 85% of cases at 1 Km range.
- AO will enable transmission at 1.8 and 2.25 Km ranges.

06-05-1997

Real time compensation schematic

AOA
Adaptive Optics Associates

Acquisition CCD

Celestron

Tip Tilt Mirror

Pupil Imager

from Xmtr

WFS

Reduction Telescope

DM

06-05-1997

Shack-Hartmann wavefront sensing for optical metrology

AO PC architecture
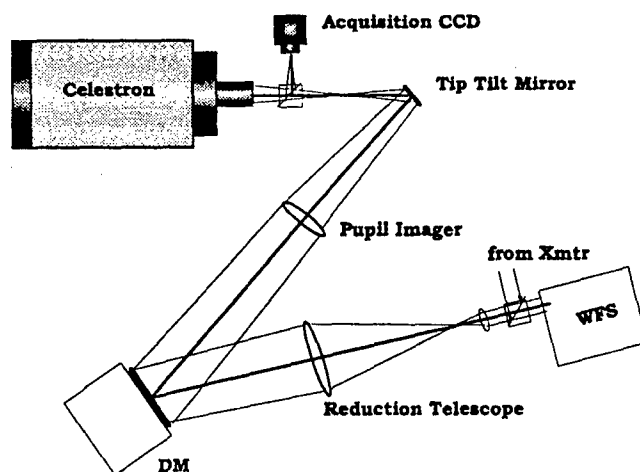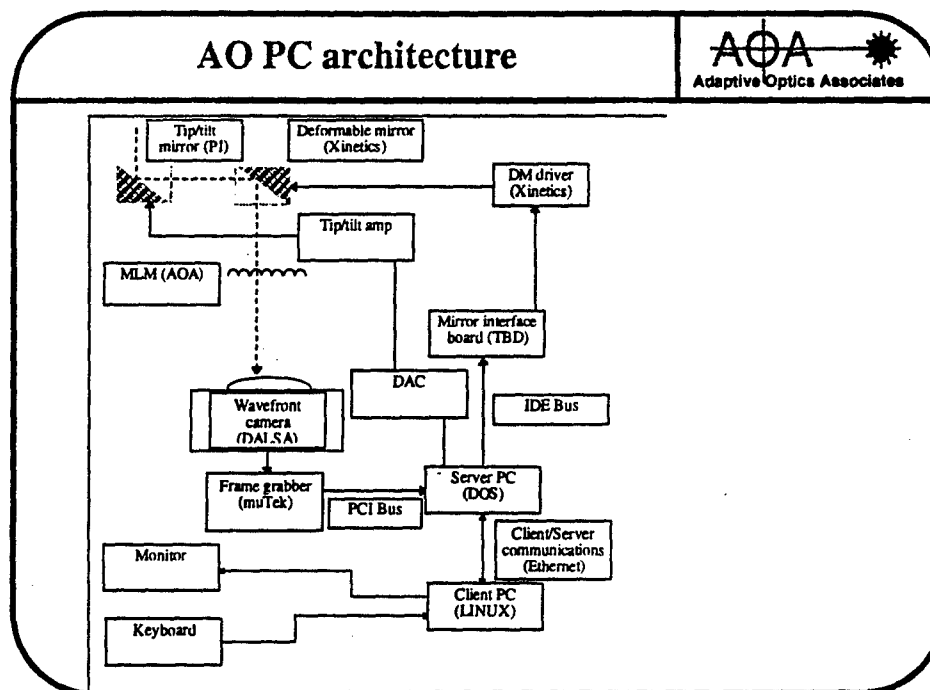
06-05-1997

WCP AO processing benchmarks

Computer	Operating system	Speed (Hz) (1,000 frames)	
		37 actuators	100 actuators
200 Mhz Pentium	Win 95 DOS/32 bit C	2500	
180 Mhz Pentium Pro	DOS 32 bit C	3750	952
180 Mhz Pentium Pro	Linux/gcc	1562*	303*
180 Mhz Pentium Pro	DOS/16 bit C	303*	
SGI INDIGO'	IRIX	1010*	225*
SPARC IPX	SunOS	183*	40*

* does not include data unpacking

• Computational speed <u>not</u> a bottleneck

06-05-1997

Page 13

Shack-Hartmann wavefront sensing for optical metrology

Hardware benchmark speed

- Same software but with interrupt lines monitored
- 200 MHz Pentium Pro/DOS/32bit C

Total period

Frame grab/transfer

Computation
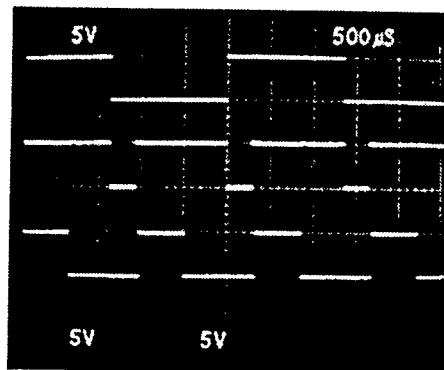
06-05-1997

Summary

- Shack-Hartmann wavefront sensing can be automated for metrology
- Partial atmospheric corrections can enhance laser beam propagation over horizontal paths
- PC AO implementation feasible

06-05-1997

ADAPTIVE WAVEFRONT SENSOR

Valeri A.Tartakovski, Vladimir P.Lukin

Institute of Atmospheric Optics of Russian Academy of Sciences ♦Tomsk ♦ 634055 ♦ Russia
Fax: (3822) 259086 ♦ E-mail: tv@cnod•iao•tomsk•ru

The objective of this paper is to direct your attention on research of wavefront measurement for adaptive optics, taken under strong scintillation conditions. Both the fundamental and technological problems, concerning this priority area on optics, must be investigated. We suggest to solve the phase measurement problems under strong intensity fluctuations, in which case there is no continuity of the wavefront, by means of selective and consecutive processing of the speckles. The expected practical result of this solving is a gain in efficiency in optical systems for imaging, energy transfer, atmospheric communications, high power lasers, and astronomy.

Lomonosov and Descartes had known about the first principles of the wavefront measurements. Wavefront sensing concerns testing any kind of optical system, from telescopes to microscopes, to industrial imaging and lasers. Popular sensors are the Shack-Hartmann and curvature sensors. Other sensors employ lateral shearing or point diffraction interferometry.

All these sensors may not be complicated but they all assume *a priori* the continuity of the measured wavefront. This may not be true when dealing with imaging through strong turbulence. This is because the best place to measure a wavefront is at a plane which is Fourier conjugate (or nearly so) to the focal plane. In this measurement plane, intensity is assumed to be rather constant. When the turbulence level rises, this assumption is broken: the intensity changes (sometimes at a very fast rate) not only in the focal domain but also in its Fourier conjugate, where the wavefront is measured. These intensity variations, also called scintillations, develop and phase dislocations or wavefront branch cuts spring up.

Under these conditions the Hartmann sensor fails because the fixed position, the small number of its subapertures, and the locations of the foci are not useful any more to tell the wavefront. Most of the information lies in the high intensity scintillations which might be missed by the Hartmann subapertures. The curvature sensor fails here as it assumes a wave of constant intensity, a condition violated under scintillations. The same limitation applies to other wavefront sensors.

The wavefront dislocations disturb the processing of wavefront sensors, since the processing is based on the assumed continuity of the phase function. Such disturbances can be even due to only one dislocation. In addition, wavefront dislocations cause disintegration of the wavefront into separate beams which might be uncorrelated. Moreover, the amount of energy in the neighbourhood of dislocations is limited. As a result the phase at these points is not well characterised.

Hence measurement of high-energy sections of the wavefront, and subsequent separate fitting of these sections to the adaptive mirror should be the right way for measuring and controlling the wavefront in such adaptive systems.

To this end, it is necessary to formulate properly the unexplained concept of a wavefront under strong scintillation conditions. A proper mathematical description, adequate to the nature of this problem, has to be provided. Having done that, effective algorithms have to be developed for data processing for this case.

♣ The first stage will be to find in what way to change the spatiotemporal resolution during measurement and according to the light intensity at the input aperture. It should be borne in mind that the areas with high intensity must be measured more precisely and processed with less delay, as compared with the low intensity areas.

♣ The second stage is to find a way to control the size of the single Hartmann-Shack subaperture according to a level of intensity and wavefront fluctuations so as to change the focal spot size and its motion range.

♣ In the third stage, an algorithm will be developed to restore the phase along closed and unclosed lines in the aperture plane, going through areas with high intensity, avoiding areas with very low intensity, and connecting the phase from the separate areas to unique phase function.

♣ In the fourth stage, is to be obtained an method of estimation of restored phase errors.

♣ Finally, new forms of the wavefront regularisation will be developed in order to realise common adaptive optics principles. For example, a wave calculated from an exact phase but without the true amplitude, may be

1

worse, after conjugation, than some other wave which phase is corrected, using the true amplitude information, so that to minimise the functionals:

$$\iint_O \left[a(\vec{r_o})e^{\varphi(\vec{r_o})} - e^{\varphi_m(\vec{r_o})} \right]^2 d\vec{r_o} = \min \qquad \iint_R \left| \iint_O H(\vec{r},\vec{r_o})\left[a(\vec{r_o})e^{\varphi(\vec{r_o})} - e^{\varphi_m(\vec{r_o})} \right] d\vec{r_o} \right|^2 d\vec{r} = \min .$$

The unique tracking measurements of phase

In the proposed wavefront sensor the measurements of many Hartmann's foci displacements are replaced by tracking only one focal spot, obtained from the brightest part of the field. This is a natural step forward as well as a solution of many other problems in which the parallel and sequential processing can be or are exchanged.

Each high-energy section of the wavefront must be measured separately and precisely as possible by means of dense scanning in these areas. If this is possible and there exists a continuous track with sufficiently intensity between these areas, a constant phase shift will be calculated between them. If the patches are not contiguous and the beams are uncorrelated, the shift of these parts of wavefront will be determined by successive approximations. In this case a four-dimensional analytic signal allows to circumvent singular points for connecting parts of the wavefront to create a unique phase function. The unique four–dimensional analytic signal is defined as follows:

$$W(x,y,z,t) \overset{def}{=} U(x,y,z,t) + iV(x,y,z,t), \quad V(x,y,z,t) = \underset{t}{H}U(x,y,z,t) = \underset{z}{H}U(x,y,z,t),$$

$$V[p(x,y,z),t] = \underset{x}{H}U[p(x,y,z),t] = \underset{y}{H}U[p(x,y,z),t], \quad V[x(\tau),y(\tau),z(\tau)] = \underset{r}{H}U[\Phi^{-1}(\alpha_c r)] \Big|_{r=\Phi(\tau)/\alpha_c}$$

Here H is the Hilbert transform operator; $W(x, y, z, t)$ is the object wave and the analytic signal (AS); the AS imaginary part is $V(x, y, z, t)$, it is Hilbert transform of real part $U(x, y, z, t)$ over argument x, t, or z which is a propagation direction; $p(x, y, z)$ is the turned recording plane. τ is the parameter of the curvilinear cross-section in three-dimensional space, on which the wave phase is monotonic. α_c is the spatial carrier frequency on this cross-section. $\Phi(\tau)$ is a function for the compression-extension transformation of the cross-section. Some approximation of arg $W(\tau)$ could be used as this function. Naturally, the function $\Phi(\tau)$ could be known, if $V(\tau)$ had been defined before. From fourth expression follows the existence of the problem solution and the solution itself can be found by the method of successive approximation.

It gives a guarantee that the phase of the four-dimensional wave function, determined by the AS, introduced as a function of the line parameter τ, on the scanning line, is the corresponding cross section of the unique four-dimensional phase function determined by the AS as a function of the time or the propagation direction.

The practical use of these expressions is that they enable one to design the algorithms of phase measurement in various spatiotemporal, one–dimensional and multidimensional cross–sections and provide its coincidence with the unique four-dimensional phase in these cross–sections. It is possible now to measure the two or one-dimensional sections of the four-dimensional phase separately and apart from each other.

This phase exists only as a consequence of narrow bandwidth of the temporal and spatial wave spectra. Determined by analytic signal, the amplitude $|W(\tau)|$ and the phase arg $W(\tau)$ are invariant relative to the replacement of the Hilbert transform argument and consequently are unique.

Description of possible concept of the sensor is as follows.

A deflector shifts laterally the input beam into a single Hartmann subaperture which creates a focal spot. As in any Hartmann case, the focal spot position (abscissa and ordinate) and intensity can be measured by a sensitive quadrant detector or a few pixels inside a sensitive CCD camera. Simultaneously the deflector angular position serves as reference signals (abscissa and ordinate).

The differences between the focal spot co-ordinates and the reference co-ordinates from the deflector are two spatial derivatives of the phase (tip-tilt) as a function of time, as the input beam is scanned over the subaperture. These spatial derivatives are multiplied by the temporal derivatives of the track which are proportional to the temporal derivatives of the reference abscissa and ordinate.

The temporal derivatives of the track are formed in two feedback loops. The loops originate from the focal

2

spot detector (the spot intensity signal), then in each loop there is a temporal integrator, connected with the actuator of the beam deflector. These feedback loops maximise some objective (cost) function and realise the tracking law. The products of two derivatives are added and integrated over time. The result of this integrator is the phase as a function of time. The equation

$$\varphi(t) = \int_0^t \left(\frac{\partial \varphi}{\partial x} \frac{dx}{dt} + \frac{\partial \varphi}{\partial y} \frac{dy}{dt} \right) dt \quad \text{is used to integrate the phase on the trajectory line, which is defined by the}$$

parametric equations $x = x(t)$, $y = y(t)$.

The technical feasibility of the sensor is not limited in principle. There are some limitations in the tracking speed, due to the deflector actuators. However, these limitations are less as time goes by. Deformable mirrors is now available off the shelf and their price keeps dropping. They can reach a few kHz over acceptable areas. Thus, applicability of the sensor is limited by the level of fluctuations in the medium, and by the strength of the reference signal.
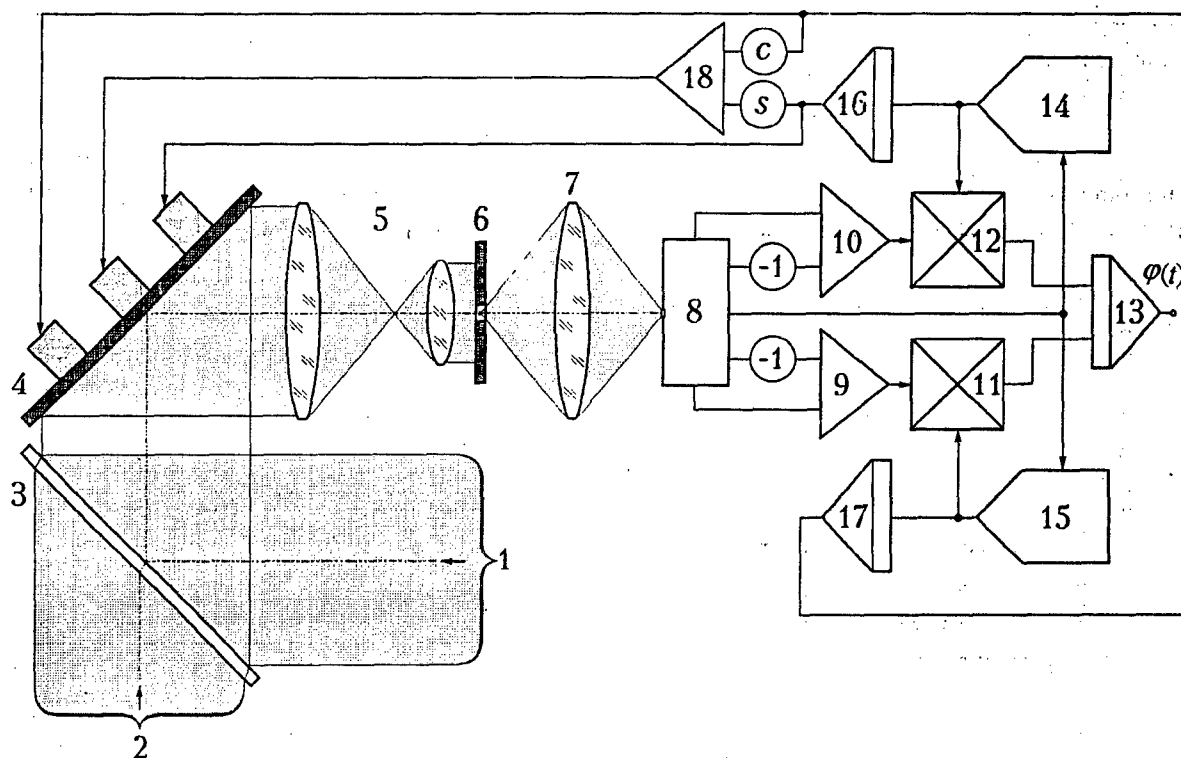
Fig. 1. Scan–Hartmann wavefront sensor

Object beam 1. Reference beam 2. Optical summator 3. Deflector with actuators 4. Scale optical system 5. Only subaperture Hartmann screen 6. Lens-Fourier transformer 7. Coordinator to track total energy and displacement of two focal spots 8. Summator to calculate the object spot relative displacement 9, 10. Multiplicator to form the phase derivative by tracking parameter 11, 12. Integrator to form the phase as a function of tracking parameter 13. Generator of derivative of trajectory by tracking parameter 14, 15. Integrator of trajectory to form the first and second actuator control 16, 17. Summator for control forming of the third deflector actuator 18.

A posteriori estimation of the restored phase error

The most interesting property of the Scan–Hartmann wavefront sensor operation is a possibility to estimate the restored phase error a posteriori using differing and orthogonal scanning in the same areas. It is possible to use for this goal the double orthogonal evolvent Fig.3. It is possible to estimate the restored phase error without using the statistical samples, when only one two-dimensional sample is available. It is reached using some orthogonal scanning directions.

Let us consider the following phase functions: an original phase $\varphi_0(i, j)$, phase restored from x-cross-section of wave $\varphi_x(i, j)$, phase restored from y-cross-section of wave $\varphi_y(i, j)$, estimate of the original phase

$\varphi_e(i,j)=[\varphi_x(i,j) + \varphi_y(i,j)] / 2$, and the following RMS values:

$$\varepsilon^2_{xy} = \frac{\sum\limits_{i,j \in G}[\varphi_x(i,j) - \varphi_y(i,j)]^2}{2\sum\limits_{i,j \in G}\varphi^2_e(i,j)}, \quad \varepsilon^2_{oe} = \frac{\sum\limits_{i,j \in G}[\varphi_o(i,j) - \varphi_e(i,j)]^2}{\sum\limits_{i,j \in G}\varphi^2_o(i,j)},$$

and peak-to-valley values as well:

$$p_{oe} = \max|\varphi_o(i,j) - \varphi_e(i,j)|, \quad p_{xy} = \max|\varphi_x(i,j) - \varphi_y(i,j)|.$$

Here G is the domain of the wave definition, N is the number of the readings, x and y-cross-sections are orthogonal each another, for example, in a simple case they may be parallel to the co-ordinate axes.

A functional dependence is discovered between the real errors of restored phase ε_{oe}, p_{oe} and the estimates of restored phase errors ε_{xy}, p_{xy}. On Fig.2 is shown this connection between the calculated and unknown in an experiment real error. They fitted well by the first order regression lines: $\varepsilon_{oe} = -0.003(7) + 1.14(3)\varepsilon_{xy}$, $p_{oe} = 0.01(1) + 0.66(6)p_{xy}$.

The rms deviation to last significant digit is given in brackets here. The correlation coefficient is equal to 0.99 for the normalised rms error, Fig. 2a, and 0.94 for the pv error, Fig.2b. The rms deviations from regression lines are equal to 0.01 and 0.04, respectively.
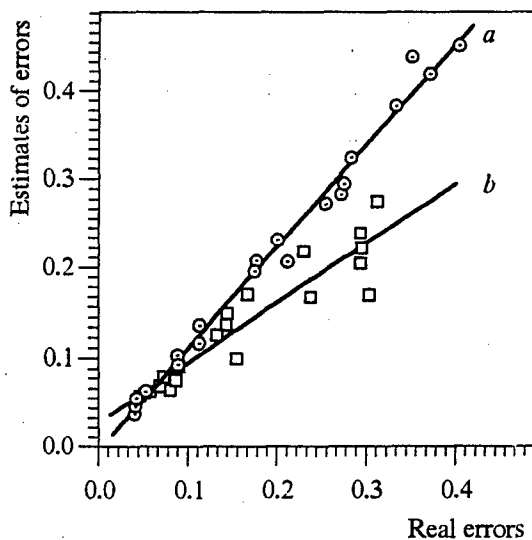
Fig.2.Estimates of the restored phase errors versus the real errors of restored phase: normalised RMS. error (a) $\odot$. Peak-to-Valley error (b) $\square$, parts of λ. Regression lines —
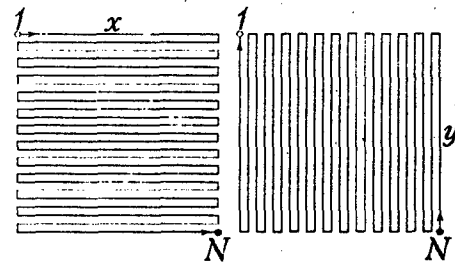
Fig.3. Double orthogonal evolvent

References

1. V.Tartakovski, V.Lukin (1996), Scan-Hartmann wavefront sensor. Adaptive optics. OSA Technical digest series. July 8-12. Vol.13. 241-42 (1996). Opt. Society of America. Maui. Hawaii.

2. E. Vitrichenko, V.Lukin, L.Pushnoi, V. Tartakovski (1990), The book Problems of Optical Testing. 351 pp. Publishing house "Nauka" ("Science"), Novosibirsk.

3. L. Barabina, V. Lukin, V.Tartakovski (1988) Numerical Model of the Hartmann Wavefront Sensor with FFT. Optical wave propagation in the random inhomogenous medium. Tomsk. IOA SO AN SSSR. P. 49–55.

Adaptive Optics for the Human Eye

David R. Williams, Junzhong Liang, Donald T. Miller and Austin Roorda
Center for Visual Science, University of Rochester, Rochester, NY 14627

1. Introduction

The first known attempt to correct the optics of the human eye occurred more than 700 years ago. Spectacles have been used to correct defocus at least as early as the 13th century[1,2] and the eye's astigmatism has been corrected since the 19th century[3]. Based on subjective observations of a point source of light, Helmholtz argued that the eye suffered from a host of aberrations that are not found in conventional, man-made optical systems[3]. There have been a number of methods developed to quantify these aberrations[4-8]. Liang et al[9] developed a technique based on the Hartmann-Shack principle to measure the eye's wave aberration. This method provides a rapid, automated, and objective measure of the wave aberration simultaneously at a large number of sample points across the eye's pupil. By increasing the density of samples taken of the wavefront slope in the pupil and increasing the number of Zernike modes used in reconstruction, Liang and Williams[10] provided a more complete description of the aberrations of the eye. These measurements quantified the irregular aberrations predicted by Helmholtz's and subsequent investigators[3-8]. While any of a number of methods could be used to recover the wave aberration in the eye, we focus here on the Hartmann-Shack method due to its recent success in an adaptive optics system for the eye.

The effect of these aberrations on retinal image quality is illustrated in Fig. 1, which shows the point spread function of the eye at various pupil sizes. These point spread functions were calculated from wave aberration data obtained with a Hartmann-Shack wavefront sensor[10] for a single subject. The effects of defocus and astigmatism, which are correctable with conventional spectacles, have been removed. At pupil diameters of 2-3 mm, which correspond to the diameter of the pupil in very bright viewing conditions, diffraction is the single largest source of retinal image blur. As pupil size increases, aberrations begin to dominate, reducing optical quality. A small pupil roughly 3 mm in diameter generally provides the eye with the best optical performance in the range of spatial frequencies (<20-30 cycles/deg) that are important for normal vision. If the eye's aberrations could be corrected across the fully-dilated 8 mm pupil, resolution could be increased more than 2.7-fold over that obtainable with a 3 mm pupil. This increase in resolution allows single cells in the retina, which have dimensions on the order of a few microns, to be imaged in the living eye.

Spectacles and contact lenses do not correct any aberrations except defocus and astigmatism. There have been various attempts to correct these additional aberrations in the laboratory. For viewing sinusoidal gratings, all aberrations of the eye can be avoided with interference fringes imaged on the retina[11-14]. However, this technique is impractical for viewing stimuli other than gratings and is of no use for improving normal vision and the quality of fundus images. Another approach is to use a contact lens to null the refraction at the first surface of the cornea. This approach has the advantages of simplicity and low cost. However, contact must be made with the optics of the eye and the effectiveness of the method depends on the extent to which the corneal surface dominates in the combined effects of refractive index variations throughout the eye's optics. A recent attempt to use a special contact lens to increase the axial resolution of a confocal laser scanning ophthalmoscope[15] showed only modest improvement.

Adaptive optics is well-suited to cope with the large variation in the pattern of aberrations from eye to eye and can correct the wave aberration of the eye without making contact with it. Dreher et al. first used a deformable mirror in conjunction with the human eye[16]. They succeeded in correcting the astigmatism in one subject's eye based on the prescription provided by a conventional refraction. The recent development of a Hartmann-Shack wavefront sensor for the eye[9] has improved the measurement of the eye's aberrations[10]. Liang, Williams, and Miller[17] have combined a Hartmann-Shack wavefront sensor with a deformable mirror to correct these aberrations, and have applied this device to study both the visual performance and retinal images of eyes corrected to provide supernormal image quality. In normal eyes in which light scatter is not an important limitation of image quality, adaptive optics offers the possibility of obtaining retinal image quality limited only by diffraction at the dilated pupil.

2. Measuring the Wave Aberration of the Eye

2.1 Hartmann-Shack Wavefront Sensor for the Eye

The position of the subject's eye is fixed with respect to the optical system by having him clench his teeth on a dental impression. The optical axis of the wavefront sensor passes through a chosen reference axis in the eye, such as the line connecting the center of the dilated pupil to the foveal center.

A collimated, linearly polarized beam of a low power laser incident on the pupil is focused to a small spot on the retina, which the subject fixates. This small spot is equivalent to the guide star or laser beacon in astronomical applications

1

of adaptive optics. Its angular subtense is kept small enough that its retinal image corresponds to the point spread function of the eye. The use of a small diameter for the beam at the pupil, approximately 1.5 mm, ensures that the image on the retina is diffraction-limited and relatively unaffected by changes in the refractive state of the eye. Liang and Williams used light from a 5 mW, 632.8nm He-Ne laser and we currently use 750 nm light from a diode laser. Semiconductor diode lasers in the near infrared are particularly convenient because they are compact and the point source appears less bright for the subject. In a typical measurement at 750 nm, the retina is illuminated for a 2 seconds with a total power entering the eye of less than 15 micro-watts, which is more than an order of magnitude below the ANSI maximum permissible exposure[18].

Depolarized light from the retina is transmitted by a polarizing beamsplitter that rejects the unwanted reflections from the relay lenses and the first surface of the cornea, which retain their polarization. The relay lenses image the subject's pupil onto an array of 217 lenslets. We represented the wave aberration with the sum of 65 Zernike polynomials, corresponding to aberrations up to and including 10th order[19].

2.2 The Wave Aberration of the Normal Human Eye

Despite the large differences in the wave aberration between eyes of different observers, the wave aberrations of left and right eyes of the same observer are often rather similar, when the left eye imaged is flipped about a vertical axis for comparison with the right eye. This indicates that the aberrations are not random defects.

These aberrations generally increase toward the margin of the pupil and often do not correspond to the classical aberrations of man-made optical systems. Fig. 2 shows the RMS wavefront error contributed by each Zernike order for a 3.4 mm pupil (triangular symbols), a 7.3 mm pupil (square symbols), and an artificial eye with a 6.7 mm pupil (round symbols). The average RMS wavefront error decreases monotonically as the Zernike order increases for both pupil sizes in the human eye, though the pattern varies somewhat among individual observers. The RMS error for the small pupil lies 3-4 times lower than that for the large pupil of real eyes. This illustrates the well-known fact that aberrations grow with increasing pupil size.

Fig. 2 also shows the RMS wavefront error for an artificial eye (round symbols) measured with the same instrument. The artificial eye consisted of a achromatic doublet (f = 16 mm) and a diffuser to mimic the retina. Though our measurements reveal some expected spherical aberration in the artificial eye, the mean RMS value of each order averages about one order of magnitude lower than in human eyes for the large 7.3 mm pupil. Evolution has not yet created optics in the human eye, at least, that can rival those fabricated by man.

3. Adaptive Compensation

3.1 Technique

The experimental setup is shown on figure 3. A deformable mirror (Xinetics, Inc.) compensated for the eye's wave aberration. The mirror consisted of an aluminized glass faceplate with 37 lead zirconate-lead titanate (PZT) actuators mounted in a square array on the back surface. The stroke of the mirror beneath each actuator was plus and minus 2 mm, allowing a wavefront shift of 8 mm in the reflected beam. The mirror lay in a plane conjugate with both the eye's pupil plane and the lenslet array of the wavefront sensor. The spacing of adjacent actuators on the mirror was 7 mm. The eye's pupil plane was magnified 6.25 times at the deformable mirror, so that the actuator spacing in the pupil plane was 1.12 mm.

Compensation was achieved with closed-loop feedback control. Loops were repeated until the rms wavefront error could be reduced no further, which usually required 10-20 loops. The improvement in the optical quality of the eye provided by the deformable mirror was evaluated by measuring the observer's contrast sensitivity for gratings viewed through the deformable mirror, and by examining the quality of the images of the living retina taken through the deformable mirror. All experimental measurements used a 6 mm artificial pupil conjugate with the entrance pupil of the eye. The psychophysical and retinal imaging experiments were performed by sliding a mirror into the path between the wavefront sensor and the deformable mirror.

3.2 Results

To determine which aberrations were corrected by the deformable mirror, the wave aberration of the eye was decomposed into 65 Zernike modes up to 10th order. A comparison of the measured rms wavefront error of each Zernike order for the eyes without adaptive compensation with the error after adaptive compensation showed that lower Zernike orders up to and including 4th order were significantly reduced while aberrations beyond 6th order remain almost unchanged. Our results show that with adaptive compensation we not only can correct the eye's defocus and astigmatism but also coma, spherical aberration, and other irregular aberrations in the eye.

Vision through Adaptive Optics. Stimuli such as edges viewed through the compensating deformable mirror have a strikingly crisp appearance consistent with the supernormal quality of the retinal image. Liang, Williams and Miller showed that observers with normal vision had enhanced contrast sensitivity when looking through adaptive optics. Contrast

sensitivity measurements for two observers before and after adaptive compensation are shown in Fig. 4. Filled symbols show contrast sensitivity without adaptive compensation, i.e. with the deformable mirror flat. Unfilled symbols show the contrast sensitivity when the mirror corrects the eye's aberrations. At 55 cycle/deg, neither observer could detect the grating when the deformable mirror was flat even at 100% contrast. This was true no matter what pupil size they tried and despite attempts to correct defocus and astigmatism with trial lenses. With adaptive compensation, the observers required about 40% contrast on average to detect the grating. At another spatial frequency, 27.5 cycles/deg, contrast sensitivity was improved by about a factor of 6 by adaptive compensation.

Imaging the Retina. Estimates of the dimensions of microscopic structures in living human retinas have been obtained using coherent[20] and incoherent light[21] under conditions in which only defocus and astigmatism in the eye were corrected. Cone spacing of living retinas can be estimated based on the power spectra of retinal images in coherent light, but laser speckle associated with coherent imaging and imaging blur due to the eye's aberrations prevent the resolution of the retinal structures in single exposures. Miller et. al. showed, using incoherent light, that when defocus and astigmatism are carefully corrected, the cone mosaic can sometimes be resolved in individual retinal images. Liang, Williams, and Miller[17] showed that adaptive optics offers substantial improvement in the quality of these images.

In their experiments, the observer fixated a crosshair which determined the retinal location to be imaged. When the subject was ready, a krypton flash lamp delivered a 4 msec flash, illuminating a retinal disc 1 deg in diameter. The short 4 msec exposure helped to prevent motion blur due to the movement of retina during each exposure. The lamp output, which was broad band white light, was filtered with narrow band interference filter to the desired imaging wavelength. The retinal irradiance of the flash was 5.7 mW/mm^2 which is about 90 times less that the ANSI maximum permissible exposure for this retinal image size[18]. To acquire images of the retina, a scientific grade CCD was positioned conjugate with the retina, in the plane that previously contained the grating stimuli used in the psychophysical experiments. Each CCD pixel subtended 8 arc sec, corresponding to a sampling frequency at the retina of 450 cycles/deg. Images were acquired when the mirror was flat (uncompensated imaging) and when the mirror was warped to correct the eye's wave aberration (compensated imaging). For both the compensated and uncompensated imaging, astigmatism was corrected with trial lenses using the amount of astigmatism measured with the wavefront sensor when the mirror was flat. For uncompensated imaging, the optimum focus was determined by translating in tandem the eye and the nearest lens to the eye to achieve the highest contrast retinal images. For compensated imaging, the optimum focus was provided directly by adjusting the focus to compensate for the chromatic aberration between the wavefront sensor wavelength and the imaging wavelength.

Fig. 5 shows how image quality is improved by using adaptive compensation. The two images are of the same retinal location (1 degree eccentricity) for subject JW, without and with adaptive compensation, respectively. The image without compensation was obtained with the best focus and astigmatism correction. After adaptive compensation, the photoreceptor array is better resolved and has a higher contrast.

The depth of field is short compared to the retinal thickness and by adjusting the focus different structures can be observed. Figure 6 shows two images of the same retinal location for a single subject JP. The capillaries lie on top of the retina and appear as shadows, back-illuminated by the out of focus photoreceptor array. By focusing approximately 100 μm deeper into the retina the photoreceptor array is clearly seen with the blood vessels appearing as dim shadows across the image. In these images, there is no evidence of variation in image quality across the image. This indicates that the isoplanatic patch, which limits the compensated field of view to only a few arcseconds for ground-based telescopes[22], is at least as large as the one degree field of the present instrument.

Wavefront sensing in the eye may have important applications in refining laser surgical procedures such as PRK or in improving the design of contact lenses. Adaptive optics allows microscopic features to be resolved in the living human retina, which may have interesting application in basic and clinical research on the eye, and ultimately in the diagnosis and treatment of eye disease.

References

1. G. T. Willoughby Cashell, "A short history of spectacles," Proc. Roy. Soc. Med. **64**, 1063-1064 (1971).
2. M. L. Rubin, "Spectacles: Past, Present and Future," Survey of Ophthalmology **30**, 321-327 (1986).
3. H. von Helmholtz, *Helmholtz's Treatise on Physiological Optics*. J. P. C. Southall, Eds., (Optical Society of America, New York, 1924).
4. M. S. Smirnov, "Measurement of the wave aberration of the human eye," Biophysics **7**, 766-795 (1962).
5. F. Berny, S. Slansky, "Wavefront determination resulting from foucault test as applied to the human eye and visual instruments," in *Optical Instruments and Techniques* , J. H. Dickenson, Eds. (Oriel Press, Newcastle, 1969), pp. 375-386.
6. G. Van den Brink, "Measurements of the geometrical aberrations of the eye," Vision Res. **2**, 233-244 (1962).
7. M. C. Campbell, E. M. Harrison, P. Simonet, "Psychophysical measurement of the blur on the retina due to optical aberrations of the eye," Vis. Res. **30**, 1587-1602 (1990).
8. H. C. Howland, B. Howland, "A subjective method for the measurement of monochromatic aberrations of the eye," J. Opt. Soc. Am. **67**, 1508-1518 (1977).

9. J. Liang, B. Grimm, S. Goelz, J. Bille, "Objective measurement of the wave aberrations of the human eye using a Hartmann-Shack wavefront sensor," J. Opt. Soc. Am. A **11**, 1949-1957 (1994).

10. J. Liang, D. R. Williams, "Aberrations and retinal image quality of the normal human eye," J. Opt. Soc. Am. A , *in press*.

11. Y. L. Grand, "Sur la mesure de l'acuite visuelle au moyen de franges d'interference," Academie Des Sciences **200**, 490-491 (1935).

12. G. Westheimer, "Modulation thresholds for sinusoidal light distributions on the retina," Journal of Physiology **152**, 67-74 (1960).

13. F. W. Campbell, D. G. Green, "Optical and retinal factors affecting visual resolution," J. Physiol. (Lond.) **181**, 576-593 (1965).

14. D. R. Williams, "Aliasing in human foveal vision," Vision Res. **25**, 195-205 (1985).

15. D. Bartsch, G. Zinser, W. R. Freeman, "Resolution improvement of confocal scanning laser tomography of the human fundus," Vision Science and Its Applications, 1994 Technical Digest Series, Vol. 2 (Optical Society of America, Washington, DC) , 134-137 (1994).

16. A. W. Dreher, J. F. Bille, R. N. Weinreb, "Active optical depth resolution improvement of the laser tomographic scanner.," Appl. Opt. **24**, 804-808 (1989).

17. J. Liang, D. R. Williams, D. T. Miller "Supernormal vision and high resolution retinal imaging through adaptive optics" J. Opt. Soc. Am. A *in press*

18. ANSI, *American national standard for the safe use of lasers ANSI Z136.1-1993* (Laser Institute of America, Orlando, Florida, 1993).

19. M. Born, E. Wolf, *Principles of Optics* (Pergamon Press, Oxford, 1983).

20. S. Marcos, R. Navarro, P. Artal, "Coherent imaging of the cone mosaic in the living human eye", J. Opt. Soc. Am. A **13**, 897-905 (1996).

21. D. T. Miller, D. R. Williams, G. M. Morris, J. Liang, "Images of the cone mosaic in the living human eye," Vision Res. **36**, 1067-1079 (1996).

22. J. Hardy, "Instrumental limitation in adaptive optics for astronomy," in *Active Telescope Systems*, F.J. Roddier ed., Proc. Photo-Opt. Instrum. Eng. **1114**, 2-13 (1989).

Figure Captions

Fig. 1. PSFs verses pupil size for a single subject. The PSFs are calculated based on the subject's aberrations measured with the Hartmann-Shack wavefront sensor.

Fig. 2. Zernike description of the eye's aberrations. The upper curve (square symbols) shows the RMS wavefront error of each Zernike order for a 7.3 mm pupil averaged across 14 human eyes. Error bars indicate the standard deviation among eyes. For the 2nd order Zernike modes, only astigmatism is shown. The average amount of astigmatism in these observers was 0.6 diopters, corresponding to a mean RMS value of 0.77 mm. The middle curve (triangular symbols) shows the data for a 3.4 mm pupil averaged across 12 eyes. The lower curve (round symbols) is for an artificial eye. The error bars shows the standard deviation of 10 repeated measurements.

Fig. 3. System for vision testing or retinal imaging with adaptive optics.

Fig. 4. Contrast sensitivity plots for two subjects before and after adaptive compensation.

Fig. 5. Images before and after adaptive compensation for aberrations for JWs right eye. Both images are of the same retina area at 1 deg from the central fovea. Images were taken with 550 nm light (25 nm bandwidth) through a 6 mm pupil. Each image has been normalized to its mean intensity and both are displayed within the same gray scale range. The dark vertical band across each image is an out-of-focus shadow of a blood vessel.

Fig. 6. 1 deg images of JP's right eye of the same retinal location at two focal planes. In the left image, capillaries on the order of 10 μm are seen. By focusing deeper into the retina, the underlying photoreceptor mosaic can be seen and the capillaries appear as faint shadows.

Figure 1

2 mm	3 mm	4 mm
5 mm	6 mm	7.3 mm

━━ 3 arcmin   DM

Figure 2

RMS wavefront error (μm) vs Zernike order

- Eye (7.3 mm)
- Eye (3.4 mm)
- Artificial eye (6.7 mm)

Ast. 3 4 5 6 7 8 9 10 11

Zernike order

Figure 3

Wavefront Compensation
Deformable Mirror

Light Delivery
Krypton flash lamp

Vision Testing or Retinal Imaging
stimulus or CCD

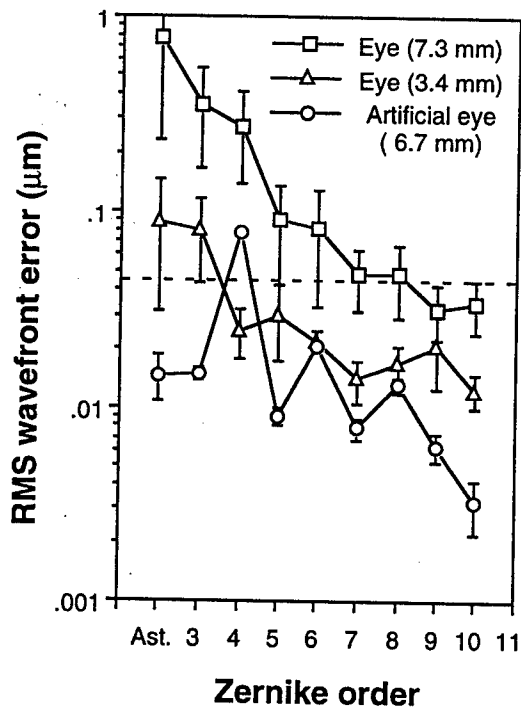**Wavefront Sensing**
laser
lens array
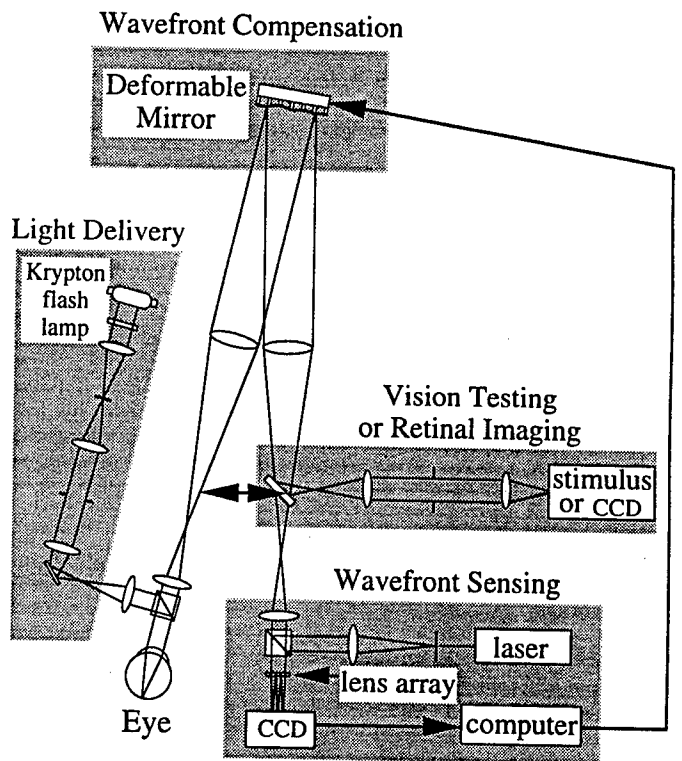CCD → computer

Eye
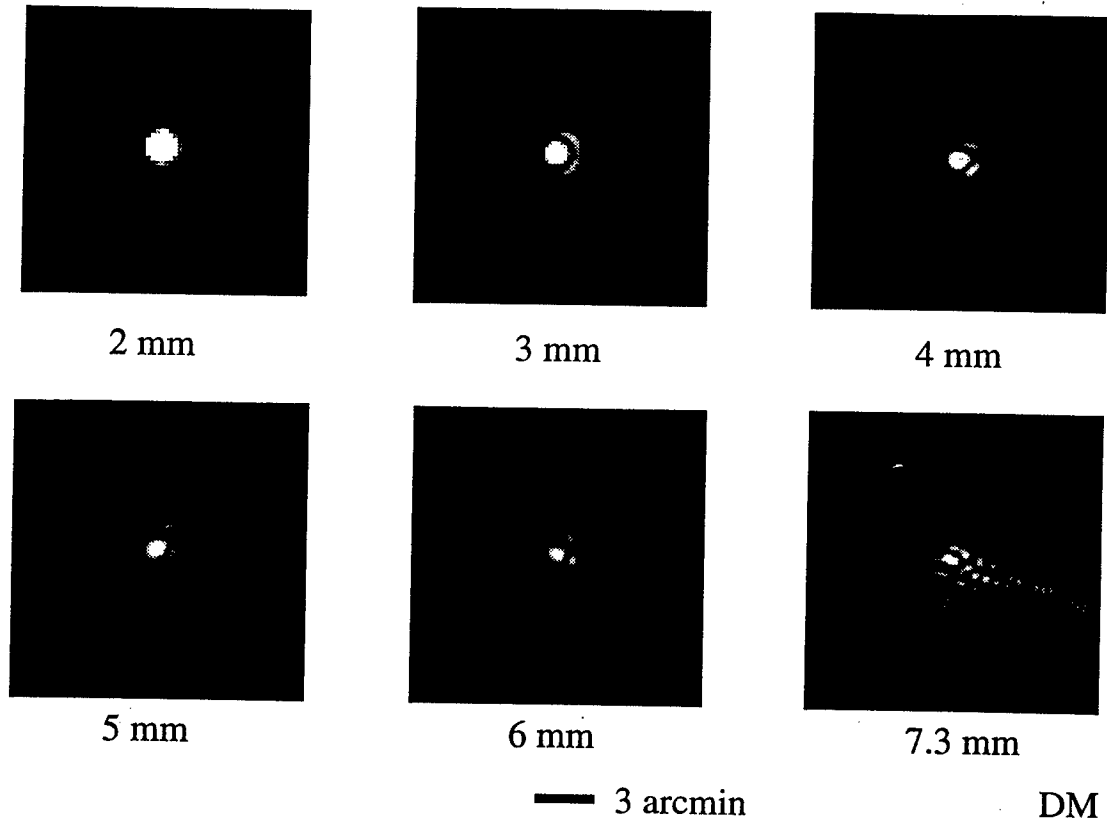
Figure 4

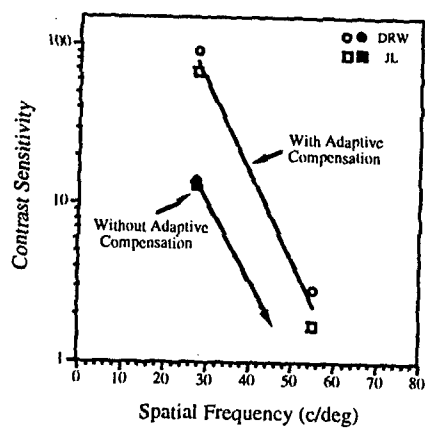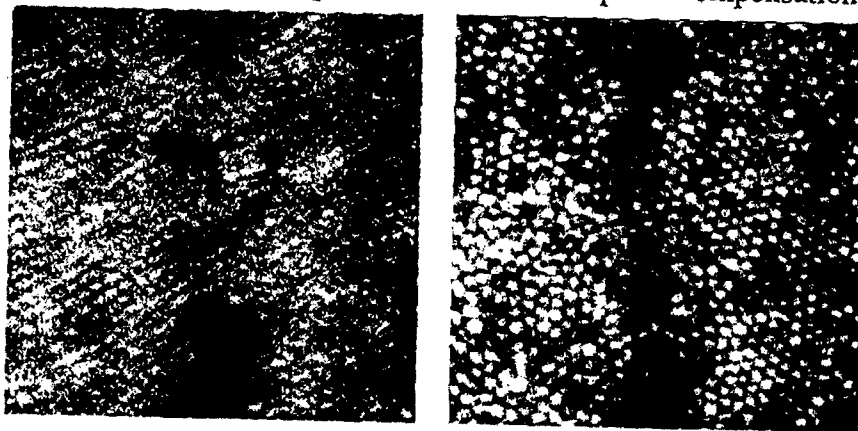## Figure 5

Without Adaptive Compensation   With Adaptive Compensation
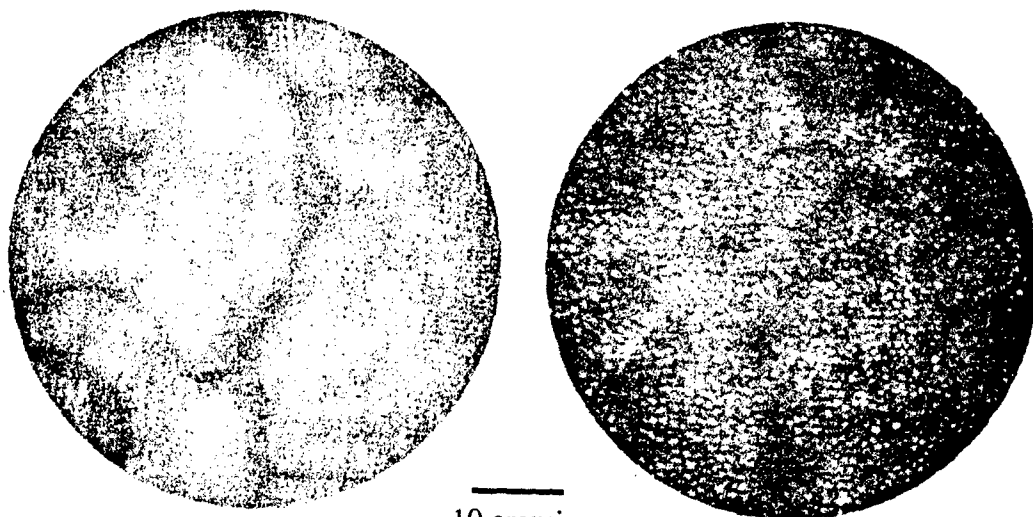

10 arcmin
(48.6 µm)

Figure 6

Capillaries   Photoreceptors

10 arcmin
(48.6 µm)

Adaptive optics for direct correction of a human vision.

Gleb Vdovin, Simon Middelhoek
Laboratory of Electronic Instrumentation, Delft University of Technology,
P.O.Box 5031, 2600 GA, Delft, The Netherlands
Phone: 31-15-2785756, Fax: 31-15-2785755, email: gleb@ei.et.tudelft.nl

May 27, 1997

Abstract: *Inexpensive micromachined varifocal mirrors, providing very wide range of focal distance control are described. The focal distance of a mirror with a clear aperture of 1cm can be controlled in the range ∞ to +0.25m (four diopters) in a frequency band of up to 75Hz by applying control voltages in the range of 0 to 300V. Applications for focus control in a CCD camera and for direct correction of the accommodation depth of a human eye are reported.*
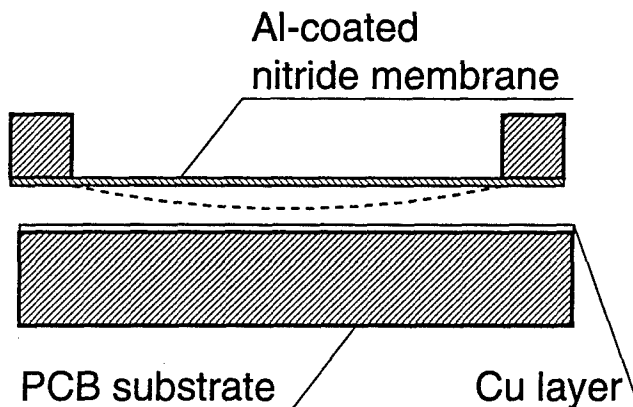
Figure 1: Scheme of micromachined adaptive mirror.

Figure 2: Micromachined defocus corrector mounted onto PCB.

Fast focus adjustment is desirable in many imaging optical systems. Adaptive mirrors [1, 2], used for correction of aberrations with low amplitude are in general much faster than existing mechanical autofocus systems used for deep focus adjustment. Recently developed silicon micromachined adaptive mirrors [3, 4] provide very wide range of surface deformations, making possible direct focus control in imaging optical systems. Incorporation of an adaptive mirror into imaging lens system introduces a certain design problem, because an additional space should be provided to separate the incident and the reflected light paths and because the oblique incidence onto the deformed adaptive mirror results in additional aberration. Here we consider two configurations which use varifocal adaptive mirrors for quick adjustment of the distance to the sharply imaged plane in the range ∞...0.3m with acceptable optical quality.
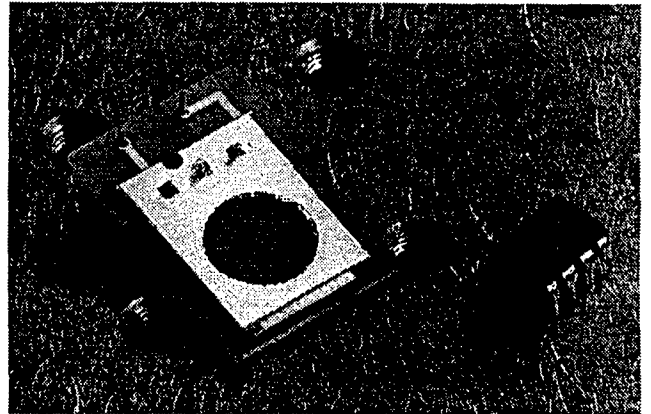
The schematic of micromachined membrane adaptive mirror [5] with a wide range of focal distance control is shown in Fig. 1. The mirror is fabricated using bulk silicon micromachining. The reflective surface is formed by a circular 0.5 ... 1μm-thick silicon-reach nitride membrane, which is coated by a reflective aluminum layer. The chip with circular stretched membrane is mounted 75μm over metalized printed circuit board (PCB). The radius of the membrane curvature is controlled in the range ∞...0.5m by applying voltage in the range 0...160V between the membrane and the metalization layer of the PCB. The complete device measures 20x30x5mm and weights approximately 5g -see Fig. 2. Interferometric patterns correspondent to the initial and deformed surface of the mirror are shown in Fig. 3.

The dynamics of the mirror response depends onto the resonant frequency of the membrane and the air damping. Under normal atmospheric pressure the mirror is essentially over-damped, demonstrating linear frequency response in the range 0...75Hz (the particular mirror used in experiments). Cutoff frequency can be extended into kHz range by increasing the membrane tension during the membrane fabrication, which will also rise the necessary control voltage. To measure the dynamics of mirror response, the variation of local near-field intensity of a collimated light beam was registered after reflection from the dy-
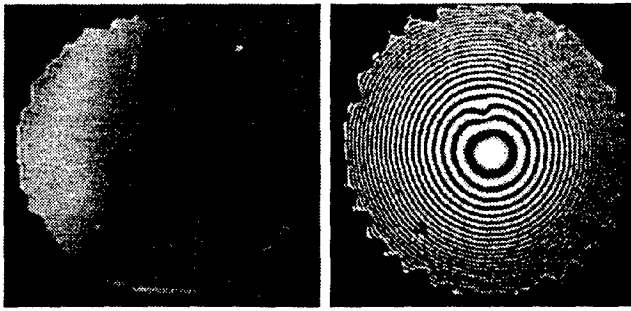
Figure 3: Interferogram of initial mirror surface with active diameter of 10mm, the same under control voltage of 90V, corresponding to the focal distance of 75cm.
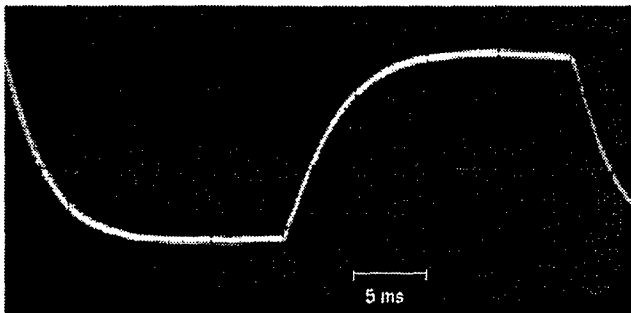

Figure 4: Response of the mirror to 25Hz meander input signal.

namically deformed mirror, using method similar to one described in [3]. The oscillogram, correspondent to the mirror response to the rectangular input signal with amplitude 150V and frequency 25Hz, corresponding to switching the focus distance in the range $\infty \ldots 0.3$m 50 times per second, is shown in Fig. 4. The device is sufficiently fast to provide independent focus adjustment for each frame with a standard rate of 25 frames per second. Micromachined adaptive mirrors are reliable - similar devices have been continuously driven during six months with a frequency of 100Hz and the range of deflection of 10μm ($\sim 1.5 \cdot 10^9$ deformation cycles) without any observable change of optical, mechanical or electrical characteristics.

Optical setups used for correction of image focus are shown in Fig. 5. In the first configuration, the adaptive mirror replaces the reflective coating on one of pentaprism surfaces. The angle of axial incidence onto the mirror surface equals to $\varphi = \arcsin(n \cdot \sin 22.5^o) \sim 34^o$, where n is the refraction coefficient of the prism material, so the deformed mirror introduces considerable amount of astigmatism into the wavefront transmitted by the system. The angular field is limited to approximately 24° by the prism system [6] and the image is inverted. Described system was used in combination with a CCD camera, equipped with 50mm F1/5 lens focused to infinity. The system was quickly and efficiently fo-

cused using the adaptive mirror in the range from infinity (zero control voltage) to 30cm (control voltage of 150V). Example of fast focus switching (switching time approximately 10ms, 'still exposition 30ms) between two objects placed at distances 75cm and 50cm respectively is shown in Fig. 6. The observed image quality at distances shorter 1m was slightly lower than that obtained by direct manual focusing of the camera lens, but still acceptable as all important details were resolved. Focusing in the range 1m to ∞ produced images with a quality indistinguishable from direct lens focusing.
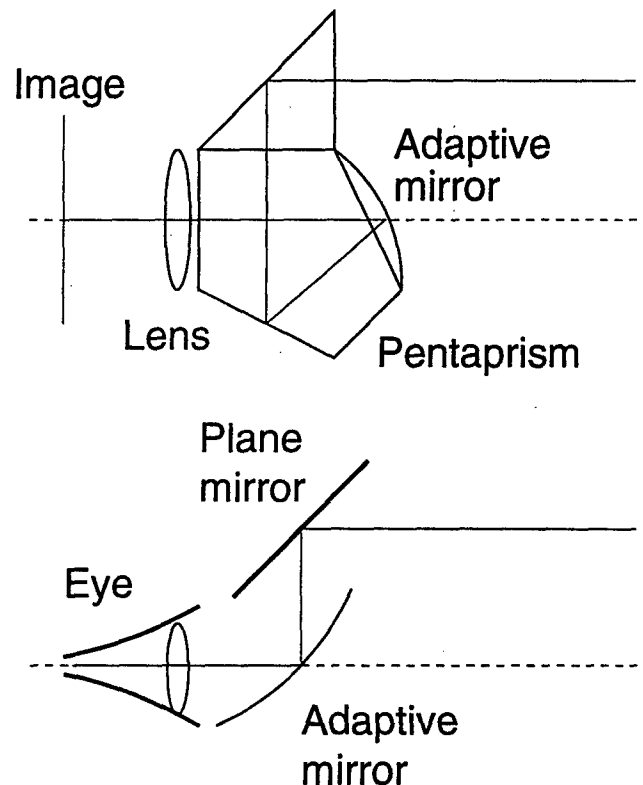
Figure 5: Two configurations used for focus adjustment.

The second setup, used for direct correction of the accommodation depth of the human eye, consists of two mirrors in periscope-like configuration -see Fig. 5. Due to the large angle of incidence ($\sim 45^o$), the deformed adaptive mirror introduces a considerable amount of astigmatism when the eye is accommodated to infinity and the system is focused to a short distance. Ray-tracing analysis showed that the axial resolution of the system (eye lens was considered ideal with a focal distance of 17mm and diameter 5mm) drops down to 15 lines per millimeter in the case of focusing to a distance of 0.3m. Compensation of astigmatism introduced to the model improved the resolution to 40 lines/mm. Visual experiments, performed by the author and a group of colleagues, aged 21 to 65, demonstrated practical efficiency of the reported scheme. In the experiment, two text patterns

2

Figure 6: Two consequent frames (time separation 40ms), obtained by focusing the system to the distance of 75cm (top) and 50cm (bottom). Both images are mirrored to improve readability.

were placed in front of the system: one at the distance of four meters (poster, 56pt Helvetica) and the second (textbook 10pt Times-R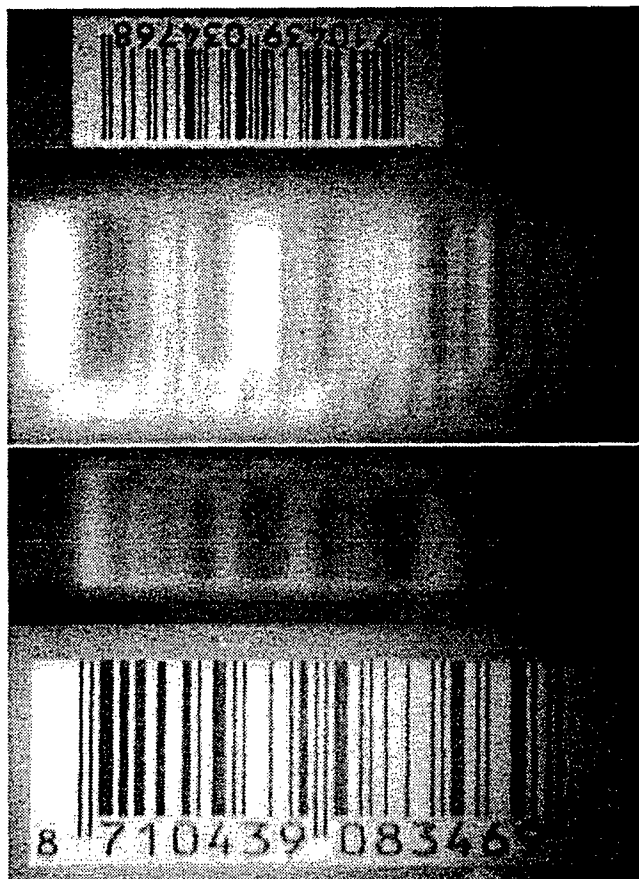oman) at the distance of approximately 15cm. When no voltage was applied to the adaptive mirror, the poster was clearly readable by all participants of the experiments, the text in the near zone was readable by approximately 40% of all participants with a considerable eye effort. After applying the voltage of 150V to the adaptive mirror, all participants could read the textbook without any considerable eye-strain, but the poster was absolutely unreadable for all participants. All participants characterized the quality of the corrected image as acceptable, with slightly distorted field of view. The correction setup for one eye provides field of view of approximately 30°, measures 15x25x35mm and weights less than 40g. The deformable mirror is connected to the voltage source via resistor of 5 MOhm for safety reasons.

The optical quality of both systems can be further improved by using astigmatic varifocal mirror to reduce the aberration introduced by the oblique incidence onto the surface of the deformed mirror. Elliptical membrane will provide necessary alteration of the optical power without introducing on-axis astigmatism at oblique angles in the whole range of focus control. More complex aberrations can be corrected using multi-electrode control structures. Both reported setups were not optimized with respect to resolution, aberrations and field of view. Special design of a system including the varifocal mirror will certainly provide much higher optical performance.

Reported experiments show that micromachined varifocal mirrors can be used for fast focus adjustment in imaging systems like surveillance cameras, industrial vision systems, binoculars, photo-cameras, camcorders, eye-testing equipment and devices for direct correction of vision acuity.

References

[1] R.H. Freeman, J.E. Pearson, Deformable mirrors for all seasons and reasons, Applied Optics 21, 580–588 (1982)

[2] R.P. Grosso, M. Yellin, The membrane mirror as an adaptive optical element, Journal of the Optical Society of America 67, 399–406 (1977)

[3] G. Vdovin and P.M. Sarro, "Flexible mirror micromachined in silicon", Applied Optics 34, 2968–2972 (1995)

[4] L.M. Miller, M.L. Argonin, R.K. Bartman, W.J. Kaiser, T.W. Kenny, R.L. Norton, E.C. Vote, Fabrication and characterization of a micromachined deformable mirror for adaptive optics applications, Proc. SPIE 1945, 421–430 (1993)

[5] G. Vdovin, S. Middelhoek, P.M. Sarro, "Micromachined mirror with a variable focal distance", in Free-Space Microoptical Systems – the Digest of EOS Topical Meeting, edited by M. Gale, pp. 28–29, April 1-3 1996.

[6] W.J. Smith, "Modern optical engineering, the design of optical systems", McGraw-Hill, p.84–101, 1966.

3

Controlling of the Optical Parameters in Biotissues

Valery V. Tuchin, Dmitry A. Zimnyakov

Saratov State University,
Precise Mechanics and Control Institute of Russian Academy of Science,
83 Astrakhanskaya, Saratov, 410026 Russia
e-mail: <tuchin@scnit.saratov.su>
FAX: (8452)24-04-46

Introduction

In vivo tissue optical properties control is very important for many applications. A number of laser surgery, therapy and diagnostic technologies include tissue compression and stretching used for better transportation of laser beam to underlying layers of tissue. The human eye compression technique allows to perform transscleral laser coagulation of the ciliary body and retina/choroid. The possibility of selective clearance of the upper tissue layers should be very useful for developing of the eye ball diaphanoscopy techniques and for detecting of local inhomogeneities hidden by a highly scattering medium in functional tomography. In this report we present results on the human sclera optical and temporal properties controlled by employing administration of osmotically active chemicals. These results should be very useful for developing of computer-aided eye tissues photocoagulation systems as well as eye ball tomographic systems.

Biotissues optical characteristics control

Method	Technique	Tissue	The main result
Addition of absorbers (dyeing, sensitization, irradiation et al.)	Adding of dyes, drugs and "sunscreen" creams	All types	Increasing of selectivity and sensitivity for photochemical and photodestructive reactions, decreasing of transmittance, changing of reflection
	UV-irradiation (erythema, melanogenesis, radiation dyeing)	Skin, eye lens	
Addition of scatterers	Adding of "sunscreen" creams	Skin	Decreasing of transmittance
	Reducing of temperature (9-12 ^{0}C)	Eye lens	Decreasing of transmittance (cold revezible cataract)
Extraction of absorbers and scatterers	Adding of water and aqueous lactic acid (during 0.5-4 hrs)	Skin	Increasing of transmittance, changing of reflection
	Compression and stretching	Blooded soft tissues	
Destruction of absorbers	Intensive light irradiation (photobleaching)	All types of sensitized tissues	
	Chemical bleaching		
Immersion	Adding of oils, creams, water, drugs (matching of refractive indices)	Skin, sclera	
		Cornea	Changing of polarization anisotropy
Decreasing of thickness	Compression, stretching, and puncture	Soft tissues skin, sclera	Increasing of transmittance
Increasing of thickness	UV-irradiation (hyperplasia)	Skin	Decreasing of transmittance
Dehydration	Tissue refrigerating at 4 ^{0}C (24-72 hrs), about 40% lost of tissue sample weight	Human aorta	Increasing of the absorption coefficient by 20-50%
Thermal damage (protein coagulation)	Constant temperature water bath (100 ^{0}C, 300 s)	Human aorta	Increasing of the reduced scattering coefficient by 10-45% in the visible and 30-150% in the NIR

Scleral tissue model

The human sclera is a turbid, nontransparent medium covers about 80% of the eye ball and serves as a protective membrance. It is a strong fibrous tissue which is mainly consists of cojunctive collagen fibers packed in lamellar bundles which are immersed within amorphous ground (interstitial) substance. For normal sclera tissue $\mu_a \ll \mu_s$. For example, for porcine sclera at 633 nm $\mu_a \cong 0.2$ mm^{-1}, $\mu_s \cong 80$ mm^{-1}, $g \cong 0.9$ (M.Hammer et al., *Phys. Med. Biol.* Vol.40, pp.963-978, 1995).

Refrective indices matching - optical enlightening effect

The ratio of the scattering coefficients for different degree of collagen fibrils and interstitial substance refractive indices matching has a view

$$\mu_s(t) \cong \mu_s^{(0)} \left\{ \frac{\dfrac{n_c}{n_I(t)} - 1}{\dfrac{n_c}{n_I(0)} - 1} \right\}^2 .$$

where n_c, n_I are the refractive indices of collagen and interstitial substance, respectively;

$$n_I(t) = n_I(0)c_1(t) + n_x c_x(t),$$
$$c_1(t) + c_x(t) = 1,$$

c_1 and c_x are relative volume concentrations of initial interstitial medium and administrated chemical agent (osmolyte), respectively; $n_I(0)$ and n_x are the corresponding values of refractive indices.

For a highly matching what is easely attainable in experiments:
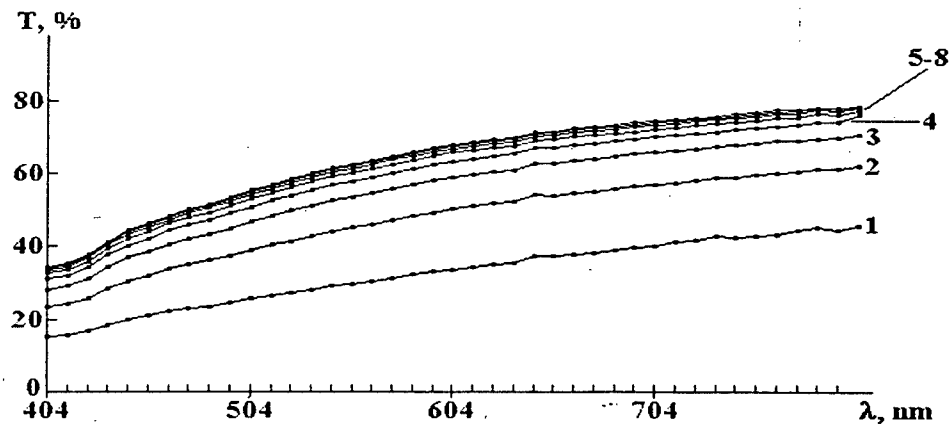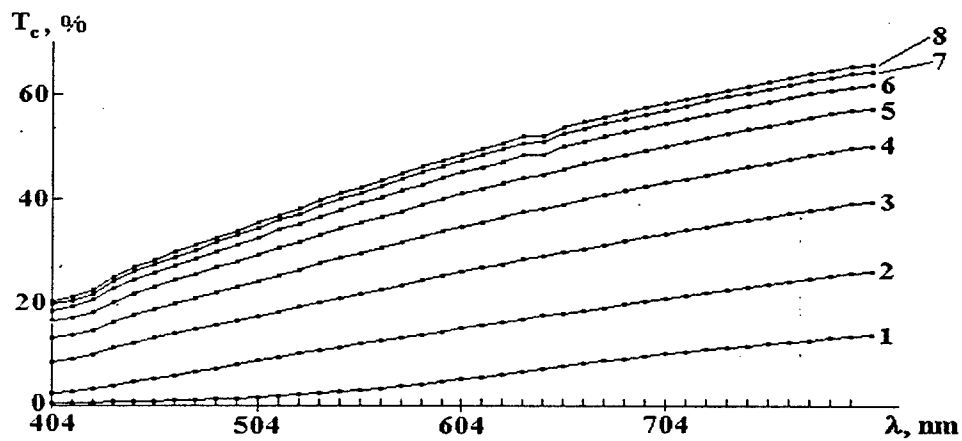
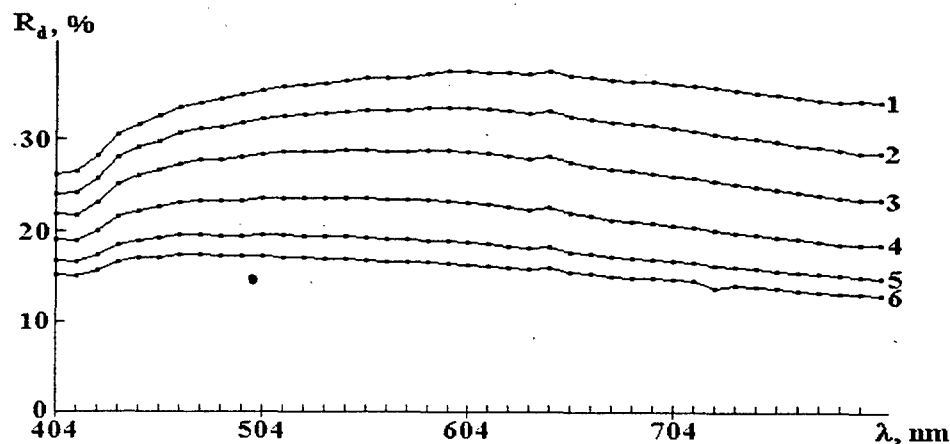$$n_c/n_I(t) \cong 1.001, \quad \text{when} \quad n_c/n_I(0) \cong 1.1,$$
$$\mu_s(t) \cong 10^{-4} \mu_s(0)$$
$$T_c(t) \sim \exp\left\{ -\left[\mu_s(t) + \mu_a\right]l\right\},$$

where $\mu_a \ll \mu_s(0)$, l is the tissue thickness.

The human sclera spectral characteristics

Typical experimental spectra of the human sclera samples measured for different time intervals of 60% Trazograph solution administration. Spectra numbered 1 were measured in 1 min after sample immersing into solution, spectra 2-8 were measured subsequently at 2 min intervals. An individual spectrum measuring time scanning from higher to lower wavelengths was about 85 sec. a - the collimated transmittance, T_c, sample thickness - 0.6 mm; b - the total transmittance, T, sample thickness - 0.7 mm; c - the diffusion reflection R_d, sample thickness - 0.7 mm (heavy pigmented tissue).

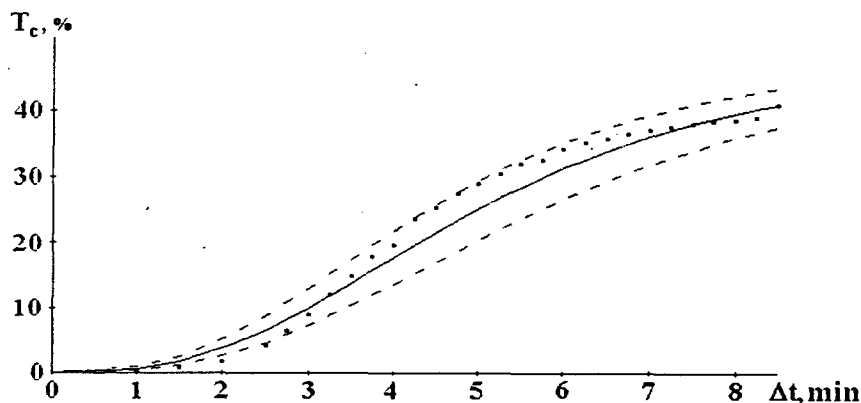### Optical monitoring of matter diffusion through the scleral tissue

Basing on the first Fick's law for the large external volume of a chemical agent we can find that its concentration within a tissue sample has an exponential temporal dependence

$$c_{int} \cong c_{ext}\left\{1 - \exp(-t/\tau)\right\},$$

where

$$\tau = l^2/D,$$

l is the tissue layer thickness, c_{ext} = const, D is the chemical agent diffusion coefficient

The time-dependent collimated transmisttance (dots) of the sclera sample of thickness 0.5 mm measured at 633 nm concurrently with 60% Trazograph administration. The solid line and dashed lines represent the mean value and the upper and lower limits of T_c obtained by a calculation of T_c using experimental data: D_T=1.46·10^{-5} ± 1.90·10^{-6} cm^2/s (see Table, sample #1).

Mean values and rms of diffusion coefficient for Trazograph D_T in the human sclera samples defined on the base of experimental data for T_c(t)

Sample	Thickness of sample, mm	Coefficient of diffusion, cm^2/s	RMS of diffusion coefficient, cm^2/s
#1	0.5	1.46·10^{-5}	1.90·10^{-6}
#2	0.5	4.00·10^{-6} ...	1.15·10^{-6}
#3	0.4	5.29·10^{-6}	7.58·10^{-7}
#4	0.4	1.20·10^{-5}	1.01·10^{-6}

Efficiency of the bovine scleral samples optical enlightening
(T_{cmax}. %) due to various solutions administration at room temperature

λ, nm / Solution	450	500	600	700
Trazograph, 60%	13	18.7	70.2	76.3
Trazograph, 76%	39.2	50.3	84.1	99.2
Glucose, 45%	21.6	29.5	69.4	73.8
PEG, 80% (20000)	46.4	58.3	81.7	99.2

Efficiency of the scleral samples optical enlightening (T_{cmax}) and time of enlightening (t_{max})
via temperature of PEG (20000) 80% solution at λ=700 nm

Solution temperature, °C	18.5	20	27.5	30	33	38	40	43	46.5
T_{cmax}, %	81.0	82.2	83.5	85.4	87.2	89.6	90.1	94.8	98.5
t_{max}, min	27	25	23	21	18	12	10	8	5

Estimated coefficient of diffusion for diffrent chemical agents in the bovine sclera samples
Trazograph (76%)

Sample	Coefficient of diffusion, cm^2/s	RMS of diffusion coefficient, cm^2/s
#3	$1.18 \cdot 10^{-4}$	$1.20 \cdot 10^{-5}$
#4	$6.28 \cdot 10^{-5}$	$1.50 \cdot 10^{-5}$
#5	$9.08 \cdot 10^{-5}$	$1.85 \cdot 10^{-5}$
#6	$1.26 \cdot 10^{-4}$	$2.67 \cdot 10^{-5}$
#7	$5.88 \cdot 10^{-5}$	$7.07 \cdot 10^{-6}$
Mean value	$9.13 \cdot 10^{-5}$	$2.75 \cdot 10^{-5}$

Glucose (45%)

Sample	Coefficient of diffusion, cm^2/s	RMS of diffusion coefficient, cm^2/s
#8	$6.23 \cdot 10^{-5}$	$7.48 \cdot 10^{-6}$
#9	$8.29 \cdot 10^{-5}$	$2.45 \cdot 10^{-5}$
#10	$1.46 \cdot 10^{-4}$	$1.20 \cdot 10^{-5}$
#11	$4.37 \cdot 10^{-4}$	$2.29 \cdot 10^{-4}$
#12	$3.38 \cdot 10^{-4}$	$2.32 \cdot 10^{-5}$
Mean value	$2.13 \cdot 10^{-4}$	$1.48 \cdot 10^{-4}$

PEG (80%)

Sample	Coefficient of diffusion, cm^2/s	RMS of diffusion coefficient, cm^2/s
#13	$1.64 \cdot 10^{-4}$	$2.71 \cdot 10^{-5}$
#14	$3.92 \cdot 10^{-4}$	$1.10 \cdot 10^{-4}$
#15	$1.52 \cdot 10^{-4}$	$7.56 \cdot 10^{-5}$
#16	$5.54 \cdot 10^{-5}$	$1.23 \cdot 10^{-5}$
Mean value	$1.91 \cdot 10^{-4}$	$1.24 \cdot 10^{-4}$
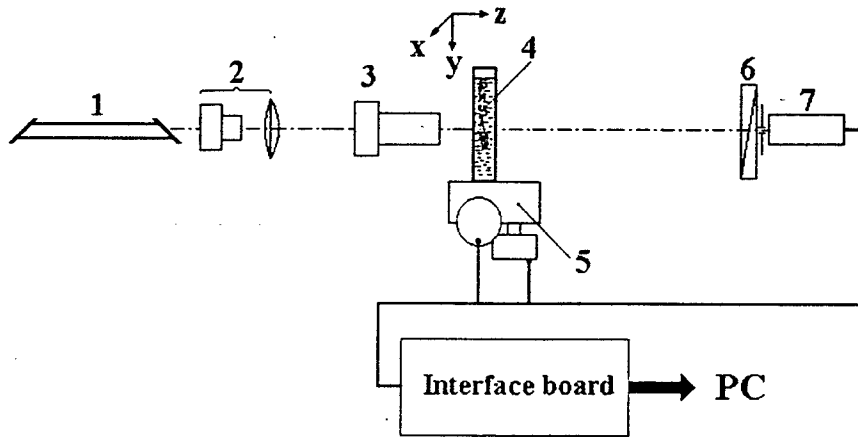
Optical scheme of the scanning polarization sensitive spatial speckle correlometer. 1 - monomode He-Ne laser (633 nm. 2 mW) with linear polarization of its radiation; 2 - telescope; 3 - focusing micro-objective; 4 - tissue under study; 5 - computer controlled 2D-scanning device; 6 - manually rotating polarizer; 7 - photomultiplier with a pinhole.

Because in the correlation experiments only the fluctuating component $\tilde{I}_s(t) = I_s(t) - \langle I_s(t)\rangle$ of the scattered light intensity is usually determined. the corresponding autocorrelation function can be obtained as:

$$\tilde{g}_2(\tau) = \langle \tilde{I}_s(t)\tilde{I}_s(t+\tau)\rangle / \langle \tilde{I}_s^2(t)\rangle .$$

In the region of the small temporal scales the analysis of the intensity fluctuations can be more precisely carried out by the study of the asymptotic behavior of corresponding structure functions $D_I(\tau)$

$$D_I(\tau) = \langle [I(t+\tau) - I(t)]^2\rangle .$$

Generalized parameter which can be used for characterizing of this behavior is the exponential factor

$$v_I = \frac{\ln(D_I(\tau_2)/D_I(\tau_1))}{\ln(\tau_2/\tau_1)} ,$$

where values of τ_1 and τ_2 determine the boundaries of the region of temporal scales for which v_I is estimated.
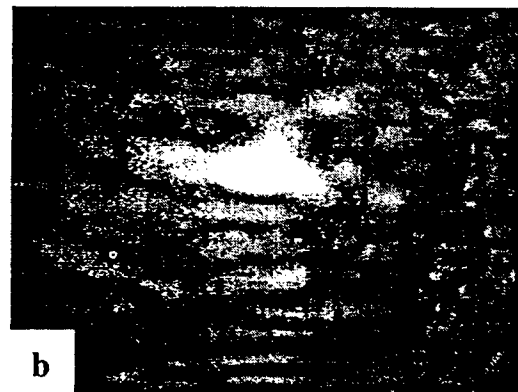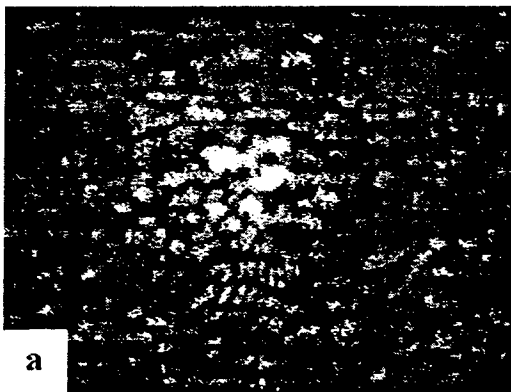
CCD images of the far-zone speckle patterns for early (~ 2.5 min) (a) and later (~ 10 min) (b) stages of the sclera enlightenment using Trazograph (60%) administration.
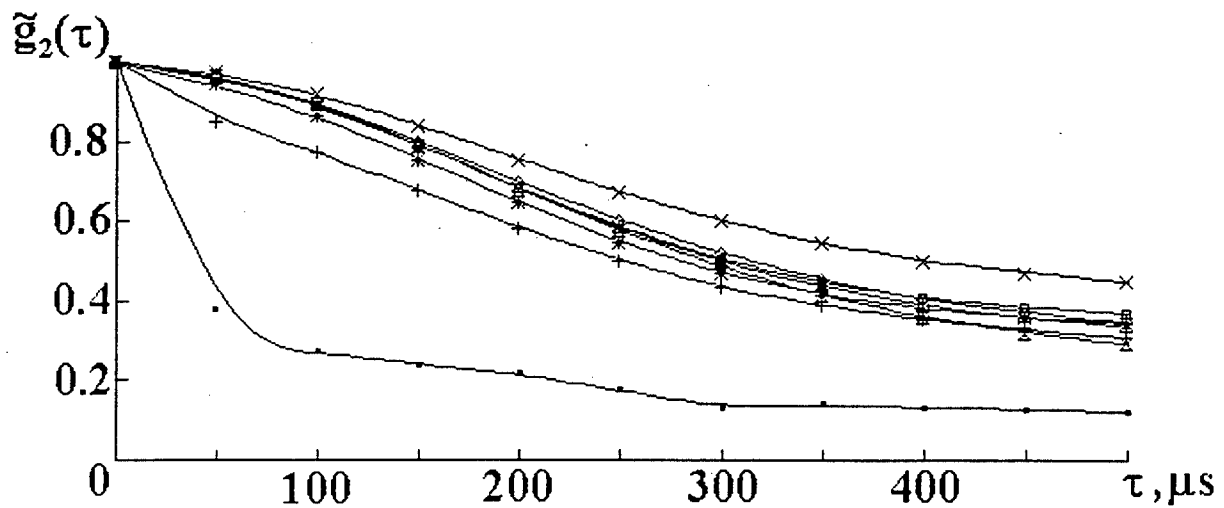
The human sclera samples autocorrelation functions of the far-zone speckle intensity fluctuations measured using scanning spatial speckle correlometer. a - the large time scale, sample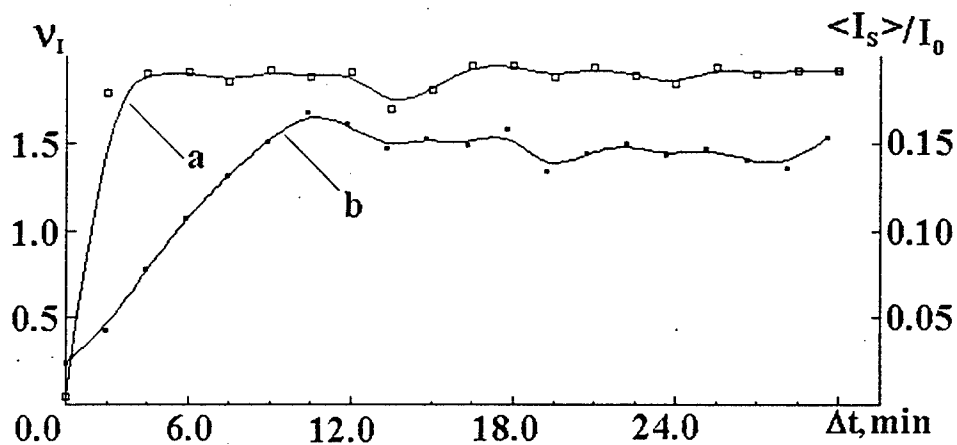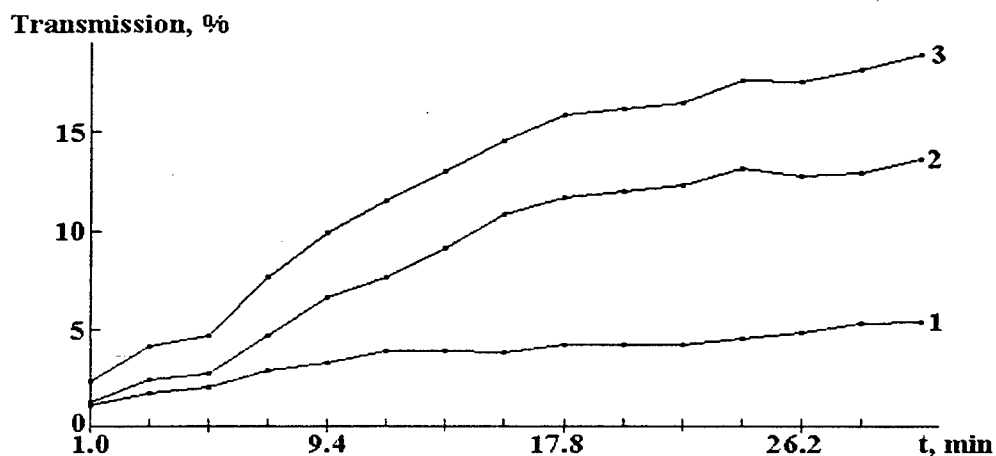 partly enlightened by Trazograph (60%); b - the time evolution of the form of autocorrelation peak (the small time scale) with the sclera turbidity decay, sample thickness 0.55 mm, measurements were done for different time intervals of Trazograph (60%) administration: $\bullet$ - 120 s; + - 220 s; $*$ - 320 s; $\square$ - 420 s; × - 520 s; $\lozenge$ - 620 s; Δ - 720 s; $\boxtimes$ - 820 s.

Typical dependencies of exponential factor v_1 (a) and normalized value of the average intensity $<I_s>/I_0$ (b) measured in the observation point on time period of Trazograph administration.

Transmission, %

20
15
10
5
0

3
2
1

0.3   2.55   5.15   t, min

Transmission, %

25
20
15
10
5
0

3
2
1

1.7   7.3   13.6   19.2   t, min
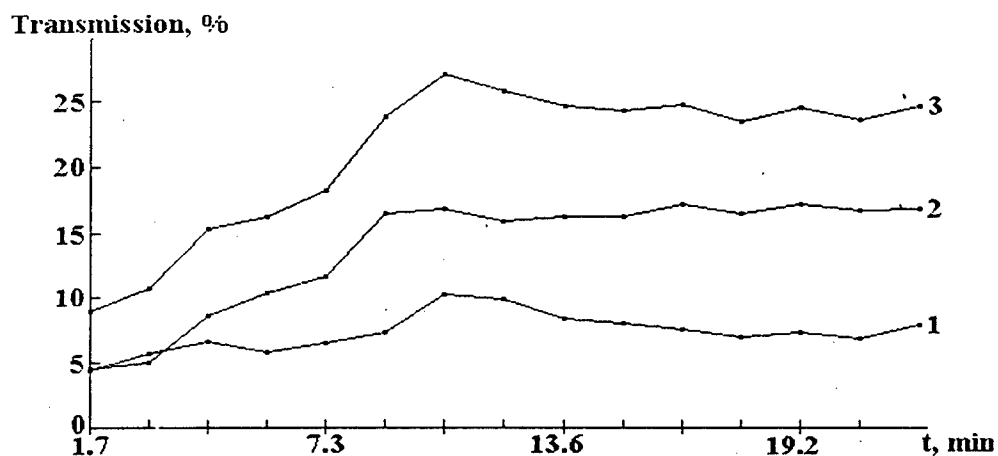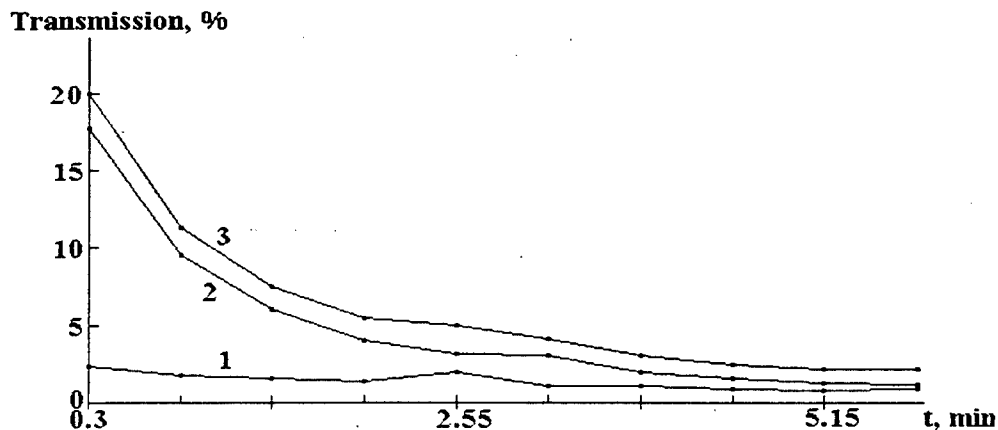
The time-dependent averaged over the scanning trace (1.5 mm) values of the mean speckle intensity $<I_s>$ (curves 3) and its polarization components $<I_\perp>$ (curves 1) and $<I_\parallel>$ (curves 2) measured in the paraxial region for the human sclera sample of thickness 0.4 mm: a, b and c - are the subsequent measurements for sample kept at first in Trazograph (60%) solution (a), then in physiological solution (0.9% NaCl) (b), and finally again in Trazograph (60%) solution (c); λ=633 nm.

•   Conclusion

The results of this study show that administration of osmolytes to the sclera effects the refractive index matching of the collagen fibrils and interstitial fluid what leads to dramatic changing (reducing) of the scattering properties of sclera.

Dynamics of the scleral tissue optical enlightening using osmolytes is defined by the characteristic time response about 3-10 min.

Presented results are general and can be applicable for description of many other fibrous tissues.

The wide range of the sclera scattering parameters changing allows to understand and to describe the transition from diffuse mode of light scattering to a coherent light propagation through tissue.

The intensity polarization measurements should be very helpful in study of tissue structure changing. The optical enlightening of fibrous tissue technology using the suitable chemical agent should be very important for developing of computer-aided adaptive laser systems for coagulation of tissue disorders hidden under the high scattering tissue layers.

Acknowledgment

Authors highly appreciate the help of A. A. Mishin in preparation of this report.

References

1. V. V. Tuchin, *Tissue Optics: Applications in Medical Diagnostics and Therapy*, SPIE Milestone ser. MS102, Bellingham (1994).
2. S. F. Barett, C. H. G. Wright, M. R. Jerath et al., "Computer-aided retinal photocoagulation system", *J. Biomedical Optics* 1, 83-91 (1996).
3. I. F. Cilesiz, A. J. Welch, "Light dosimetry: effect of dehydration and thermal damage on the optical properties of the human aorta, *Applied Optics* 32, 477-487 (1993).
4. V. V. Tuchin, "Laser light scattering in biomedical diagnostics and therapy", *J. Laser Applications* (Laser Inst. of America) 5, (2&3), 43-60 (1993).
5. H. Liu, B. Beauvoit, M. Kimura, B. Chance, "Dependence of tissue optical properties on solute - induced changes in refractive index and osmolarity", *J. Biomedical Optics* 1, 200-211 (1996).

6. B. Grzegorzewski. S. Yermolenko, "Speckle in far-field produced by fluctuations associated with phase separation", *Proc. SPIE* **2647**. 343-349 (1995).

7. V. V. Tuchin. I. L. Maksimova, D. A. Zimnyakov et al., "Light propagation in tissues with controlled optical properties", *J. Biomedical Optics* **1**. (1997).

8. V. V. Tuchin. I. L. Maksimova, D. A. Zimnyakov, I. L. Kon, A. H. Mavlutov, A. A. Mishin, "Light propagation in tissues with controlled optical properties", *Proc. SPIE* **2925**, 118-142 (1996).

9. V. V. Tuchin. I. L. Maksimova, V. I. Kochubey, I. L. Kon, A. H. Mavlutov, A. A. Mishin, S. V. Tuchin, D. A. Zimnyakov, "Optical and osmotic properties of human sclera. *Proc. SPIE* **2979-96** (1997).

10. P. Rol. P. Niederer, U. Dürr, P.-D. Henchoz, F. Fankhauser, "Experimental investigation on the light scattering properties of the human sclera", *Laser Light Ophthalmol*. **3**. 201-212 (1990).

11. V. V. Tuchin. Coherent and polarimetric technologies for the analysis of tissue structure (overview). *Proc. SPIE* **2981-15** (1997).

12. D. A. Zimnyakov, V. V. Tuchin, K. V. Larin. "Speckle patterns polarization analysis as an approach to turbid tissues structure monitoring". *Proc. SPIE* **2981-17** (1997).

13. I. L. Kon. V. V. Bakutkin. N. V. Bogomolova, S. V. Tuchin, D. A. Zimnyakov, V. V. Tuchin, "Trazograph influence on osmotic pressure and tissues' structures of human sclera", *Proc. SPIE* **2971-45** (1997).

14. V. V. Tuchin. T. G. Anishchenko, A. A. Mishin, O. O. Soboleva. "Control of bovine sclera optical characteristics with various osmolytes", *Proc. SPIE* **2982-33** (1997).

Liquid Crystal Phase Modulators for Time Varying Phase Distortion ~~Simulations~~

Production & AO.

Stephen Browne
the Optical Sciences Company

Alexis Kudryashov
⟶ John Gonglewski
Air Force Phillips Laboratory, PL/LIMI, Albuquerque, NM 87117
(505) 853-3253, FAX (505) 846-2045

Ron Highland
Kaman Sciences Corp., 6400 Uptown Blvd. Suite 300E, Albuquerque, NM 87112
(505) 846-1432, FAX (505) 846-2045

June, 1997

BC-905
- 1 -

the
Optical
Sciences
Company

Overview

- We have used a 127-element liquid crystal Spatial Light Modulator (SLM) to produce phase screens that simulate atmospheric turbulence.

- We have introduced the turbulence as a disturbance to a Shack-Hartmann wavefront sensor (WFS).

- The error signal from the WFS has been used to drive a deformable mirror so as to correct the disturbance.

- The performance of the adaptive optical system is demonstrated by measuring open and closed loop Strehl ratios for various turbulence strengths.

- We comment on using LCPM as a "Deformable Mirror"

Background

- Liquid Crystal (LC) phase modulators or retarders can induce controlled, repeatable, dynamic aberrations into optical systems at low cost, low complexity, and high flexibility.

- Used as wave front correctors they have several advantages
  - low power density (10^{-4} - 10^{-5} W/cm^2)
  - wide range of phase delay (up to 6 mm)
  - high transparency (> 70%) for $0.5 \le \lambda \le 6$ μm

- LC's show promise for atmospheric wave front correction, but as yet are limited to low temporal and spatial frequencies. Using the device for simulating atmospheric turbulence is an important demonstration of the limitations and potentialities of such modulators.
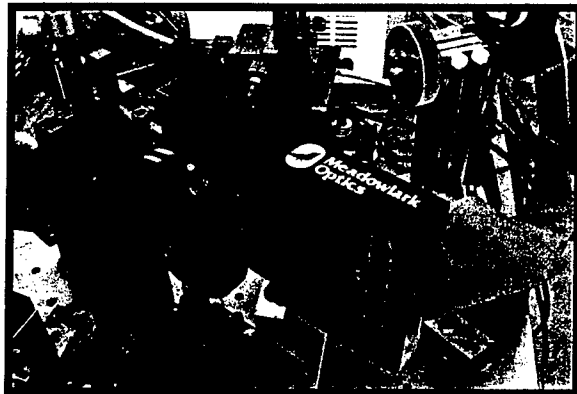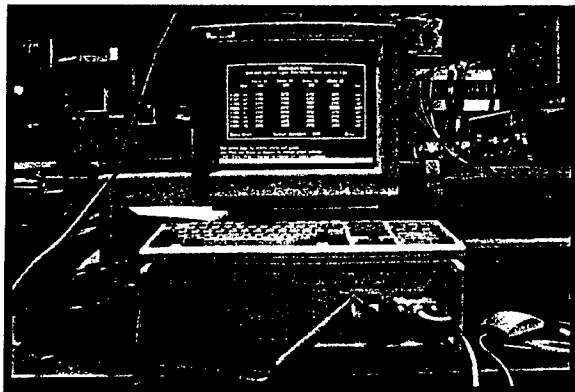
Meadowlark SLM-127
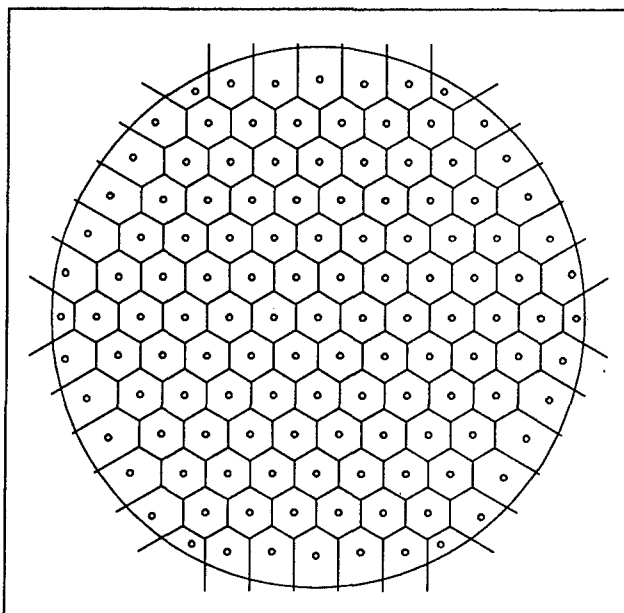
- 127 hexagonal elements
- 13 x 13 array
- D = 1.1 cm
- 1 full wave of phase retardance at λ=670 nm
- 0 – 10V AC operation
- Meadowlark controller operates from PC
- Hollow dots represent element center locations for modeling

Liquid Crystal Phase Modulator (LCPM)

Meadowlark Optics Hex127

- Element Area - 2.81 mm^2
- 1 HeNe Wave (0.63 μm) Phase Delay
- Transmission > 95% @ 0.67 μm
- Diffraction Losses ~ 4%
- Separation Between Elements - 25 μm
- LC Thickness - 2.5 μm
- Threshold Voltage - 1.2 V
- Control Voltage Range 0-10 V
- Control Voltage Frequency - 2 kHz

Present Experimental Configuration

Laser Source · SLM Disturbance · Deformable Mirror · Relay Optics · Focal Plane · Shack-Hartmann Wave-Front Sensor · Wave-Front Reconstructor and AO Control System
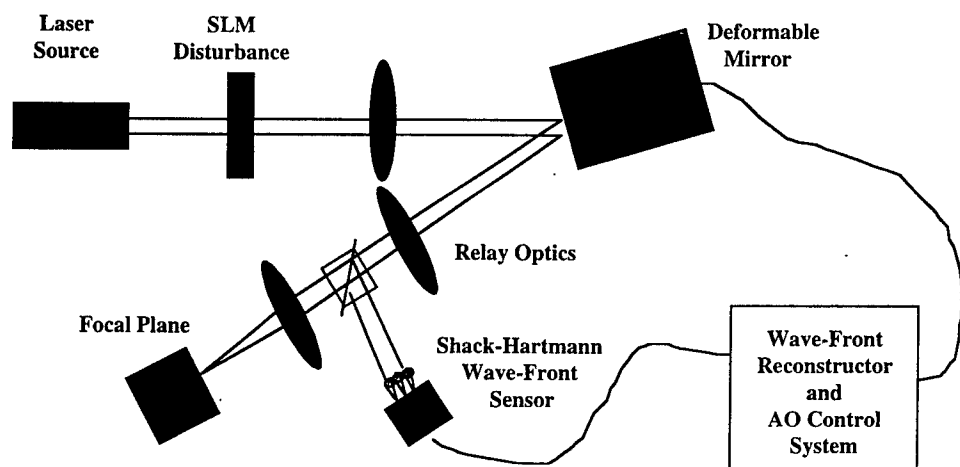
Present Laboratory Configuration: SLM Disturbance
DM Correction
Shack-Hartmann WFS

Moving Turbulence

- We represent non-slewing turbulence at any instant as a single phase screen equivalent to a stack of "frozen" virtual screens, each moving with wind velocity, v, in its own random direction perpendicular to the line of sight (LOS).

- For each frozen virtual screen, the phase fluctuation at position, r, and time, t, is the same as at position r+vΔt at time t+Δt.

- Isotropy dictates that the temporal statistics of turbulence are a function of the magnitude of v, and not its direction. For a non-slewing LOS,

$$v = 2.34 f_G r_0$$

Moving Turbulence (Continued)

- We use an FFT approach to generate the Zernike coefficients, $a_i(t)$:
  - initialize a 64-element complex array of temporal frequencies with uniformly distributed random variables of unity standard deviation,
  - force the negative frequency elements to be the complex conjugate of the positive frequencies, and the DC term to be zero,
  - multiply by a filter function proportional to $(\omega/v)^{-11/6}$,
  - take the Fourier transform, and
  - multiply the resulting time sequence of numbers by

$$\left[C_{ii} (D/r_0)^{5/3} \right]^{1/2}$$

Experimental Setup for Atmospheric Phase Screen Simulation
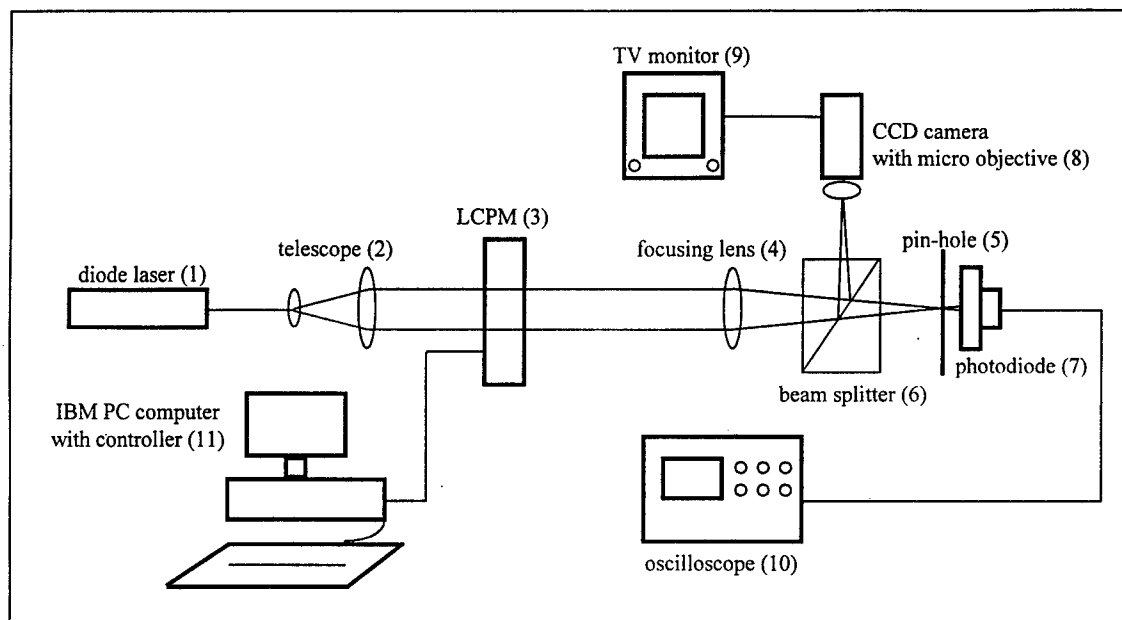
Diode laser wavelength = 670 nm, lens focal length = 300 mm, pinhole diameter = 25 μm

$$D/r_0 = 12$$

experiment: r0=0.08, number 2   theory: r0=0.08, number 2
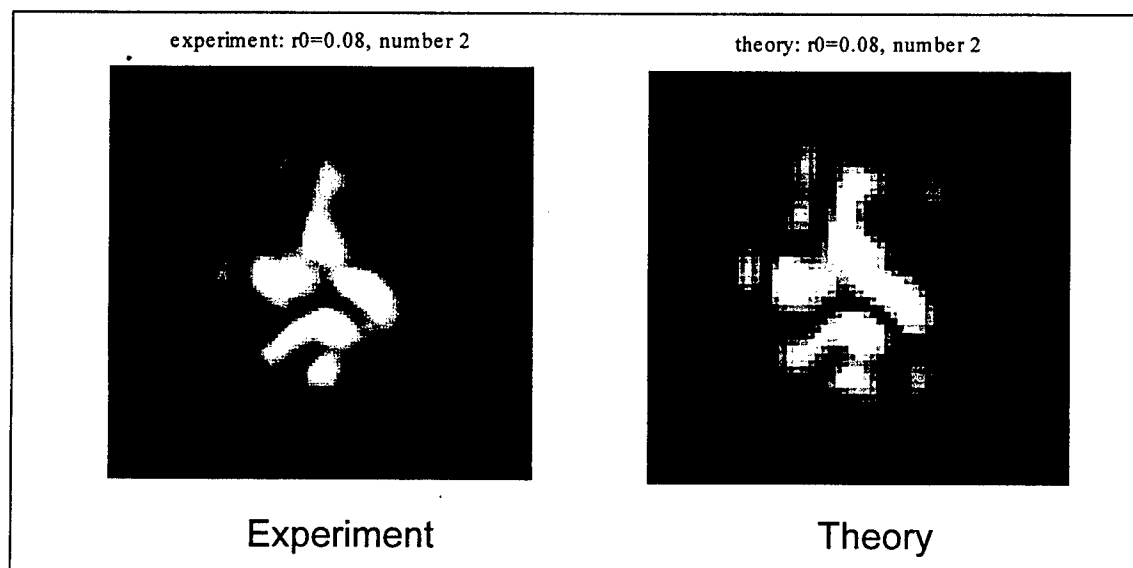
Experiment   Theory

Far-Field Intensity Patterns for Time-Correlated Moving Turbulence

- $D/r_0 = 25$
- $f_G = 0.25$ Hz
- $\Delta T = 0.5$ sec
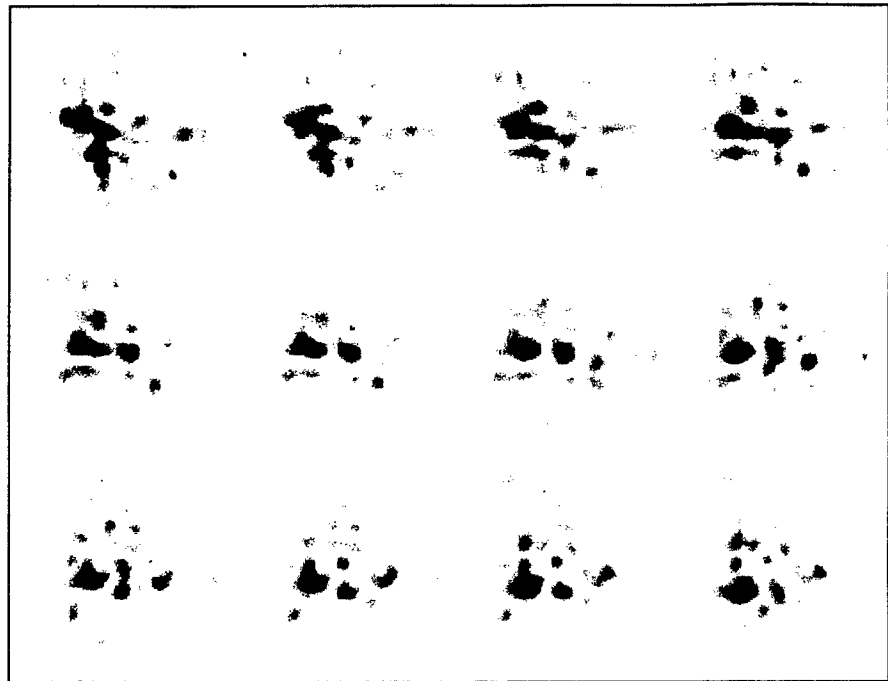
Sequence is horizontal raster scan, top left to bottom right

BC-905
- 20 -

The Optical Sciences Company

Dynamic Characteristics of SLM

- Transition time depends on initial voltage, step amplitude, and step direction
- LCs are normally slower switching from high to low voltage than reverse
- LCs are normally slower switching over a small positive step than a large one
- For our SLM, this means a long (~200 msec) settling time from one arbitrary phase screen to the next
- Major improvements in switching times will have to be made on these devices before they are useful as real-time atmospheric turbulence simulators

The Optical Sciences Company

Liquid Crystal Phase Modulator/ Adaptive-Optics Experiment
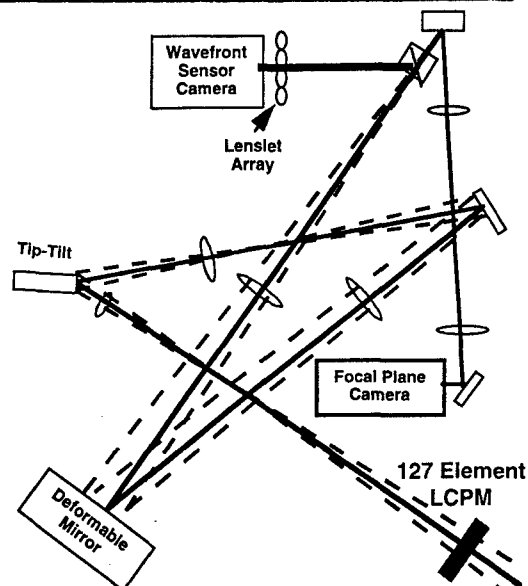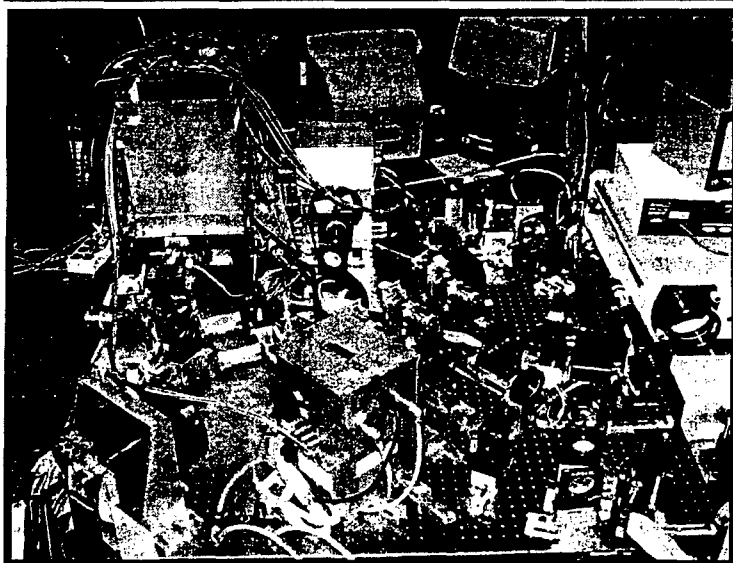
Focal Plane Camera
128X128 Si CCD
250 FPS
Low Noise

Pupil Plane Camera
64X64 Si CCD
1000 FPS
Low Noise

Mirror
Stroke 6 μm
163 Active Actuators
Hexagonal Pattern
Digital Storage of all Frames
Image Stabilizing Tracker

Meadowlark Optics Hex127
LC Thickness - 2.5 μm
Threshold Voltage - 1.2 V
Control Voltage Range 0-10 V
Control Voltage Frequency - 2 kHz
Element Area - 2.81 mm²

Dynamic Response of SLM

- We switched the SLM from a flat phase screen to 1.0 waves of focus error

- 100 msec is required to switch from flat to 1 wave defocus

- 400 msec is required to switch from defocus back to flat

- The long switching time in the "fast" direction is due to those SLM elements which experience a small phase change

Focus Disturbance Switching Times

- These two switching times suggest a slow, 2 Hz disturbance bandwidth

The
Optical
Sciences
Company
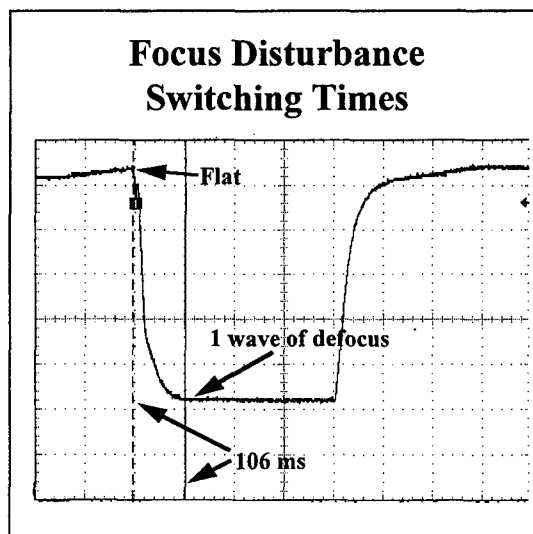
Disturbance, Sensor, and Corrector Geometric Relationships

- **Hexagonal SLM, used for disturbance, introduces piston in each element**
- **Hexagonal lenslet array used for Hartmann wavefront sensor**
  - magnified 1:1 to match SLM elements
  - shifted in both x and y, since Hartmann WFS can't detect piston
  - each SLM actuator piston appears as slopes in three WFS subapertures
- **Hexagonal deformable mirror with 169 elements used as corrector**
  - magnified 1:1 to match WFS subapertures
  - shifted in x and y for a triangular geometry

Simulation Results
Cross-Section of Shack-Hartmann Spot
Two Segments Per SH Sub-Aperture

SLM Displacement Two Segments Across SH Sub-Aperture
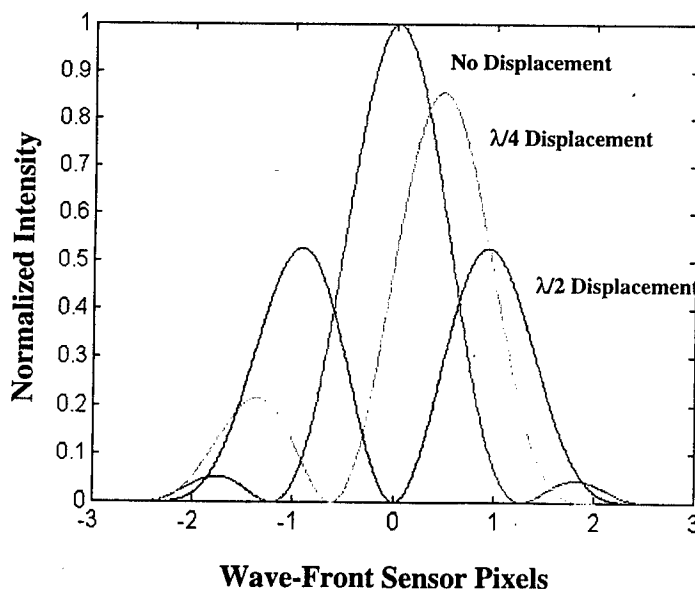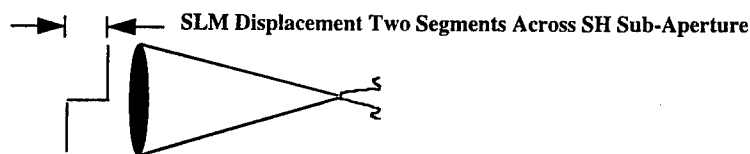
- **Hartmann Spot Becomes Bi-Modal As SLM Segment Displacement Approaches $\lambda/2$**
- **Centroid Measurement Error Goes to 100 Percent**

No Displacement

$\lambda/4$ Displacement

$\lambda/2$ Displacement

Normalized Intensity

Wave-Front Sensor Pixels

Simulation Results
Shack-Hartmann Centroid Error
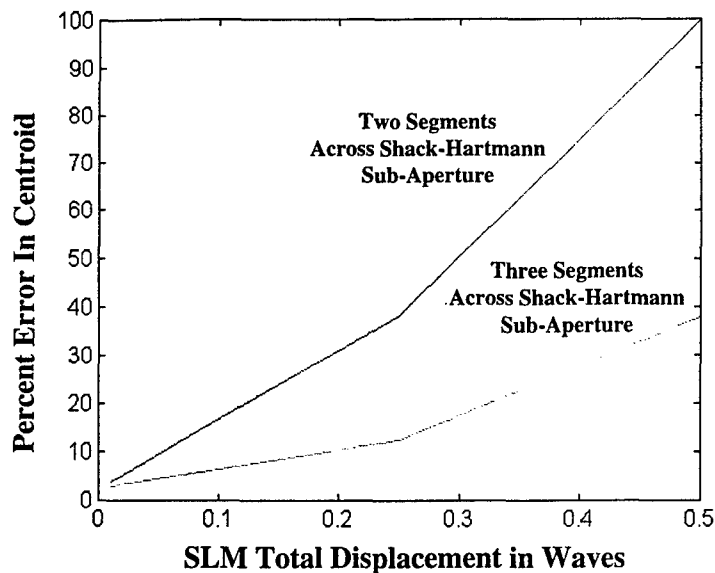
Percent Error In Centroid vs. SLM Total Displacement in Waves

Two Segments Across Shack-Hartmann Sub-Aperture

Three Segments Across Shack-Hartmann Sub-Aperture

Two Segments Across Shack-Hartmann Sub-Aperture
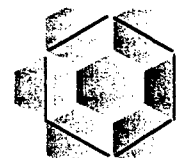
Three Segments Across Shack-Hartmann Sub-Aperture

SLM Element and WFS Subaperture Geometric Relationship

Active Area of SLM

--- 127 SLM Elements
— 148 Subapertures

Active Area of Mirror
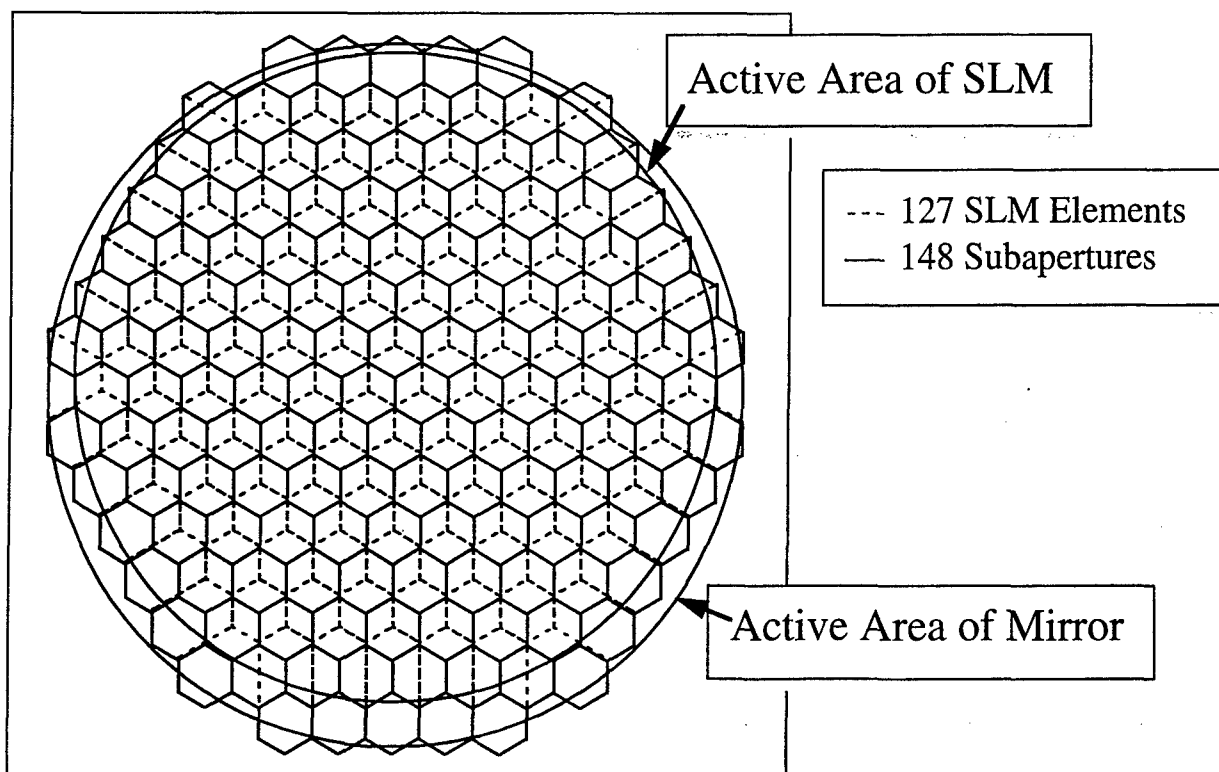
Correcting the SLM Disturbance

	25 λ\D	12 λ\D	8 λ\D
Open Loop	Strehl=0.22	Strehl=0.30	Strehl=0.46
Closed Loop	Strehl=0.34	Strehl=0.65	Strehl=0.63
	$D/r_0 = 25$	$D/r_0 = 12$	$D/r_0 = 8$
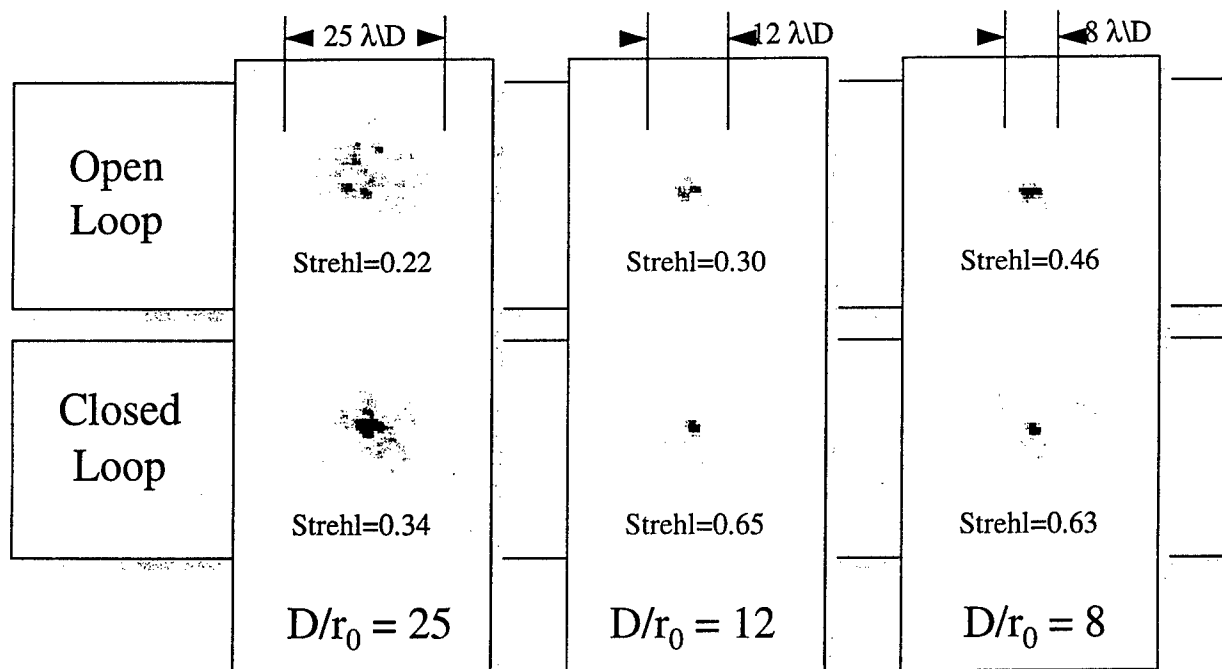
Open and Closed Loop Comparison

12		Open
		Closed
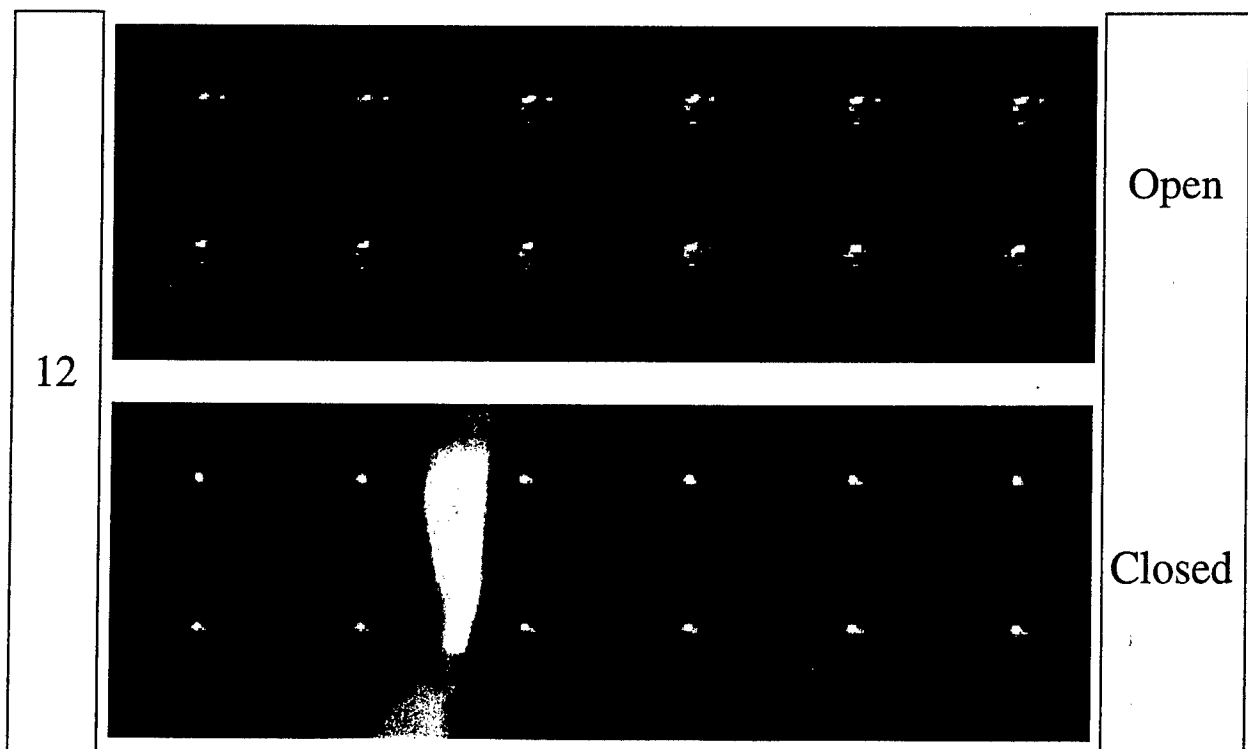
Conclusions

- **SLM -- Low Cost Adaptive Optics for Instrumentation**
- **When Used With Shack-Hartmann Sensor**
  - High Order Shack-Hartmann Spot Aberrations
  - Inter-Segment Discontinuity Must Be Constrained $< \lambda/2$
- **Phase Shifting Interferometer(PSI)**
  - Measures Phase Directly
  - More Complicated
  - May be More Appropriate — OR OTHER WFS ??
- **Future Work**
  - Laboratory Experiments With PSI
  - Closed Loop Operation of SLM with DM as a Disturbance Source

SLM Wave-Front Corrector Proposed Configuration
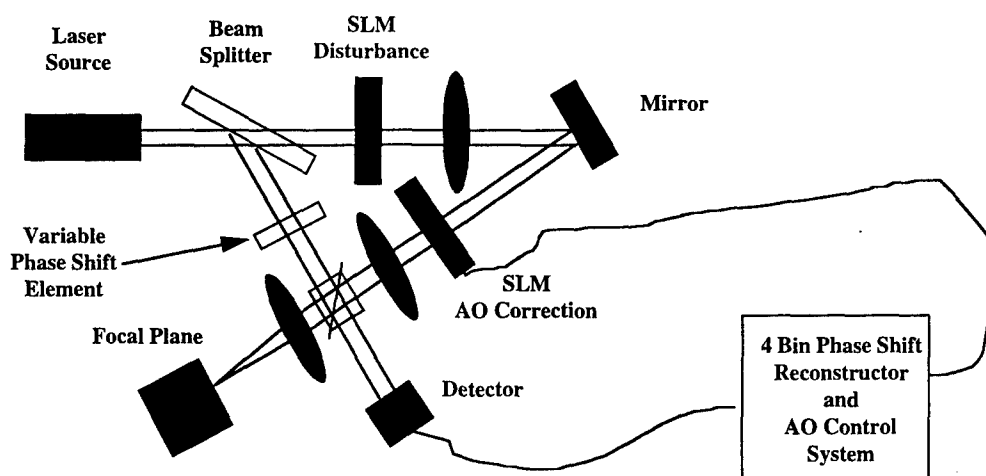
A Fast SLM for the Future

- **Goal**
  - λ/10 performance
  - 1 msec settling time to provide 500 Hz operation
- **Solution**
  - Dual-frequency LC material
  - TNE timing calibration
    - * 200-element pre-calibrated look-up table
      - 10 voltage steps
      - 10 starting voltages
      - 2 directions
    - * electronics
      - 10 μsec resolution
      - "smart" DACs that each access the look-up table and switch voltages based on the initial and final phases between two states
      - 30 VAC driving capability with two frequencies on all channels
      - temperature stabilization of SLM

BC-905
- 23 -

The
Optical
Sciences
Company

The electrical and optical properties of liquid devices for adaptive optics.

Gordon D. Love[*†], David F. Buscher[†], Alan Purvis[*]
David J. Robertson[†], and Ray M. Sharples[†].

Nathan Doble..

[*]School of Engineering and [†]Department of Physics
University of Durham, South Road, Durham, DH1 3LE, U.K.
Tel: +44-191-374-7496
Fax: +44-191-374-3709
Email: g.d.love@durham.ac.uk

The use of adaptive optics (AO) for wavefront compensation other than for atmospheric turbulence is an emerging, exciting field. The required system specifications will obviously be dependent on the particular application, and indeed may not be well-characterized for many of the potential uses. Liquid crystal spatial light modulators (LC-SLMs) are also an emerging technology within the field of AO. With this in mind we present here a summary of the specifications of both currently available and predicted LC-SLMs which may be used as wavefront correctors, and discuss how they may be particularly suited for use in non-astronomical AO systems.

Liquid crystal devices have generally been used as amplitude modulators in the display industry, but they may equally well be used as phase modulators. In general there are two classes of liquid crystals of interest, namely *nematics* and *ferroelectrics*. Here we concentrate on describing nematic devices, because currently they are more suitable for analog phase modulation (this state of affairs may change in the future as fast analog ferroelectric devices become available). The available devices can also be sub-divided into electrically addressed and optically addressed. We describe the electrically addressed devices, simply because they can be thought of as analogous to a deformable mirror in a conventional AO system. Other authors have described work on all-optical AO systems (e.g. the review by Pepper[1]).

Table 1. shows a summary of the specifications of nematic LC-SLMs. We describe the properties using usual AO terminology, rather than typical LC parameters which are generally aimed towards display applications. These specifications are stroke or throw, number of actuators, actuator impulse function, fill factor, optical quality, transmittance, dispersion, temperature effects, hysteresis, polarization effects, response time, electrical drive requirements and cost. We invite correspondence from workers who are interested in parameters which we have not mentioned here. We also note that table 1. represents the current state-of-the-art as we see it, of an evolving area.

Parameter	Typical Value	Notes
Stroke (Phase Shift)	Typically several visible waves (~2μm)	Stroke = birefringence x cell thickness Typical birefringence = 0.2 . Typical cell thickness = 10μm Larger strokes are available simply by increasing cell thickness
Number of actuators (pixels)	127 total in currently available devices specifically for AO[2]. LCTVs have also been used for AO with very large no's of pixels.	Much larger arrays are available. E.g. 128x128 or 256x256 in currently available VLSI designs which potentially are suitable for AO.
Actuator impulse function	Piston-only	Tip-tilt actuators have also been made which could be adapted into arrays[3].
Fill factor	>90%	
Optical Quality	<λ/5 P-V	Typically LC displays do not have good optical quality. It is possible to build very high quality devices, e.g. λ/26 P-V, λ/142 rms. (at 0.633 μm) has been measured[4].
Transmittance	>90%	Devices need to be made from index matched materials with AR coatings. Note also that LCs can be made to operate in reflection or transmittance.
Wavelength Bandwidth	Full visible and most of IR	LCs transmit from the blue to >10μm except for particular molecular absorption bands in the IR[5].
Dispersion	Typically 5% over 150nm bandwidth in the visible	In the IR the average dispersion is small, except near absorption bands.
Temperature Effects	Change in birefringence with temperature is small	LCs are only in the liquid crystalline state at certain temperatures, typically 0 to 100°C.
Hysteresis	None	
Polarization Effects	Generally, LCs can only phase modulate polarized light	Can use device with 2 LC layers[2], or a quarter-wave plate in reflection[6] to modulate unpolarized light.
Response time	Typically 45ms for a 1λ round trip time, if total excursion is	Faster materials are being assessed, in particular using the dual frequency

		effect[7,8].
	restricted to be 1 λ. For several waves time ~100's ms.	
Driving requirements	~0 to 10V AC (~10KHz)	LCs draw negligible current and hence do not require large power supplies
Cost	~ 5K to 30K US$.	Cost varies greatly depending on device. They have the ability to become low-cost if large numbers are required.

Table 1. Summary of the specifications of liquid crystal devices for adaptive optics.

The above specifications show that LC-SLMs have a number of features which mean they may be particularly useful for industrial and medical applications of adaptive optics. They are low cost in comparison to typical deformable mirrors (although not necessarily in comparison to new micro-machined mirrors). They have been proven as precise wavefront controllers whose pixels can be simply controlled. They operate (in general) in transmission and so can be incorporated into optical systems simply. For astronomical AO systems the largest drawback of LCs has been their relatively slow response time (although this point is now being addressed), which may not be an issue for many non-astronomical applications. Devices are currently being planned which have a very large number of actuators (> 64x64) pixels, and so if one is interested in a very high degree of correction LCs may be the only option available.

In contrast LCs cannot handle very large optical power densities and so may be unsuitable for certain laser applications. They may also not be suitable where extreme temperature fluctuations are to be expected (>100°C).

[1] D M Pepper , C.J. Gaeta, and P.V. Mitchell. "Real-time holography, innovative adaptive optics, and compensated optical processors using spatial light modulators." In *Spatial Light Modulator Technology*, U. Efron, Ed. pp585-665, Marcel Dekker, Inc. (1995).

[2] Gordon D. Love, Sergio R. Restaino, Richard C. Carreras, Gary C. Loos, Rob V. Morrison, Tom Baur, and Greg Kopp. "Polarization insensitive 127-segment liquid crystal wavefront corrector." OSA summer topical meeting on adaptive optics. (1996).

[3] Gordon D. Love, John V. Major, and Alan Purvis. "Liquid crystal prisms for tip-tilt adaptive optics." *Opt. Lett.* 19(15):1170-1173 (1994).

[4] Gordon D. Love. "Wavefront correction and production of Zernike modes with a liquid crystal spatial light modulator." *Appl. Opt.* 36(7):1517-1524 (997)

[5] S.T. Wu, U Efron, and L.D. Hess." Infra-red birefringence of liquid crystals." *Appl. Phys. Lett.* 44(11):1033-1035 (1984).

[6] G.D. Love. "Liquid crystal phase modulator for unpolarized light." *Appl. Opt.* 32(13):2222-2223 (1993).

[7] M. Schadt. "Low-frequency dielectric relaxations in nematics and dual frequency addressing of field effects." *Mol. Cryst. Liq. Cryst.* 89:77-92 (1982).

[8] A.A. Vasil'ev, A.F. Naumov, and V.I. Schmal'gauzen. "Wavefront correction by liquid crystal; devices." *Sov. J. Quantum. Elec.* 16(4): 471-474 (1986).

THE CONTROL FEATURES OF LIQUID CRYSTAL MODULATORS FOR ADAPTIVE OPTICAL APPLICATIONS

Alexander F.Naumov (naumov@info.ssu.samara.ru)

Russian Academy of Sciences P.N. Lebedev Physical Institute Samara Branch,
Novo-Sadovaya st.221, Tel: (007)(846 2) 34-73-96, Fax: (007)(846 2) 35-56-00

INTRODUCTION

The commercially available liquid crystal (LC) light valves were developed in the middle of 1970s and had been extensively used for display applications [1], later for laser optics [2,3], for radar applications [4] and even for generation of femtosecond optical pulses [5]. However in adaptive optics LCs became to use recently. Probably, not all resources of deformable mirrors were exhausted. Now the situation has changed. Already there are a high technology of manufacturing of commercially available liquid crystal wavefront correctors for adaptive optics specially [6] and hardware for their control. I shell not repeat all merits and demerits such devices. You can find its in Ref. 7 and references therein. But, as rule, no one take attention features of LCs except for a necessity of alternating control voltage using to prevent the electrolytic dissociation of LC molecules. In my report I would like to attract attention to features of adaptive optical elements based on nematic LCs with initial planar orientation and to regard use of these features for adaptive optic applications.

0. FEATURES LC ADAPTIVE OPTIC ELEMENTS

1. The necessity to use of an alternating control voltage to prevent the electrolytic dissociation and polarization of LC molecules.
2. Phase delay in the LC layer is determined by the effective value of the voltage modulus.
3. Nonlinear character of the response time of LC correctors, depending on the control voltage and the layer thickness.
4. It is necessary to take into consideration the spectral composition of the control voltage.
5. LC correctors have parametric capacitance.
6. Scattering near the threshold and at the moment of inversion of dielectric anisotropy for LCs with low-frequency sign inversion of dielectric anisotropy.
7. Optoelectronic characteristics have strong temperature dependency.
8. Existence of the threshold voltage and possibility variation of it by initial orientation selection .

1. ALTERNARING CONTROL VOLTAGE

The control birefringence of LC layer can be induced both by static and alternating electrical field. In the case of static fields the current must flow through electrodes, so electrodes' processes become important. The electric field in the liquid crystal layer becomes inhomogeneous and is determined by anisotropy conditions. Double layers are formed at the electrodes, which decrease the field in the cell, so a higher applied voltage is needed to reorient the layer as in the case of alternating fields. Development of the double layers takes several seconds [8], so they can be completely neglected for alternating fields.

1

The use of unipolar voltage is no desirable too. The unipolar pulse voltage causes polarization of liquid crystal and this circumstance increases the relaxation time after switching off of control voltage [9].

Low frequency dual polarity control voltage can stimulate electro-hydrodynamical instability [10] when the frequency $\omega<1/\tau_e$ [11] where $\tau_e \approx \varepsilon_{\parallel}/4\pi\sigma_{\parallel}$ is the dielectric relaxation time, $\varepsilon_{\parallel}$ is dielectric permittivity along initial orientation, and $\sigma_{\parallel}$ is specific electric conductivity measured in the same direction. Besides, conductive currents can simulate hysteresis [12]. This circumstance can be avoided by changing LCs with high $\sigma_{\parallel}$.

In practice, in order to avoid ion displacements we shall use an alternating bipolar voltage of frequency greater then the carrier relaxation frequency. In the case of alternating field we assume the frequency to be high enough that the alignment of the molecules cannot follow the alternation of the field (typically>100Hz) but low enough, that the polarization can follow it (typically<10^6Hz).

2. MODULUS OF CONTROL VOLTAGE

The orientation of nematic LC molecules (the phase delay value) depends on the effective value of the voltage modulus. This allows to develop a new type of wavefront correctors [13]. I have named theirs modal wavefront correctors because theyhave control distributed in aperture like modal deformable mirrors. The simplest modal LC corrector is a cylindrical adaptive lens (Fig. 1a). The cylindrical lens has the transparent low-Ohmic electrode and the transparent high-Ohmic electrode coated by two equidistant line conducting contacts over aperture cell edge. Electrically this element can be represented by means of distributed capacity and resistance (Fig. 1b). Electrical voltage distribution is described by the Laplace equation:

$$\frac{\partial^2 U}{\partial x^2} = RC(U)\frac{\partial U}{\partial t}. \tag{1}$$

In approximation $RC = const$, the stationary distribution of voltage can be obtained for harmonic control voltages $U_1=U_0\sin(\omega t)$ and $U_2=U_0\sin(\omega t+\varphi)$ analytically. But now we are developing the more common model which includes the dynamics of modal LC correctors. The results of numerical observations are shown in Fig. 2a,b.
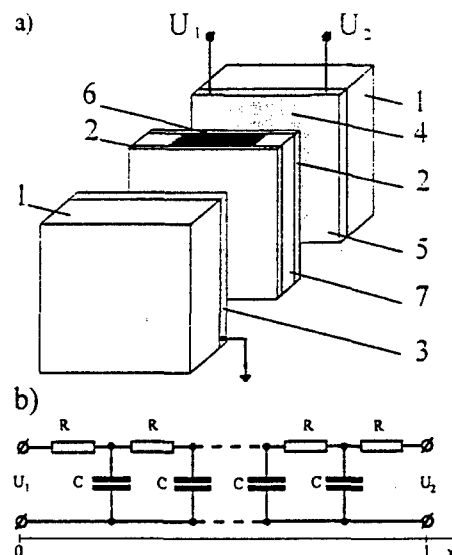

Fig. 1 Adaptive cylindrical lens - a) set-up, b) equivalent electrical scheme: (1) glass substrates, (2) oriented covers, (3) transparent low-Ohmic electrode, (4) transparent high-Ohmic electrode, (5) equidistant conductive contacts, (6) LC layer, (7) spacers. (U_1 and U_2) control voltages.
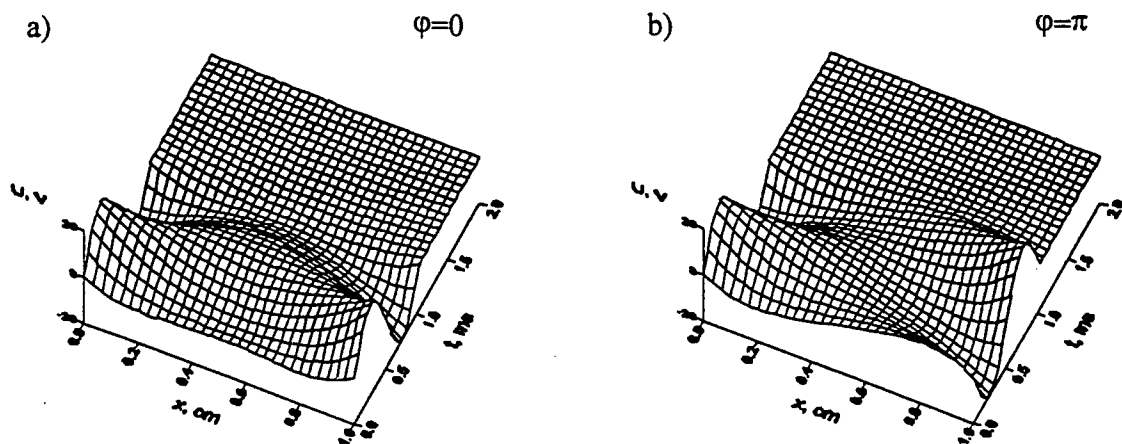
a)   φ=0   b)   φ=π

Fig. 2. Dynamics of voltage variation in cylindrical adaptive lens.

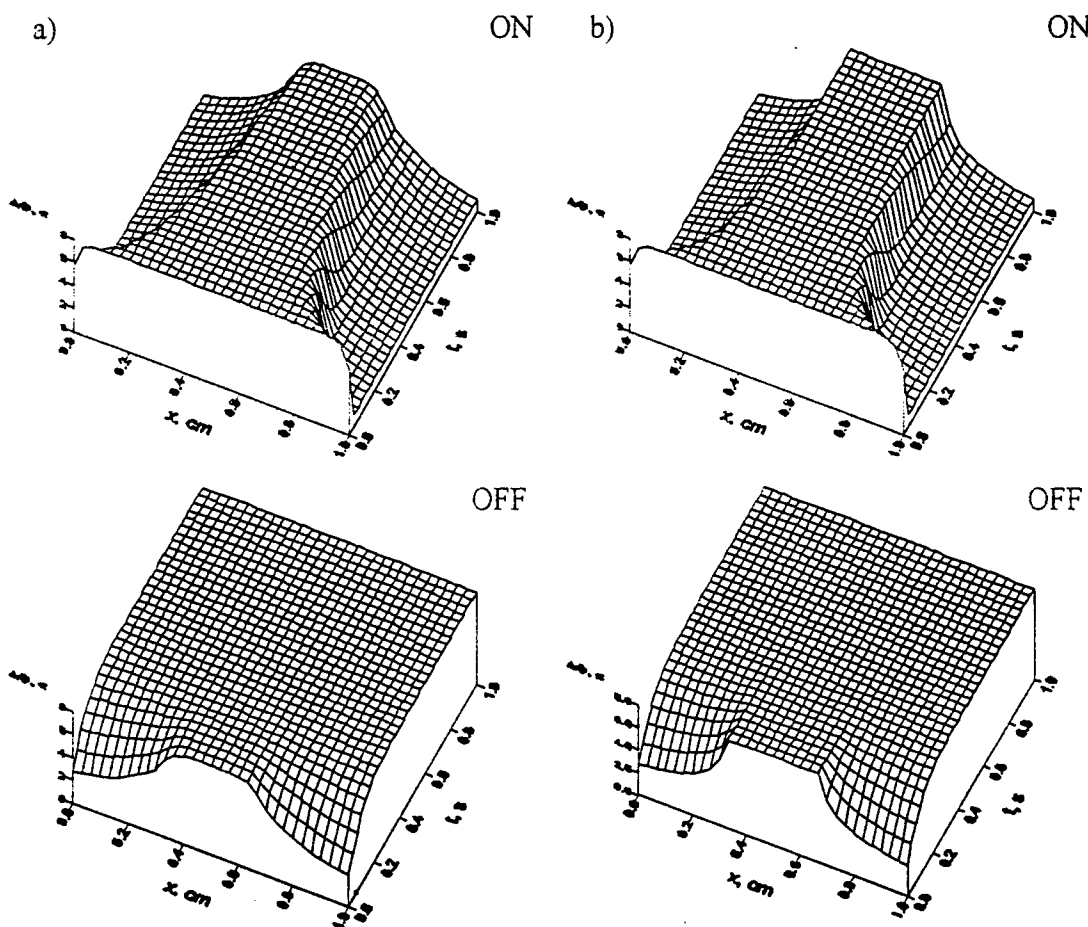a)   ON   b)   ON

OFF   OFF

Fig. 3. Phase replay of LC layer.

I have cut off transition process from switching on moment of control voltage till $S \cdot RC$ where S is square of the LC cell. I have kept one period of voltage variation and transition process of voltage switching off. This will be important in our subsequent consideration. LC phase replays at shown in Fig. 2a,b voltage distributions are represented in Fig. 3a,b, accordingly. It is necessary to say that these figures were calculated without taking account for electrical transition process. This is very rough approximation but temporal scales in

Fig. 2 and Fig. 3 differ in one thousand times. The processes of switching on and switching off are shown separately. The phase delays have cylindrical shapes and LC cell works like a cylindrical lens. The shape of phase delay distribution depends on RC and feeding voltage parameters.

Modal LC correctors can be control by variation of feeding voltage spectrum. For example, the rectangular and serrated dual polarity feeding voltage give different phase distributions (Fig. 4a,b). Represented results have been obtained for first ten harmonics and experimental dependency $\Delta\Phi(U)$. Searching of the controlling voltage shape at the desirable profile of phase delay distribution is enough challenge. In the simplest case we can attempt to find the feeding voltage shape to minimize the mean square deviation from parabola phase delay distribution [14]. The phase delay distribution, voltage modulus one and the intensity distribution in focal plane are shown in Fig. 5 for the ideal LC cylindrical lens (Fig. 5a), for real lens with simple sine feeding voltage (Fig. 5b) and with feeding voltage of complex shape (Fig. 5c). This shape is represented in (Fig. 5d).
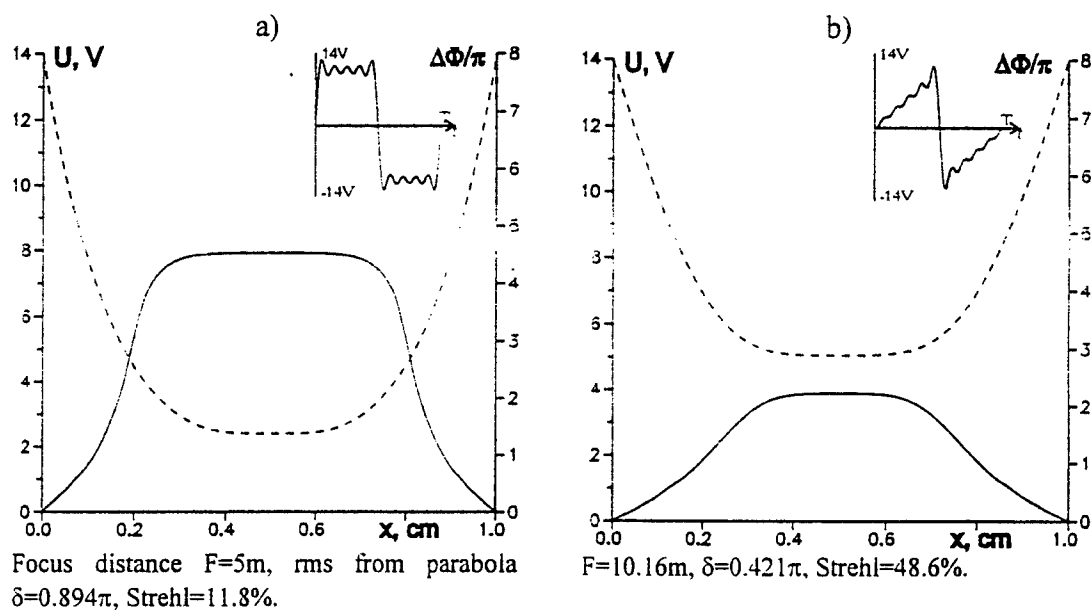

Focus distance F=5m, rms from parabola δ=0.894π, Strehl=11.8%.

F=10.16m, δ=0.421π, Strehl=48.6%.

Fig. 4. Control voltage shape. modulus of them distribution (dotted line) and LC phase replay.

The adaptive spherical lens has the same design but the conducting contacts should be made in the circle form.

The another more complex modal correctors is shown in Fig. 6. It has 16×16 electrodes with 0.3mm gaps between them. The resistance between neighbours electrodes is 20kOm, and the LC thickness is 12μ. From Eq.1 at boundary condition $U_{x=0}=U_0\sin(\omega t)$ and $U_{x=\infty}=0$ we can obtain the voltage distribution for any separate electrode:

$$U(x,t) = U_0 \exp(-\alpha x)\cos(\omega t - \alpha x),\qquad(2)$$

where $\alpha = \sqrt{\omega RC/2}$. By increasing feeding voltage frequency the mutual influence between electrodes is decreasing. This is illustrated by means interferograms in Fig. 7.

Thus, to suppress wavefront aberrations by means such corrector in the first place it is necessary to introduce low frequency control voltages for low-order aberrations, and then to add high frequency control voltages.

F=4.95m, δ=0π, Strehl=100%.

F=4.95m, δ=1.004π, Strehl=6.47%.

F=4.95m, δ=0.089π, Strehl=83.8%.

Fig. 5. Selection of optimal control voltage: a)-c) phase delay and voltage modulus distributions (dotted line) and intensity distribution in focal plane (upper part of drawing); d) shape of optimal control voltage. The real interferogram is placed. in the right lower corner of b)
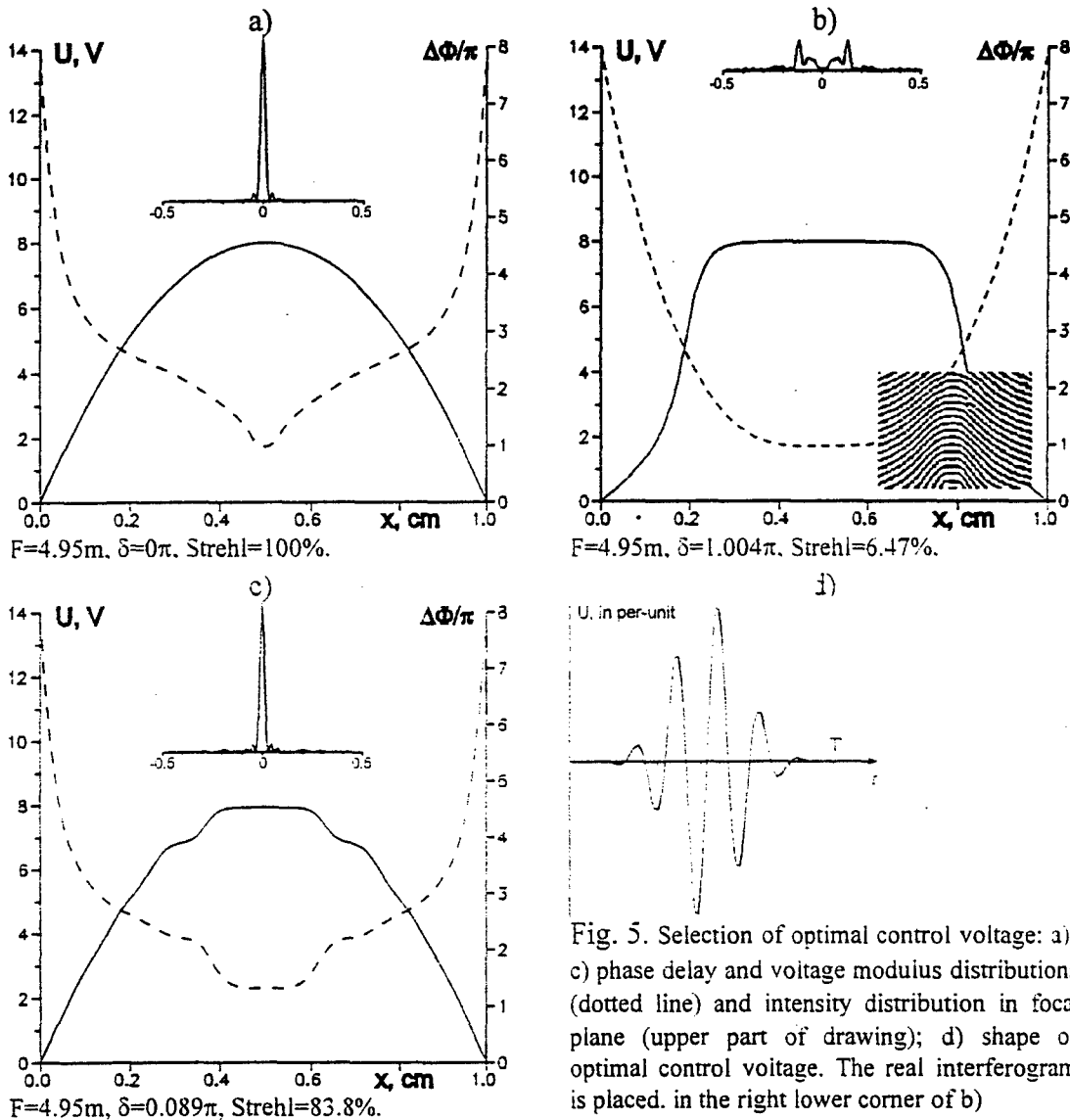
Fig. 6. Many electrodes modal corrector: (1) LC layer; (2) glass substrate; (3) transparent low-Ohmic layer; (4) high-Ohmic layer; (5) control electrodes; (6) spacers; (7) oriented covers; (8) dielectric mirror.
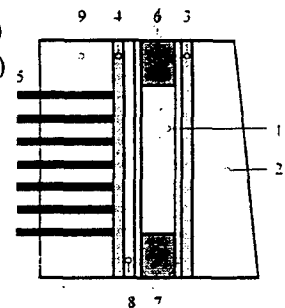

Fig. 7. Response function of one electrode: a) frequency is 2kHz; b) frequency is 20kHz; c) frequency is 200kHz, U=10V.

5

3. RESPONCE TIME OF LC CORRECTORS

The rapidity of LC correctors is determined by the liquid crystal layer thickness as $\sim 1/d^2$ therefore thin cells are preferable for fast phase modulation. However, there are two problems. The first is a small depth of modulation which is more limited then given by theory [11]. The second is high probability of breakdown or short circuit. There is a critical value $60V/\mu$ [9] of the strong electrical field. In the real substrates the liquid crystal molecules surface alignment is seldom uniaxial due to the surface roughness, defects or irregular alignment treatments. The "virtually inactive" thickness is defined by the quality and preparation of the substrates. Under the conditions of strong anchoring and good surface quality, the thickness of the partially disordered surface layers is reduced. On the other hand, the large "virtually inactive" thickness is expected for weak anchoring and rough surface alignment. In Ref. 15 "virtually inactive" thickness is estimated as $\sim 0.3\mu$ for each surface, and in Ref. 16 an estimate of 0.5μ for the thickness of the inactive volume per cell is thus obtained.

The another important parameter for rapidity is amplitude of control voltage. Well known that the rise time decreased on increase in the control voltage as U^{-2} and the decay time do not depend from control voltage.

Adaptive systems with simple amplitude control have not high rapidity. The typical characteristic of such system is shown in . ___ ٦ۑe-ۑۑۑۑۑeۑ adaptive system represented stabilized interferometer operating on the basis of the aperture probing principle [17]

The dynamic control can be realized by varying switching on and switching off time at fixed voltage amplitude. Such control can be used for modal correctors. For example, the desirable focus distance can be achieved by this method. Fig. 9 shows focus variation of cylindrical lens after switching on and off of control voltage.
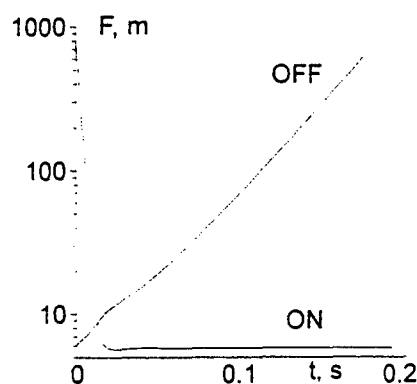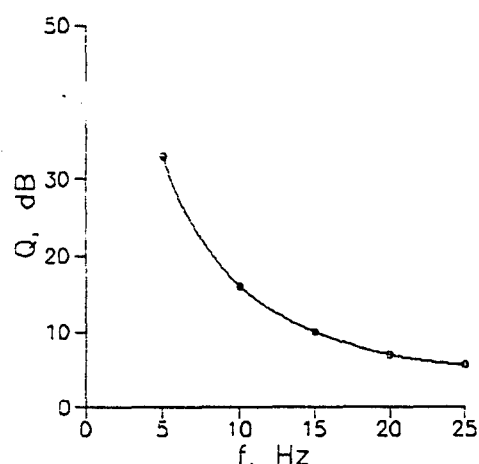

Fig. 8. External perturbations suppression coefficient Q in system with aperture probing, f is frequency of external perturbations.

Fig. 9. Focus variation according to Fig. 3a.

This method was modified for LCs with a low-frequency sign inversion of dielectric anisotropy. In this case the t_{off} value is comparable with the t_{on} and the first is determined by applied voltage as well. To decrease the phase delay by the quantity $\Delta\Phi$ it is necessary to apply a low-frequency voltage at the time $t_S = \Delta\Phi/\Phi_S'$ where Φ_S is the S-effect rate. In order to decrease the phase delay by the same quantity it is necessary to apply a high-frequency voltage at the time $t_B = \Delta\Phi/\Phi_B'$ where Φ_B is the B-effect rate. The ratio between t_S and t_B determines the birefringent state of the liquid crystal layer in dynamics. The static value of $\Delta\Phi$ depends on

harmonics of control voltage. Dual frequency control allows to increase rapidity significantly (Fig. 10) [18].

The idea of transient nematic liquid crystal effect [19] is to utilize the fast decay time due to the small relaxation angle because of highly deformed liquid crystal directors. A relatively high ac voltage is initially applied to the liquid crystal cell. As a result, almost all the molecules are aligned by the electric field almost orthogonal to the substrate surfaces except in the boundary layers. When these highly deformed directors start to relax, i.e., the voltage is removed completely, the directors undergo free relaxation. However, when the phase delay reaches the desirable value (this is possibly because of 2π phase degeneration), a voltage is applied to the cell to stop the directors' motion.
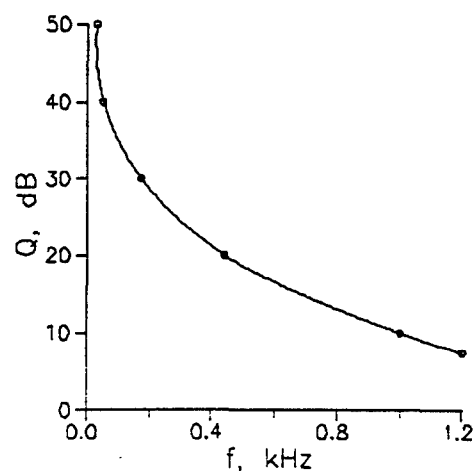

Fig. 10. External perturbations suppression coefficient in phase conjugation in stabilized interferometer.

Authors of [19] make difference between this mode of operation and bias voltage effect [20] (sometimes called surface mode), because bias voltage is constantly present during the relaxation process. The presence of this holding voltage provides an intermediate stopping force to the LC directors and, thus, decreases the relaxation time. In reality these effects have the same cause - bias voltage. In case of transient effect the control voltage represents the periodic or quasiperiodic pulse sequence. The periodic pulse voltage has low-frequency harmonic compositions which play a role of "bias" voltage. This will be clear from next section.

4. SPECTRAL COMPOSITION

When we use bipolar rectangular control voltage we can drive a modulator by variation of pulse period-to-pulse duration ratio $q = T/\tau$; T is period of pulse sequence, τ is pulse duration. Amplitude of m harmonics is given by

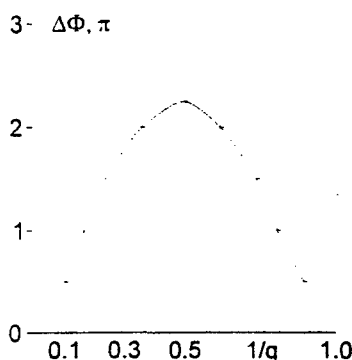$$a_m = \frac{2U_0}{\pi m} \sin\left(m\pi \frac{\tau}{T}\right).$$

(2)

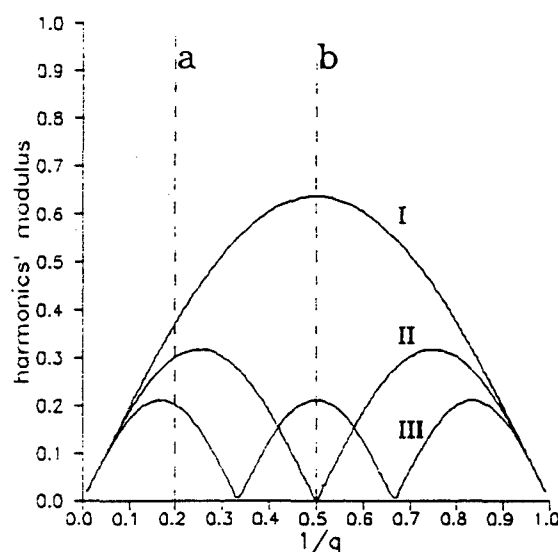Fig. 12. Dependence of the electrooptical response of LC on $1/q$; U_0=10V.

Fig. 11. Variation of harmonics' modulus as function of $1/q$; (I) first harmonics, (II) second harmonics, (III) third harmonics.

The given voltage represents a number of harmonics and each harmonics makes its contribution in the birefringence magnitude. Variation of parameter q leads to harmonics' amplitude change and, consequently, to variation of phase modulation depth in liquid crystal layer. For example, the total effect from harmonics in cases "a" and "b" (Fig. 11) is different. The experimental dependence $\Delta\Phi(1/q)$ is shown in Fig. 12

5. PARAMETRIC CAPACITANCE

The dependence $\Delta\Phi(1/q)$ is non-monotone. It repeats the sum of first harmonics' modulus. However, higher harmonics are shunted by a modulator capacitance.

Capacitance variation has the same nature as birefringence variation. This is orientation change of LC molecules. But in really this connection is more complex because of dielectric losses tangent.

Results of measurements of capacitance and electrooptic replay $|\Phi|=\Delta\Phi_{max}-\Delta\Phi$ are presented in Fig. 13. Here $\Delta\Phi_{max}=2d\Delta n/\lambda$ in π unit, d is LC layer thickness, Δn is optic anisotropy, and λ is wavelength. I have used the sine control voltage. In the case of voltage increasing curves $|\Phi|(U)$ and $C(U)$ are similar (Fig. 13a). For LCs with a low-frequency sign inversion of dielectric anisotropy frequency dependence is more complex (Fig. 13b). Since capacitance dependence correlates with the phase delay dependence, this complicates the feedback design significantly.
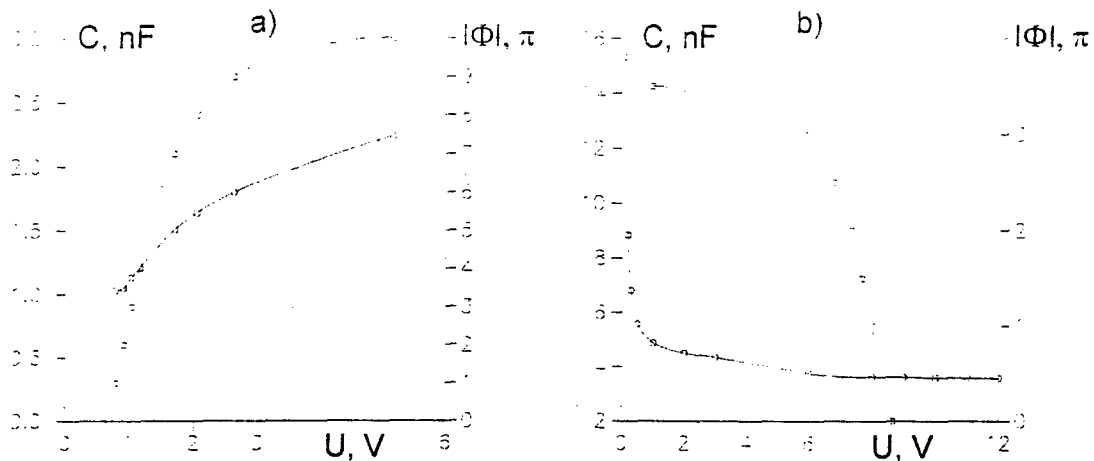

Fig. 13. Capacitance dependence of (solid line)on applied voltage for LC cell with LC654 (a) (f=1kHz) and frequency for LC1001 (b) ($U_{effective}$=10V); Electrooptic relay is shown by dotted line.

6. SCATTERING

Two-frequency addressing first have been proposed for dynamic-scattering-type liquid crystal displays. The cutoff frequency marks the transition from conductivity anisotropy regime to a dielectric anisotropy induced alignment regime [23].

In dual-frequency control experiment we also observed the light scattering at the instant of control voltage frequencies switching. However, the false error signal was not registered because it had the frequency beyond the transmission bandwidth of the feedback loop. The scattering can limit the rapidity of adaptive systems.

The another scattering types are connected with threshold existence and temperature fluctuations. They are wrote in literature in detail [24, 25].

7. TEMPERATURE DEPENDENCY

The rapidity and phase delay value have strong dependency from temperature. The first is connected with dynamic viscosity γ_1 which can be decreased by increasing temperature: $\gamma_1 \sim \exp(A/kT^\circ)$ where A is an activation energy [11], and k is the Boltzmann constant. But in this case elastic constant K_{11} is decreasing also: $K_{11} \sim S^2$ where S is the order parameter of the liquid crystal. The linear decrease of γ_1^* / K_{11} (this relation define the rapidity [22]) is observed when temperature is increased to some optimal temperature T_{opt}. Above T_{opt}, the elastic constant drops more significantly than the effective viscosity does, resulting in slower decay time [26].

8. THRESHOLD VOLTAGE

In wavefront sensors based spatial filtration there are some difficulties associated with formation and alignment of spatial filters. Space light modulators (SLM) which operate the light passing through them can be able to overcome these problem. When SLM operating in self-consistent filtration regime are used as the filters then the mentioned difficulties can be partially eliminated. Here the filter is produced automatically in accordance with the optical signal and no alignment is needed when the light beam incidence angle at the input of the optical system is changed. Existence of the threshold voltage can be used to select zero spatial component. We used this possibility for visualization phase distortions by the Foucault knife-edge method, by the autoreference interferometer and by the Zernike valve method [27]. The last was used for compensation of weak phase distortions as well [28].

The threshold voltage can be changed by initial orientation of LC because of elastic constants' values depend on the method of orientation. In the case of planar orientation K_{ii} (i=1, 2, 3) are greater than in the tilted one, and the decay time is shorter [9].

REFERENCES
1. Z..U.Gotra, L.K.Vistin', V.V.Parhomenko, L.M.Smerklo, E.P.Dzisjak, V.T.Fechan, "Indicator devices on liquid crystals", Moscow, "Soviet radio", 240 p. (1980), rus.
2. W.P.Bleha, "Progress in liquid crystal light valves", Laser Focus/Electro-Optics, October, pp.111-120 (1983).
3. S.D.Jacobs, K.A.Cerqua, K.I.Marshall, A.Schmid, M.J.Guardalben, K.J.Skerrett, "Liquid-crystal laser optics: design, fabrication, and performance", J. Opt. Soc. Am. B, Vol.5, No.9, pp.1962-1979 (1988).
4. N.A.Riza, "Liquid crystal-based optical control of phased array antennas", Journal of Lightwave Technology, Vol.10, No.12, pp.1974-1984 (1992).

5. M.M.Wefers, K.A.Nelson "Analysis of programmable ultrashort waveform generation using liquid-crystal spatial light modulators", J. Opt. Soc. Am., Vol.12, No.7, pp.1343-1362 (1995).

6. Meadowlark Optics, 7460 Weld Country Road 1, Longmont, Colo.80504-9470.

7. G.D.Love, "Wave-front correction and production of Zernike modes with a liquid-crystal spatial light modulator", Appl. Optics, Vol.36, No.7, pp.1517-1524 (1997).

8. L.Bata, A.Buka, J.Janossy, "Reorientation of nematic liquid crystal films by alternating and static fields", Solid State Communications, Vol.15, No.3, pp.647-649 (1974).

9. F.L.Vladimirov, I.E.Morichev, L.I.Petrova, N.I.Pletneva, "Light modulators based on fields effects in nematic liquid crystals", Optical-mechanical industry, No.5, pp.11-13 (1987), rus.

10. W.S.Quon, E.Wiener-Avnear, "Transient laser phenomena in nematic liquid crystals subject to ac electric fields", Applied Physics Letters, Vol.24, No.11, pp.529-531 (1974).

11. L.M.Blinov, "Electro- and magneto-optics of liquid crystals", Moscow, "Science" publ., 384p. (1978), rus or "Electro-Optical and Magneto-Optical Properties of Liquid Crystals", Wiley, New York (1983).

12. H.J.Deuling, W.Helfrich, "Hysteresis in the deformation of nematic liquid crystal layers with homeotropic orientation", Applied Physics Letters, Vol.25, No.3, pp.129-130 (1974).

13. A.F.Naumov "Modal Wavefront Correctors", Proceeding of P.N.Lebedev Physical Institute. v.217, 1993, p.177-182, rus.

14. S.P.Kotova, M.J.Loktev, A.F.Naumov, T.N.Sapsina, A.V.Parfenov "The control of liquid crystal phase transmission", accepted for publication in Bulletin of Samara University, 1997, rus.

15. S.T. Wu, U.Efron. "Optical properties of thin nematic liquid crystal cells", Applied Physics Letters, Vol.48, No.10, pp. 624-626 (1986).

16. U.Efron, S.T.Wu, T.D.Bates,"Nematic liquid crystals for spatial light modulator: recen studies", Journal of the Optical Society of America B, Vol.3, No.2, pp.247-252 (1986).

17. M.A.Vorontsov, J.D.Dumarevskij, S.V.Kolobkov, A.N.Malov, A.F.Naumov, V.I.Shmal'gauzen "Stabilizated interferometer", patent 1404811 A1, 04/14/1986, rus.

18. V.A.Dorezyuk, A.F.Naumov, V.I.Shmal'gauzen "Control of liquid-crystal correctors in adaptive optical systems", Sov. Phys. Thech. Phys., v.34(12), 1989, p.1389-1393;

19. S.T. Wu, Chiung-Sheng Wu, "Small angle relaxation of highly deformed nematic liquid crystals", Applied Physics Letters, Vol.53, No.19, pp.1794-1796 (1988).

20. V.V.Belyaev, A.A.Vasil'ev, I.N.Kompanets, A.A.Matsvejko, A.V.Parfenov, Yu.M.Popov, "Increasing of rapidity of liquid crystal light modulators", Letters to Journal of Technical Physics, Vol.6, No.14, pp.845-847 (1980), rus.

21. A.A.Vasil'ev, A.F.Naumov, S.A.Svistun, V.G.Chigrinov "Pulse control of a phase corrector liquid crystal cell", Letters to Sov. Phys. Thech. Phys., v.14(5), 1988, p.397-400.

22. A.F.Naumov, V.N.Belopukhov " Dynamic dual-frequency control of nematic liquid crystals in adaptive optics systems", preliminary report for European Office of Aerospace Research and Development, contract No F61708-97-W0047, 33p., 1997.

23. T.S.Chang, E.E.Loebner, "Crossover frequencies and turn-off time reduction scheme for twisted nematic liquid crystal displays", Applied Physics Letters, Vol.25, No.1, pp.1-2 (1974).

24. G.Labrunie, J.Robert, "Transient behavior of the electrically controlled birefringence in a nematic liquid crystal", Journal of Applied Physics, Vol.44, No.11, pp.4869-4874 (1973).

25. A.Yu.Valkov, V.P.Romanov, "Fluctuation and scattering of light in nematic liquid crystals", Journal of Experimental and Theoretical Physics, Vol.83, No.5, pp.1777-1787 (1982), rus.

26. S.T. Wu, "Phase retardation dependent optical response time of parallel-aligned liquid crystals", Journal of Applied Physics, Vol.60, No.5, pp.1836-1838 (1986).

27. V.A.Katulin, S.P.Kotova, A.N.Malov, A.F.Naumov, "Light-light modulator in the lens focuse", Laser and Optoelectronoc engineering, Springer-Verland Berlin, pp.200-203 (1987).

28. A.A.Vasil'ev, A.F.Naumov, A.V.Parfenov, "Liquid crystal Zernike valve", in "Optics of Liquid Crystals", the first USSR seminar, Leningrad, pp.249-251 (1987), rus.

Prediction and Adaptive Correction of Optical Beam Jitter Caused by Organized Structure in Dynamic Air Flow Using Linear Stochastic Estimation

Lenore McMackin
USAF Phillips Laboratory
3550 Aberdeen Ave SE
Kirtland AFB, NM 87117
505 / 846-2047

C. Randall Truman
University of New Mexico

Robert E. Pierson, Kenneth P. Bishop, Ellen Y. Chen
ATA, Inc

Motivation

Open loop adaptive optics correction based on turbulence prediction rather than closed-loop measurement and correction at all aperture points
- Measurement at a few points predicts aberration over the aperture
- Beacon measurements are unnecessary

Outline

- Introduction to prediction-based adaptive optics
- Spatially and temporally structured turbulence
- Optical correction experiment geometry: beam jitter signal
- Prediction method: LSE description, jitter prediction
- Simulation and experiment results
- Future directions

I want to present our experiments in adaptive optics correction that are based on the prediction of turbulence rather than measurement of the aberration at every point in the aperture. In this way only a few measurements at the time of correction are necessary so that the system could potentially operate at very high speed. And there is no need for a beacon measurement, that is a measurement of the uncorrected signal or of the corrected signal. The system operates open loop.

This talk will first introduce predicton based adaptive optics. I'll show the kinds of spatially and temporally structured turbulence we want to correct as well as the system used to correct it. The method of prediction we use is called Linear Stochastic estimation. I'll present the results of our simulations and experiments showing that the technique actually works and then I'll discuss some implications of the work.

Introduction

Prediction - Based Optical Wavefront Correction

Turret

Beam projection and imaging thru high speed aircraft shear and boundary layers

Point Anemometer Measurement

Optical Path Correction
Image Correction
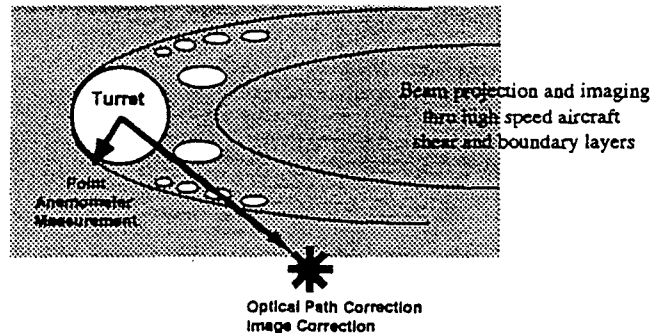
Linear Stochastic Estimation

- Correction of structured turbulence otherwise not easily described by statistical models
- Measurement of flow at a few points predicts aberration at other locations and time
- Open loop correction system: no beacon measurement or feedback loops
- Lower operational bandwidth required

Highly structured turbulence such as aircraft boundary and shear layers requires very high bandwidth measurement and correction systems especially when high spatial resolution is required. The highly organized features of such turbulence and their intermittancy are difficult to describe using statistical turbulence models

We propose a system by which stochastic estimates of flow properties are developed from previous flow measurements. This information is combined with a few point measurements of the flow at the time of correction to predict the necessary correction that takes place at another location in the flow.

So rather than making measurements at all points in the aperture and driving all apertures of an adaptive optics system based on those measurements in a closed loop system, we are making open loop corrections based on an stochastic estimate of the flow, imposing a condition on that flow from a few point measurements and then inferring the optical aberration in the area of interest. Shown here is a point temperature measurement taken at the front of an aircraft turret, used to predict the tilt along a beam path at the back of the turret.

Key advantages of predictive systems are that only a few measurements and calculations need to occur at the time of correction lowering the operational bw requirements of the system. And no beacon measurements of the turbulence are required. We don't measure the beam we simply correct it.
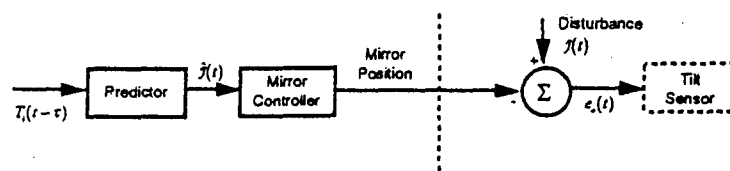
Potentially we may be able to use a few point measurements to infer larger spatial areas usable for image correction. In this case we have pictured a point measurement inferring a path integral for simple jitter correction.
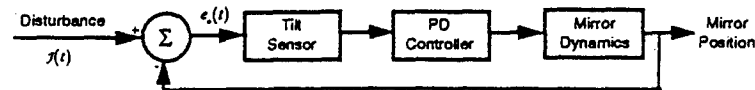
Here, I want to illustrate the differences between our system and a traditional closed loop system

In the closed loop case, the mirror position is measured, fed back, subtracted from the disturbance signal and residual signal is sensed. This is the beacon signal I mentioned, a signal that is constantly monitoring the performance of the adaptive optics and feeding it back.

In the predictive system a guess is made of the form of the disturbance based on past information. In this case, LSE is the means by which the past information is used to make the prediction. The tilt sensor is only a performance monitor for experimental convenience in this system. It does not contribute to the correction signal.

Notes:

PD Controller= Proportional derivative controller, produces weighted value of the current mirror position and the difference between the current position and the last position.

Predicts mirror movement ahead of time so that mirror response dynamics (phase lag times) can be accounted for.

Suggest the possibility that these types of systems might work together in a single adaptive optics system. An example will be shown at the end.
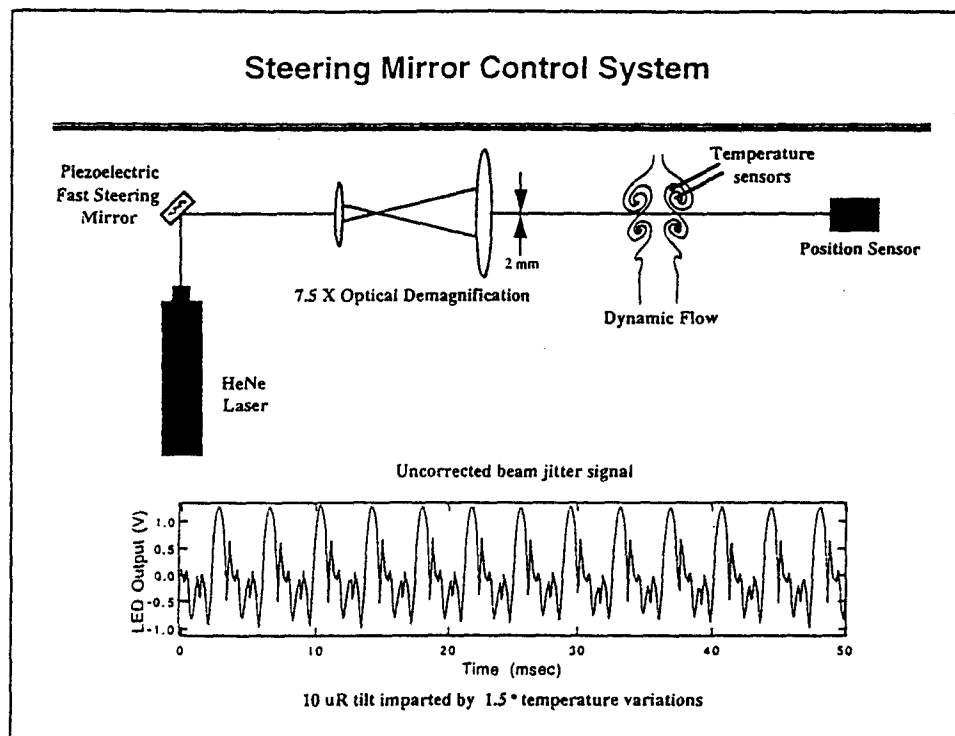
Orientation of Anemometer probes
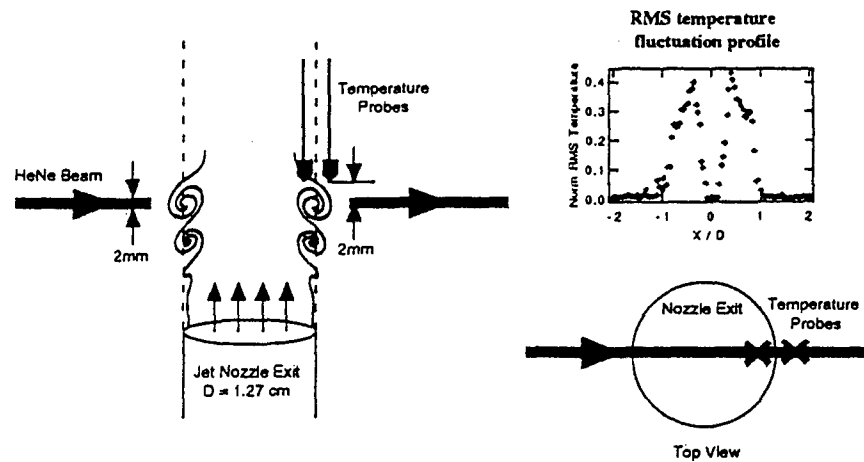
Placement of 2 constant current anemometer probes
determined by location of largest temperature fluctuation

Typical probe locations and how those locations can be chosen. Probe location
is in general related to the areas with the highest frequency content and the
strongest signal fluctuations. The RMS temperature profile shows that the
strongest fluctuations occur near the geometrical edge of the flow defined by
the nozzle exit edge. Typically, one probe is located inside the edge and the
other probe is located outside.

Probe location is not always critical as long as enough frequency components
are present to truly represent the flow events that cause optical aberration.

Steering Mirror Control System

Piezoelectric
Fast Steering
Mirror

Temperature
sensors

Position Sensor

2 mm

7.5 X Optical Demagnification

Dynamic Flow

HeNe
Laser

Uncorrected beam jitter signal

LED Output (V)

1.0
0.5
0.0
-0.5
-1.0

0   10   20   30   40   50
Time (msec)

10 uR tilt imparted by 1.5° temperature variations

System diagram

The system is composed of a He Ne laser and a piezoelectric steering mirror. The 2 mm wide beam propagates through a disturbance, a heated air flow in this case, and the position of the beam is monitored using a position sensitive detector. Dynamic temperature variations in the air flow cause the beams position to wander. The piezo mirror is used to compensate for this beam jitter. The mirror is driven by a tilt prediction produced by a combination of a statistical knowledge of the flow combined with 2 point temperature measurements taken just before correction is to occur.

Piezo mirror is driven in 1 D not by direct flow measurements but by the jitter signal estimated from 2 anemometer probe temperature measurements

Heated Round Jet flow structure

- Kelvin - Helmholtz instabilities form highly structured vortices that create optical distortion
- flow visualizations
- flow can be controlled using acoustic forcing from ordinary speaker

Rather than use an aircraft geometry we have chosen a laboratory air flow that provides interesting features and coherent strucutures while maintaining some level of controllability

I will show a visualization of the flow showing the kinds of structure that can cause optical distortions in the beam.

In another kind of visualization, where quantitative temperature measurements are made using a 1-dimensional Hartmann sensor we can see some of the different states of the flow that we can induce by acoustically forcing the flow.

More details about Hartmann sensor measurements of the flow are given in:

L. McMackin, B. Masson, N. Clark, K Bishop, R. Pierson and E. Chen, "Hartmann wavefront sensor studies of dynamic organized structure in flow fields," AIAA Journal 33 (11), 2158-2164, 1995.

- Predict path-averaged beam jitter from several point temperature measurements near path

- Estimate formed from unconditional correlations of the temperature and the jitter.

  – Take linear term from power series expansion of expected value of jitter, $\hat{J}_r(t)$ given temperature at positions x_i, $T_i(t)$

  – minimize mean square error between estimate and jitter

  – results in correlation expression solved for coefficients, A_j "Weights"

- LSE for 2 reference points

  | These calculations are performed before correction |

$$\hat{J}_r(t) = \langle J_r(t) | T_i(t - \tau_i) \rangle$$
$$= A_i T_i(t - \tau_i) = A_1 T_1 + A_2 T_2$$

$$\frac{\partial \left[\{ J_r(t) - \hat{J}_r(t) \}^2 \right]}{\partial A_i} = 0$$

$$\langle T_i\, T_j \rangle \cdot A_j = \langle T_i(t - \tau_i)\, J_r(t) \rangle$$

$$\begin{bmatrix} \langle T_1 T_1 \rangle & \langle T_1 T_2 \rangle \\ \langle T_2 T_1 \rangle & \langle T_2 T_2 \rangle \end{bmatrix} \begin{bmatrix} A_1 \\ A_2 \end{bmatrix} = \begin{bmatrix} \langle T_1 J_r \rangle \\ \langle T_2 J_r \rangle \end{bmatrix}$$

This slide explains we really doing with the temperature probe signals:

What is LSE?

We are trying to predict the jitter caused by temperature variations that occur along the entire path of the beam through the flow from just a couple of point temperature measurements. What makes this kind of estimate very useful is that it is produced from unconditional correlations of temperature and jitter so that we do not have to wait for a particular "event" to trigger the prediction from a conditional average.

The usual expression for the expected value of the jitter given a temperature measurement T, can be expanded in a power series in T. It has been shown that the linear term in the expansion is sufficient to describe coherent organized structure in flow. So our estimate then takes the form of the linear combination of weighted temperature signals. We need to calculate the weights, that is the "A" coefficients. By minimizing the mean-square error between the estimate and the jitter we obtain an expression that depends upon the correlations between the measured temperature and jitter signal and also depends upon correlations between the temperature signals. We solve for the A's by solving a set of linear equations shown here in matrix form for two temperature measurements T1 and T2. I want to emphasize that these calculations are accomplished before correction occurs. This is a kind of "training" done ahead of time and is based on actual measurements of the jitter.

LSE Cont'd

$$\begin{bmatrix} \langle T_1 T_1 \rangle & \langle T_1 T_2 \rangle \\ \langle T_2 T_1 \rangle & \langle T_2 T_2 \rangle \end{bmatrix} \begin{bmatrix} A_1 \\ A_2 \end{bmatrix} = \begin{bmatrix} \langle T_1 J_r \rangle \\ \langle T_2 J_r \rangle \end{bmatrix}$$

Examine the temporal delays, τ, that maximize the
probability that the estimated jitter is best represented by
the measured temperature

- Choose "lags" τ_i to maximize the Temperature-Jitter correlations

$$\tau_i : SUP \langle T_i J_r \rangle$$

- Evaluate Temperature-Jitter correlations at τ_i

$$\langle T_i(t - \tau_i) J_r(t) \rangle \big|_{\tau_i}$$

- Evaluate Temperature-Temperature correlations at τ_i

$$\langle T_i(t - \tau_i) T_j(t - \tau_j) \rangle \big|_{\tau_i}$$

In order to find the best values of the correlations to put into the matrix expression we have to find the particular time tau at which to evaluate the correlations. The best tau is the time lag at which the temperature-jitter correlation is maximized. We evaluate both the temperature-jitter correlation and the temperature-temperature correlations at this time lag and input the results into the matrix expression.

SUP= mathematical expression for supremum (maximum value)

LSE References:
T. Luna, "Linear Stochastic Estimation of Optical Beam Deflection through a Heated Round Turbulent Jet," MS Thesis, Dept of Mechanical Engineering, University of New Mexico, 1996.

T. Luna, C. R. Truman,"Linear stochastic estimation of optical beam deflection through a heated jet," AIAA paper 97-0072, 35th Aerospace Sciences Meeting, Reno, NV Jan 6-10, 1997.

LSE "Training"

$$\tau_i : SUP\langle T_i J_r \rangle$$

$$\langle T_i J_r \rangle\big|_{\tau_i} = \sum T_i(t - \tau_i) J_r(t)$$

$$\langle T_i T_j \rangle\big|_{\tau_i} = \sum T_i(t - \tau_i) T_j(t - \tau_j)$$

$$\begin{bmatrix} \langle T_1 T_1 \rangle & \langle T_1 T_2 \rangle \\ \langle T_2 T_1 \rangle & \langle T_2 T_2 \rangle \end{bmatrix} \begin{bmatrix} A_1 \\ A_2 \end{bmatrix} = \begin{bmatrix} \langle T_1 J \rangle \\ \langle T_2 J \rangle \end{bmatrix}$$

LSE Prediction

• 2 temperature signals in
• weighted linear sum

$$\hat{J}_r(t) = A_i T_i(t - \tau_i) + A_j T_j(t - \tau_j)$$
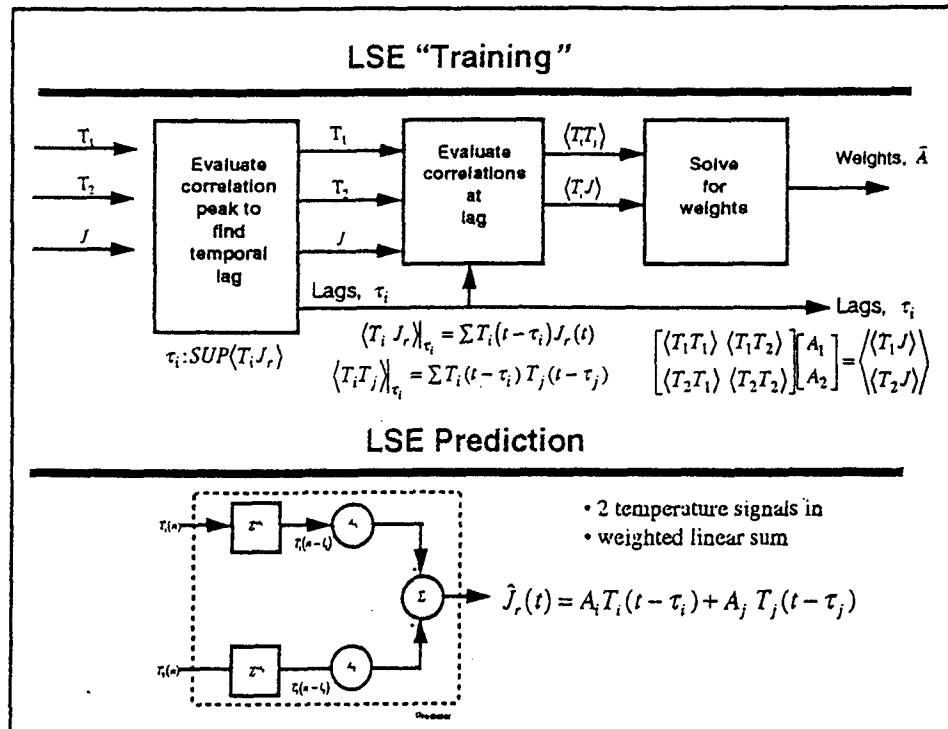
This is the LSE procedure shown in block diagram form where two temperature signals and a measured optical jitter signal are input. The "lags" are found from the time at which the T-J correlations are maximum. The T-T correlations are then evaluated at this lag. The set of linear equations defined by the matrix expression given previously are solved for the coefficients Aj "weights". This is the way LSE is "trained" on the flow.

These weights and lags are then used in the actual correction stage.

To make the actual prediction the weights and lags are applied to two new temperature measurements made at the time of correction. The linear combination of the weighted signals at the appropriate time delays creates the prediction.

LSE Simulation and Experiment

Simulation

$J'(t)$
$T_1'(t)$
$T_2'(t)$

LSE Algorithm — weights, $\vec{A}$ — Prediction Algorithm — $\hat{J}'(t)$ — + — $J_r'(t)$ Simulated Error

lags, $\vec{\tau}$

$\downarrow J(t)$

Experiment

$T_1(t)$ → Prediction Algorithm → $\hat{J}(t)$ → Drive Mirror → + → $J_r(t)$ Measured Error

$T_2(t)$ →

In simulation
• temperature and jitter are used to create the weights and lags
• Weights and lags are applied to the same temperature signals to make estimate
• Estimated jitter is compared to jitter signal used in the LSE to determine the error.

In experiment
• weights and lags are applied to 2 new temperature signals
• Estimate is used to control a steering mirror
• Residual is compared to the jitter signal used to create the weights and lags.

In the correction stage the weights and lags are given. These weights and lags are applied to new temperature measurements that are taken at the time of correction to produce the estimated jitter signal $J^\wedge$, which is a linear summation of the AT_i's, i.e. $J^\wedge = A_1 T_1 + A_2 T_2$

This diagram is to illustrate the difference between the simulations that we have used to examine how well LSE can do to correct our jitter signal, and the experiments we have actually performed.

In the simulations the 2 temperature signals and the jitter signal are used to create the weights and lags, the weights and lags are then applied to the prediction algorithm in which the same temperature signals are used. The resulting estimated jitter signal is then compared to the measured jitter signal used in the LSE to determine the residual jitter.

In the experiment, the weights and lags are applied to the new temperature signals measured during the correction. The jitter estimate is used to control a steering mirror and the residual jitter is measured. To determine the amount of jitter correction that has taken place, the measured residual is compared to the jitter signal used to create the weights and lags.

The next five slides show the simulation and experimental results illustrating that the LSE prediction can be effective in reducing beam jitter.

Simulation Results—Forced Flow

Measured Temperature (Probe 1)

Counts — 5000, 0, -5000

time [msec] — 0 10 20 30 40

Measured Temperature (Probe 2)

Counts — 5000, 0, -5000

time [msec] — 10 20 30 40
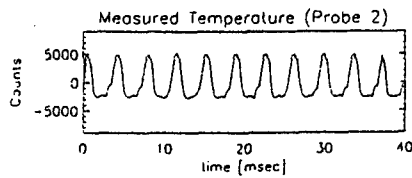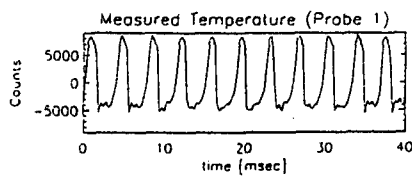
$A_1 = -0.28$, $\tau_1 = 0.9$ msec
$A_2 = -0.38$, $\tau_2 = 1.6$ msec
<Percent Reduction>: 59%
8 m/s flow, 530 Hz forcing,
height = 2.0D, $\Delta T = \sim 4°C$

Measured Tilt, RMS=2597.74

Counts — 5000, 0, -5000

time [msec] — 0 10 20 30 40

Predicted Tilt, RMS=2499.41

Counts — 5000, 0, -5000

time [msec] — 0 10 20 30 40

Residual, RMS=1129.51

Counts — 5000, 0, -5000

time [msec] — 0 10 20 30 40
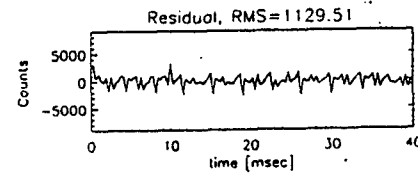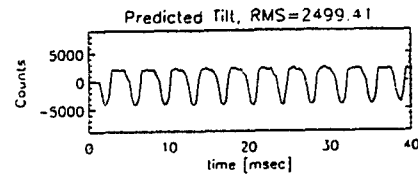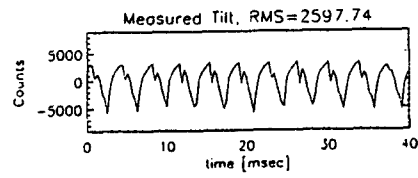
In simulation, 2 temperature signals and a measured jitter signal are measured and used to produce the weights and lags describing the flow at a downstream position of 2 nozzle diameters (~ 2.5 cm). The weights and lags are then applied to the same temperature measurements to predict the jitter. When compared to the measured tilt, the predicted jitter signal would remove 59% of the RMS jitter signal.

Experimental Results—Forced Flow, 2-pt. LSE

Comparison to experimental results. In this case the predicted jitter is used to move a piezo mirror to compensate for the jitter. The results show a 41% (on average) correction compared to nearly 60% in simulation.

Simulation Results—Unforced Flow
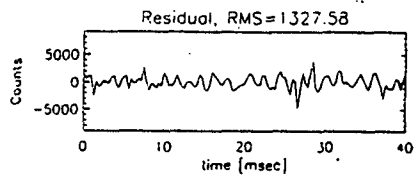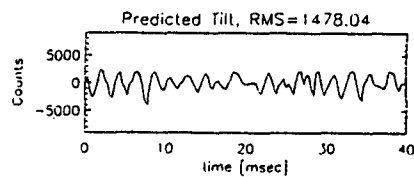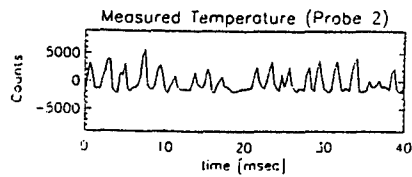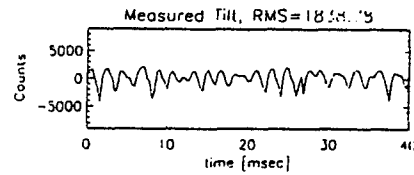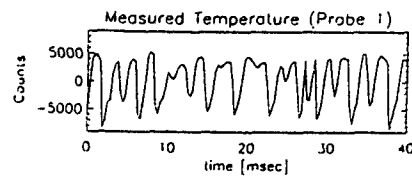
$A_1 = -0.22$, $\tau_1 = 0$ msec
$A_2 = -0.51$, $\tau_2 = 0.3$ msec
<Percent Reduction>: 17%
8 m/s flow, height = 2.0D, $\Delta T = \sim 4°C$

We also looked at an unforced flow case where the flow structures are intermittant rather than periodic as in the forced case. As expected the prediction is not as accurate in the case averaging about 17% as compared to almost 60% for the forced case. Although the reduction in prediction accuracy is not completely understood and these results are preliminary, it may in part be due to smaller correlations between the jitter and the temperature measurements as well as a lack of symmetry in the unforced flow along the beam path. In this case only 2 measurements do not predict events along the entire beam path very well.

Experimental Results—Unforced Flow, 2-pt. LSE
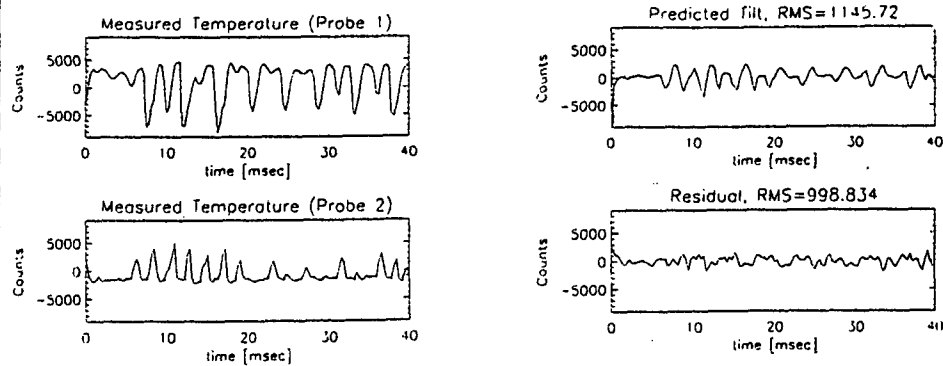
Comparison to experimental results. In the unforced case experimental correction is about 16% compared to the simulated value of 17%.

Simulation and Experimental Results for 2-pt. LSE vs. 4-pt. LSE
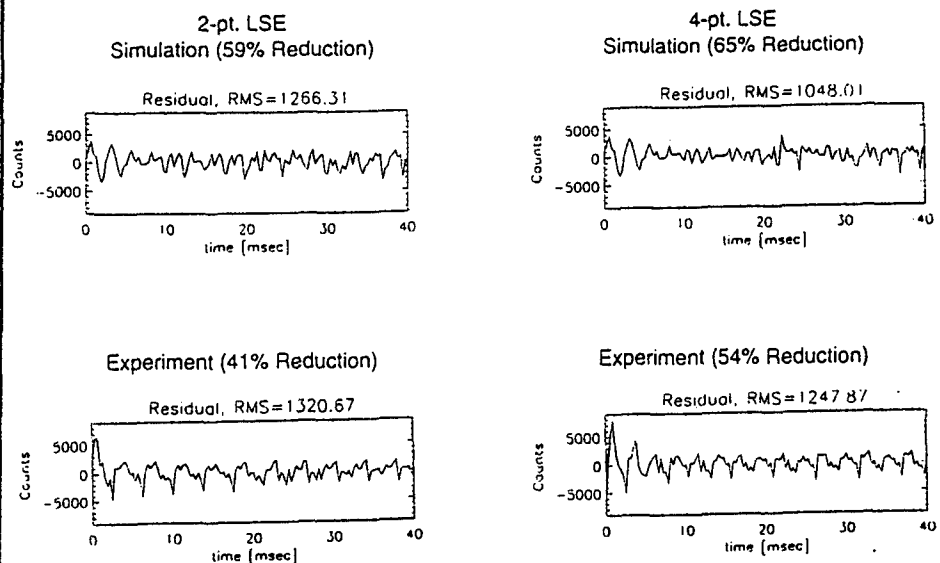
Comparison of 2-point LSE to 4-Point LSE . As expected prediction accuracy increases as the number of point measurement inputs increases.

Implications for Adaptive Optics

- Extension of thin beam to spatially resolved correction
  - Tomography system allows multiple non-intrusive point measurments
  - MEMS devices, concept of multiple aperture adaptive optics
- Combination of predictive and closed loop correction

High Speed Optical Tomography
2-D temperature measurements at 5 KHz

•spatial and temporal measurement can allow higher resolution predictionover larger spatial areas

•suitable for MEMS or other multiple aperture adaptive optics systems

Wide Image bearing beam

Compensated Image

Tomographic measurement plane

Dynamic Aberration

Multi-aperture adaptive optics control system

Predictive compensation computations
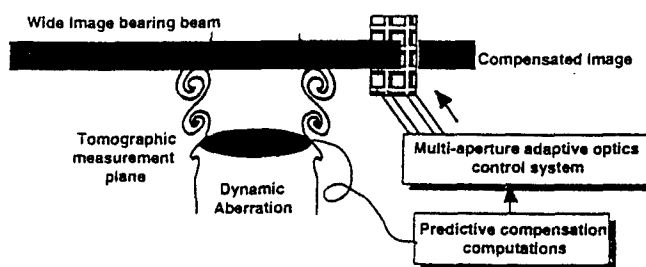
In other work at the Phillips Lab we have achieved high spatial and temporal resolution optical tomography for measuring the temperature of dynamic flows. Although there is no time to discuss the details of this system, what we get from the system are 2 dimensional measurements of the temperature. In these tomographic reconstructions we represent the temperature as a grey level so that it looks like a picture. But we really have a 64 x 64 spatially resolved temperature measurement taken with a speed of 5 KHz.

Using the spatial and temporal fidelity of this measurment could allow the predicitive algorithms to be applied to many spatial points at once.

Tomography references:

R. E. Pierson, E. Y. Chen, K. P. Bishop, L. McMackin, "Modeling and measurement of optical turbulence by tomographic imaging of a heated air flow," SPIE Procedings vol. 2827, p. 130-141, Digital Image Recovery and Synthesis III, Denver, CO, Aug 5-6, 1996.

L. McMackin, B. Masson, N. Clark, K Bishop, R. Pierson and E. Chen, "Hartmann wavefront sensor studies of dynamic organized structure in flow fields," AIAA Journal 33 (11), 2158-2164, 1995.

C. R. Truman, T. Luna, L. McMackin, B. Masson. K. P. Bishop, E. Y. Chen, "Optical tomographic study of the effect of excitation of a heated round jet," AIAA Paper 96-2323, Plasma Dynamics and Lasers Conference, New Orleans, June 1996.

Improve Current Control Systems

- Combination of Prediction and Closed-Loop System
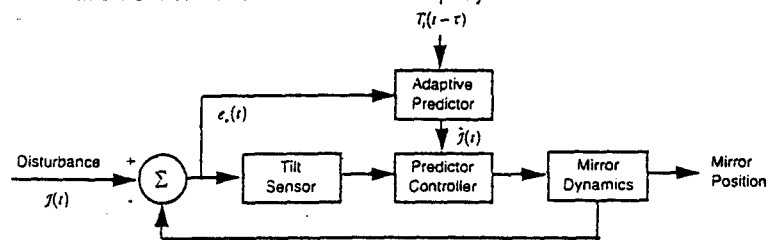
- Adaptive Predictor
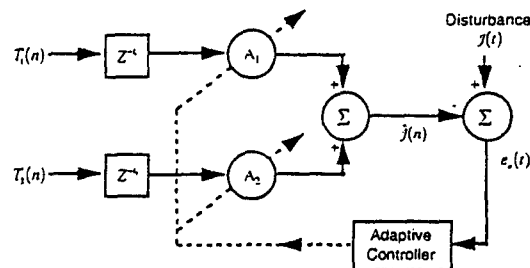
Example of how predictive procedures (such as LSE) can be used to improve the correction results from closed loop adaptive optics systems.

In this case rather than simply feeding back the residual disturbance to the tilt sensor, the error is also used to drive an adaptive prediction system in which the temperature signals as well as the feedback signal are used to compute the weights. In this way both feedback and prediction are used to adaptively correct for dynamic aberrations.

Fiber Phase Conjugator as Wave Front Corrector for Industrial Laser Systems
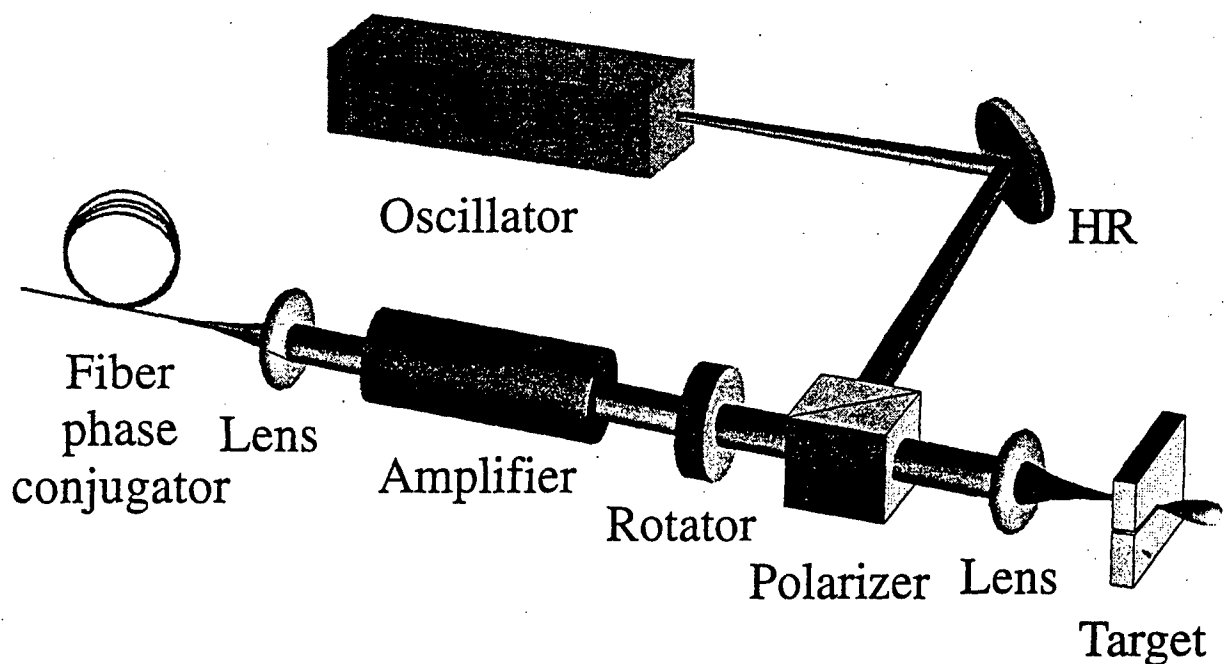
Outline
- ✓ Beam quality improvement
- ✓ Fiber phase conjugator
- ✓ MOPA-arrangement
- ✓ Summary and outlook
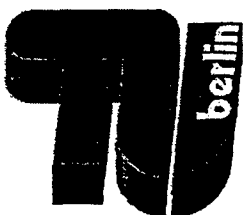
H.J. Eichler, A. Dehn, A. Haase, B. Liu, O. Mehl
Technical University, Berlin

1

Phase Conjugation for High Power Solid State Lasers

| Four Wave Mixing | Photorefractive Semiconductors, Thermal Grating, Liquid Crystals, Laser Materials |
| Self-pumped SBS | Gases, Liquids, Solids |

Focusing with single lens (Brillouin cell)

Better: multimode glass fiber (not toxic)

diameter 25-400μm

Lens

SBS grating effect.

Beam Quality Improvement of High Power Solid State Lasers up to 1 kW

Problem: Phase distortions decrease beam quality

Slab Laser → Phase Conjugation ← Diode Pumping

Amplifier rod

Conventional mirror

Amplifier rod

PCM

2

Measurement of Fiber Properties

Fiber

Pulse width 30 ns
Coherence length 50 cm
Peak power up to 1.3 MW
$M^2 = 1.1 \times DL$

SBS threshold
R = 2%

Far field fidelity F

Reflectivity
$R = \dfrac{E_2}{E_1}$

Lens L_1

E_1

reflected Beam

Isolator Wedge

E_2

Lens L_2

Oscillator
amplifier
system

Pinhole

200 µm

E_3

Oscillator beam

Intensity

F = 100%

86%

200 µm

Reflected beam

Intensity

$F = \dfrac{E_3}{E_2 \cdot 0.86}$

E_3/E_2

200 µm

Demonstration of Phase Conjugation

Behind phase
distortions

Core diameter 200 µm
Length > 2m

Double pass with
conventional
mirror

$M^2 = 10$

f=40 mm

Short fiber as
phase distorting
object (l = 8.7cm)

Input beam

f=150 mm

Nd:YAG
Laser

SBS double pass

Measurement of brillouin shift leads to 17 GHz

Fibers with Different Core Diameters

Core diameter [µm]	SBS threshold [kW]	Max. Reflectivity [%]	M² limit [xDL]
400	29	40	125
200	17	54	63
100	6.4	51	31
50	2.0	53	16

SBS threshold of a 25 µm fiber: 200W
=> cw-pumped Q-switched laser systems with SBS
▶ Second talk after coffee break

SBS in 200 µm Fibers

50%
Fiber length 4.1 m
P_{th}=17 kW
Reflectivity [%]
Input power [kW]

93%
1.5 GW/cm² > Damage threshold > 500 MW/cm²
Fidelity [%]
Input power [kW]

MOPA System with Fiber Phase Conjugator

FWHM 150 ns

$f = 100$ Hz
$P = 3.5$ W
$M^2 = 1.1$

burst emission

Nd:YALO ring oscillator

ext. Feedback

Ap Cr^4:YAG

Etalon

YAP

$\lambda/2$

Rotator   Pol.

Optical isolation

Amplifier

Multimode fiber PCM
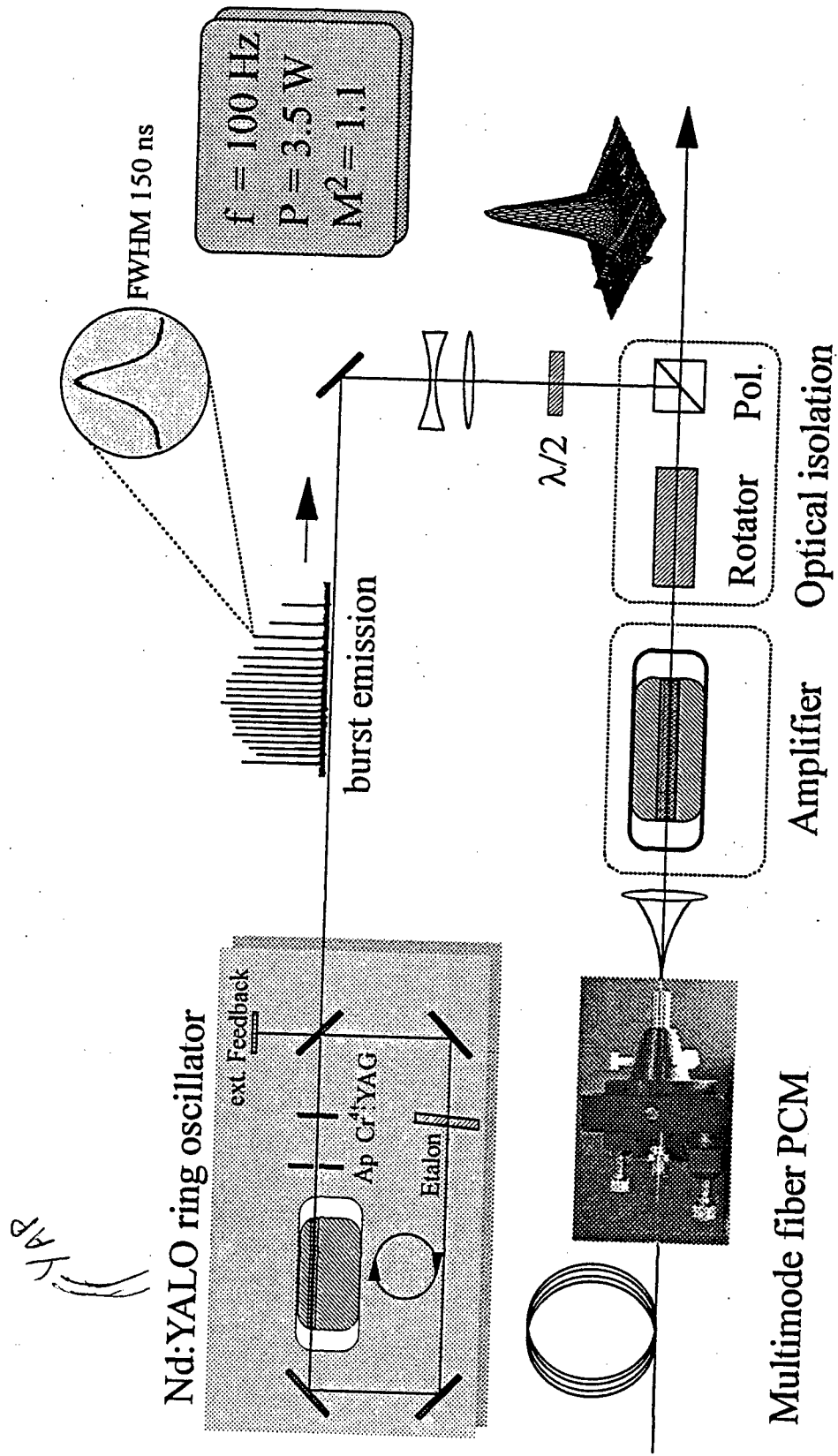
Choice of active medium

Problem: Stress birefringence of Nd:YAG

Pol | Nd:YAG | Pol | CCD
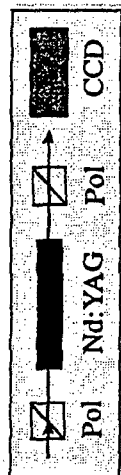
➪ Optical isolation fails

➪ Reduced beam quality, Backscattered beam into the oscillator, Bifocusing for circular and azimutal polarized beams

➪ Double pass schemes become complicate
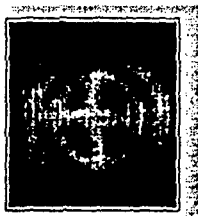
Solution: Nd:YALO as active material

Anisotropic crystal
- No stress birefringence → simple optical arrangement
- Bifocusing for linear polarised beam

Only compensation of bifocusing required

perpendicular }
parallel } to polarization

Focal length / cm — Average pumping power / kW
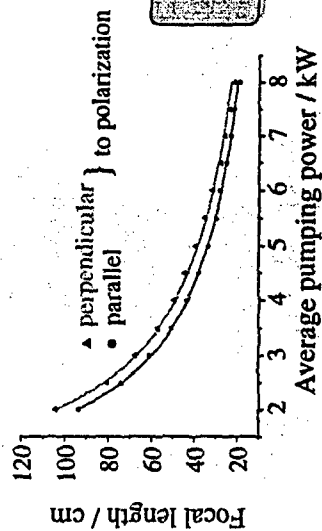
Single Amplifier System with 200 µm Fiber-PCM
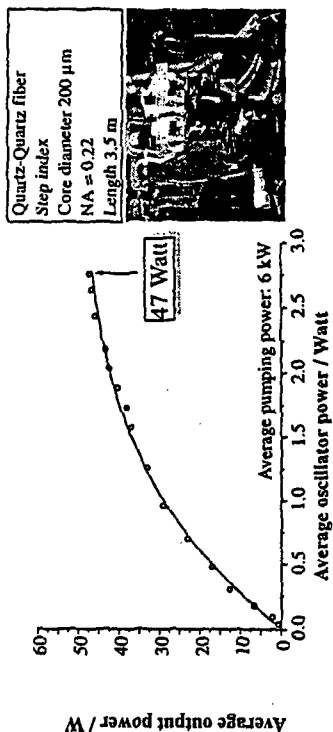
Quartz-Quartz fiber
Step index
Core diameter 200 µm
NA = 0.22
Length 3.5 m

47 Watt

Average pumping power: 6 kW

Average output power / W — Average oscillator power / Watt

10 W   20 W   30 W   40 W
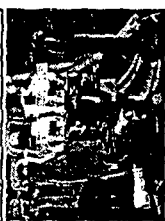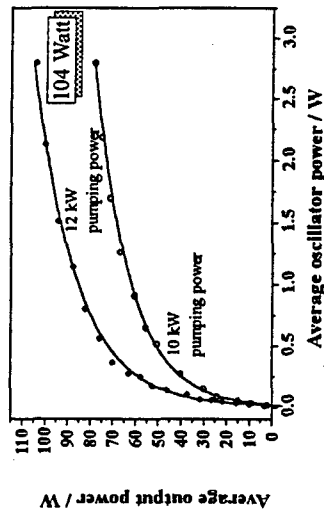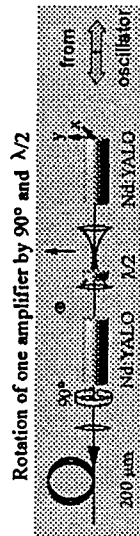
Summary and Outlook

Advantages of Fiber Phase Conjugator

➤ Inexpensive, easy to handle and not toxic
➤ Low SBS threshold down to 2 kW
➤ Better behavior for highly distorted beams
➤ High damage threshold (average and peak)

Fiber Phase Conjugator Applied

➤ High power pulsed MOPA-systems
➤ Average output power up to 104 Watt
➤ Average repetition rate 2 kHz
➤ Compensation of thermal lensing

Future Work

High power continuously pumped Q-switched lasers with fiber phase conjugator

---

Dual Amplifier System with 200 µm Fiber Phase Conjugator

Rotation of one amplifier by 90° and λ/2

from oscillator

200 µm   Nd:YALO   λ/2   Nd:YALO

104 Watt

12 kW pumping power

10 kW pumping power

Average output power / W

Average oscillator power / W

PHASE CONJUGATE MIRROR BASED ON ND:YAG CRYSTAL FOR HIGH POWER LASER SYSTEMS

O.L. Antipov, S.I. Belyaev, A.S. Kuzhelev

Institute of Applied Physics of the Russian Academy of Science,
46 Ulyanov Str., Nizhny Novgorod,603600, Russia
Fax: +7(831)2363792, E-mail: antipov@appl.sci-nnov.ru
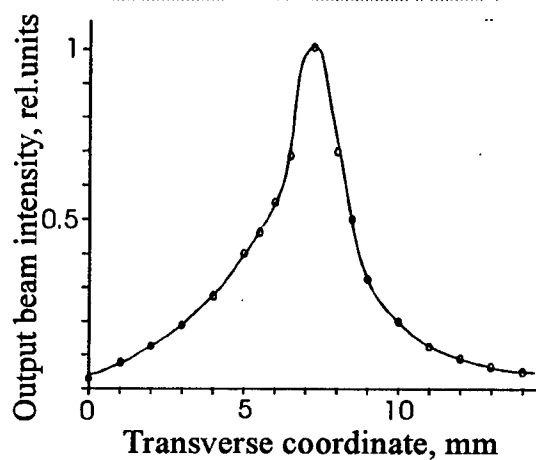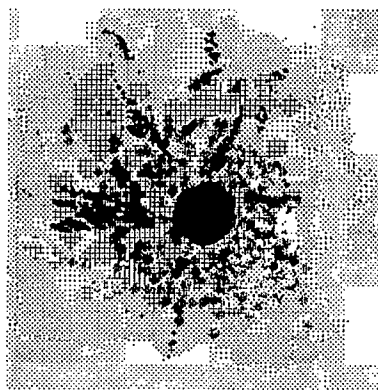
Experimental sheme

Wave vector diagrammes
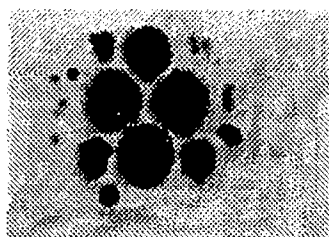
2
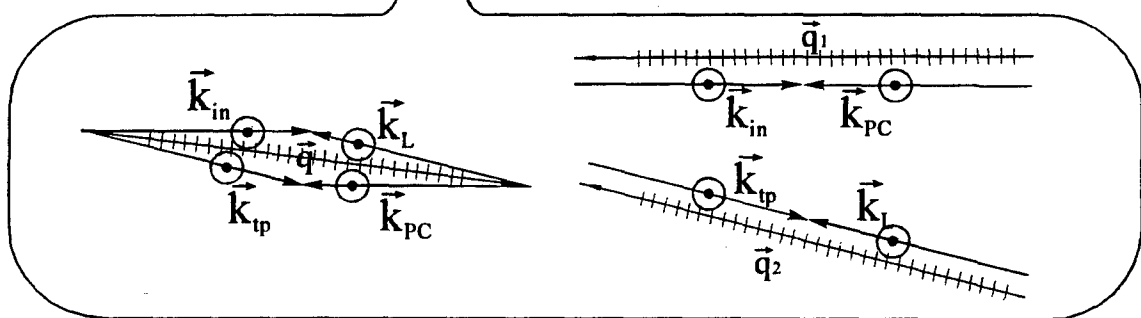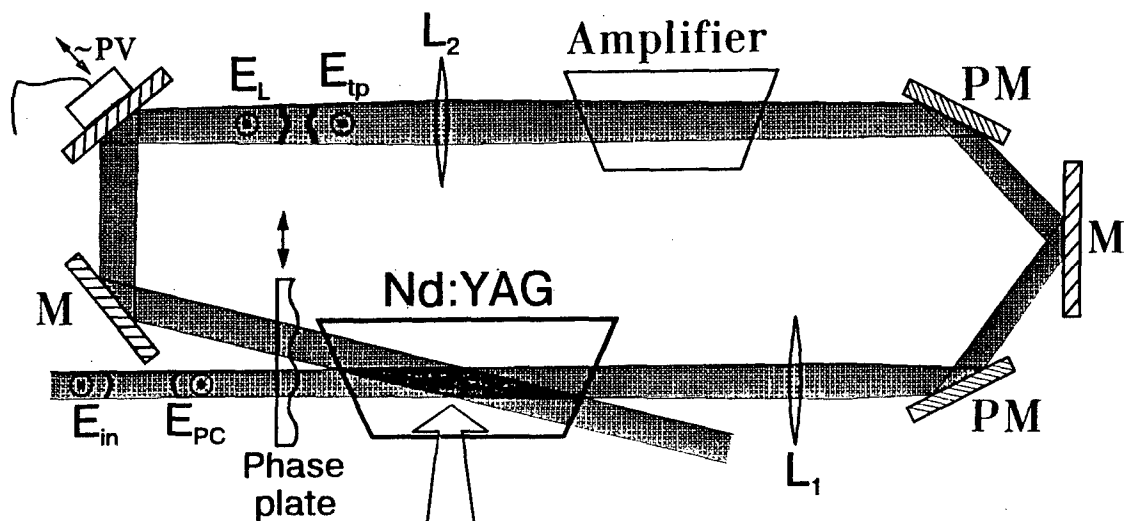
Experimental scheme for counter-running beams.

PV M L Amplifier PM

E_{sc}

M

Nd:YAG M

E_{in} E_{PC}

E_{tp} "nonlinear" amplifier

PM

3
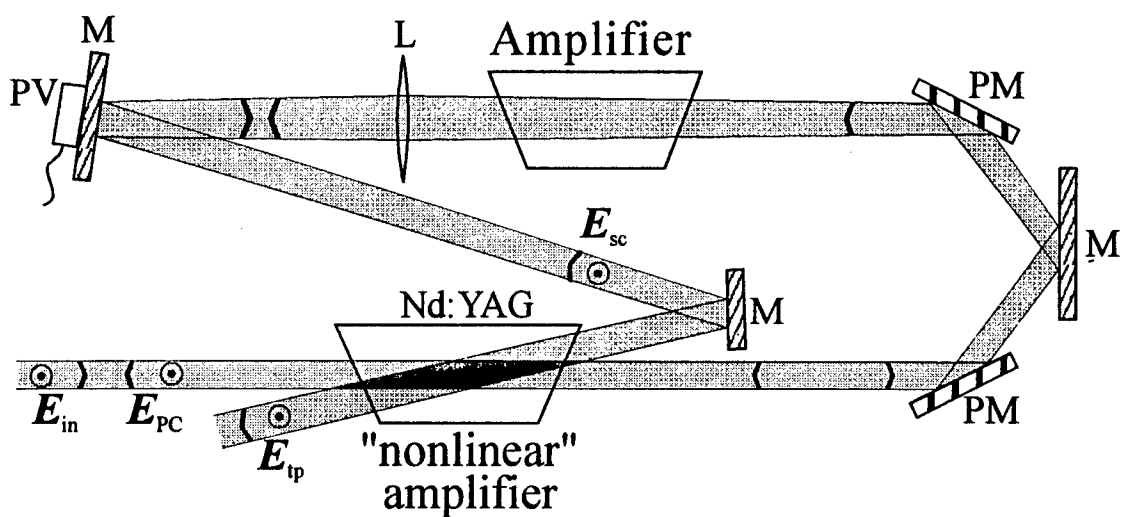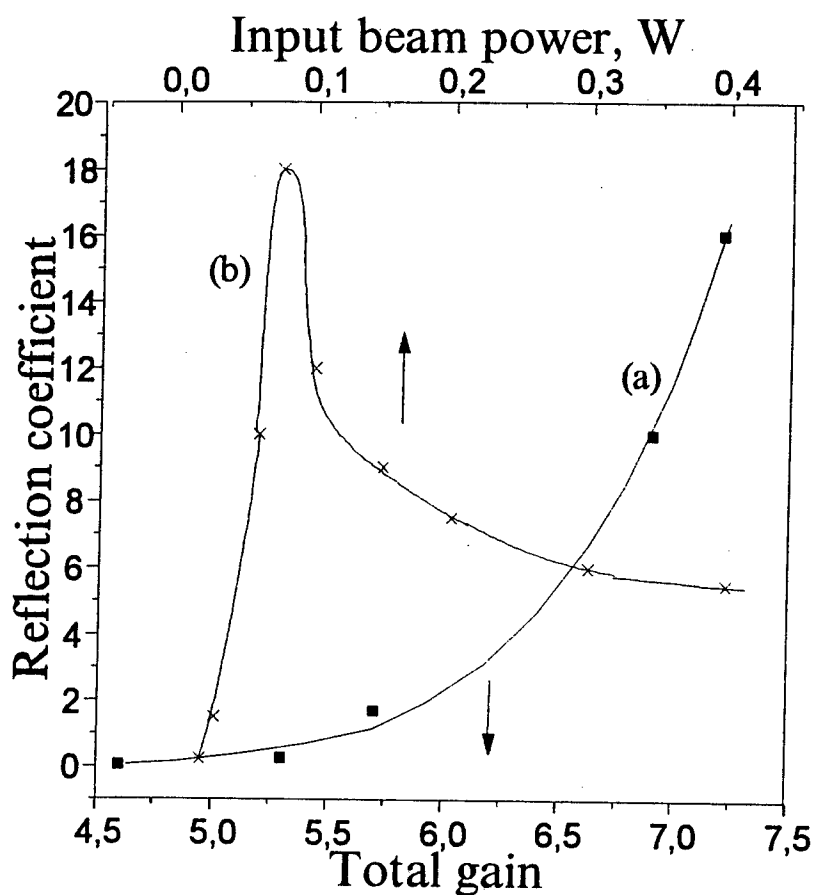
Experimental dependences of the reflection coefficient of the SPPC system at the peak power on the total gain of "nonlinear" and FL amplifiers with the peak power of the incident beam 0.075 W (a), and on the peak power of the incident beam with the total gain 7.2 at the single pulse regime (b).
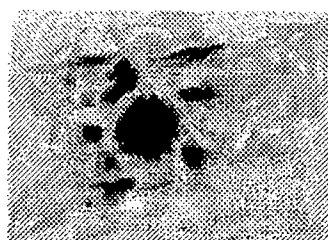
Amplification coefficient 130
Incoherent pumps

Amplification coefficient 90
Coherent pumps
Incoherent pumps

4
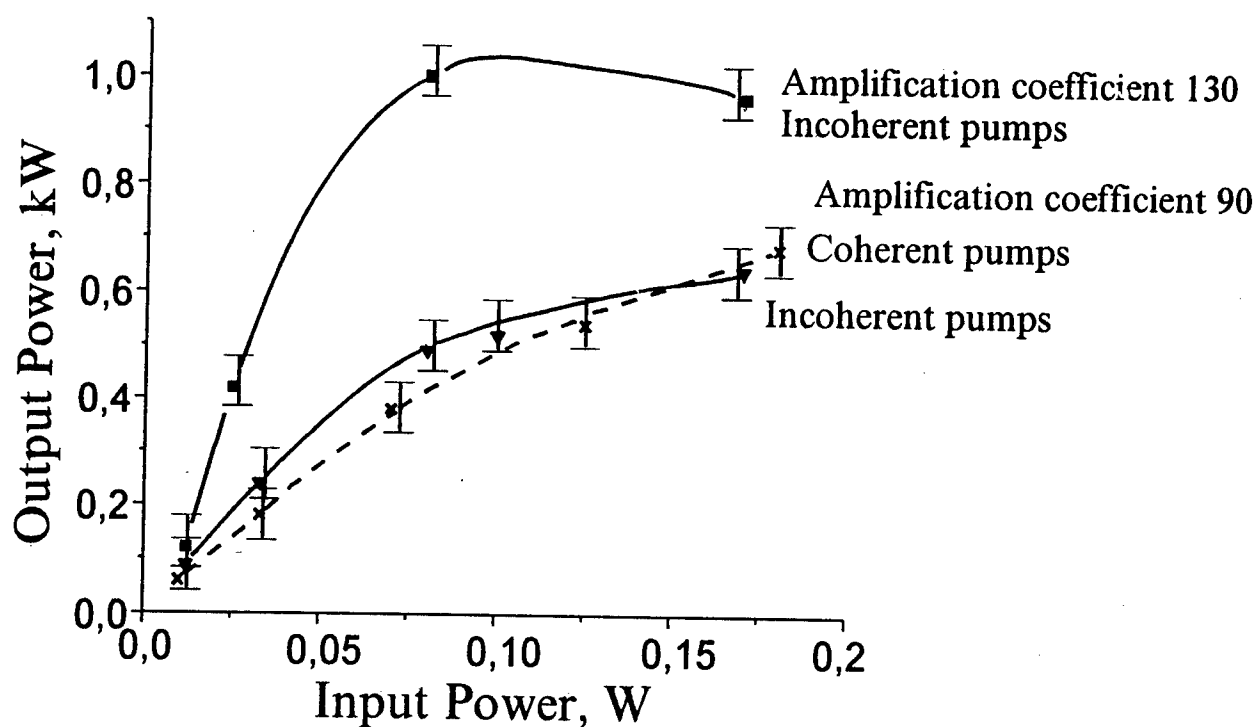
Phase conjugation of the phase - distorted beam

(a)

(b)

Transverse ctructure of recovered image "net"
for the same pumping beam diameters (a)
and for the different diameters (b).

Three-loop scheme
gain $\alpha l = 3.5$

One-loop scheme
$\alpha l = 4.3$

Two-loop scheme
$\alpha l = 3.5$

Initial beam pulse

The pulse of generated beam
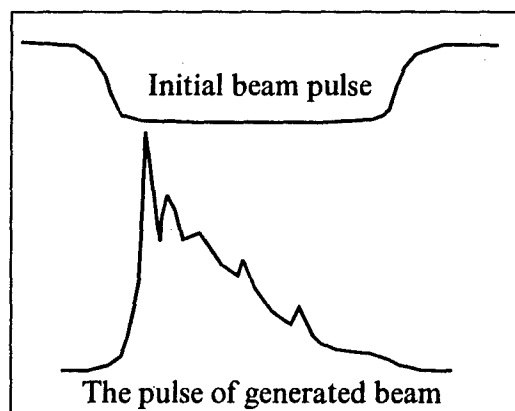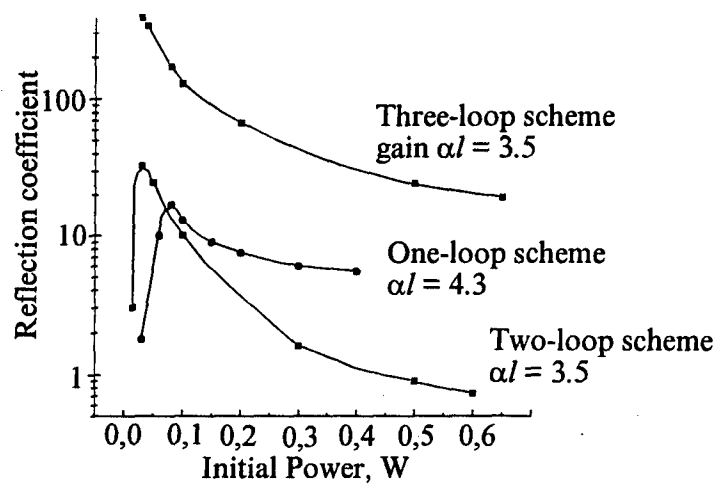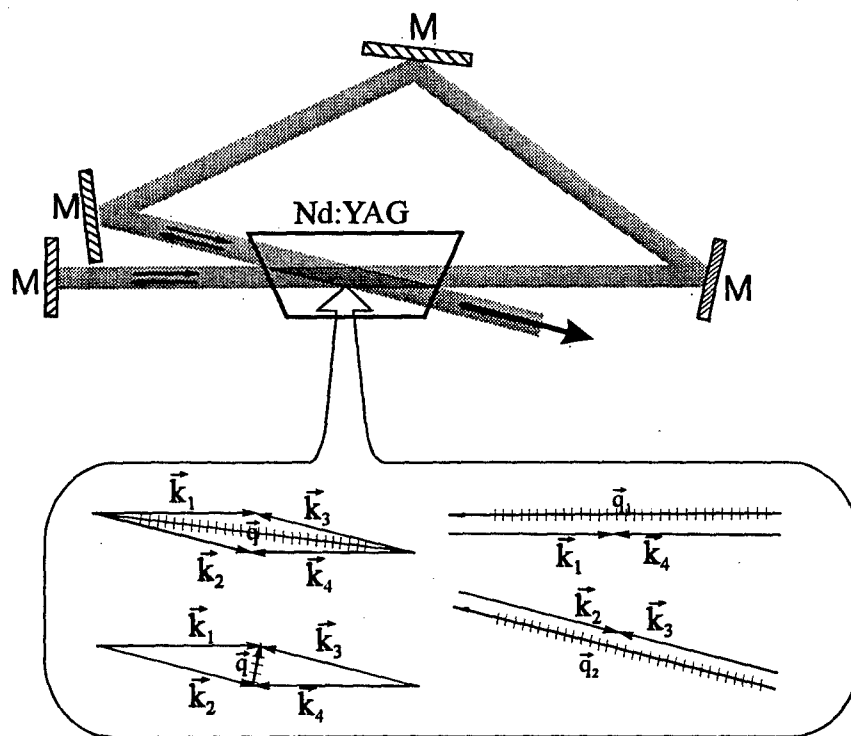
Self-adaptive Nd:YAG laser formed by population inversion grating and wave vector diagrams of the interacting beams into the laser crystal
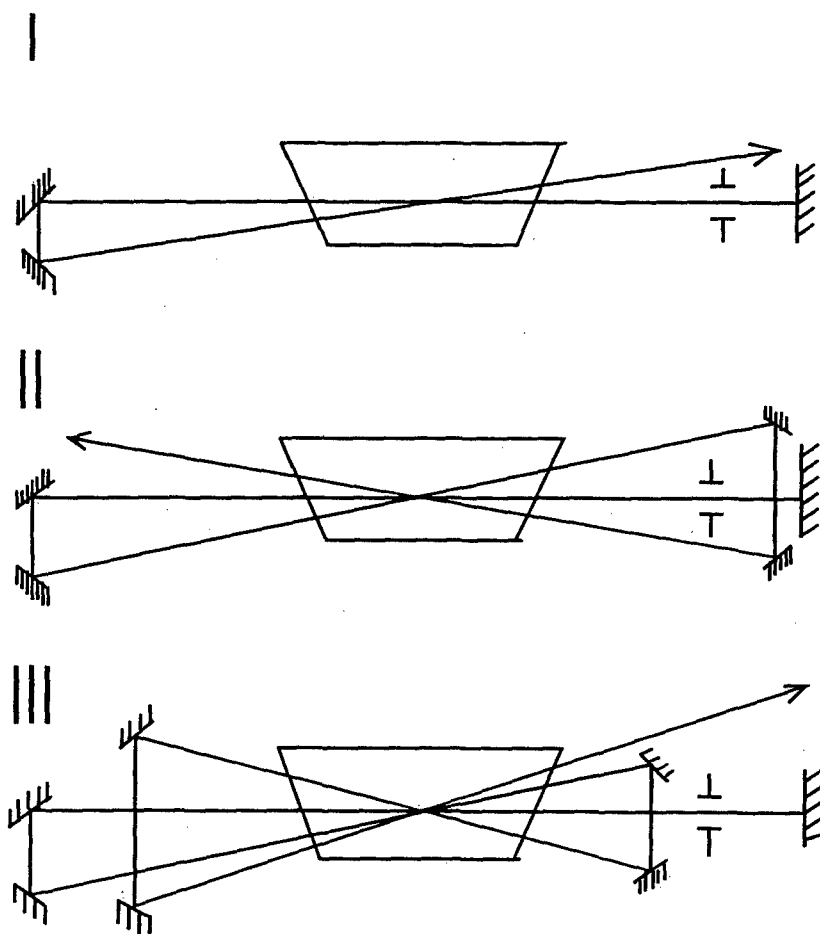
Different schemes of laser with distributed feedback on the population inversion gratings.
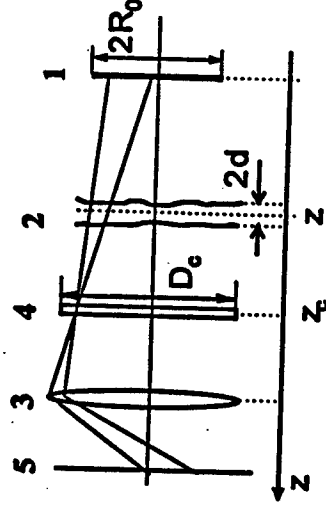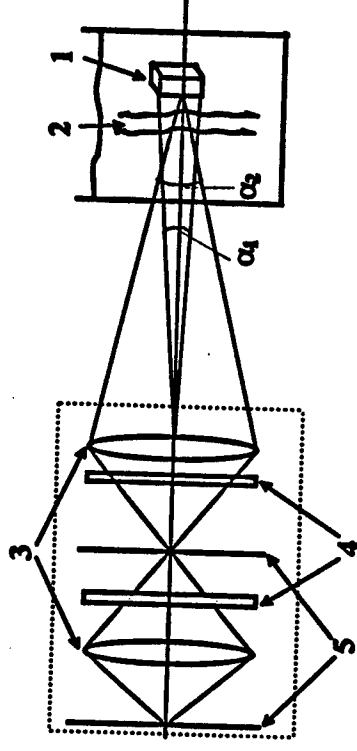
ANISOPLANATIC EFFECT IN VIEWING AT SHORT DISTANCES

V.I.Shmalhausen, N.A.Yaitskova

Moscow State University

Physics Department, International Laser Center.

1. Anisoplanatism in adative optics

2. Modification of the control algorithm
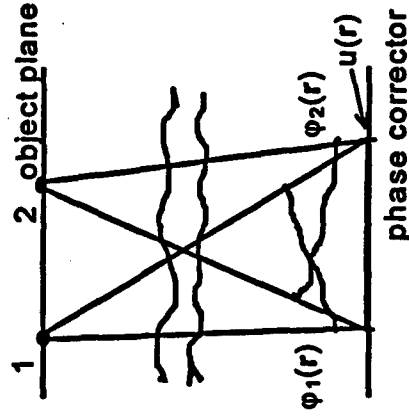
3. Position of the phase corrector

An adaptive system for turbulent distortion compensation and its equivalent

1. Object
2. Turbulent medium
3. Lenses
4. Wavefront corrector
5. Image plane

Extended object correction

$$u(\mathbf{r}) = \frac{1}{S_0}\int_{S_0}\varphi(\rho,\mathbf{r})\,d^2\rho$$

$$\varepsilon^2(\rho) = \frac{1}{S_A}\int_{S_A}<(\varphi(\rho,\mathbf{r})-u(\mathbf{r}))^2>\,d^2\mathbf{r}$$

$$I = \frac{1}{S_0}\int_{S_0}\varepsilon^2(\rho)\,d^2\rho = \sum_i \bar{\varepsilon}_i^2$$

$$\bar{\varepsilon}_i^2 = \frac{1}{S_0}\int_{S_0}\varepsilon_i^2(\rho)\,d^2\rho = <c_i^2>(1-\bar{K}_i)$$

$$\bar{K}_i = \frac{1}{S_0^2}\int_{S_0}\int_{S_0}K_i(\rho,\rho')\,d^2\rho\,d^2\rho'$$

Residual errors for two separated points in the object plane

$$\varphi_1(\bar{r}) = \sum_i c_i Z_i(\bar{r})$$

$$\varphi_2(\bar{r}) = \sum_i c'_i Z_i(\bar{r})$$

$$u(\bar{r}) = \sum_i a_i Z_i(\bar{r})$$

$$\varepsilon^2 = \sum_i <(c_i - a_i)^2>$$

$$\varepsilon'^2 = \sum_i <(c'_i - a_i)^2>$$

$$I = \frac{1}{2}\left(\varepsilon^2 + \varepsilon'^2\right)$$

1.

$$a_i = c_i \;\Rightarrow\; \varepsilon^2 = 0$$

$$\varepsilon'^2 = \sum_i <(c'_i - a_i)^2> = \sum_i \left(<c_i^2> + <c'^2_i> - 2<c_ic'_i>\right) = \sum_i \varepsilon_i^2$$

$$\varepsilon'^2_i = 2<c_i^2>(1-K_i) \qquad K_i = \frac{<c_ic'_i>}{<c_i^2>}$$
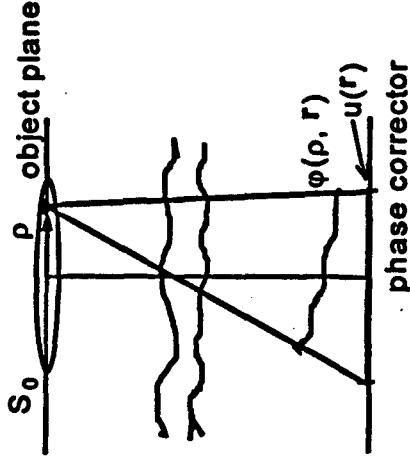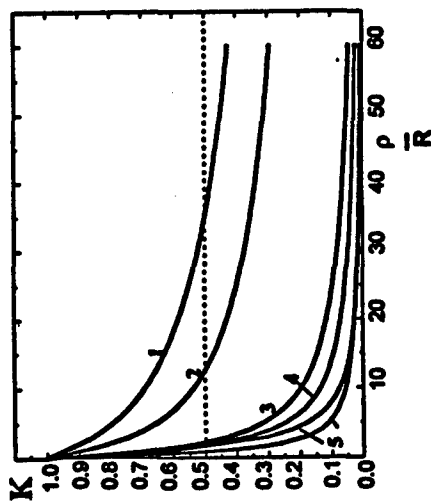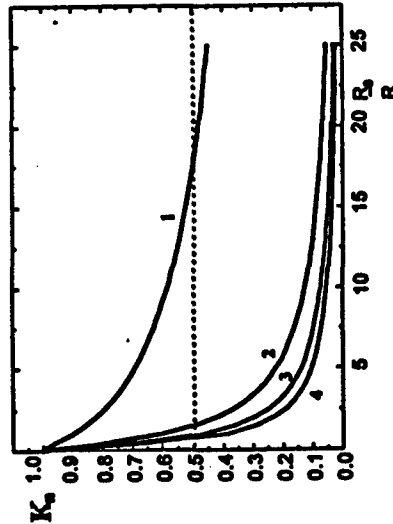
$$I_1 = \frac{\varepsilon'^2}{2} = <c_i^2>(1-K_i)$$

2.

$$I \to min \quad \Rightarrow \quad a_i = \frac{1}{2}(c_i + c'_i)$$

$$\left(\varepsilon_i^2 + \varepsilon'^2_i\right) = \frac{<c_i^2>}{2} + \frac{<c'^2_i>}{2} - <c_ic'_i>$$

$$I_2 = \frac{I_1}{2} = 0.5<c_i^2>(1-K_i)$$

Spatial correlation of Zernike coefficients

1 - X-tilt
2 - Y-tilt
3 - X-astigmatism
4 - defocus
5 - Y-astigmatism
6 - Spherical

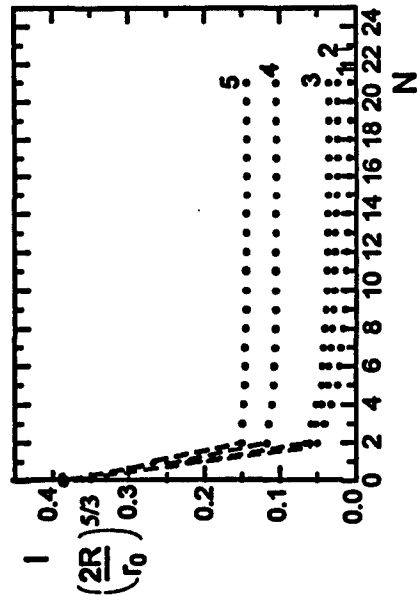# Spatial correlation of Zernike coefficients averaged over the object

1 - $n=1$ --tilts
2 - $n=2$ --defocus and astigmatism
3 - $n=3$ --coma

$$K_1(x) \approx \frac{1.33}{\sqrt[3]{x}}, \quad K_2(x) \approx \frac{1.32}{x}, \quad K_3(x) \approx \frac{0.76}{x}, \quad K_4(x) \approx \frac{0.54}{x},$$
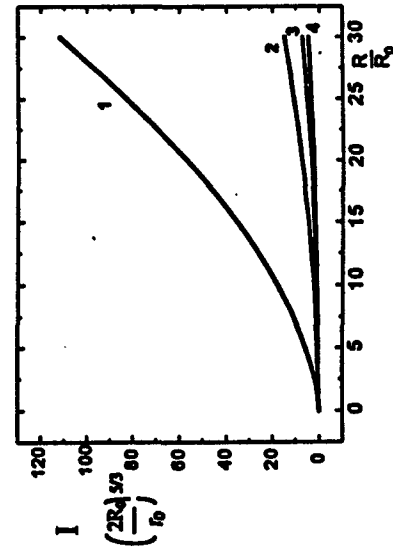
$$x = \frac{R_0}{R}, \quad x>1$$

Residual error in dependence on the number of corrected modes

Object radius

1 - $R_0=0$
2 - $R_0=0.25R$
3 - $R_0=0.5R$
4 - $R_0=2.5R$
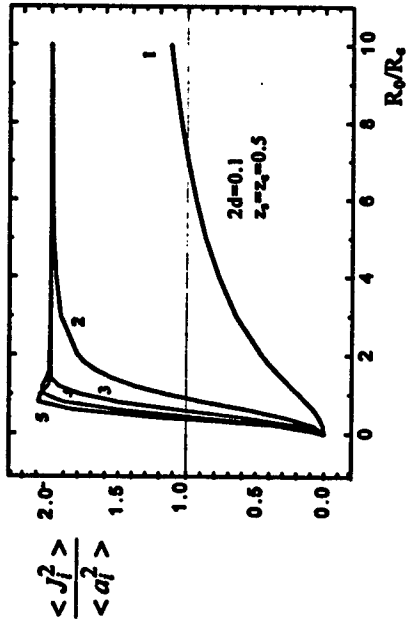5 - $R_0=5R$

Residual error in dependence on the aperture

Corrected modes:

1 - no correction
2 - tilts
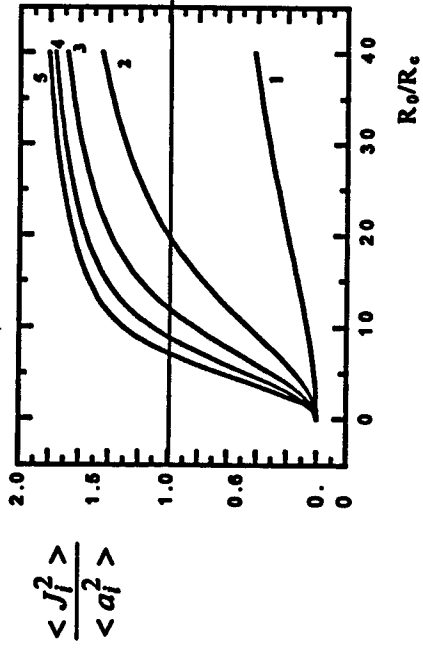3 - tilts and second order aberrations
4 - modes with $n=1,2,3$

Residual errors averaged over a circle

corrector in the aperture plane

$\dfrac{\langle J_i^2 \rangle}{\langle a_i^2 \rangle}$

$2d=0.1$
$z_r=z_\xi=0.5$

R_0/R_c

modes

1 - n=1

2 - n=2

3 - n=3

4 - n=4

corrector in the middle of the layer

$\dfrac{\langle J_i^2 \rangle}{\langle a_i^2 \rangle}$

R_0/R_c

modes

1 - n=1

2 - n=2

3 - n=3

4 - n=4

Residual error for the modified correction algorithm

$\langle J_i^2 \rangle$

$\left(\dfrac{D_c}{z_r r_0}\right)^{5/3}$

$n=l\ m=l\ l=-1$
$z_r=0.5$
$z_\xi=1$

ρ/R_c
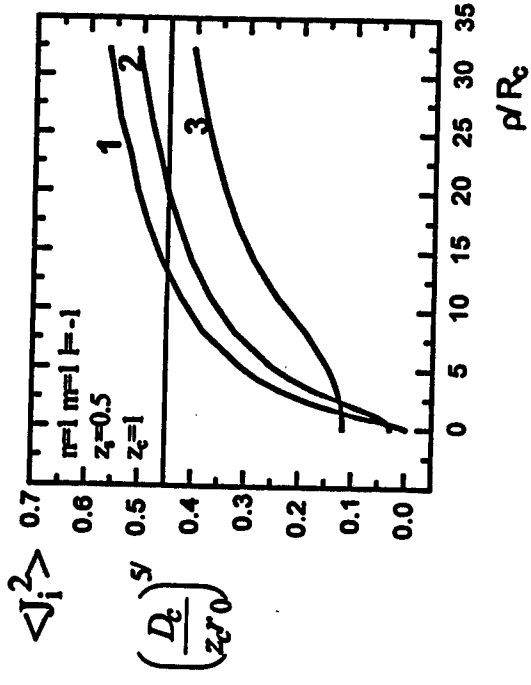
1 - $R_0=0$

2 - $R_0=2R_c$

3 - $R_0=10R_c$

Residual correction error in dependence on the coordinate of the phase corrector

Thin layer 2d=0.02

$<J_i^2>$

$\left(\dfrac{D_c}{z_c r_o}\right)^{5/3}$
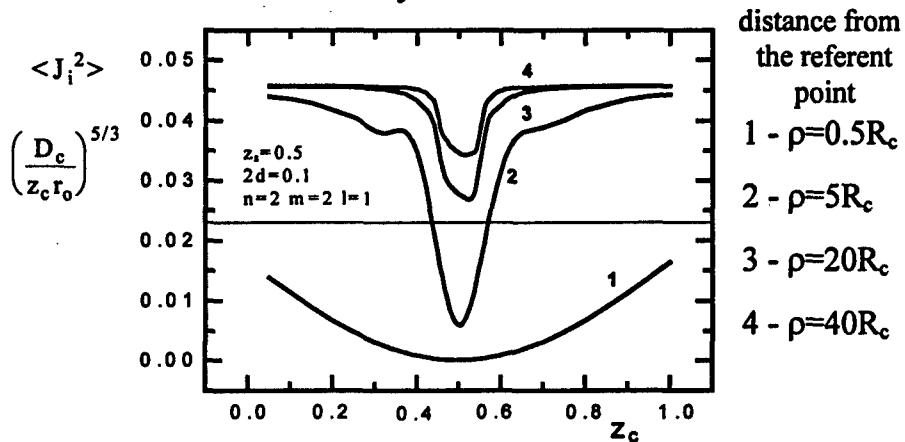
0.05
0.04
0.03
0.02
0.01
0.00

$z_s = 0.5$
$2d = 0.02$
$n=2\ m=2\ l=1$

0.0   0.2   0.4   0.6   0.8   1.0

z_c

distance from
the referent
point

1 - $\rho = 0.5R_c$

2 - $\rho = 5R_c$

3 - $\rho = 20R_c$

4 - $\rho = 40R_c$

Thick layer 2d=0.1

$<J_i^2>$

$\left(\dfrac{D_c}{z_c r_o}\right)^{5/3}$

0.05
0.04
0.03
0.02
0.01
0.00

$z_s = 0.5$
$2d = 0.1$
$n=2\ m=2\ l=1$

0.0   0.2   0.4   0.6   0.8   1.0

z_c

distance from
the referent
point

1 - $\rho = 0.5R_c$

2 - $\rho = 5R_c$

3 - $\rho = 20R_c$

4 - $\rho = 40R_c$
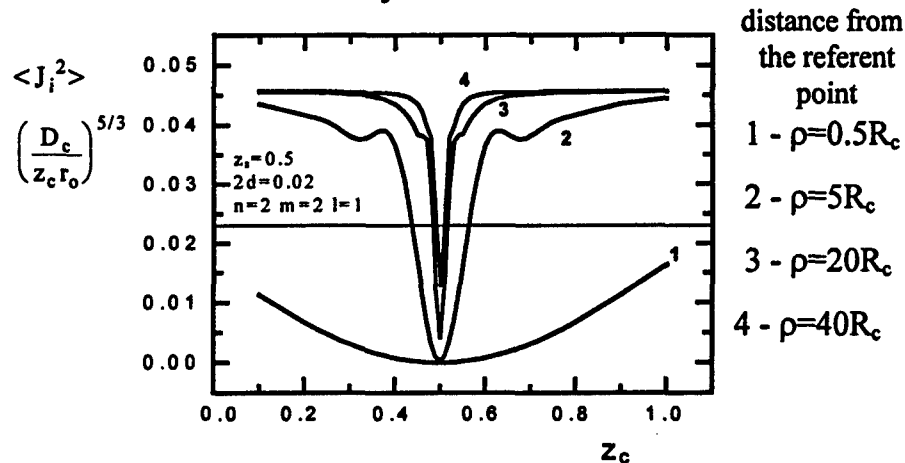
Residual error as a function of the distance from the referent point

The graph shows curves labeled 4, 5, 6 in the upper region and 1, 2, 3 in the lower region. The vertical axis is labeled $\langle J_i^2 \rangle$ with values from 0.00 to 0.05 and a factor $\left(\dfrac{D_c}{z_c r_0}\right)^{5/3}$. The horizontal axis is labeled ρ/R_c ranging from 0 to 30. Parameters: $2d=0.02$, $n=2$ $m=2$ $l=1$.
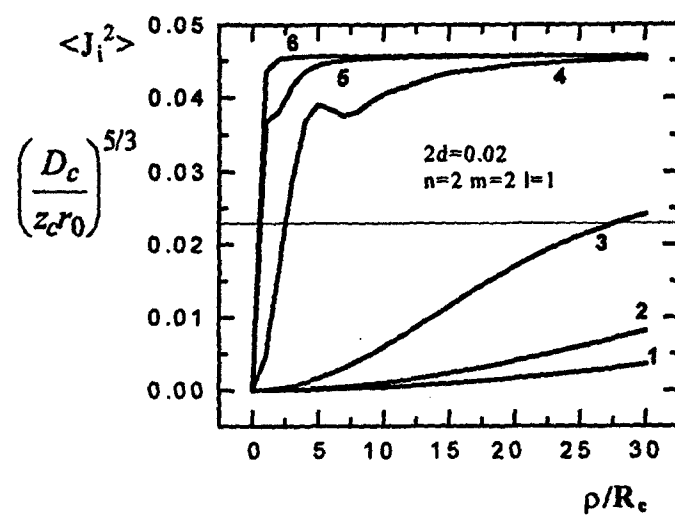
1,2,3 - corrector in the centre of the layer
1 - $z_c = z_s = 0.8$
2 - $z_c = z_s = 0.5$
3 - $z_c = z_s = 0.2$
4,5,6 - corrector in the input aperture plane
4 - $z_s = 0.8$
5 - $z_s = 0.5$
6 - $z_s = 0.2$